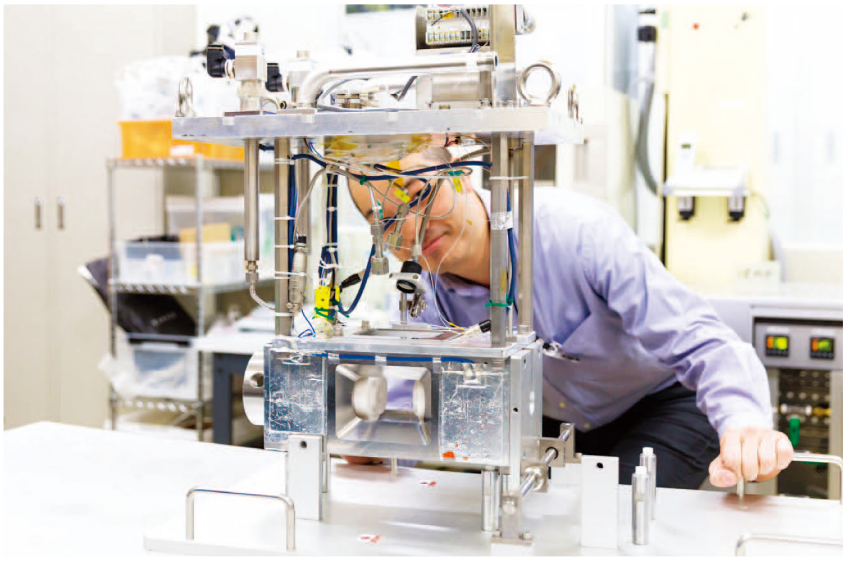

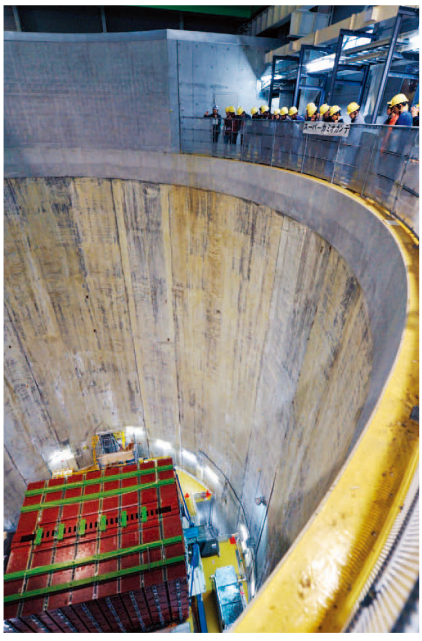

J-PARC

ANNUAL REPORT 2019

Vol.2: Materials and Life Science Experimental Facility

MLF ANNUAL REPORT

Cover photographs

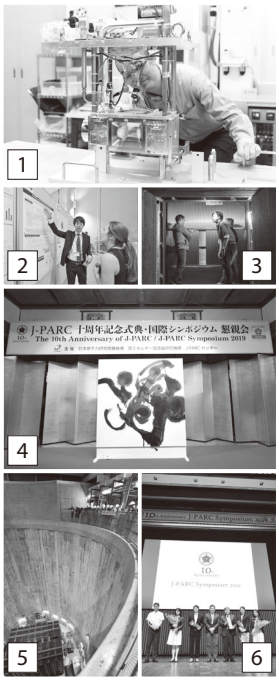

1 : Experimental setup at BL11 PLANET.

2 : Poster presentation at the J-PARC Symposium 2019.

3 : Participants at the 4th Neutron and Muon School and MIRAI PhD School 2019 take a tour inside the BL15 TAIKAN detector.

4 : Ceremony to mark the 10-year Anniversary of J-PARC at the J-PARC Symposium 2019.

5 : Site visit to the neutrino facility during the 4th Neutron and Muon School and MIRAI PhD School 2019.

6 : An awards ceremony at the J-PARC Symposium 2019.

J-PARC MLF
Materials and Life Science Division
J-PARC Center
https://mlfinfo.jp/en

J-PARC was jointly constructed and is now operated by the High Energy Accelerator Research Organization (KEK) and the Japan Atomic Energy Agency (JAEA).

Comprehensive Research Organization for Science and Society
https://neutron.cross.or.jp/en

J-PARC 20-02

Preface

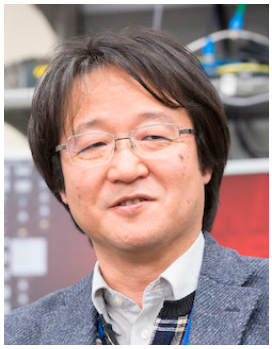

Toshiya Otomo
Division Head of Materials and Life Science Division, MLF

In fiscal year 2019, continuous efforts had been made for establishing stable operations of neutron and muon targets with high-power proton beam at the Materials and Life Science Experimental Facility (MLF). MLF ran the user program for 8 months with the proton beam power of 500 kW demonstrating the durability of the neutron mercury target and the graphite muon target under such power level. The validity of the system design to accommodate the final goal of 1-MW power was reconfirmed by a 1-MW test for ten hours on July 3. In the summer outage period, a newly designed mercury target vessel was installed to reduce the thermal stress on the target with the coupling-free structure between the inner mercury and the surrounding outer water. The muon target was also replaced with a brand-new spare in the summer outage. There are two lessons to be learned regarding the target operation: one is the gas processing of the neutron target which took longer than expected to secure its operation with sufficient radiation safety and the other is the replacement of the whole muon target system after a high-proton power operation minimizing the risk of radiation hazard during the replacement work. These experiences will result in a more robust and reliable system improvements.

Due to the stable operation of the facility, the MLF was able to produce many outcomes in various research fields. The research activities at the MLF resulted in more than 150 papers and 12 press releases. For realization of new instruments, the commissioning of a polarized neutron inelastic instrument, POLANO, and the continued efforts to increase the ultraslow muon intensity at the U-Line were in progress. New devices were developed, such as a brand new T0 chopper, an elliptical focusing mirror and a two-dimensional neutron detector whose spatial resolution is about 200 μm. Naturally, safety research was also essential to these research activities at MLF.

Maintaining the expansion of the total activities at MLF, we kept collaborating not only with domestic but also with foreign scientific facilities, such as ANSTO (Australia) and CSNS (China), in the areas of personnel, technique, and research exchange. Also, we were making efforts to communicate with members of the neutron and muon society through the annual meeting of industrial application at MLF held on July 18 and 19 (282 participants), the J-PARC symposium (909 participants), the 4th Neutron-Muon School (MIRAI PhD School) held from October 28 to November 2 (41 participants), and the CROSSroads Workshop (70 participants).

At the end of JFY2019, the COVID-19 pandemic affected the user program mainly because users could not travel to J-PARC, even though the applied proposals reached a record number in 2019B. Some of the planned experiments were done by instrument groups and others were carried over. Quantum Beam Science Festa, which is an annual conference mainly for domestic users of MLF J-PARC and IMSS KEK, was planned to be held in Mito on March 12 and 13, 2020, but was canceled due to COVID-19.

In the annual report, the research highlights and technical developments in 2019 are described in detail.

Materials and Life Science Division, Japan Proton Accelerator Research Complex
https://mlfinfo.jp/en

Preface

Mitsuhiro Shibayama
Director, CROSS

As a member of the Materials and Life Science Experimental Facility (MLF), the Comprehensive Research Organization for Science and Society (CROSS) is honored to release the J-PARC MLF ANNUAL REPORT 2019, which includes sections on Research and Development Highlights, Neutron Source, Neutron Science, Muon Science, and other topics. CROSS is the registered institution of the specific neutron beam facilities of J-PARC, appointed in 2011 by the Government of Japan, and it also supports the activities of the MLF. CROSS is engaged in operating the user program and running a fair and open proposal selection system for the seven Public Beamlines of the MLF: BL01 4SEASONS, BL02 DNA, BL11 PLANET, BL15 TAIKAN, BL17 SHARAKU, BL18 SENJU, and BL22 RADEN. It provides high-quality user support and promotes facility utilization for both academic and industrial researchers.

In 2019, the neutron beam was stably operated mostly at 500 kW, which ensured highly reliable machine operation even though in 2019B, the operation period was shortened due to a target problem. As of July 7, 2020, the total number of neutron proposals conducted at the MLF was 357 and the number of scientific papers published from MLF in 2019 was 153 (excluding proceedings). The details are included in the Research and Development Highlights collected in this volume. As for the Public Beamlines, 163 proposals (46% of the total neutron proposals) were conducted and 56 papers were published. Furthermore, 9 press releases came from the Public Beamlines. These numbers illustrate the high activities of the Public Beamlines, which have been used by a wide range of users from the academia and various industries.

It should be emphasized that a new web page "J-PARC MLF Next to Meet@MLF" was released in 2019 (https://mlfinfo.jp/en/), which delivers up-to-date information on the MLF. For example, the "Statistics" page released in November 2019 (https://mlfinfo.jp/en/aboutmlf/statistics.html), reports the statistics of the user program, beam operation, and the achieved results. The special program for new users "New User Promotion (NUP)", which started in 2016, was operated also in 2019, and 11 NUP neutron users conducted experiments at the MLF. Long-Term Proposals, started in 2017B, continued its successful run in 2019. J-PARC Join, an entry web page of J-PARC MLF also played an important role as a window for potential users, where CROSS members, together with four Science Coordinators, served as consultants. As a new activity of CROSS, Functional Polymer Consortium was launched in 2019. The consortium consists of five chemical companies and universities, and it has common scientific goals, namely, understanding the structure/properties of polymer and inorganic material interface in humid conditions.

I hope this Annual Report would provide useful information about the current status of the MLF operations and recent scientific achievements, the technical R&D reports, and so on. On behalf of CROSS, I extend a warm welcome to the past, current, and future MLF users.

Neutron Science and Technology Center, Comprehensive Research Organization for Science and Society
https://neutron.cross.or.jp/en

Contents

Research and Development Highlights

Neutron Source

Neutron Science

Muon Science

MLF Safety

MLF Operations in 2019

Organization Chart

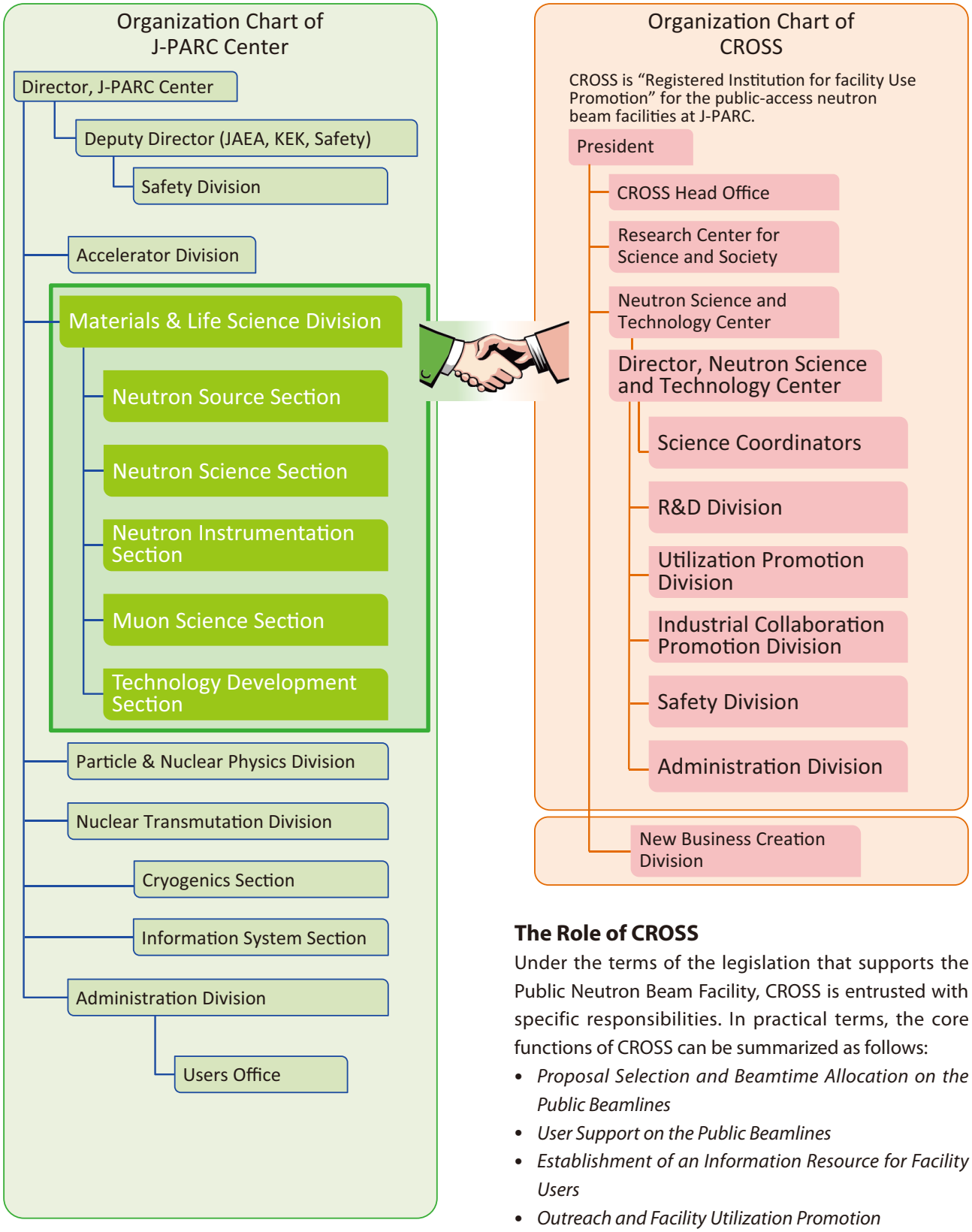

The Role of CROSS

Under the terms of the legislation that supports the Public Neutron Beam Facility, CROSS is entrusted with specific responsibilities. In practical terms, the core functions of CROSS can be summarized as follows:

- *Proposal Selection and Beamtime Allocation on the Public Beamlines*
- *User Support on the Public Beamlines*
- *Establishment of an Information Resource for Facility Users*
- *Outreach and Facility Utilization Promotion*
- *Contract Beamline Assessment and Selection*

J-PARC Map

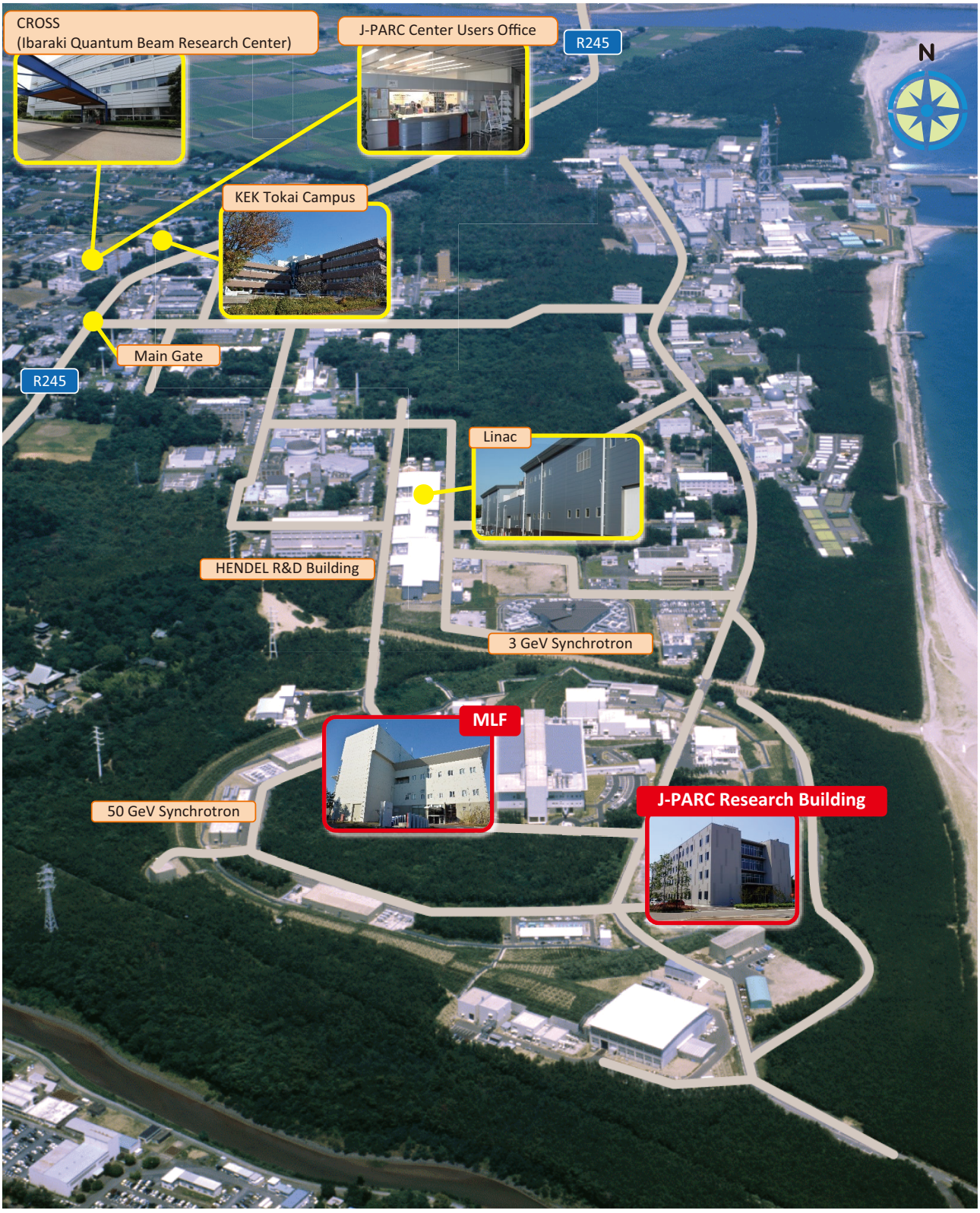
CROSS
(Ibaraki Quantum Beam Research Center)
J-PARC Center Users Office
R245
N
KEK Tokai Campus
Main Gate
R245
Linac
HENDEL R&D Building
3 GeV Synchrotron
MLF
50 GeV Synchrotron
J-PARC Research Building

Muon and Neutron Instruments

Muon Source

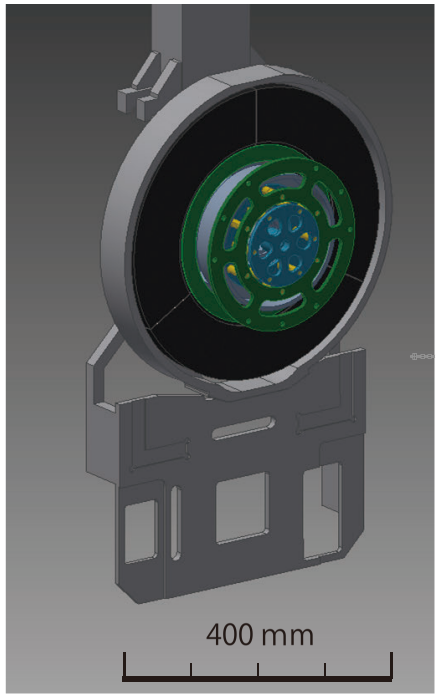

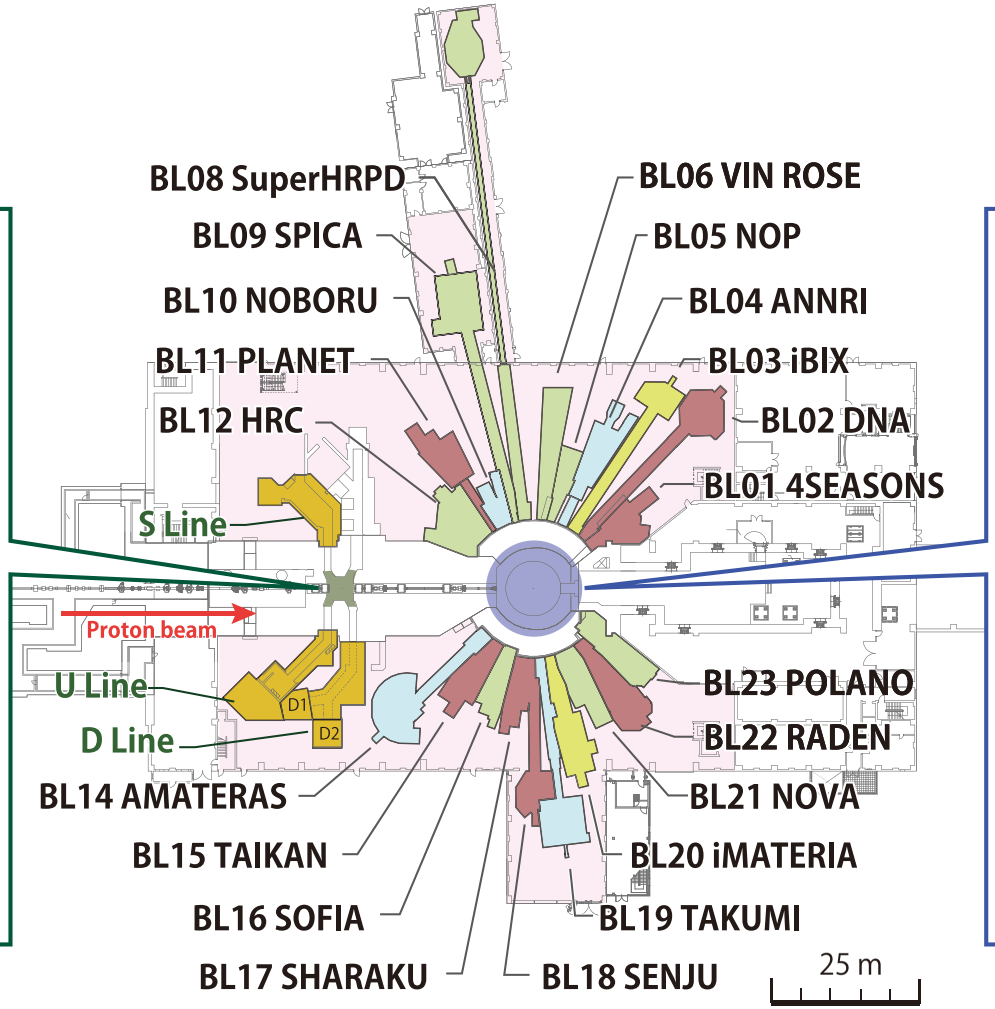

Neutron Source

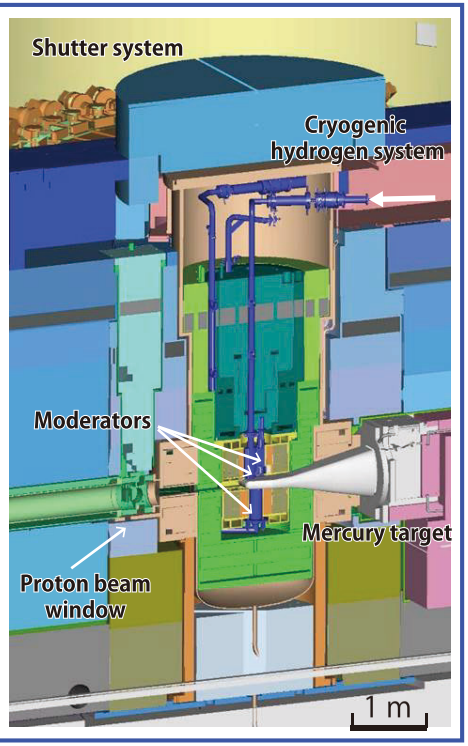

Muon Instruments

Neutron Instruments

JAEA

KEK

Public beam lines

Ibaraki Pref.

As of March 2020

Research and Development Highlights

Strong Local Moment Antiferromagnetic Spin Fuctuations in V-Doped LiFeAs

1. Introduction

Orbital selectivity plays an important role in iron-based superconductors, which are essentially multi-orbital systems. Our previous inelastic neutron scattering study reveals that Fermi surface nesting can tune the strength of spin excitations due to intra-orbital scattering and further affect the superconductivity in LiFeAs [1]. However, the effect of inter-orbital scattering on spin excitations and superconductivity is still unknown. In Vanadium-doped LiFeAs, a combined study of angle-resolved photoemission spectroscopy (ARPES) and transport measurements have demonstrated that the non-Fermi-liquid behavior is associated with the Fermi surface (FS) nesting between the hole Fermi pocket of d_{yz}/d_{xz} orbital at the Brillouin zone center and the electron pocket of d_{xy} orbital character at the corner [2]. However, the evidence of whether such kind of FS nesting could affect spin excitations is still missing.

In addition, based on the previous inelastic neutron scattering experiments on the total spin-fluctuating moment, the "122" and "111" families of iron pnictides are suggested to have the same nature, where the effective spin-fluctuating moment $S_{eff} \approx 1/2$, except for the LiFeAs and "11" families. Therefore, to fully understand the key ingredients of magnetism in iron-based superconductors, it is important to figure out the evolution of S_{eff} and the role of the itinerant or localized moment plays in different hole-doped families, which are believed to be more correlated and have large effective local moment.

2. Experiment

We prepared 7.2 g of $LiFe_{0.955}V_{0.045}As$ single crystals, which have a nearly perfect nesting between the d_{yz}/d_{xz} hole pockets and the d_{xy} electron pocket, and the superconductivity in this compound is completely suppressed. Among them, 1.8 g of the single crystals were synthesized by using isotope ^7Li to reduce the neutron absorption. All samples were co-aligned and glued on five 40 × 40 mm aluminum plates with the mosaic less than 5° in the glove box because of the air and humidity sensitivity of the samples. The inelastic neutron scattering experiment was carried out on the time-of-flight 4D-Space Access Neutron Spectrometer (4SEASONS) at Materials and Life Science Experimental Facility (MLF). The spectrometer was equipped with a highly efficient Fermi chopper, which could provide the multi-Ei mode with moderate resolution to collect the weak inelastic signals during the experiment.

3. Data analysis method

Due to the considerable unknown amount of Vanadium-containing flux from the growth of the single crystals used in our experiment, the traditional normalized method to get the absolute magnetic neutron-scattering intensity (by comparing it with the Vanadium standard) is unreliable, therefore we used the phonon normalization method, where we dealt with our data of V-doped samples by comparing the intensity of its phonon with the same phonon of other samples, which we have already carried out experiments on. Furthermore, we used the DFT+DMFT calculations to compute the electronic structure and spin dynamics of V-doped LiFeAs in the paramagnetic state. The DFT part is based on the full-potential linear augmented plane wave method implemented in WIEN2k in conjunction with Perdew–Burke–Ernzerhof generalized gradient approximation [3] of the exchange correlation functional. DFT+DMFT is implemented on top of WIEN2k and documented in ref. [4].

4. Results and conclusion

Our results compare the energy evolution of the spin excitations in $LiFe_{0.955}V_{0.045}As$ with the calculations based on the DFT+DMFT method for 10%-hole doping (about $LiFe_{0.967}V_{0.033}As$) (Fig. 1). Spin excitations display a small elongation along the longitudinal direction at 3 ± 1 meV, as the energy transfer increases from E = 3 to E = 18 meV, the elongation of the elliptical spin fluctuations changes from the longitudinal to transverse direction, which is similar to that in the hole-doped $Ba_{1-x}K_xFe_2As_2$, indicating the hole–electron Fermi surface nesting contribution from itinerant electrons.

From the energy dependence of theoretical and experimental local dynamical spin susceptibility depicted in the illustration (Fig. 2(a)), the low-energy magnetic excitations show a dramatical enhancement in the Vanadium doping LiFeAs, and this is double-checked through the constant-energy cuts result (Fig. 2(b)). We argue that such a strong enhancement of observed spin excitations cannot be simply attributed to the

extra moments introduced by magnetic impurities. Instead, we attributed the origin of such enhancement to a "spin mixing" process with enhanced inter-orbital scattering between $d_{xz/yz}$ and d_{xy} orbitals. Our results suggest that the inter-orbital scattering between $d_{xz/yz}$ and d_{xy} orbitals are bad for superconductivity and may dynamically mix the spin states of Fe^{2+} ions.

Moreover, we summarize the evolution of the effective magnetic moment S_{eff} in different families, including the results of the Vanadium doping in LiFeAs from our experiment, and introduce a spin crossover ground state from the inter-orbital scattering of itinerant electrons to understand the enlarged S_{eff} by doping holes with Vanadium in LiFeAs (Fig. 3).

The work has been recently published in ref. [5].

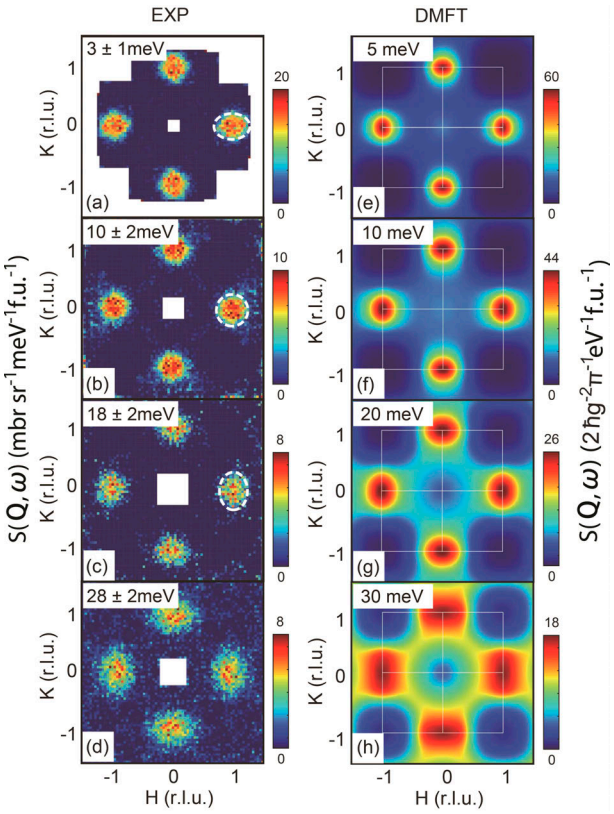

Figure 1. The two-dimensional image of energy dependence of the magnetic scattering of $LiFe_{0.955}V_{0.045}As$ with that of the DFT+DMFT calculations.

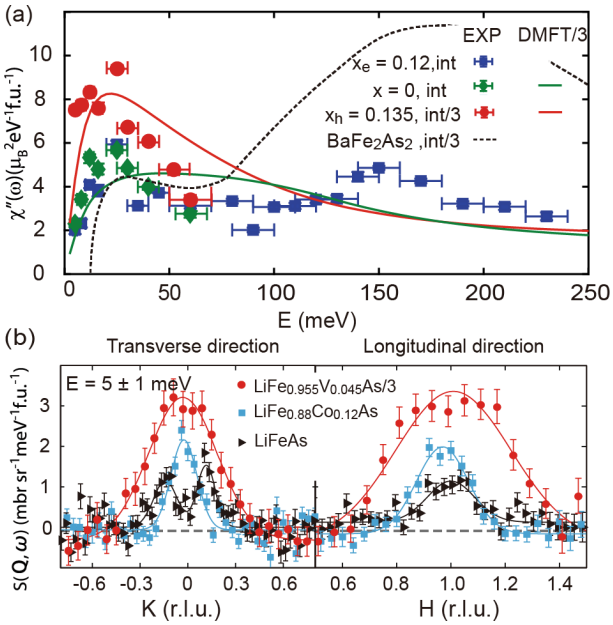

Figure 2. (a) Constant-energy cuts of spin excitations along the transverse [1,K] (left) and longitudinal [H,0] (right) directions for LiFeAs, $LiFe_{0.88}Co_{0.12}As$ (electron doping), and $LiFe_{0.955}V_{0.045}As$ (hole doping) at E = 5 ± 1 meV, respectively. (b) Theoretical and experimental local dynamical spin susceptibility in LiFeAs, $LiFe_{0.88}Co_{0.12}As$, $LiFe_{0.955}V_{0.045}As$, and $BaFe_2As_2$.

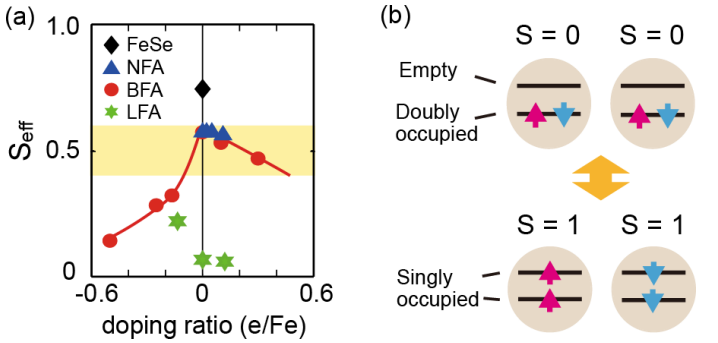

Figure 3. (a) The effective spin S_{eff} in various iron pnictide/chalcogenides superconductors obtained from neutron-scattering experiments. NFA, BFA, and LFA represent NaFeAs, $BaFe_2As_2$, and LiFeAs families, respectively. The energy integration range of χ'' (E) for the LiFeAs family of materials varies from 0 to about 60 mev and thus does not represent the total local dynamic susceptibility. (b) Schematics of the dynamic mixing of spin states with S = 0 and 1.

References

[1] Y. Li et al., Phys. Rev. Lett., **116** 247001 (2016).
[2] L. Y. Xing et al., Phys. Rev. B., **94** 094524 (2016).
[3] J. P. Perdew et al., Phys. Rev. Lett., **77** 3865 (1996).
[4] K. Haule et al., Phys. Rev. B, **81** 195107 (2010).
[5] Z. Xu et al., npj Quantum Materials, **5** 1 (2020).

Z. Xu[1], R. Kajimoto[2], K. Ikeuchi[3], X. Lu[1], and P. Dai[4]

[1]*Center for Advanced Quantum Studies and Department of Physics, Beijing Normal University;* [2]*Neutron Science Section, Materials and Life Science Division, J-PARC Center;* [3]*Neutron Science and Technology Center, CROSS;* [4]*Department of Physics and Astronomy, Rice University*

Quantum Dynamics of Hydrogen in the Iron-Based Superconductor Measured with Inelastic Neutron Spectroscopy

1. Introduction

In this study, we propose a direct method of detecting the superconducting gap in an iron-based superconductor via coupling to the hydrogen motion at interstitial sites. If there are two or more interstitial sites of hydrogen in the neighborhood, the overlap of wave functions gives rise to the splitting of the hydrogen energy levels [1, 2]. This is known as tunneling splitting as previously observed in superconductors using inelastic neutron scattering (INS) [1, 3]. The magnitudes of the tunneling splitting are usually much smaller in comparison with the superconducting gap. Here, we report that the hydrogen vibration in iron-based superconductors is highly anharmonic at the interstitial sites. As a result, generalized tunneling splitting has an exceptionally large energy of the order of 10 meV. This means that the hydrogen motion serves as a good probe to the superconductivity. Such the local dynamics is not affected by the sample quality; thus, the hydrogen probe has a unique advantage compared to conventional spectroscopies.

2. Experimental

We prepared a powder sample of $FeAsO_{0.9}D_{0.1}$ (D-sample) under high pressure. Hydrogen anions (D^-) were replaced for O^{2-} anions. In addition, owing to a tiny amount of H in the deuterated reagents, H and D mixture is inevitable with the H/D ratio ~0.02. We also prepared $LaFeAsO_{0.9}F_{0.1}$ (F-sample) under ambient pressure as the reference of D-sample. INS intensities for D- and F-samples were measured using a chopper spectrometer (4SEASONS) [4] at BL01 in the pulsed-neutron source in MLF at J-PARC. Data were collected at incident neutron energies of $E_i = 9.3$, 17.5, and 44.5 meV [5]. The time-of-flight data from position-sensitive detectors were converted into the Q-angle average S(Q, ħω) angle of the dynamical structure factor by the UTSUSEMI program [6].

3. Results and discussion

Figure 1 illustrates S(Q, ħω) for D- and F-samples (S_D and S_F) with their difference S_{D-F} [7]. We find three excitations at 6 K below T_c [Fig. 1(a)], all of which are insensitive to Q. However, they exhibit a strong diffusive character over the entire energy range at 41 K above T_c [Fig. 1(b)]. In sharp contrast to S_D, the results of S_F exhibit neither flat excitations at 6 K [Fig. 1(c)] nor diffuse scattering at 41 K [Fig. 1(d)]. Instead, temperature-insensitive phonon scatterings are visible at ħω ≈ 12 meV. In the difference map S_{D-F}, the three distinct features U,

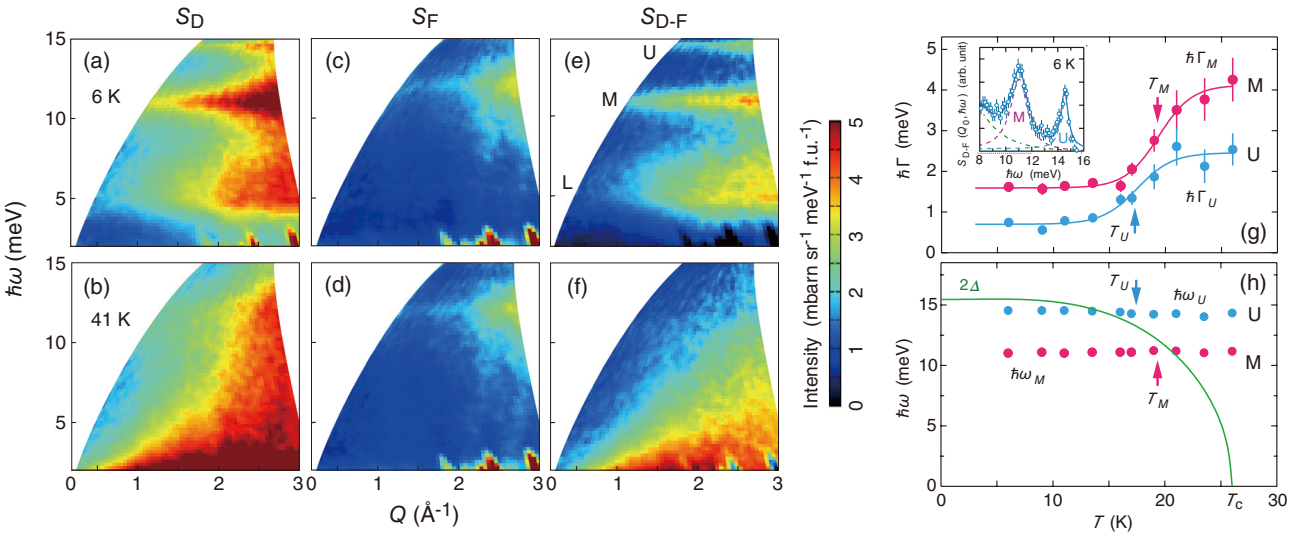

Figure 1. Color plots of S(Q, ħω) at 6 K (a), (c), (e), and 41 K (b), (d), (f). The incident neutron energy is $E_i = 17.5$ meV. (a), (b) S_D from D-sample; (c), (d) S_F from F-sample; (e), (f) the difference map S_{D-F}. Temperature dependence of (g) the linewidth ħΓ(T) and (h) the peak position ħω for the U and M modes. Inset of (g) represents scattering intensities with incident neutron energy E_i = 17.5 meV at 6 K for $Q_0 = 2.15 \pm 0.15$ Å^{-1}. The green solid line shows the temperature dependence of the BCS gap function 2Δ(T).

M, and L are clearly observed in Fig. 1(e). Since D- and F-samples have almost the same electric and superconducting properties, the strong excitations in S_{D-F} must arise from hydrogen.

Inset of Fig. 1(g) displays the energy spectra of S_{D-F} at 6 K with $Q_0 = 2.15 \pm 0.15$ Å^{-1} [7]. We fit the scattering peaks by using a Lorentzian spectrum with a linewidth $\hbar\Gamma(T)$. Figure 1(g) plots the temperature dependence of $\hbar\Gamma(T)$ for U and M modes. They indicate minute temperature dependence for $T < 15$ K, but increase rapidly at around 20 K. Eventually, both linewidths are weakly temperature dependent toward $T_c \sim 26$ K. Contrastingly, each peak position $\hbar\omega$ is nearly constant against temperature [Fig. 1(h)].

We deem that the rapid increase of $\hbar\Gamma$ at $T < T_c$ arises from the coupling of the hydrogen motion and the electronic excitations. With increasing temperature toward T_c, the superconducting gap $\Delta(T)$ decreases so as to satisfy $\hbar\omega > 2\Delta(T)$. Based on this mechanism, S_{D-F} serves as a probe for detecting the superconducting gap. The change of width is interpreted in terms of a Korringa-type relaxation due to the conduction electrons, which becomes active as the superconducting gap decreases.

Firstly, we determine the inflection point of $\hbar\Gamma$ at T_U and T_M. Next, we evaluate the superconducting gap Δ_0 assuming the BCS-type gap dependence. The estimated value $\Delta_0 = 7.8 \pm 0.7$ meV, which agrees reasonably well with the relation $\hbar\omega = 2\Delta(T_\alpha)$ (α = U and M) [Fig. 1(h)]. The Δ_0 gives the ratio $2\Delta_0/k_BT_c = 7.0$, which characterizes this compound as a strong-coupling superconductor. According to the point-contact spectra on $LaFeAsO_{0.9}F_{0.1}$ [8], two gaps have been reported, $\Delta_1 \approx 7.9$ meV and $\Delta_2 \approx 2.8$ meV, the former of which matches our result.

We proceed to consider the microscopic origin of the observed excitations. In order to investigate the stable positions of the interstitial hydrogen, we carried out first-principles calculations using VASP code. Figures 2(a) and 2(b) illustrate the crystal structure $LaFeAsO_{0.9}D_{0.1}$ and the contour map of the calculated effective potential $\Delta E(\boldsymbol{r})$ on the xy plane at $z = 0.425$ [7]. Four potential minima appear in at (0.11, 0.11, 0.425) and their crystallographically equivalent positions related by the four-fold rotational symmetry at H_{int}. A Bader charge analysis gives the charge of hydrogen at H_{int} to be 1.33, implying the interstitial hydrogen to be hydride.

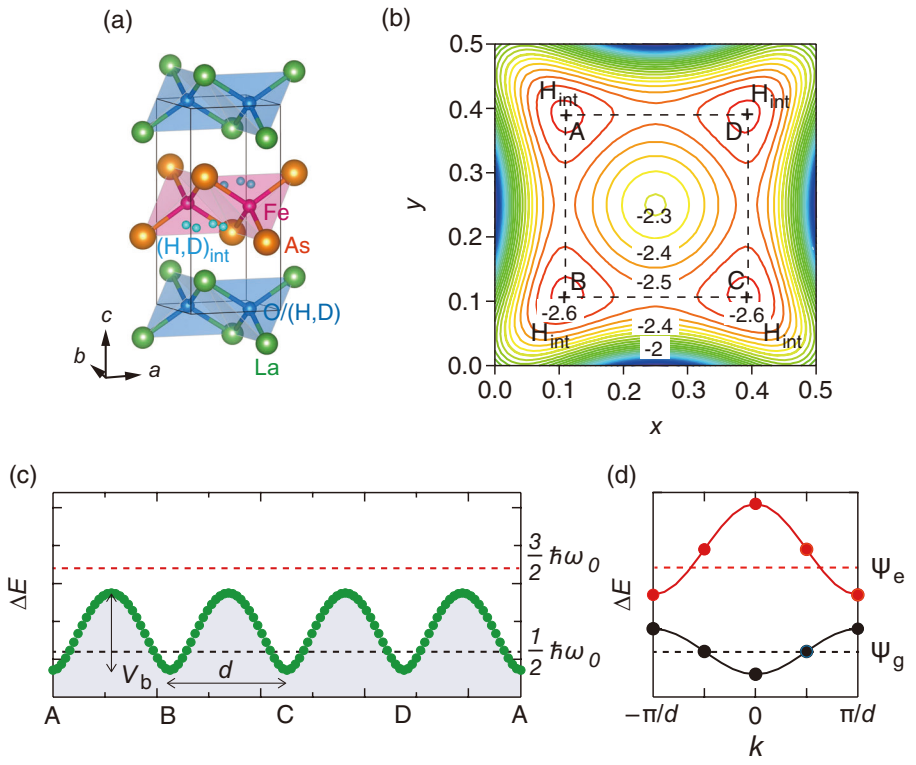

Figure 2. (a) Crystal structure of $LaFeAsO_{0.9}D_{0.1}$ with the interstitial site H_{int}. (b) Contour map of hydrogen potential ΔE in units of eV on the xy plane at $z = 0.425$. (c) The line profiles of ΔE through the minima A-B-C-D-A of (b) on $z = 0.425$. The tunneling distance d and the potential barrier V_b between the minima are described. The black and red dashed lines represent the ground state and the first excited state, respectively. (d) The black line shows the spectrum of the tunneling splitting, and the red line shows that of the highly anharmonic phonons called as quantum rattling.

We consider the dynamics of the interstitial hydrogen. Figure 2(c) plots the line profile through the minima A-B-C-D-A as seen in Fig. 2(b) [7]. This corresponds to the pathway of hydrogen migration. The profile features a periodic potential with a tunneling distance d = 1.13 Å and potential barrier V_b = 102 meV. Assuming the sinusoidal potential, the angular frequency ω_0 is given by $\omega_0^2 = 2\pi^2 V_b/(md^2)$, where m is the isotope mass. We obtain $\hbar\omega_{0,H}$ = 81 meV for H and $\hbar\omega_{0,D}$ = 57 meV for D. Considering the cross section ratio $\sigma_{inc}(H)/\sigma_{inc}(D) \approx 40$ and the concentration ratio $n_H/n_D \approx 0.02$, the scattering intensities from the two isotopes should be comparable. Hence, we propose that the U and M modes come from the interstitial H and D, respectively. The ratio $\omega_U/\omega_M \approx 1.3$ is rather close to the square root of the atomic mass ratio $\sqrt{m_D/m_H} = \sqrt{2}$. This might be regarded as the isotope effect for harmonic phonons.

We now check the possibility tunneling motion of hydrogen for U and M modes. The magnitude of the tunneling splitting is known to be sensitive to the distance and mass of the isotopes [1, 3]. For example, the tunneling splittings ratio $\omega_H/\omega_D \approx 10$ for Nb [9] and $\omega_H/\omega_D \approx 4$ for α-Mn [10] were reported. Hence, the present value $\omega_U/\omega_M \approx 1.3$ is not consistent with the identification of tunneling splitting.

We here propose that the excitations at $\hbar\omega_U$ and $\hbar\omega_M$ are associated with a different type of extremely anharmonic phonons, which can be called quantum rattling. In this consideration, the potential barrier is so low that the ordinary excited state is actually extended along the pathway connecting the four potential minima [Fig. 2(c)]. In the four potential minima system, the eigenstates are characterized by the wave numbers k = 0, $\pm\pi/(2d)$, and $\pm\pi/d$, as described in Fig. 2(d). In addition, the eigenstates are related to the superposition of localized phonons, which have energies $(n+1/2)\hbar\omega_0$ with n = positive integer. If we assign $\hbar\omega_M$ = 11.1 meV as the deuterium excitation from Ψ_g (k = 0) to Ψ_e (k = π/d), the corresponding protium excitation is expected at 16.6 meV, which agrees with the experimental value $\hbar\omega_U$ = 14.5 meV.

4. Future Plans

The hydrogen spectroscopy has a unique feature to scan along the temperature axis with a fixed energy against other spectroscopies scanning along the energy axis. The hydrogen interstitial sites as calculated in the present work may be common in iron-based superconductors. Thus, we will try to determine the superconducting gaps for iron-based materials that lack single crystals and include magnetic impurities. With a further refinement of both measurement and analysis, the hydrogen probe should provide more useful information for clarifying the superconducting gap.

References

[1] Y. Fukai, The Metal-Hydrogen System: Basic Bulk Properties, Springer series in materials science Vol. **21** (Springer, Berlin, 2003).

[2] Hydrogen in Metals I: Basic Properties, Topics in Applied Physics Vol. **28**, ed. by G. Alefeld and J. Völkl (Springer, Berlin, 1978).

[3] Hydrogen in Metals III: Properties and Applica-tions, Topics in Applied Physics Vol. **73**, ed. by H. Wipf (Springer, Berlin, 1997).

[4] R. Kajimoto et al., J. Phys. Soc. Jpn., **80** SB025 (2011).

[5] M. Nakamura et al., J. Phys. Soc. Jpn., **78** 093002 (2009).

[6] Y. Inamura et al., J. Phys. Soc. Jpn., **82** SA031 (2013).

[7] J. Yamaura et al., Phys. Rev. B, **99** 220505(R) (2019).

[8] R. S. Gonnelli et al., Eur. J. Phys., **7** 251 (2009).

[9] A. Magerl et al., Phys. Rev. Lett., **56** 159 (1986).

[10] A. I. Kolesnikov et al., Physica B, **263–264** 421 (1999).

J. Yamaura[1], H. Hiraka[2], S. Iimura[1], Y. Muraba[1], J. Bang[1], K. Ikeuchi[4], M. Nakamura[5], Y. Inamura[5], T. Honda[3], M. Hiraishi[3], K. M. Kojima[6], R. Kadono[3], Y. Kuramoto[3], Y. Murakami[1,3], S. Matsuishi[1], and H. Hosono[1]

[1]Materials Research Center for Element Strategy, Tokyo Institute of Technology; [2]Korea Atomic Energy Research Institute; [3]Institute of Materials Structure Science, KEK; [4]Neutron Science and Technology Center, CROSS; [5]Neutron Science Section, Materials and Life Science Division, J-PARC Center; [6]Centre for Molecular and Materials Science, TRIUMF

The Effects of Metal Cations on the Hydration Water between Phospholipid Bilayers

1. Introduction

Specific ion effects on biological systems have attracted considerable attention in recent decades [1]. For biological membranes in physiological environments, the interactions between metal cations and lipid headgroups are essential and significant. Monovalent and divalent cations such as Na^+, K^+, Mg^{2+}, and Ca^{2+} exist in high concentrations in biological environments and play important roles in regulating cell polarization and action potentials. The interactions of ions with membranes also influence biological functions. Ions bound to biological membranes reduce the membrane dipole potential and influence the hydration structure. Specific ion interactions with proteins are also important for various biological functions. For example, divalent cations such as Mg^{2+}, Fe^{2+}, and Zn^{2+} are important for certain enzymatic reactions.

Although the effects of salts on lipid bilayers have been intensively studied, several aspects of the mechanism by which salts affect the physical properties of lipid bilayers remain unclear. Recently, Alsop et al. studied the effects of divalent cations on lipid membranes in stacked 1,2-dimyristyl-sn-glycero-3-phosphocholine (DMPC) lipid bilayers using high-resolution X-ray diffraction (XRD) [2]. The location of cation binding on the lipid membrane was found to depend on the cation; Ca^{2+} and Zn^{2+} preferred to bind close to the glycerol group, while Mg^{2+} and Fe^{2+} bound near the phosphate group. Owing to the size effect, Fe^{2+} receded further from the glycerol group compared to Mg^{2+}. The distance of the binding site from the lipid-water interface was found to increase in the following order: $Fe^{2+} < Mg^{2+} < Ca^{2+} < Zn^{2+}$. The number of water molecules, n_w, interacting with metal ions, was shown to correlate with the distance from the interface with approximate n_w values of 12 for Fe^{2+}, 9 for Mg^{2+} and Ca^{2+}, and 8 for Zn^{2+}. The results also suggested that the location of the ion could be related to the swelling of the lipid bilayer. Yang et al. systematically calculated the free energies of Na^+, K^+, Ca^{2+}, and Mg^{2+} bound to phospholipids, and the calculation results were consistent with the XRD analysis [3]. These findings are important to understand the effects of metal cations on lipid membranes and their biological functions. However, several questions remain unanswered. How do divalent cations modify the hydration structure? How is the number of hydration water molecules determined? What is the role of the Hofmeister effects? What is the molecular mechanism involved in increasing the intermembrane distance?

Biological molecules such as nucleic acids, proteins, and carbohydrates are surrounded by water molecules, and function in complex environments. While the importance of the structure and dynamics of water molecules near biological molecules is acknowledged, few detailed studies have been carried out on these systems due to experimental difficulties. Quasi-elastic neutron scattering (QENS) is a powerful technique to investigate the dynamic behavior of water molecules around biological molecules [4]. In our recent QENS study on water molecules sandwiched between perdeuterated lipid bilayers of multilamellar vesicles (MLV) [5], the QENS spectra were analyzed in terms of the dynamic behaviors of three types of hydration water: (1) free water, whose dynamics are slightly different from those of bulk water due to the confinement effect; (2) loosely bound water, for which the dynamics are one order of magnitude slower than those of free water; and (3) tightly bound water, which exhibits cooperative dynamics with DMPC molecules. The number of tightly bound water molecules per lipid molecule was found to be approximately 7 at 275 K and was reduced to 2 when the temperature was increased to 316 K. In contrast, the number of loosely bound water molecules per lipid molecules was also ~7 at 275 K and increased to 12 at 316 K. The number of free water molecules remained constant in the measured temperature range. The results suggest that changing the temperature can modulate the ratio of tightly to loosely bound water molecules without changing their sum.

In this work, further QENS experiments were carried out on the effects of metal cations on hydration water between phospholipid bilayers. The binding of Mg^{2+} and Fe^{2+} to lipid headgroups was found to drastically change the number of tightly bound water molecules, whereas the binding of Ca^{2+} did not affect the dynamic behavior of hydration water to a significant extent [6].

2. Experimental

Perdeuterated lipid *d*67DMPC with an isotopic purity of more than 99% was purchased from Avanti Polar Lipids Inc.; it was used without further purification. The QENS measurements were carried out using the time-of-flight near-backscattering spectrometer DNA (BL02). The power of the injected proton beam incident on the neutron target was 300 kW (in the case of $CaCl_2$) or 500 kW (in the cases of $MgCl_2$ and $FeCl_2$).

3. Results and Discussion

As in the case of the mixture without salt, the hydration water sandwiched between the lipid bilayers could be classified as one of three hydration water types with different dynamic behaviors: tightly bound water molecules, loosely bound water molecules, and free water molecules. According to this model, the observed QENS profiles were fitted with the sum of three Lorentz functions convoluted with the resolution function.

The half-width at half-maximum (HWHM) of the Lorentz function corresponding to the tightly bound water is proportional to Q^2, and the properties of the tightly bound water can be explained by simple diffusion. On the other hand, the Q^2 dependence of the HWHM's of Lorentz functions corresponding to the loosely bound water and the free water can be interpreted using the jump diffusion model as in the cases of the bulk water with and without salt.

The diffusion coefficients *D* of all samples are summarized in Fig. 1 along with the data from the literature for comparison. The *D* values of the samples with salts were nearly the same as those of the sample without salt. The *D* value of water in an aqueous solution of $CaCl_2$ was in the same order of magnitude as those of free water incorporated between lipid bilayers and slightly less than that of bulk water.

The numbers of the three types of water molecules in the mixtures of *d*67DMPC-37H_2O-0.25XCl_2 (X = Ca, Mg, Fe) were estimated by analyzing the coefficients of the Lorentz functions. The numbers of the three types of water molecules in the sample with $CaCl_2$ were nearly identical to those in the sample without salt. This suggests that the presence of $CaCl_2$ does not affect the hydration water to any significant extent.

In contrast, the estimated numbers of different types of water molecules in *d*67DMPC-37H_2O-0.25$MgCl_2$ and *d*67DMPC-37H_2O-0.25$FeCl_2$ were strikingly different compared to the sample with $CaCl_2$. Compared to the $CaCl_2$ system, the numbers of tightly bound water molecules were clearly higher in the $MgCl_2$ and $FeCl_2$ systems, while the numbers of free water molecules were lower. On the other hand, the numbers of loosely bound water molecules in these systems, along with their temperature dependences, were nearly identical to those in the corresponding systems without salt. (See Fig. 2.)

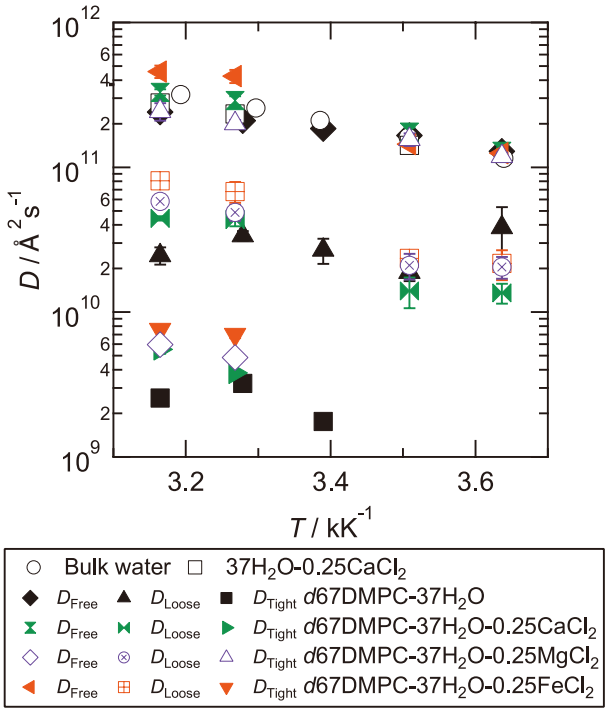

Figure 1. Arrhenius plot of the diffusion coefficients of *d*67DMPC-37H_2O-0.25XCl_2 (X = Ca, Mg, Fe). The diffusion coefficients of bulk water and the three types of hydration water in *d*67DMPC-37H_2O without salt [5] are shown for comparison.

High-resolution XRD studies have indicated that Mg^{2+} and Fe^{2+} ions bind near the phosphate groups of lipid molecules, while Ca^{2+} binds near the glycerol group [2]. In addition, the number of hydration water molecules (n_w) seems to depend on the binding position of each cation. The findings of the present study are consistent with these XRD results but provide a more detailed description of the hydration structures and dynamics. The sum of tightly bound water and loosely bound water comes to approximately 21 molecules per lipid molecule for the $MgCl_2$ and FeC_2 systems; in contrast, this sum is approximately 13 molecules per lipid molecule for the systems without salt and with $CaCl_2$. The present study indicates that the number of loosely bound water molecules does not change upon the addition of salt, suggesting that the number of loosely bound water molecules is determined by the nature of the DMPC membrane.

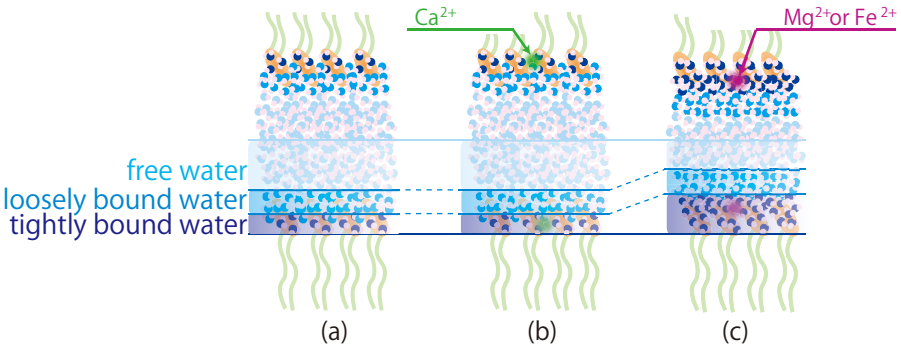

Figure 2. Schematic image of the positions of metal cations and the numbers of three types of water.

References

[1] P. L. Nostro and B. W. Ninham, Chem. Rev. **112**, 2286 (2012).
[2] R. J. Alsop, et al., Soft Matter **12**, 6737 (2016).
[3] J. Yang, et al., J. Chem. Theory Comput. **11**, 4495 (2015).
[4] T. Yamada and H. Seto, Front. Chem. **8**, 8 (2020).
[5] T. Yamada et al., J. Phys. Chem. B **121** 8322 (2017).
[6] H. Seto and T. Yamada, Appl. Phys. Lett. **116** 133701 (2020).

H. Seto[1, 2] and T. Yamada[3]
[1]Neutron Science Section, Materials and Life Science Division, J-PARC Center; [2]Institute of Materials Structure Science, KEK; [3]Neutron Science and Technology Center, CROSS

Sliding Motion of Ring Molecules in Polyrotaxane

1. Introduction

Polyrotaxane (PR) is topologically connected supramolecular assembly composed of multiple ring molecules and an axial polymer chain. The unique feature of PR is that the rings can slide along the axial chain. The sliding motion leads to various types of applications of PR as molecular shuttles [1], drug delivery systems [2], and slide-ring materials with slidable cross-links [3]. However, the sliding dynamics of the rings in PR has not been fully studied.

In this study, we investigate molecular dynamics of polyrotaxane (PR), composed of α-cyclodextrins (CDs) and a poly(ethylene glycol) (PEG) axis chain, in solution by means of quasi-elastic neutron scattering (QENS) measurements and full-atomistic molecular dynamics (MD) simulations [4]. First, we estimated the diffusion coefficients of CDs and PEG monomers in PR via QENS experiments with deuterium labelling technique. Then, we performed molecular dynamics (MD) simulations to evaluate the sliding diffusion coefficient of CD on PEG in PR.

2. Experimental

For the QENS experiments, PR was synthesized with α-cyclodextrin (CD) as a cyclic molecule and polyethylene glycol (PEG) with an average molecular weight of 35,000 as a polymer chain. The coverage of CD on PEG was 6.9%. In order to separate the relaxation components of CD and PEG, we prepared hPR with hydrogenated PEG and dPR with deuterated PEG (Fig. 1). The PRs were dissolved in DMSO-d_6 with concentration of 10 wt%. QENS measurements were conducted with Biomolecular Dynamics Spectrometer (DNA) at Japan Proton Accelerator Research Complex (J-PARC). The Q range was 0.08 to 1.98 Å^{-1}, the energy resolution ($\Delta E/E$) was 3.6 μeV and the energy transfer range was –40 to 100 μeV in all the measurements. The measurements were conducted at 30°C

For the MD simulations, we used CHARMM force field and GROMACS2016.5. We fabricated the model of PR with 3 CD molecules and a PEG with 80 mer (Fig. 2). For the initial structure, one PR was set in a 15×15×15 nm simulation box filled with DMSO molecules. We conducted a 200-ns NPT calculation at 300 K, and obtained mean-squared displacement (MSD) of hydrogen atom of PEG and CD in PR.

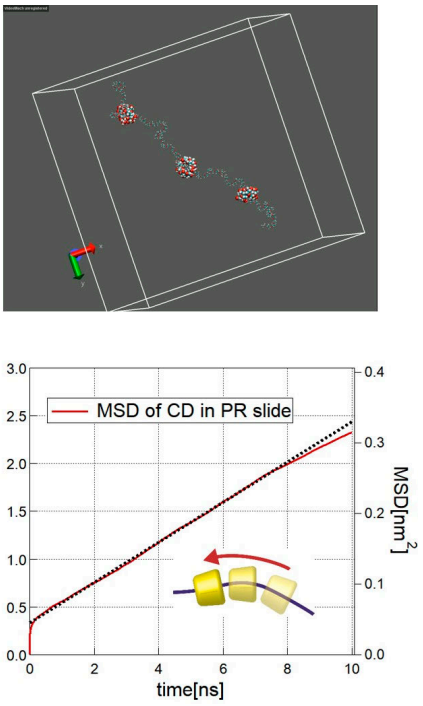

Figure 2. A smapshot of PR in the full-atomistic MD simulation and MSD corresponding to the sliding motion of CDs along PEG in PR [4].

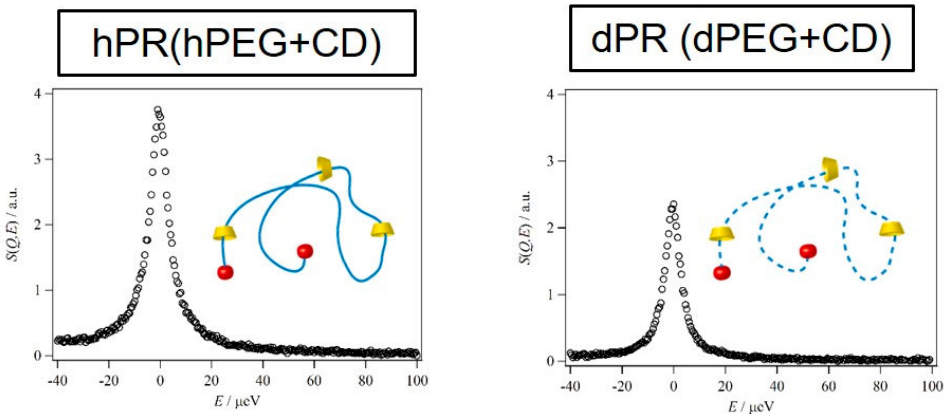

Figure 1. Dynamic structure factors for polyrotaxanes with hydrogenated and deutrated main chains in solution [4].

3. Results and discussion

Figure 1 shows the dynamic structure factors $S(Q, \omega)$ of hPR and dPR in solution. From the dynamic structure factor of dPR, we evaluated the dynamics of CD in PR. In addition, by subtracting $S(Q, \omega)$ of dPR from that of hPR, we can extract the dynamics of PEG in PR. The estimated diffusion coefficient of CD in PR was estimated as 11 Å^2/ns, which is a little smaller than that of free CD, 13 Å^2/ns. The topological connection with PEG in PR hardly influences the dynamics of CD because PEG is flexible. On the other hand, PEG in PR shows heterogeneous dynamics. The PEG monomers inside/near CDs slowly diffuse due to the existence of CDs, whereas the PEG monomers apart from CDs exhibit the same high mobility as the free PEG. The inhomogeneity of the PEG dynamics in PR suggests that the sliding dynamics in PR is slower than the observed translational diffusion modes of CDs and PEG monomers.

For further analysis, we performed full-atomistic MD simulations on PR solutions (Fig. 2). From the MD simulations, we calculated the translational diffusion coefficients of CD and PEG monomers in PR solutions and confirmed that the obtained results were in quantitative agreement with those from the QENS experiments. By analyzing the MSD of CDs along the PEG axis (Fig. 2), we successfully observed and quantified for the first time the sliding motion of CD along the PEG chain. The diffusion coefficient for the sliding motion was almost 6 times slower than that of the translational diffusion of CD in PR at room temperature. The slowing down of the sliding motion was caused by the energy barrier on PEG. From the temperature dependence of the diffusion coefficient for the sliding motion (Fig. 3), it was found that the sliding motion of CD on PEG did not follow the Einstein-Stokes equation for Brownian diffusion. We proposed a simple equation for the sliding motion composed of the Einstein-Stokes part for Brownian diffusion and the jump diffusion part with an energy barrier along the axial chain:

$$D_{\mathrm{slide}} \propto \frac{k_{\mathrm{B}}T}{\eta(T)} \exp\left(-\frac{E_{\mathrm{a}}}{RT}\right).$$

where D_{slide} is the diffusion coefficient of the sliding motion in PR, k_{B} is Boltzmann constant, T is absolute temperature, η is viscosity of the solvent, R is the gas constant, and E_{a} is an activation energy corresponding to the energy barrier on PEG. This work provides a general strategy for the molecular designs to control the sliding motion in PR.

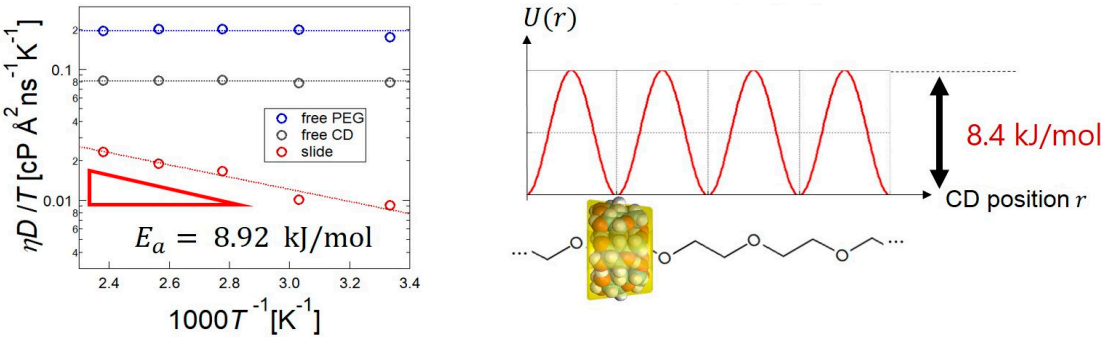

Figure 3. Temperature dependence of the normalized diffusion coefficient for the sliding motion of PR and energy profile of CDs along PEG [4].

References

[1] P. L. Anelli, N. Spencer, and J. F. Stoddart, , J. Am. Chem. Soc., **113**, 5131 (1991).
[2] N. Yui and T. Ooya, Chem, Eur. J., **12**, 6730 (2006).
[3] K. Ito, K. Kato and K. Mayumi, "Polyrotaxane and Slide-Ring Materials", Royal Society of Chemistry (2015).
[4] Y. Yasuda, Y. Hidaka, Y., K. Mayumi, T. Yamada, K. Fujimoto, S. Okazaki, H. Yokoyama and K. Ito, J. Am. Chem. Soc., **141**, 9655 (2019).

K. Mayumi[1], Y. Yasuda[1], T. Yamada[2], and K. Ito[1]
[1]*Graduate School of Frontier Sciences, The University of Tokyo;* [2]*Neutron Science and Technology Center, CROSS*

Neutron Crystallography Captures a Key Structure of Copper-containing Nitrite Reductase

1. Introduction

The denitrification process is one of the anaerobic respiratory systems of microorganisms. It uses nitrogen oxide molecules as electron acceptors and releases dinitrogen back into the atmosphere. Copper-containing nitrite reductases (CuNIRs) catalyzes the important step in denitrification: one-electron reduction of nitrite to nitric oxide ($NO_2^- + 2H^+ + e^- \rightarrow NO + H_2O$), which generates gaseous NO and results in the removal of terrestrial fertilizer. Despite many X-ray crystallographic studies [1–3], the reaction mechanism of CuNIRs has not been clarified yet. Among the steps of the chemical reaction, the mechanism of proton transfer (PT) coupled with electron transfer (ET) [4] is the most ambiguous because of the difficulty in detecting the positions of hydrogen (H) atoms by X-ray diffraction (XRD) analysis. Neutron diffraction (ND) crystallography is an alternative tool to visualize H atoms. Neutrons are diffracted by atomic nuclei and the amplitude of neutron scattering depends on the structures of the atomic nuclei. Therefore, H atoms and atoms of its isotope deuterium (D) can contribute to neutron scattering to the same extent as C, N, and O atoms. Another advantage of neutron crystallography in protein science is the much weaker energy of neutron beams than X-ray ones, which enables determination of intact protein structures. To understand the reaction mechanism of CuNIRs, we performed time-of-flight neutron diffraction experiment at BL03 iBIX in the Materials and Life Science Experimental Facility (MLF) of the Japan Proton Accelerator Research Complex (J-PARC) and obtained a high-quality ND structure of CuNIR from *Geobacillus thermodenitrificans* (*Gt*NIR) [5].

2. Protonation states at the catalytic site

We collected ND and XRD data from a single *Gt*NIR crystal at 100 K. We then performed joint neutron and X-ray refinement. The final R_{work}/R_{free} values for the ND (1.50 Å resolution) and XRD (1.30 Å resolution) data were 14.1/15.8 and 9.73/11.2%, respectively, which showed that the obtained structure was of high quality. The data clearly visualized the locations of H/D atoms in *Gt*NIR. A total of 3,043 H/D atoms and 285 hydrating water positions were identified. The catalytic site of CuNIRs is composed of a Cu ion, called T2Cu, and three histidine residues coordinating to T2Cu. There are two essential catalytic residues above the T2Cu site: aspartate (Asp^{CAT}) and histidine (His^{CAT}). Previous XRD analyses showed the presence of five water molecules located around the *Gt*NIR T2Cu site (Wat0, Wat0', Wat1, Wat2, and BW). We were able to observe all of these water molecules in the present study and determine the positions of D atoms on them (Fig. 1). Moreover, we could show that Asp^{CAT} was deprotonated and His^{CAT} was protonated. These observations accord with the earlier density functional theory (DFT) calculation showing that protonated His^{CAT} is stabilized when Asp^{CAT} is deprotonated [6].

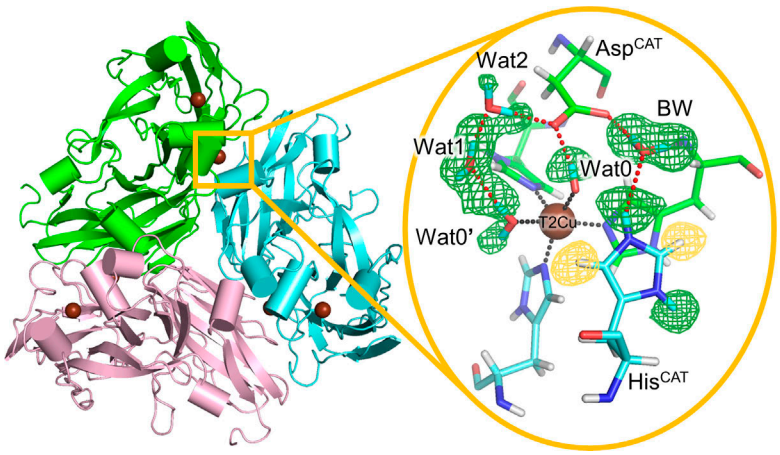

Figure 1. Cartoon structure of *Gt*NIR (left) and stick model of the catalytic site (right). A brown sphere indicates the T2 Cu ion. Positive and negative peaks of neutron scattering length density (contoured at ± 3 σ) are illustrated by green and yellow meshes.

3. Direct observation of a hydroxide on Cu

The obtained neutron-scattering length map indicated that one of the D atoms in the Wat0 molecule directed Asp^{CAT}. However, we could not observe the positive peak of the other D atom. All other water molecules at the T2Cu site clearly showed two positive peaks around them (Fig. 1). When we refined the structure with a deuterated hydroxide model (OD^-) of Wat0, it showed good agreement with the observed data. Such OH-type molecules are usually interpreted as a result of the rotational disorder of water molecules. However, the observed Wat0 molecule showed a low B-factor value for the O atom and its rotational motion was geometrically restricted. Therefore, we concluded that Wat0 is a hydroxide ion, not a water molecule. Distinguishing water from hydroxide (the difference of only one H atom) must be a remarkable achievement by ND analysis. A previous quantum chemical study shows that the T2Cu site of *Gt*NIR energetically prefers a $[Cu(OH)]^+$ state after the nitrite reduction reaction and direct release of NO [7]. Our structure supports this reaction mechanism.

4. Intramolecular electron transfer pathway

A previous computational study suggests that the intramolecular ET pathway includes a hydrogen-bond jump and is not composed only of covalent peptide bonds [8]. Neutron scattering length density around the D atom on the N^δ atom in His134 was less clear than those of other two His ligands to T2Cu. Because the X-ray data showed the presence of the H/D atom on the N^δ atom of His134, we considered that the neutron scattering from the D atom at this position was canceled by negative scattering from a partially occupied H atom. The result of the occupancy refinement was that only in 31% of the cases the H atom on the N^δ atom in His134 was replaced with the D atom, while the other two His ligands to T2Cu showed 100% H-D exchange. This observation indicates that the proposed ET pathway has a tight hydrogen bond, which suppresses H-D exchange reactions. Such a tight hydrogen bond decreases reorganization energy in the ET reaction and thus facilitates the efficient ET.

5. Future plans

Our study shows that neutron crystallography is a powerful technique to investigate enzymatic mechanisms, which are difficult to reveal only by X-ray crystallography. Our data obtained from ND analysis show good agreement with the results from quantum chemistry. Therefore, our study can seamlessly connect structural biology and theoretical chemistry, facilitating the understanding of biological processes at an electronic level beyond an atomic level. By using BL03 iBIX, we have collected new data and solved neutron crystal structures of *Gt*NIR in different states. These structures will provide further details of the chemical reaction and we may be able to completely comprehend CuNIRs.

References

[1] J. W. Godden et al., Science, **253** 438 (1991).
[2] M. E. P. Murphy et al., J. Biol. Chem., **272** 28455 (1997).
[3] E. Tocheva et al., Science, **304** 867 (2004).
[4] S. Brenner et al., J. Biol. Chem., **284** 25973 (2009).
[5] Y. Fukuda et al., Proc. Natl. Acad. Sci., **117** 4071 (2020).
[6] S. Ghosh et al., J. Am. Chem. Soc., **131** 277 (2009).
[7] M. Lintuluoto and J. M. Lintuluoto, Biochemistry, **55** 210 (2016).
[8] R. G. Hadt et al., J. Am. Chem. Soc., **136** 15045 (2014).

Y. Fukuda[1], Y. Hirano[2], K. Kusaka[3], T. Inoue[1], and T. Tamada[2]
[1]Graduate School of Pharmaceutical Sciences, Osaka University; [2]Institute for Quantum Life Science, National Institutes for Quantum and Radiological Science and Technology; [3]Frontier Research Center for Applied Atomic Sciences, Ibaraki University

Discovery of a New Oxide-ion Conductor Dion–Jacobson Type $CsBi_2Ti_2NbO_{10-\delta}$ and Structure Origin of the High Oxide-ion Conductivity

1. Introduction

Oxide-ion conductors have received considerable attention due to their wide applications in many electrochemical devices, such as solid-oxide fuel cells (SOFCs), oxygen gas sensors and oxygen separation membranes [1, 2]. Since oxide-ion conductivity in solid oxides is strongly related to their crystal structure, high oxide-ion conductivities have been achieved in a limited number of structure families. Therefore, it is important to explore a new structure family of oxide-ion conductor for further development in this field.

Recently, we have discovered $CsBi_2Ti_2NbO_{10-\delta}$ as the first example of the Dion–Jacobson-type oxide-ion conductor [3]. Dion-Jacobson-type structure is one of the layered perovskites. Various layered perovskites are known to exhibit high oxide-ion conductivity. However, there are no reports on oxide-ion conduction in the Dion–Jacobson phases, although several Dion-Jacobson-type materials are known as cation conductors, such as proton, lithium, and sodium conductors. We have targeted the Dion-Jacobson-type oxides, because it is a layered perovskite, and some compositions, such as $CsBi_2Ti_2NbO_{10-\delta}$, are found to show relatively low bond-valence-based energy barrier for the oxide-ion migration. In this report, we briefly describe the electrical properties, crystal structure, and origin of the high oxide-ion conductivity of the new oxide-ion conductor $CsBi_2Ti_2NbO_{10-\delta}$.

2. Synthesis and electrical conductivity

$CsBi_2Ti_2NbO_{10-\delta}$ was synthesized by a solid-state-reaction method using Cs_2CO_3, Bi_2O_3, TiO_2, and Nb_2O_5 as starting materials. The electrical conductivities were measured by the AC impedance method in the temperature range of 573–1173 K. The equivalent circuit analyses were carried out to extract the bulk conductivity and grain boundary conductivity at each temperature. The bulk conductivity of $CsBi_2Ti_2NbO_{10-\delta}$ is 8.9×10^{-2} S cm^{-1} at 1073 K. The bulk conductivities of $CsBi_2Ti_2NbO_{10-\delta}$ were higher than those of YSZ and comparable with those of the best oxide-ion conductors (Fig. 1), which indicates the high potential of the Dion–Jacobson phase $CsBi_2Ti_2NbO_{10-\delta}$ as a basic composition for oxide-ion conductors. Oxygen concentration cell measurements were performed to determine the oxide-ion transport number (t_{ion}). The t_{ion} values were 1.00–0.98 between 873 and 1173 K in air/O_2, 0.97–0.95 between 873 and 1173 K in air/N_2, and 0.87 at 873 K in air/5% H_2 in N_2. The dc conductivities of $CsBi_2Ti_2NbO_{10-\delta}$ under wet and dry condition agreed well. Therefore, the major charge carrier in $CsBi_2Ti_2NbO_{10-\delta}$ was shown to be oxide-ion. No significant change was observed before and after the conductivity measurements, which indicated the high phase stability of $CsBi_2Ti_2NbO_{10-\delta}$. The bulk conductivities abruptly increased between 673 and 873 K on heating, which was attributed to the increase in the carrier (oxygen vacancy) concentration and the phase transition.

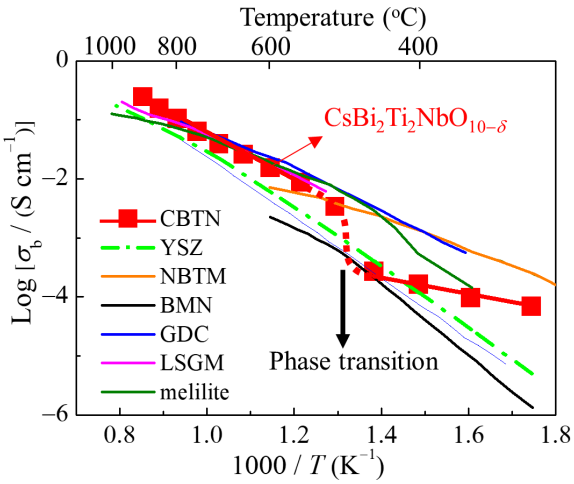

Figure 1. Comparison of the bulk conductivity of $CsBi_2Ti_2NbO_{10-\delta}$ with that of the best oxide-ion conductors: $(Y_2O_3)_{0.08}(ZrO_2)_{0.92}$ (YSZ), $Na_{0.5}Bi_{0.49}Ti_{0.98}Mg_{0.02}O_{2.965}$ (NBTM), $Ba_3MoNbO_{8.5}$ (BMN), $Ce_{0.9}Gd_{0.1}O_{1.95}$ (GDC), $La_{0.9}Sr_{0.1}Ga_{0.8}Mg_{0.2}O_{2.85}$ (LSGM), and $La_{1.54}Sr_{0.46}Ga_3O_{7.27}$ (melilite). *Copyright © 2020, Springer Nature*

3. Crystal structure

In order to understand the origin of the high oxide-ion conductivity in $CsBi_2Ti_2NbO_{10-\delta}$, the crystal structure of $CsBi_2Ti_2NbO_{10-\delta}$ was investigated at various temperature using the neutron diffraction data taken on the SuperHRPD diffractometer [4]. The diffraction data were analyzed by the Rietveld method using the Z-Rietveld program [5]. The neutron scattering length density distribution in $CsBi_2Ti_2NbO_{10-\delta}$ at 973 K was investigated using the maximum-entropy method (MEM). Furthermore, the Bond-valence-based energy of $CsBi_2Ti_2NbO_{10-\delta}$ at 973 K was calculated to investigate the anisotropic thermal motions and diffusion paths of the oxide ions.

The Rietveld refinements of the neutron-diffraction data of $CsBi_2Ti_2NbO_{10-\delta}$ were successfully carried out using a single orthorhombic *Ima*2 structure at 297–813 K regions and a single tetragonal *P*4/*mmm* structure at 833–1073 K regions on heating (Fig. 2), showing a layered Dion–Jacobson type perovskite structure. The presence of oxygen vacancies (δ) was confirmed from the refined occupancy factors of oxygen. The δ are responsible for the novel oxide-ion conductivities of $CsBi_2Ti_2NbO_{10-\delta}$ as described below.

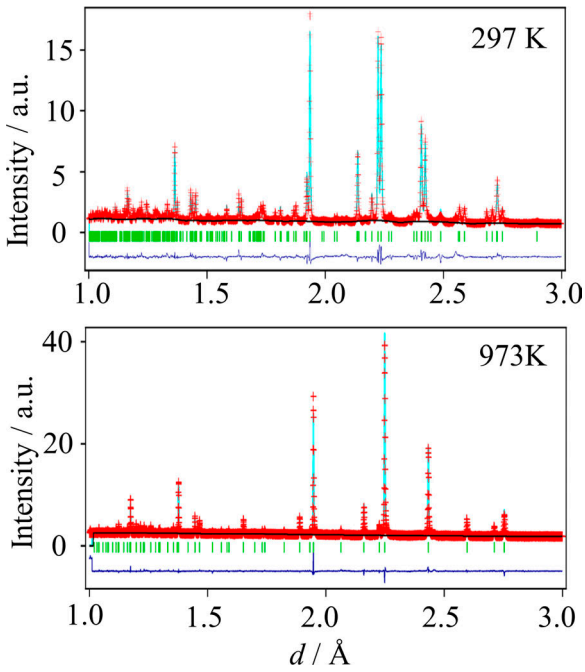

Figure 2. Rietveld patterns at 297 K and 973 K of neutron-diffraction data taken by the backscattering bank of the SuperHRPD diffractometer. The observed and calculated intensities and difference plots are shown by red marks, light blue and blue solid lines, respectively. Green tick marks stand for calculated Bragg peak positions. *Copyright © 2020, Springer Nature*

The tetragonal structure of $CsBi_2Ti_2NbO_{10-\delta}$ (973 K) consists of an oxide-ion conducting inner perovskite layer, two outer perovskite layers, and an insulating rock-salt layer (Fig. 3a). The refined equivalent isotropic atomic displacement parameters of the equatorial oxygen atom, O1, and apical oxygen, O2, in the oxide-ion conducting inner perovskite layer were much higher than those of the equatorial O3 and apical O4 atoms in the outer perovskite layers. Therefore, the O1 and O2 atoms exhibited larger thermal motions than the O3 and O4 atoms. In particular, the anisotropic atomic displacement parameters of the O1 and O2 atoms were extremely large. The large values of the anisotropic atomic displacement parameters indicate high anisotropic thermal motions along the *c* and *a* axes, respectively, which suggests the O1–O2 oxide-ion diffusion. Similarly, the O1–O1 oxide-ion diffusion was confirmed. The bond-valence-based energy landscapes (BVELs, blue isosurfaces in Fig. 3b) and the isosurfaces of the neutron scattering length density obtained by the maximum-entropy method (MEM) (yellow isosurfaces in Fig. 3c) showed the O1–O2 and O1–O1 oxide-ion diffusion paths. In addition, the O2–O3 diffusion path was observed in the BVELs (the black dotted arrows in Fig. 3b). These results indicate two-dimensional (2D) oxide-ion diffusion along the edges of the octahedron in the oxide-ion conducting inner perovskite layer. We attribute the high oxide-ion conductivity of $CsBi_2Ti_2NbO_{10-\delta}$ not only to the existence of oxygen vacancies but also to the 2D oxide-ion diffusion and the extremely high atomic displacement parameters of the O1 and O2 atoms.

At last, we proposed a new concept to explain the structural origin of the high oxide-ion conductivity of $CsBi_2Ti_2NbO_{10-\delta}$. Large bottlenecks for oxide-ion migration was created by the large size of Cs^+ and Bi^{3+} displacement. The bottlenecks in the $CsBi_2Ti_2NbO_{10-\delta}$ are the Bi–Bi–Ti triangles (the yellow and pink triangles in Fig. 4. The large bottlenecks can be explained using the new concept: Cs^+ expands the Bi–Bi distance along the *b* axis due to the occupational ordering of the large Cs^+ cations. Bi^{3+} is displaced along the *c* axis apart from the Ti/Nb1–O1 layer by electrostatic forces. The Bi^{3+} displacement increases the Bi–Bi distance along the *c* axis. The increase in the Bi–Bi distances along both the *b* (=*a*) and *c* axes leads to large bottlenecks for the O1–O2 (the yellow areas) and O1–O1 (the pink areas) oxide-ion diffusion.

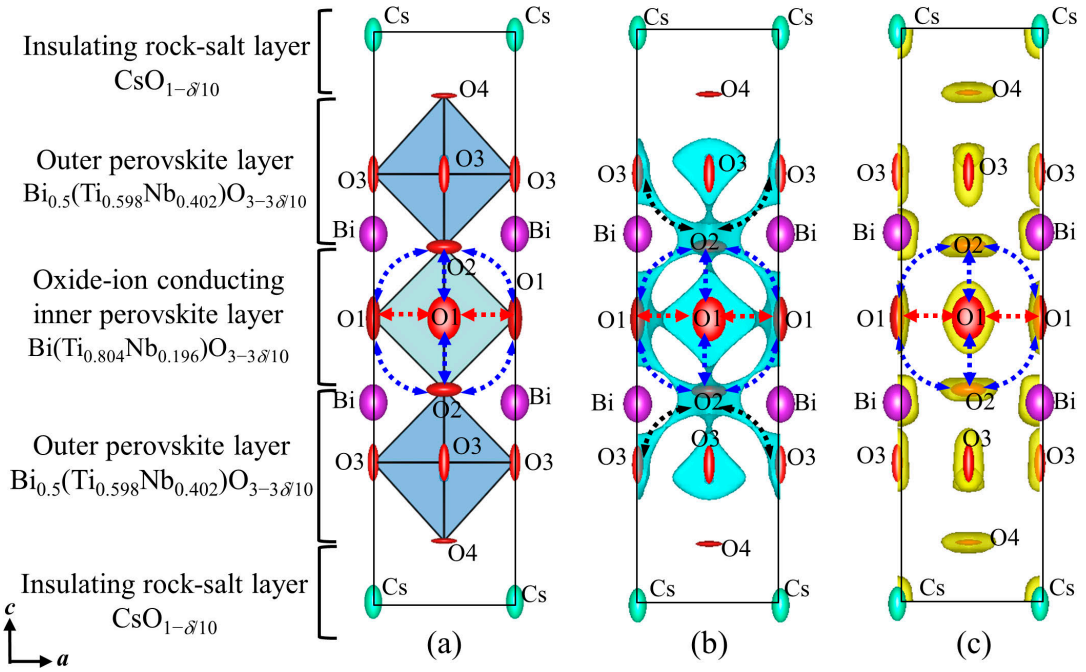

Figure 3. (a) Refined crystal structure of $CsBi_2Ti_2NbO_{9.80(2)}$ at 973 K, which was obtained by Rietveld analysis of neutron-diffraction data. (b) Blue isosurfaces of the bond-valence-based energy for an oxide ion at 0.6 eV for the structure at 973 K. (c) Yellow isosurfaces of the neutron scattering length density at 1.0 fm $Å^{-3}$ with the structure (973 K). *Copyright © 2020, Springer Nature*

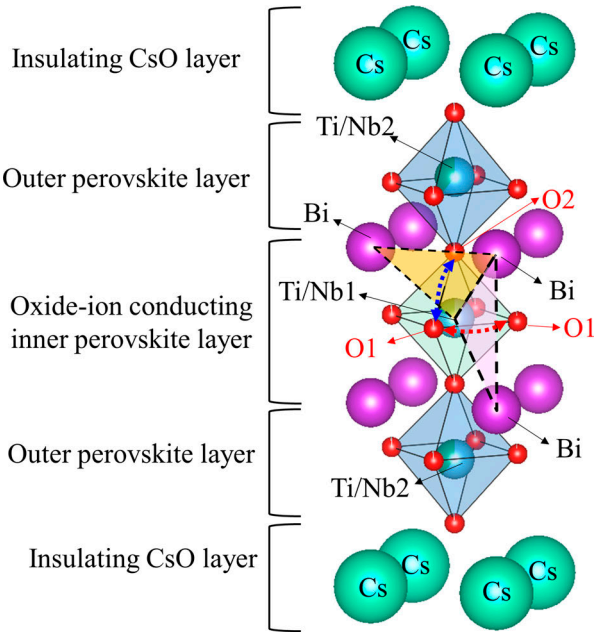

Figure 4. New concept of enlarged bottlenecks for oxide-ion migration created by large size of Cs^+ and Bi^{3+} displacement in Dion–Jacobson-type Cs/Bi-cation-ordered $CsBi_2Ti_2NbO_{10-\delta}$. *Copyright © 2020, Springer Nature*

4. Conclusion

$CsBi_2Ti_2NbO_{10-\delta}$ is the first example of Dion-Jacobson-type oxide-ion conductor, which is one of the best oxide-ion conductors. Through the neutron diffraction study using SuperHRPD diffractometer, we have clarified the oxide-ion migration path in $CsBi_2Ti_2NbO_{10-\delta}$. Furthermore, a new concept of large bottlenecks for oxide-ion migration by large size of Cs^+ and Bi^{3+} displacement was proposed based on the analyzed crystal structure. This proposed new concept should facilitate further developments of oxide-ion conductors.

References

[1] M. Yashima, *J. Ceram. Soc. Jpn.*, **117** 1055 (2009).
[2] M. Yashima, *Catal. Today* **253** 3 (2015).
[3] W. Zhang et al., *Nat. Commun.*, **11** 1224 (2020).
[4] S. Torii et al., *J. Phys. Soc. Jpn.* **80** 3 (2011).
[5] R. Oishi et al., *Nucl. Instruments Methods Phys. Res. Sect. A Accel. Spectrom. Detect. Assoc. Equip.* **600** 94 (2009).

W. Zhang, K. Fujii, and M. Yashima
Department of Chemistry, School of Science, Tokyo Institute of Technology

Interstitialcy Diffusion Pathways of F-Ions in $Ba_{0.6}La_{0.4}F_{2.4}$ Solid Electrolyte Material

1. Introduction

The fluorite-type structure is one of the key frameworks considered to ensure the high mobility of fluoride anions (hereafter referred to as F^- ions) [1, 2]. F^- ions show the highest electronegativity (= 3.98) in the periodic table and because F^- ion-conducting materials possess very high conductivity and chemical stability, there is a growing demand for them. In particular, all-solid-state fluoride shuttle batteries (FSBs) have received a lot of attention as the next-generation rechargeable battery with high power density, a wide electrochemical potential window, high reliability, and a long lifespan. In "metal (anode)/metal fluoride (cathode)" cells, the chemical reaction of a couple of F^- ions (nF^-) with a metal (M) leads to the formation of a metal fluoride (MF_n), resulting in the release of several electrons (ne^-) per metal atom. The theoretical energy density of FSBs (approximately 5000 Wh/L) is ten times higher than that of commercial lithium-ion batteries [3]. In recent studies, a "Ce or Li (anode)/BiF_3 (cathode)" pair was assembled experimentally and was characterized using $Ba_{0.6}La_{0.4}F_{2.4}$ (fluorite-type) and $La_{0.9}Ba_{0.1}F_{2.9}$ (tysonite-type) solid electrolytes [4, 5]. However, currently all-solid-state FSBs only operate at elevated temperatures. In addition, the specifications for working all-solid-state FSBs have not yet been standardized.

In this study, we performed structural investigations of the fluorite-type solid electrolyte $Ba_{0.6}La_{0.4}F_{2.4}$ using a cutting-edge neutron diffractometer, SPICA, and a suite of analysis programs, Z-Rietveld [6, 7]. Additionally, we elucidated the diffusion pathways of F^- ions in $Ba_{0.6}La_{0.4}F_{2.4}$ using the maximum entropy method (MEM) [8]. We showed that the excessive F^- ions, located at the specific interstitial sites, migrate to the neighboring F^- ion sites based on the interstitialcy diffusion mechanism at the operating temperature for all-solid-state FSBs [9].

2. Electrical conductivities

Figure 1 shows the temperature dependence of the electrical conductivity, $\sigma(T)$, of $Ba_{0.6}La_{0.4}F_{2.4}$ along with that of BaF_2. It is worth noting that the σ value includes the contributions of the bulk and the grain boundaries. With the substitution of La^{3+} for Ba^{2+}, σ increased by four to five orders of magnitude. This massive improvement in σ may be ascribed to the introduction of excessive F^- ions. The σ value for $Ba_{0.6}La_{0.4}F_{2.4}$ increased to 10^{-4} S/cm at temperatures higher than 430 K; this should be enough for creation of all-solid-state FSBs.

3. Crystal structure and diffusion pathways of F^- ions

The Rietveld refinement pattern of $Ba_{0.6}La_{0.4}F_{2.4}$ at 512 K is shown in Fig. 2; there is excellent agreement between the observed and calculated intensities (R_{wp} =

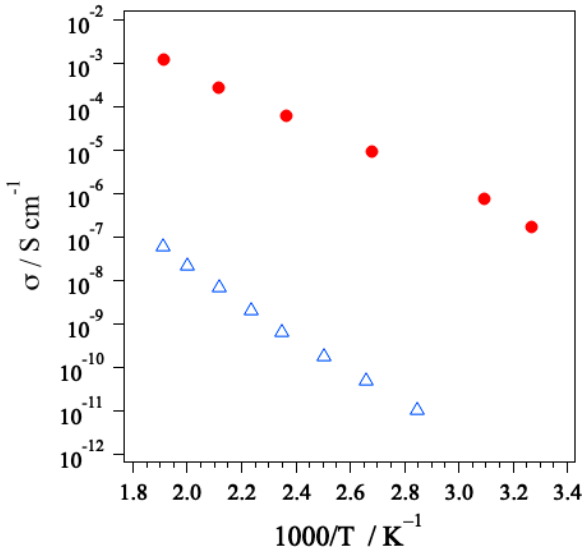

Figure 1. Temperature dependence of the electrical conductivities for $Ba_{0.6}La_{0.4}F_{2.4}$ (red circles) and BaF_2 (blue triangles).

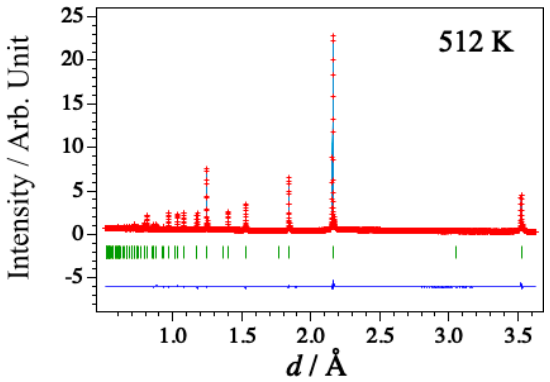

Figure 2. The neutron diffraction pattern of $Ba_{0.6}La_{0.4}F_{2.4}$ at 512 K. In the Rietveld analysis result, plus marks (red) indicate the observed neutron diffraction data while the solid line (dark-light blue) indicate the calculated neutron diffraction data. Vertical marks (green) below the neutron diffraction data denote positions of the Bragg reflections. The curve (blue) at bottom indicates the difference between observed and calculated intensities.

3.5263%; $S = 4.0550$). All the Bragg reflections of $MF_{2.4}$ ($M = Ba_{0.6}La_{0.4}$) could be indexed to the fluorite-type structure. Thus, the space group $Fm\bar{3}m$ (cubic system), was chosen for the crystal structure refinement. Furthermore, we used the split-atom model to provide the interstitial site for the excessive F^- ions, F2(x, x, x) in the 32f site, along with the M(0, 0, 0) in the 4a site and F1(1/4, 1/4, 1/4) in the 8c site, where x is the atomic position. The crystal structure of $MF_{2.4}$ at 512 K is illustrated in Fig. 3. The a, g(F1), and g(F2) values were determined and found to be $a = 6.10751(8)$ Å, $g(F1) = 0.675(3)$, and $g(F2) = 0.1312(7)$, respectively. Interestingly, the F-vacancies account for approximately 30% of the regular F1 sites. In the figure, the anisotropic displacement of F2 was more pronounced towards the F1 site (i.e. in the <111> direction), whereas those of M and F1 continued to exhibit isotropic behavior.

Next, we performed MEM calculations to visualize the diffusion pathways of the F^- ions in $MF_{2.4}$ at 512 K. Figure 3 shows the three-dimensional nuclear density distribution at 0.55 fm Å^{-3}. It seems that the F^- ion diffusion in $Ba_{0.6}La_{0.4}F_{2.4}$ can be explained based on the interstitialcy diffusion mechanism. Along the F1–[F2–F2]–F1 diffusion pathways, an F^- ion at the F2 site moves to the neighboring F1 site, and then an F^- ion at the F1 site is kicked out by the F^- ion.

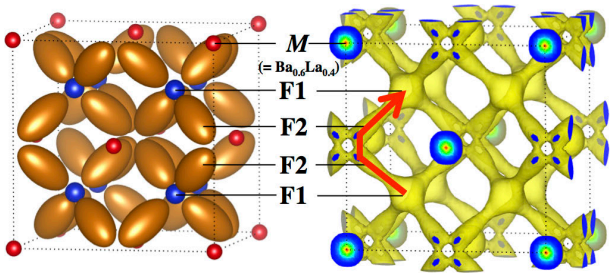

Figure 3. Crystal structure (left) and nuclear density distributions (right) calculated by the Rietveld method and the maximum enthalpy method (MEM) using neutron diffraction data for $Ba_{0.6}La_{0.4}F_{2.4}$ collected at 512 K. The red arrow indicates the predicted conduction pathways of F^- ions: F1–[F2–F2]–F1.

4. Concluding remarks

The diffusion pathways of F^- ions in the fluorite-type solid electrolyte $Ba_{0.6}La_{0.4}F_{2.4}$ at 512 K were visualized using the cutting-edge neutron diffractometer, SPICA. Of the various known fluoride-based solid electrolytes such as fluorite- and tysonite-type ones [10], $Ba_{0.6}La_{0.4}F_{2.4}$ shows higher conductivity at 430 K. However, its conductivity is not as high at room temperature. As such, it is essential to elucidate the F^- ion diffusion mechanism in these materials in greater detail. We believe that the proposed diffusion pathways of the F^- ions will aid the development of fluoride-based solid electrolytes for the next-generation all-solid-state FSBs.

References

[1] N. I. Sorokin, B. P. Sobolev, Crystallogr. Rep., **52** 842 (2007).
[2] L. N. Patro, K. Hariharan, Solid State Ionics, **239** 41 (2013).
[3] F. Gschwind et al., J. Fluorine Chem., **182** 76 (2016).
[4] C. Rongeat et al., J. Phys. Chem. C, **117** 4943 (2013).
[5] M. A. Reddy et al., J. Mater. Chem., **21** 17059 (2011).
[6] M. Yonemura, K. Mori et al., J. Phys. Conf. Ser., **502** 012053 (2014).
[7] R. Oishi et al., Nucl. Instrum. Methods Phys. Res. A, **600** 94 (2009).
[8] Y. Ishikawa et al., Physica B, **551** 472 (2018).
[9] K. Mori et al., ACS Appl. Energy Mater., **3** 2873 (2020).
[10] K. Mori et al., J. Phys. Chem. C, **124** 18452 (2020).

K. Mori[1], A. Mineshige[2], T. Saito[3,4], M. Sugiura[2], Y. Ishikawa[5], F. Fujisaki[6], K. Namba[3,4], T. Kamiyama[3,4], T. Otomo[3,4], T. Abe[7], and T. Fukunaga[6]

[1]*Institute for Integrated Radiation and Nuclear Science, Kyoto University;* [2]*Department of Applied Chemistry, Graduate School of Engineering, University of Hyogo;* [3]*Neutron Science Section, Materials and Life Science Division, J-PARC Center;* [4]*Institute of Materials Structure Science, KEK;* [5]*Neutron Science and Technology Center, CROSS;* [6]*Office of Society-Academia Collaboration for Innovation, Kyoto University;* [7]*Graduate School of Engineering, Kyoto University*

Measurement of Neutron Scattering Cross Section of Nano-Diamond for Cold Neutron Intensity Enhancement

1. Introduction

Slow neutrons, as unique probes, constitute a powerful tool in advanced material research and fundamental physics. However, additional intensity enhancement, especially below the cold neutron energy, is strongly desired.

Recently, researchers have focused on nano-diamond (ND) as attractive neutron reflection materials. Because the carbon in NDs is characterized by low neutron absorption and the sizes of NDs are comparable to the wavelengths of the neutrons of interest in the very cold energy region, NDs can serve as a good reflection material with heightened cold neutron intensity owing to coherent scattering. Although experimental studies evaluating the neutron reflection performance of NDs are underway, total neutron cross section data are unavailable for use in neutron source conceptual design studies.

Therefore, we conducted an experiment involving neutron transmission measurement to determine the total neutron cross section. In addition, we performed inelastic neutron scattering measurements to confirm the contribution of inelastic scattering to the total cross section.

2. Experiment

ND powder with the size of 5.1 nm produced by explosive synthesis at Ray Techniques Ltd. was used, as shown in Fig. 1(a). The powder was shaped into a plate by using a pressing jig in a glovebox, as shown in Fig. 1(b). The successful forming of the plate from ND powder depended on the pressing pressure. The appropriate pressing pressure was approximately 10 MPa. The ND plate weighed 0.0375 g, and its size was $10 \times 10 \times 0.57$ mm^3, resulting in a density of 0.658 g/cm^3, which is lower that its theoretical density of about 3.6 g/cm^3. The plate was stored in a pure aluminum capsule with thickness of 0.3 mm inside the same glovebox. A 0.3-mm-thick cadmium plate with an 8-mm hole at its center was placed next to the specimen to collimate the neutron beam.

Neutron transmissions with and without the ND plate were measured using a ^{3}He detector at BL10. The ^{3}He detector was covered with boron carbide resin and equipped with an opening slit of 10×20 mm^2 to reduce the background noise of the scattered neutrons. The pulsed neutron beams emitted from a decoupled moderator were used for transmission measurement.

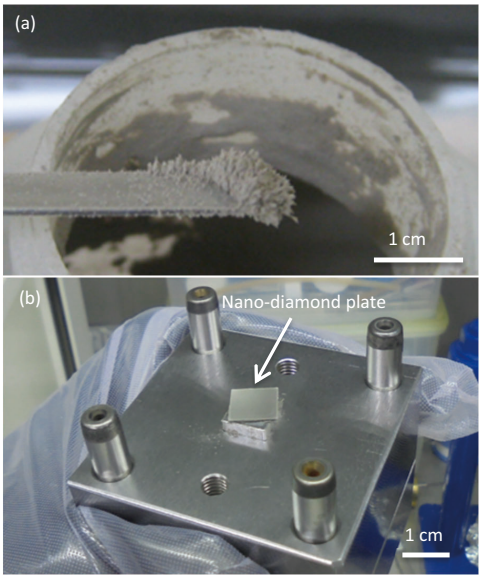

Figure 1. Nano-diamond: (a) Photograph of the nano-diamond powder, (b) Nano-diamond plate.

3. Results and Discussion

Figure 2 [1] shows the measured total cross section data with errors. The cross section of carbon in JENDL-4.0 [2] and that of graphite in ref. 3 are shown in Fig. 2 for comparison. The total cross section of the ND specimen increased with the decrease of the neutron energy to 0.2 meV. It was approximately two orders of magnitude greater than that of carbon at 0.2 meV. The total cross section of the ND plate was consistent with those of carbon and graphite within the error range at neutron energies higher than 100 meV. It is critical to understand the scattering mechanism that leads to an increase in the total cross section of the ND plate in the cold neutron energy region. First of all, inelastic neutron scattering measurement of the ND plate was performed at BL14 with incident neutron energies (E_is) of 1.2, 1.5, 1.9, 2.6 and 5.9 meV to investigate the contribution of inelastic neutron scattering to the total cross section. Figure 3 [1] shows a 2D contour map of energy transfer (ET) versus the scattering vector, q. The various colors denote the scattering intensity of the ND specimen.

The horizontal zone indicated by arrow A (ET = 0, meaning no energy transfer) represents elastic scattering of the incident neutron energy at 1.2 meV. The high scattering intensities indicated by red color were observed in the small q ($0.1 < q < 0.3$) region. Another zone shown by arrow B denotes elastic

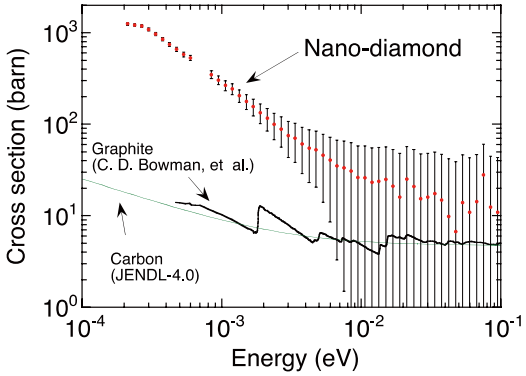

Figure 2. Total cross sections of the nano-diamond. The cross sections of carbon (JENDL-4.0, [2]) and graphite (C.D. Bowman et al., [3]) are shown for comparison.

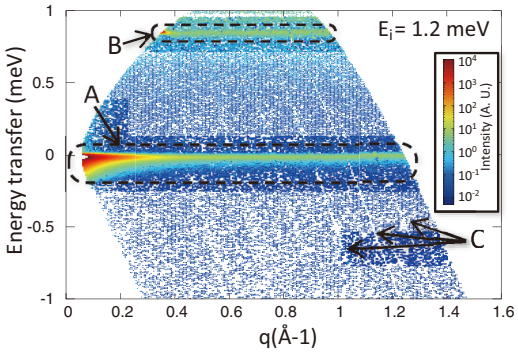

Figure 3. Result of the inelastic scattering measurement of the ND specimen at neutron incident energy (E_i) of 1.2 meV.

scattering corresponding to the next incident neutrons at 0.95 meV. The white slanting lines indicated by arrow C denote gaps in the detector arrays. No visible scattering intensities were observed in the background signal of blue color, except at ET = 0.

A similar tendency was observed for the other energies of 1.5, 1.9, 2.6, and 5.9 meV. Thus, inelastic scattering does not contribute to cold neutron energy.

To understand the large cross section at low energies, we performed small-angle neutron scattering (SANS) measurements at BL15 in J-PARC and analyzed the measured SANS data by plotting *q* versus energy (wavelength). We assumed that inelastic scattering did not contribute to the SANS data based on the result of the inelastic neutron scattering measurement.

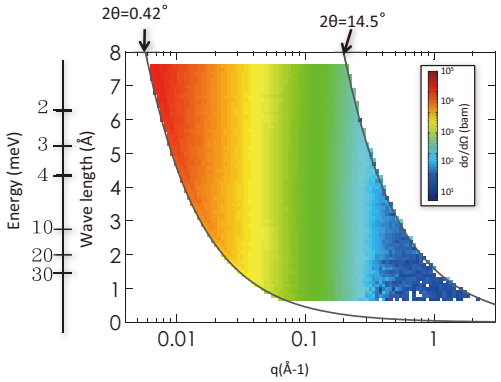

Figure 4. Two-dimensional distribution (q, E) of the scattering intensity of the ND specimen.

Figure 4 [1] shows a two-dimensional (2D) contour map of the neutron energy versus the scattering vector *q*, with the color bars representing the scattering cross section. The scattering cross section increases with decreasing the neutron energy and scattering angle, resulting in greater scattering cross sections along the forward direction at lower neutron energies. Thus, there is potential to use the ND specimen to increase the neutron intensity below the cold neutron energy.

Acknowledgements

This work was conducted under the IAEA Coordinated Research Project (Project No. F12026). The experiment at the MLF of J-PARC was performed under the user program (Proposal No. 2016P0802, 0803 and 0804).

We are grateful to K. Aizawa, group leader of the Technical development section at JAEA, and the section members W. Kambara, R. Takahashi, A. Hori, H. Tanaka, M. Sawabe, H. Isozaki and K. Aoyama for the timely help with machining, etc. We would like to thank A. Birumachi, group leader of the Machinery engineering and electronics section at JAEA, and its members M. Usami, K. Horiguchi, T. Neya and T. Abe for manufacturing the specimen holder and many jigs.

References

[1] M. Teshigawara et al., Nucl. Inst. and Meth. Phys. Res. A, **929** 113 (2019).
[2] K. Shibata et al., J. Nucl. Sci. Technol. **48** (1) (2011) 1.
[3] C.D. Bowman, et al., NSE **159** (2008) 182–198.

M. Teshigawara[1], Y. Tsuchikawa[2], G. Ichikawa[2], S. Takata[3], K. Mishima[4], M. Harada[1], M. Ooi[1], Y. Kawamura[5], T. Kai[3], S. Ohira-Kawamura[3], K. Nakajima[3], Y. Ikeda[6], and Y. Kiyanagi[2]

[1]*Neutron Source Section, Materials and Life Science Division, J-PARC Center;* [2]*Laboratory for Particle Properties, Nagoya University;* [3]*Neutron Science Section, Materials and Life Science Division, J-PARC Center;* [4]*Institute of Materials Structure Science, KEK;* [5]*Neutron Science and Technology Center, CROSS;* [6]*J-PARC Center*

Ice I_c without Stacking Disorder by Evacuating Hydrogen from Hydrogen Hydrate

1. Introduction

Water freezes below 0°C at atmospheric pressure, usually to ice I_h with a hexagonal stacking sequence. However, under certain laboratory conditions, it is also known to produce "ice I_c", nominally with a cubic stacking sequence [1]. Among over 19 polymorphs in numerous ice polymorphs, "ice I_c" has a special importance, since "Ice I_c" could ubiquitously exist in Earth's atmosphere, in comets, or even in frozen food. Despite the numerous studies on "ice I_c", its structure has not been fully verified, because the diffraction patterns of "ice I_c" show signatures of stacking disorder (hereafter, called ice I_{sd} for clarity), and ideal ice I_c without stacking disorder had not been formed until very recently [2]. In this study, we noticed that a high-pressure form of hydrogen hydrate, called C_2, has the same hydrogen-bonding framework as ice I_c. Once C_2 was synthesized under high-pressure, then it metastably recovered in decompression at low temperature for keeping the framework, and finally we managed to degas hydrogen from C_2, so that the ideal ice I_c without stacking disorder was obtained.

2. Experiments

A mixture of D_2O and MgD_2 was used as a starting material, where MgD_2 is an internal deuterium source to synthesize C_2. After loading the mixture into a pressure-temperature controlling 'Mito system' [3], MgD_2 was decomposed by heating at 403 K and 0 GPa for 1 h (at *b* in Fig. 1). Then, the samples were cooled to room temperature (at *c*) and compressed up to ~3 GPa until a C_2 phase was observed (at *d*). The sample was then cooled from 300 K to 100 K at around 3 GPa (path $d \rightarrow e$), decompressed at 100 K (path $e \rightarrow f$), and finally heated (path $f \rightarrow g$). Neutron diffraction experiments were conducted at the beamline PLANET in the MLF of J-PARC.

3. Results and discussion

Deuterium was released from MgD_2 and D_2O through a nominal reaction of $MgD_2 + 3D_2O \rightarrow Mg(OD)_2 + 2D_2 + D_2O$, forming C_2 above ~3 GPa. The neutron diffraction pattern for the C_2 phase obtained at 3.3 GPa and 300 K (at *d* in Fig. 1) was analyzed by the Rietveld method, and the calculated diffraction pattern was in good agreement with the observed one. The C_2 phase

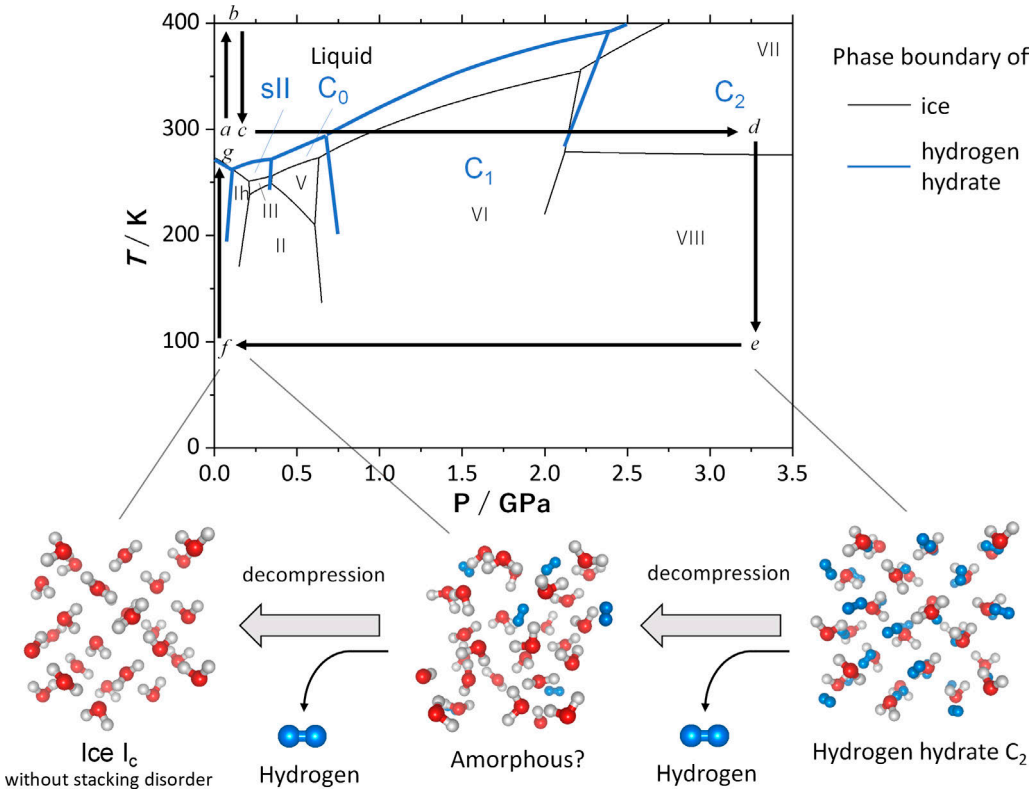

Figure 1. Phase diagram of hydrogen hydrate and ice with experimental *P-T* paths in this study.

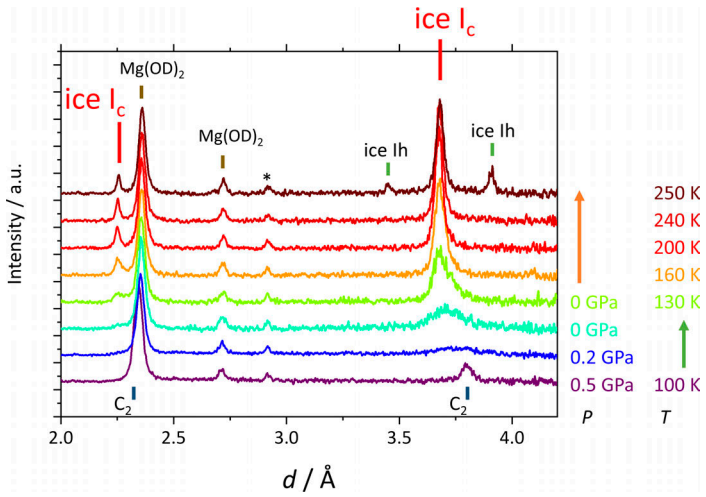

Figure 2. Neutron diffraction patterns showing the transformation from C_2 to ice I_c. The patterns were obtained with decreasing pressure at 100 K (path $e \rightarrow f$) and with increasing temperature at 0 GPa (path $f \rightarrow g$).

persisted at pressures at least as low as 0.5 GPa on decompression at 100 K (path $e \rightarrow f$). However, quite unexpectedly, the Bragg peaks of C_2 mostly disappeared at 0.2 GPa (Fig. 2), showing that the C_2 transforms to amorphous-like state. The sample was further decompressed to 0 GPa and evacuated using a turbo-molecular-pump. The broad peaks corresponding to ice I_c appeared at this stage, showing that the amorphous-like form is an intermediate transition state from C_2 to ice I_c, which forms while hydrogen (deuterium) molecules are partially degassed. The broad peak of ice I_c sharpened with the temperature increase at 0 GPa (path $f \rightarrow g$), and the obtained neutron diffraction pattern fitted well using the ice I_c structure model. The Rietveld refinement using the C_2 structure model showed that the occupancy of guest deuterium molecule was zero, within the experimental error. Also, no sign of stacking disorder was confirmed. This should be a clear indication of the presence of ideal ice I_c without stacking disorder.

It is also noteworthy that the ice I_c surprisingly persists up to at least 240 K until ice I_h starts to appear at 250 K (Fig. 2). The temperature of 240 K is significantly higher than the (meta)stability limit of previously known ice I_{sd} [1]. The notable stability of the ice I_c compared to ice I_{sd} would be derived from the lack of stacking disorder. The stacking disordered ice has more dislocations, which promote the phase transformation from ice I_{sd} to ice I_c by reducing the activation energy required to change the stacking sequence.

4. Future prospects

The discovery of ideal ice I_c will allow us to research the real physical properties of ice I_c without stacking disorder. For example, accurate heat capacity or vapor pressure measurements from low temperature will provide the free energy of ice I_c, which would settle the long-standing argument about the thermodynamic stability of ice I_c compared to ice I_h. The physical properties of the ideal ice I_c are also important to understand the role played by stacking disorder in the physical properties of ice I_{sd}. For instance, since the thermal conductivity of ice I_{sd} is significantly lower than ice I_h, the difference of thermal conductivities between ices I_h and I_c will emboss the effect of stacking disorder.

References

[1] W. F. Kuhs, C. Sippel, A. Falenty, and T. C. Hansen, Proc. Nat. Acad. Sci. **109**, 21259 (2012).
[2] L. del Rosso, M. Celli, F. Grazzi, M. Catti, T. C. Hansen, A. D. Fortes, and L. Ulivi, Nature Materials **19**, 663 (2020).
[3] K. Komatsu, M. Moriyama, T. Koizumi, K. Nakayama, H. Kagi, J. Abe, and S. Harjo, High. Press. Res. **33**, 208 (2013).

K. Komatsu[1], S. Machida[2], F. Noritake[3,4], T. Hattori[5], A. Sano-Furukawa[5], R. Yamane[1], K. Yamashita[1], and H. Kagi[1]
[1]Geochemical Research Center, Graduate School of Science, The University of Tokyo; [2]Neutron Science and Technology Center, CROSS; [3]Graduate Faculty of Interdisciplinary Research, University of Yamanashi; [4]Computational Engineering Applications Unit, RIKEN; [5]Neutron Science Section, Materials and Life Science Division, J-PARC Center

Novel Excitations Near Quantum Criticality in Geometrically Frustrated Antiferromagnet $CsFeCl_3$

1. Introduction

The investigation of the collective excitation in the low-energy range is indispensable for understanding condensed matter. According to the quantum field theory, the excitation in a system with spontaneous symmetry broken is characterized by phase and amplitude fluctuations of order parameters. The former is known as Nambu-Goldstone (NG) mode, and the latter is called amplitude mode. Even though these modes are usually separated, they are hybridized under certain conditions, and interesting phenomena are induced; for example, in a crystal lattice system, an acoustic phonon (NG mode) and an optical phonon (amplitude mode) are hybridized through anharmonic terms in a thermoelectric material PbTe, which renormalizes the phonon spectrum and leads to low thermal conductivity and a high figure of merit in thermoelectric property [1]. Such a hybridization effect could exist in other types of elementary excitations, however, as far as we know, no research has been reported, partially because the longitudinal mode itself is not trivial.

Spin $S = 1$ easy-plane antiferromagnet is one of the prototypical quantum spin systems that allows to explore the quantum phase transition (QPT) [2]. When the anisotropy D is large, the ground state is a quantum disordered (QD) singlet, as shown in Fig. 1, left panel. When D is small and the exchange interaction is large, the ground state is a magnetically long-range ordered state. A remarkable feature in the renormalized energy scheme in Fig. 1, right panel, is that the second excited state can be excited only by the longitudinal component of spin operator $S^{\parallel}$, meaning that the longitudinal mode is allowed in the system. Because the geometrical frustration in magnets could induce the hybridization of the transverse (T) and longitudinal (L) modes, spin $S = 1$ easy-plane antiferromagnet, with its geometrically frustrated lattice, is the best playground for the research of hybridized modes in magnetic materials.

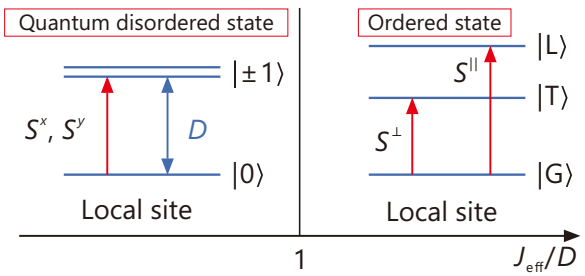

Figure 1. Schematic diagram of the $S = 1$ easy-plane antiferromagnet. In the ordered state, the doublet excited states $|\pm1\rangle$ splits into $|L\rangle$ and $|T\rangle$. Here, the former and latter have longitudinal and transverse fluctuations, respectively.

$CsFeCl_3$ is the $S = 1$ easy-plane triangular antiferromagnet. The inelastic neutron scattering (INS) study at ambient pressure revealed that the ferromagnetic chains along the crystallographic c axis are antiferromagnetically coupled in the ab plane [3]. The ground state is the QD state because of large single-ion anisotropy. The magnetic susceptibility measurement under pressures exhibited a pressure-induced magnetic order above a critical pressure of about 0.9 GPa [4]. Owing to the strong easy-plane anisotropy, the ordered moment aligns in the ab plane; the neutron diffraction revealed the noncollinear 120° structure in the LRO phase [5]. $CsFeCl_3$ is, thus, a promising host for the pressure-induced QPT in the geometrically frustrated lattice. In 2019, our group reported a new hybridization of the phase and amplitude fluctuations of the order parameter near QCP in $CsFeCl_3$[6].

2. Results

The INS spectrum measured at 0.0 GPa by using chopper spectrometer in Fig. 2(a) exhibits a single dispersive excitation with an energy gap of 0.6 meV at wave vectors $\boldsymbol{q} = (-k, 2k, 0)$ for $k = 1/3$ and 2/3. The energy gap at 0.3 GPa in Fig. 2(b) softens when approaching the ordered state. A qualitatively different spectrum is observed in the ordered state at 1.4 GP in Fig. 2(c). A well-defined gapless excitation emerges at $k = 1/3$ and 2/3 and another dispersive excitation is observed in the higher energy range. The INS spectra were collected also by using a triple-axis spectrometer in order to cover wide $\hbar\omega$–$\boldsymbol{q}$ range, and the extracted peak energies are overplotted by open symbols in Figs. 2(a)-2(c). At 1.4 GPa, the spectral lineshape at $k = 5/6$ is reproduced by double Lorentzians with broad widths, which is reflected by large error bars. The dispersion relations calculated by the extended spin-wave theory (ESW) [7] are indicated by the solid yellow curves. The calculation is consistent with the experiment in both the QD and LRO phases.

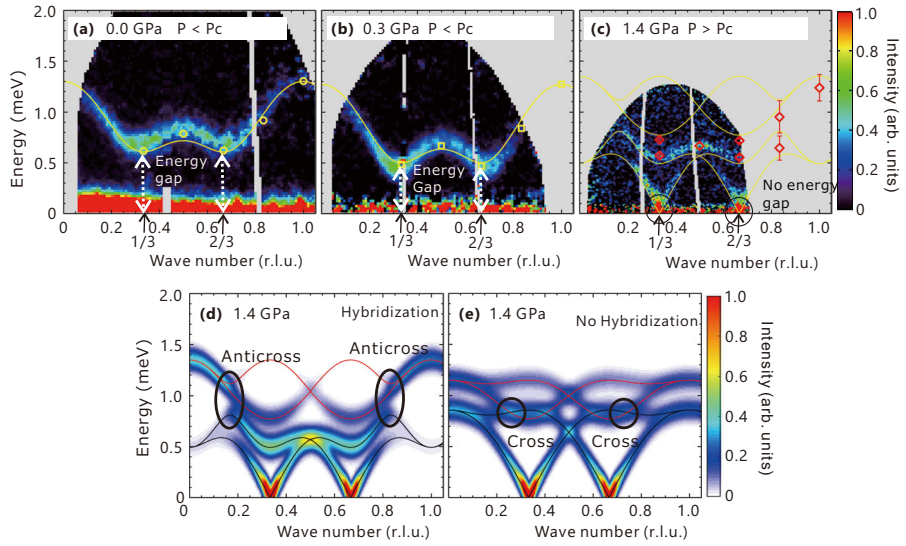

Figure 2. Inelastic neutron scattering spectra. The spectra obtained at a chopper spectrometer under (a) 0.0 GPa at 6 K, (b) 0.3 GPa at 2.7 K and (c) 1.4 GPa at 0.9 K sliced by the energy transfer - wave vector ($\hbar\omega - \boldsymbol{q}$) plane for $\boldsymbol{q} = (-k, 2k, 0)$. The yellow circles, squares, and red diamonds are the peak positions of the excitations obtained from the constant-q scans using a triple-axis spectrometer. The solid yellow curves are the dispersions calculated by ESW. Calculated neutron cross-section by the ESW under (d) 1.4 GPa at 0 K. Calculated neutron cross-section in the absence of the off-diagonal elements under (e) 1.4 GPa at 0 K. The black and red solid curves in (d) and (e) are gapless and gapped modes, respectively.

3. Discussion

In the ESW calculation, one can notice that noncollinearity of the magnetic structure creates off-diagonal elements in the Hamiltonian nonzero, leading to the hybridization of the L and T modes in one-magnon process. To understand the effects of LT-hybridization, we demonstrate the INS spectra after dropping the off-diagonal element. The results are shown in Fig. 2(e), where the black-gapless (red-gapped) modes are pure transverse (longitudinal) modes in this case. The result is inconsistent with the experiment in Fig. 2(c). When the LT-hybridization is taken into account, the off-diagonal elements lead to anticross of the modes at $k \sim 5/6$ in Fig. 2(d), and novel magnetic excitations are formed; both gapless and gapped modes are accompanied by strong longitudinal and transverse fluctuations. The result is consistent with the experiment, proving that the LT-hybridization plays an important role in magnon dynamics in the noncollinear magnet near QCP.

4. Future plans

Since the newly found excitation exists in a noncollinear spin structure, the search for excitation in different types of noncollinear structures, such as a cycloidal structure, all-in all-out structure, and skyrmion lattice would be an interesting topic. The search for the hybridized mode in other systems, including charge density wave, spin density wave, and ultra-cold atoms, would also be important. Finally, the effect of hybridization on the lifetime of the magnon and other elementary excitations would be worth exploring as well.

References

[1] O. Delaire, J. Ma, K. Marty, A. F. May, M. A. McGuire, M. H. Du, D. J. Singh, A. Podlesnyak, G. Ehlers, M. D. Lumsden, B. C. Sales, Nat. Mat. **10**, 614 (2011).
[2] M. Matsumoto, M. Koga, J. Phys. Soc. Jpn. **76**, 073709 (2007).
[3] H. Yoshizawa,W. Kozukue, K. Hirakawa, J. Phys. Soc. Jpn. **49**, 144 (1980).
[4] N. Kurita, H. Tanaka, Phys. Rev. B **94**, 104409 (2016).
[5] S. Hayashida, O. Zaharko, N. Kurita, H. Tanaka, M. Hagihala, M. Soda, S. Itoh, Y. Uwatoko, T. Masuda, Phys. Rev. B **97**, 140405 (2018).
[6] S. Hayashida, M. Matsumoto, M. Hagihala, N. Kurita, H. Tanaka, S. Itoh, T. Hong, M. Soda, Y. Uwatoko and T. Masuda, Sci. Adv. **5**, eaaw5639 (2019).
[7] R. Shiina, H. Shiba, P. Thalmeier, A. Takahashi, O. Sakai, J. Phys. Soc. Jpn. **72**, 1216 (2003).

S. Hayashida[1], M. Matsumoto[2], M. Hagihala[1,4], N. Kurita[3], H. Tanaka[3], S. Itoh[4], T. Hong[5], M. Soda[1], Y. Uwatoko[1], and T. Masuda[1,4]
[1]ISSP, the University of Tokyo; [2]Shizuoka University; [3]Tokyo Institute of Technology; [4]KEK; [5]Oak Ridge National Laboratory

Triplon Band Splitting and Topologically Protected Edge states in the Dimerized Antiferromagnet

1. Introduction

Topology is a branch of mathematics that classifies objects in terms of invariant properties under smooth deformations. A classification between a ball and a coffee cup is a common example to illustrate this concept. A ball cannot be deformed into a coffee cup without cutting or pasting its part, and in this sense, these objects are topologically distinct. It has been understood that the topological classification can be also applied to electron wavefunctions defined across a momentum space, after the discovery of a topological insulator [1, 2]. A topological insulator is an insulator that has conducting edge states due to the difference in topological invariants between inside and outside of the material. Topological invariants cannot be changed as long as the material remains insulating. At the edge, the material cannot remain insulating because of abrupt change in the topological invariants. Since the conducting edge states are protected by symmetry and free from dissipation, they are expected to be utilized for the future energy-efficient information transmission and processing.

The concept of topology has been extended not only to electron wavefunctions but also to wavefunctions of bosonic quasiparticles, such as magnons. These quasiparticles carry heat in magnetic materials as electrons carry charges in metallic compounds. Indeed, occurrence of heat flow perpendicular to both a thermal gradient and a magnetic field was discovered in the ferromagnetic insulator $Lu_2V_2O_7$ [3]. This phenomenon is called thermal Hall effect, and its origin is explained by the Dzyaloshinskii-Moriya (DM) interactions. The DM interactions induce complex hopping amplitudes of magnons, leading to the nontrivial band topology and the associated edge magnons carrying heat [4]. On the other hand, the nontrivial band topology has been rarely reported for triplons: triply degenerate excitations defined on an antiferromagnetic dimer with a singlet ground state. A rare example is $SrCu_2(BO_3)_2$, where interdimer DM interactions induce complex triplon hopping amplitudes [5, 6].

2. Dispersion relation of triplons in the dimerized antiferromagnet $Ba_2CuSi_2O_6Cl_2$.

In this report, we show that triplons can construct triplon bands with topologically protected edge states in the spin-1/2 dimerized antiferromagnet $Ba_2CuSi_2O_6Cl_2$. In this compound, an antiferromagnetic dimer is formed by a pair of CuO_4Cl pyramids, and these dimers form a rectangular lattice on the *ab*-plane [7], as shown in Fig. 1(a). Its triplon dispersion relations were investigated by inelastic neutron scattering experiment using the cold-neutron disk chopper spectrometer AMATERAS [8]. Twenty pieces of single crystals prepared by the self-flux method were coaligned on a rectangular Al plate. Intensities were collected by rotating the sample by almost 90° around the c^* axis.

A spin excitation spectrum has indicated propagation of triplons across the rectangular lattice. Figure 2(a) shows a color contour map of the excitation spectrum sliced by $K = 0$. It is overlapped by that sliced by $H = 0$ due to crystallographic domains. The intensity is integrated over the L direction since these branches are dispersionless along the L direction. The two dispersive branches between 2 and 3 meV indicate the dispersion along H and K direction. In addition, the intensity of the triplon excitations decreases at 2.6 meV, independently of the scattering wave vector.

The intensity decrease is not allowed in a regular rectangular lattice of antiferromagnetic dimers and is only possible under the small distortion in the rectangular lattice. Under the space group of this compound ($Cmc2_1$), a bond alternation in interdimer interactions is allowed, as illustrated in Fig. 1(a). The alternation induces a band inversion between the bonding- and anti-bonding triplon bands, resulting in an energy gap

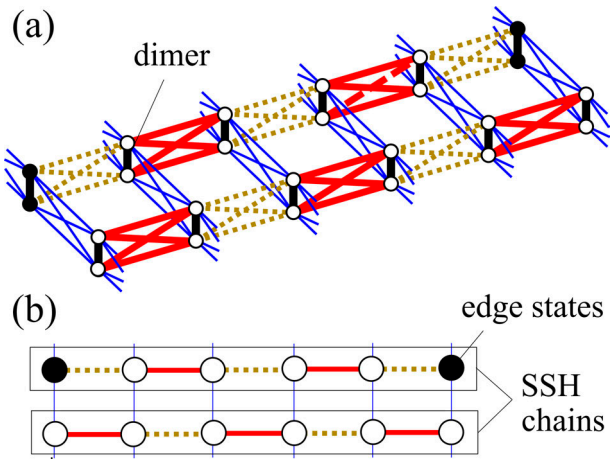

Figure 1. (a) Interdimer network in $Ba_2CuSi_2O_6Cl_2$ equivalent to (b) SSH chains weakly coupled by interchain hopping terms. Solid black circles represent triplons localized at the edge of the chains.

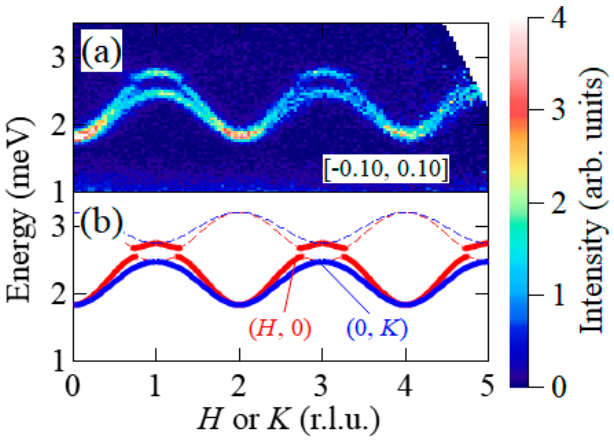

Figure 2. (a) Energy-momentum maps of the scattering intensities along the (*H*, 0) or (0, *K*) direction compared with (b) dispersion relations of the weakly coupled SSH model. The intensity is integrated for the *K* or *H* range of ±0.10 and the entire observed *L* range.

between them. If the alternation is very small, the structure factor of both bands becomes almost the same as that without the alternation. Thus, for the most part, the anti-bonding triplon bands are almost undetectable. The dispersion relation with the parameter sets that most accurately reproduces the experimental results is shown in Fig. 2(b).

3. Nontrivial topology induced by bond alternation

The nontrivial topology in triplon bands is induced by the distortion of the rectangular lattice. The distorted rectangular lattice can be regarded as a weakly coupled Su-Schrieffer-Heeger (SSH) model [9], as illustrated schematically in Fig. 1(b). The SSH model has been originally constructed to explain the electron motions of polyacetylene. The bond alternation induces an energy gap between two electron bands, and effectively introduces complex hopping amplitudes of electrons. They result in both the topologically trivial and nontrivial states depending on the hopping amplitudes. Both states cannot be connected without closing the energy gap, and in this sense, edge states expected in the nontrivial state are called topologically protected. The presence of the edge states under the bond alternation is apparent when they are described in a real space: localized electrons that cannot form a pair are left at the edge under certain hopping amplitudes.

The inelastic excitation spectrum has revealed that $Ba_2CuSi_2O_6Cl_2$ can be regarded as the quasi-two-dimensional variant of the SSH model. The topologically protected triplon edge states are induced by the bipartite nature of the distorted rectangular lattice. The edge states should be present at the center of the energy gap, 2.6 meV, and can be formed only by thermal activation.

4. Future plans

Bosonic quasiparticles, such as magnon and triplons, should exhibit different topological properties from those expected for electrons. The difference would be enhanced under strong interactions between the quasiparticles. A dimer antiferromagnet is a good playground to investigate the topological character of bosonic quasiparticles, since triplon density can be tuned by a magnetic field. Additional research may lead to further development of our understanding of energy-efficient information transmission and processing utilizing heat transport of the edge states.

References

[1] D. Hsieh et al., Nature **452**, 970–974, (2008).
[2] M. Z. Hasan and C. L. Kane, Rev. Mod. Phys. **82**, 3045–3067 (2010).
[3] Y. Onose et al., Science **329**, 297–299 (2010).
[4] L. Zhang et al., Phys. Rev. B **87**, 144101 (2013).
[5] J. Romhanyi et al., Nat. Commun. **6**, 6805 (2015).
[6] P. A. McClarty et al., Nat. Phys. **13**, 736 (2017).
[7] M. Okada et al., Phys. Rev. B **94**, 094421 (2016).
[8] K. Nakajima et al., J. Phys. Soc. Jpn. **80**, SB028 (2011).
[9] K. Nawa et al., Nat. Commun. **10**, 2096 (2019).
[10] W. P. Su et al., Phys. Rev. Lett. **42**, 1698 (1979).

K. Nawa[1], K. Tanaka[2], N. Kurita[2], T. J. Sato[1], H. Sugiyama[3], H. Uekusa[3], S. Ohira-Kawamura[4], K. Nakajima[4], and H. Tanaka[2]
[1]*Institute of Multidisciplinary Research for Advanced Materials, Tohoku University;* [2]*Department of Physics, Tokyo Institute of Technology;* [3]*Department of Chemistry, Tokyo Institute of Technology;* [4]*Materials and Life Science Division, J-PARC Center*

Localized Magnetic Excitations in the Fully Frustrated Dimerized Magnet $Ba_2CoSi_2O_6Cl_2$

1. Introduction

A coupled spin dimer system, in which antiferromagnetic dimers interact with one another through interdimer exchange interactions, provides an opportunity for correlating condensed matter physics with particle physics. This system often exhibits a nonmagnetic ground state with a finite excitation gap. In an external magnetic field exceeding the gap size, magnetic quasiparticles, magnons (or triplons), are created on the dimer. As illustrated in Fig. 1, magnons move to neighboring dimer lattice and interact with one another owing to the transverse and longitudinal components of the interdimer exchange interactions, respectively. One intriguing feature is the crystallization of magnons, in the form of a Wigner crystal, which could be a key to understanding exotic quantum phases such as supersolids [1–4] and flatband solid states [5]. The crystallized phase of magnons is expected to emerge when the frustration of the interdimer exchange interactions is so strong that magnons become localized [6–8]. To our best knowledge, until recently, the experimental studies have been limited to the Shastry-Sutherland compound $SrCu_2(BO_3)_2$ [6, 7].

Recently, we found that a new series of two-dimensional spin dimer systems, $Ba_2CoSi_2O_6Cl_2$, exhibits a sharply stepwise magnetization process with a plateau at one half of saturation magnetization M_s [8]. This suggests that the interdimer exchange interactions of this compound are almost perfectly frustrated. On the other hand, a spin dimer system can give rise to a similar $(1/2)M_s$ plateau provided that there exist two kinds of isolated dimer with equal populations. For a definitive conclusion, it is important to elucidate the magnetic excitations of this compound.

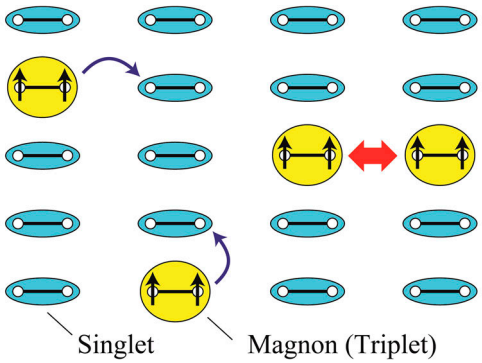

Figure 1. Image of magnons which hop to a neighboring dimer site and interact with a neighboring magnon.

Here, we report on the results of inelastic neutron scattering (INS) measurements of $Ba_2CoSi_2O_6Cl_2$ [9], using the cold-neutron disk chopper spectrometer AMATERAS installed in the Materials and Life Science Experimental Facility (MLF) at J-PARC, Japan [10].

2. Experimental details

Single crystals of $Ba_2CoSi_2O_6Cl_2$ were grown by the flux technique [8]. INS measurements were performed at several temperatures from 4 to 240 K with two sets of incident neutron energies E_i = (2.6, 5.9, 10.5, 23.6) meV and (2.9, 4.7, 7.7, 15.2) meV. Approximately 60 platelike single crystals with a total mass of ~1 g were glued on an aluminum plate, where the *a* axis (or *b* axis) for each crystal was aligned parallel to the horizontal direction. The fluoropolymer (CYTOP® [11]) employed as the glue had a negligible contribution to the background. The wave vector k_i of an incident neutron was set parallel to the *c* axis. All the data were analyzed using the software suite Utsusemi [12].

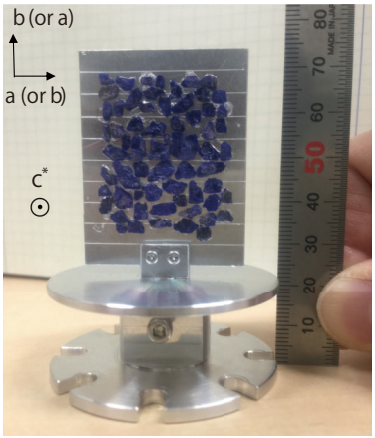

Figure 2. Photograph of a sample setup used for the inelastic neutron scattering experiment of $Ba_2CoSi_2O_6Cl_2$.

3. Results and discussion

Figures 3(a) and 3(b) show the energy-momentum map of the scattering intensity along $\boldsymbol{Q} = (Q_a, 0, 0)$ at 4 K measured with E_i = 15.2 and 23.6 meV, respectively, where the scattering intensities were integrated over Q_b and Q_c [9]. The directions of Q_a (Q_b) and Q_c are parallel and perpendicular to the dimer layer, respectively, in $Ba_2CoSi_2O_6Cl_2$. One can confirm three strong dispersionless excitations at 4.8, 5.8, and 6.6 meV and two

weak ones at higher energies of 11.4 and 14.0 meV. The noteworthy feature of the three low-energy excitations at 4–7 meV is that the scattering intensities exhibit different Q dependencies. This is more evident in the constant-energy slices of the scattering intensity shown in Figs. 3(d)–(f), where the scattering intensity is integrated over Q_c, considering the good two dimensionality, as evidenced by the observed dispersionless excitations along Q_c. The intensity of the middle excitation with the highest intensity at 5.8 meV is nearly independent of (Q_a, Q_b). On the other hand, the intensities of the upper-side (6.6 meV) and lower-side (4.8 meV) excitations exhibit local maxima when both Q_a and Q_b are integers and half-integers, respectively.

It is considered that when an excited triplet is localized, the single singlet-triplet excitation is dispersionless and its intensity is independent of Q_a and Q_b. Thus, the middle excitation peak at 5.8 meV can be assigned to the single singlet-triplet excitation to the $|t_{\pm1}\rangle$ state. Assuming that the excitation at 11.4 meV corresponds to the single singlet-triplet excitation to the $|t_0\rangle$ state, we obtain $J^{\perp} = 11.4$ meV and $J^{\parallel} = 0.16$ meV. This means that the intradimer exchange interaction closely approximates the XY model.

Because there is no other single-triplet excitation to the $|t_{\pm1}\rangle$ states, we can deduce that all the dimers are magnetically equivalent. Thus, the sharply stepwise magnetization process with a (1/2) magnetization plateau can only be described in terms of the crystallization of localized magnons owing to the strong frustration of interdimer exchange interactions [8]. From these observations, we can safely conclude that the interdimer interactions in $Ba_2CoSi_2O_6Cl_2$ almost satisfy the perfect frustration condition.

Next, we discuss the origin of the anomalous side peaks observed at 4.8 and 6.6 meV. Given that the $Ba_2CoSi_2O_6Cl_2$ crystals employed in this study are perfect crystals, the side-peak structure will be absent from the excitation spectrum. It is natural to assume that these side peaks are produced by interdimer interactions, because the energy difference between these side peaks and the middle peak is on the order of the interdimer interactions and the intensities of these side peaks are commensurate with a and b.

One plausible scenario is that the observed side peaks are caused by the three-body problem among dimer spins and a neighboring undimerized single spin produced by a vacancy of Co^{2+}. To confirm the above hypothesis based on the existence of undimerized spins and to explain the periodic intensity oscillations in the excitations at 4.8 and 6.6 meV, we calculated the differential cross section of the inelastic neutron scattering for the decoupled-dimer excitation and the excitations mediated by undimerized spins. As shown in Figs. 3(d)–(i), the calculated results provide an excellent agreement with the observed scattering intensities. We also found that a crucial factor to produce the Q-dependent oscillation was the weak mixing of singlet and triplet components in the ground and excited states owing to the entanglement with the undimerized spin state.

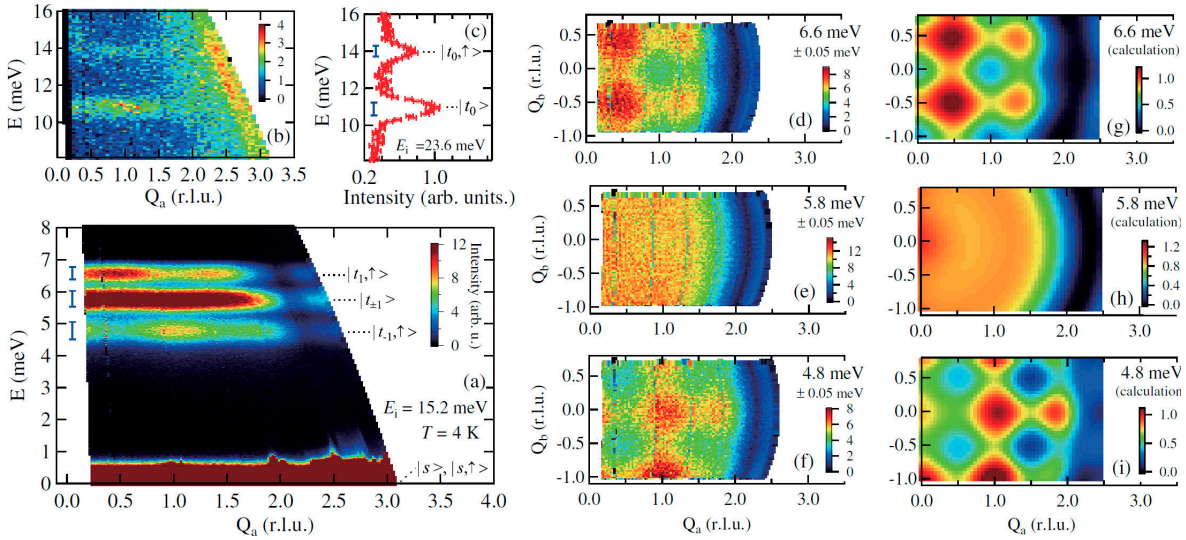

Figure 3. Energy-momentum maps of the scattering intensity along Q_a at the base temperature of 4 K measured with E_i = (a) 15.2 meV and (b) 23.6 meV, which were integrated over Q_b and Q_c. (c) Energy vs scattering intensity measured with E_i =23.6 meV, where the scattering intensity was integrated over the complete Q_a, Q_b, and Q_c range. (d)–(f) Constant-energy slices of the scattering intensity, where the scattering intensity was integrated over Q_c, and (g)–(i) the calculated ones (arb. units). In (a) and (c), vertical bars denote the energy resolution.

4. Conclusion and future plans

To summarize, we have probed the magnetic excitations of $Ba_2CoSi_2O_6Cl_2$ directly via inelastic neutron scattering measurements. The five observed types of magnetic excitation were dispersionless within the resolution limits, and hence triplet excitations were verified to be localized. Unexpectedly, three low-energy excitations at 4–7 meV exhibited characteristic *Q* dependencies of scattering intensities. It was found that the excitation spectra could reasonably be explained by considering two mechanisms independently: a "perfect frustration" scenario for interdimer interactions in the host system, and emergent three-body quantum states owing to undimerized spins induced by vacancies in the crystals. This work shows that the highly frustrated quantum magnets provide the various playgrounds of interacting quantum particles, and shows a typical case in which a small amount of vacancy has a large effect on the excitation spectra, although the vacancy effect is usually hidden by the spectra of the host system. To obtain further experimental findings to increase the understanding of this system, it is important to elucidate the field evolution of each excitation by, for example, in-field neutron scattering and electron spin resonance experiments.

References

[1] P. Chen, C. Y. Lai, and M. F. Yang, Phys. Rev. B **81**, 020409 (R) (2010).

[2] A. F. Albuquerque, N. Laflorencie, J. D. Picon, and F. Mila, Phys. Rev. B **83**, 174421 (2011).

[3] Y. Murakami, T. Oka, and H. Aoki, Phys. Rev. B **88**, 224404 (2013).

[4] D. Yamamoto and I. Danshita, Phys. Rev. B **88**, 014419 (2013).

[5] J. Richter, O. Krupnitska, V. Baliha, T. Krokhmalskii, and O. Derzhko, Phys. Rev. B **97**, 024405 (2018).

[6] H. Kageyama et al., Phys. Rev. Lett. **82**, 3168 (1999).

[7] S. Miyahara and K. Ueda, Phys. Rev. Lett. **82**, 3701 (1999).

[8] H. Tanaka et al., J. Phys. Soc. Jpn. **83**, 103701 (2014).

[9] N. Kurita, D. Yamamoto, T. Kanesaka, N. Furukawa, S. Ohira-Kawamura, K. Nakajima, and H. Tanaka, Phys.Rev.Lett. **123,** 027206 (2019). See Supplemental Material at http://link.aps.org/supplemental/10.1103/PhysRevLett.123.027206 for additional information on the experimental data and the theoretical calculations.

[10] K. Nakajima et al., J. Phys. Soc. Jpn. **80**, SB028 (2011).

[11] https://www.agcchem.com/products/specialty-materials/cytop

[12] Y. Inamura, T. Nakatani, J. Suzuki, and T. Otomo, J. Phys. Soc. Jpn. **82**, SA031 (2013).

N. Kurita[1], D. Yamamoto[2], T. Kanesaka[2], N. Furukawa[2], S. Ohira-Kawamura[3], K. Nakajima[3], and H. Tanaka[1]

[1]Department of Physics, Tokyo Institute of Technology; [2]Department of Physics and Mathematics, Aoyama-Gakuin University; [3]Materials and Life Science Division, J-PARC Center

Magnetic Skyrmion Lattice in a Centrosymmetric Breathing Kagome Lattice

1. Introduction

Topological spin orders have been of great interest since the discovery of magnetic skyrmion lattice (SkL), which is a periodic array of vortex-like spin objects, in a chiral magnet MnSi [1, 2]. Owing to the chiral crystal structure, MnSi has uniform Dzyaloshinski-Moriya (DM) interactions. Combining the DM interaction with ferromagnetic exchange interactions, MnSi exhibits long-period-modulated magnetic orders including SkLs. This established that chiral magnets with ferromagnetic interactions are promising candidates for skyrmion-host materials. In fact, there were a lot of reports on emergence of SkLs in chiral magnets such as FeGe [3], (Fe,Co)Si [4], Cu_2OSeO_3 [5], and Co-Zn-Mn alloys [6]. Subsequent theoretical studies have pointed out that centrosymmetric magnets can also host SkL without relying on DM interactions. Specifically, Okubo *et al*. revealed that magnetic frustration can induce SkL and anti-skyrmion lattice states in a centrosymmetric two-dimensional triangular lattice model [7]. Hayami *et al*. also revealed that a coupling between localized spins and conduction electrons can be a source of topological spin orders composed of multiple magnetic modulation wave vectors (*q*-vectors) [8]. Motivated by these theoretical studies, we study a centrosymmetric kagome lattice magnet $Gd_3Ru_4Al_{12}$.

2. Experiment

A single crystal of $Gd_3Ru_4Al_{12}$ was grown in a floating zone furnace. To avoid strong neutron absorption of Gd in natural abundance, we substituted it with isotope enriched ^{160}Gd. The sample was cut into a plate shape with dimensions of 2.5 × 2.0 × 0.6 mm^3. We performed small- and wide-angle neutron scattering measurements at TAIKAN instrument in BL15 of the Materials and Lifescience Experimental Facility (MLF) of J-PARC. The sample was loaded into the 4T-horizontal-magnet of BL15. An external magnetic field was applied parallel to the *c* axis of the sample.

3. Results and discussions

Figures 1(a) and 1(b) show schematic images of the crystal structure of $Gd_3Ru_4Al_{12}$. Gd^{3+} ions with spin S = 7/2 are arranged on kagome lattices, which are stacked along the *c* axis. Ru and Al atoms are located between the Gd kagome layers. In Fig. 1(c), we show a magnetic phase diagram of $Gd_3Ru_4Al_{12}$ exhibiting a variety of magnetic phases below T_{N1} = 18.6 K and magnetic field of up to 4 T. We first investigated magnetic phases in zero field. By using the small angle detectors of TAIKAN, we successfully revealed that the zero-field phases are characterized by incommensurate *q*-vectors of (*q*,0,0) and its equivalents, where *q* shows weak temperature dependence. The length of magnetic modulation, $\lambda_m = 2\pi/q$, is 2.8 nm, which is about one order of magnitude shorter than that of MnSi.

We measured field dependence of the magnetic reflections, revealing that all the magnetically ordered phases have the (*q*,0,0)-type *q*-vectors. In Fig. 2, we show the field dependence of the integrated intensity and the wavenumber *q* of the magnetic reflection at (*q*,0,0) measured at 2.4 K, as functions of magnetic field along the *c* axis. We found that the integrated intensity shows a sharp drop upon the phase transition from the ground state to the 1st-field-induced phase. This implies that the orientations of the magnetic moments abruptly change at this magnetic phase transition. To gain more insight into the magnetic structures, we also performed resonant X-ray magnetic scattering experiments on this system at BL-3A in the Photon Factory in KEK, and found that the magnetic structure changes from a screw-type structure to a cycloid-(transverse-conical) type structure upon the field-induced phase transition at the lowest temperature.

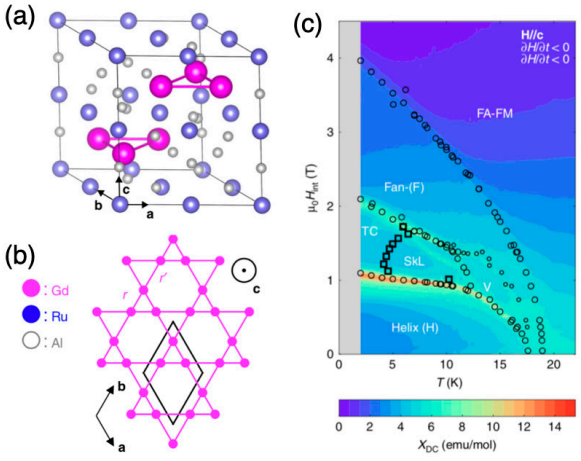

Figure 1. [(a), (b)] Schematic illustrations of the crystal structure of $Gd_3Ru_4Al_{12}$. (c) Magnetic phase diagram of $Gd_3Ru_4Al_{12}$ for magnetic field along the *c* axis. Color scale shows the real part of ac magnetic susceptibility. [cited from Ref. 10]

Having established the magnetic structures at the lowest temperature, we investigated the thermally-induced phase under magnetic field labeled "SkL" in Fig. 1(c). Similarly to the other magnetic phases, we observed three incommensurate q-vectors perpendicular to the c axis; specifically (q,0,0), (0,q,0) and (−q,q,0). Interestingly, we found that the Hall conductivity shows a hump anomaly in this phase, which is quite reminiscent of the topological Hall effect in the SkL phase of MnSi [9]. We thus expect that the spin texture of this phase is described by a superposition three q-vectors, which leads to a SkL as shown in Fig. 3(a). To obtain real-space image of the spin texture, we performed Lorentz transmission electron microscopy on a (001) thin plate of $Gd_3Ru_4Al_{12}$, and finally found that particle-like objects are arranged to form triangular lattice domains as shown in Fig. 3(b). This is the direct evidence of the SkL formation in this compound [10].

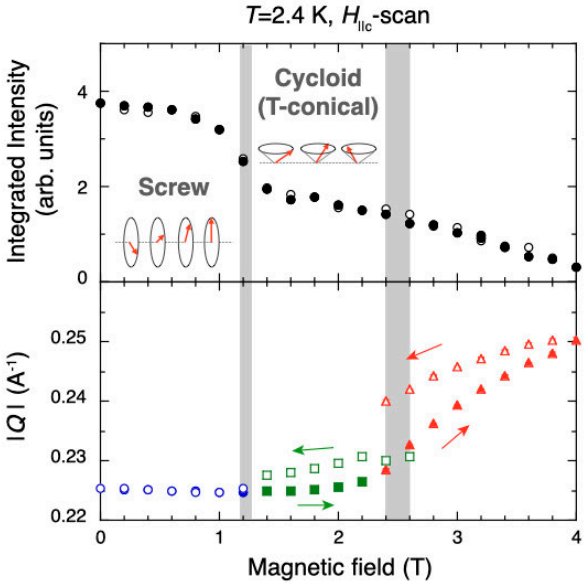

Figure 2. Field dependence of the integrated intensity, peak position and width along the radial direction for the magnetic reflection at (q,0,0) measured at 2.4 K.

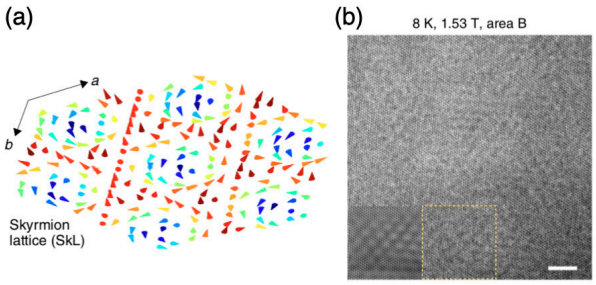

Figure 3. (a) Schematic illustration of the magnetic skyrmion on the kagome lattice of $Gd_3Ru_4Al_{12}$. (b) Real-space observation of the spin texture on the (001) plane of $Gd_3Ru_4Al_{12}$ by Lorentz transmission electron microscopy. [cited from Ref. 10]

4. Summary

We have demonstrated that the centrosymmetric kagome lattice compound $Gd_3Ru_4Al_{12}$ exhibits magnetic skyrmion lattice in the thermally induced phase under a magnetic field, suggesting that various topological spin orders can be realized in centrosymmetric systems, as evidenced by recent studies on Gd-based triangular and tetragonal systems [11, 12]. It has been established that the magnetic skyrmions in chiral magnets can be controlled by various external stimuli, such as electric current, its combination with thermal gradient, and hydrostatic/uniaxial pressure. We thus planning to explore the possibility of external field control of SkLs in cetrosymmetric crystals.

References

[1] S. Muhlbauer *et al.*, Science **323**, 915 (2009).
[2] Y. Tokura and N. Nagaosa, Nat. Nanotech. **8**, 899 (2013).
[3] X. Z. Yu *et al.*, Nat. Mater. **10**, 106 (2011).
[4] W. Munzer *et al.*, Phys. Rev. B **81**, 041203 (2010).
[5] S. Seki *et al.*, Science **336**, 198 (2012).
[6] Y. Tokunaga *et al.*, Nat. Commun. **6**, 7638 (2015).
[7] T. Okubo *et al.*, Phys. Rev. Lett. **108**, 017206 (2012).
[8] S. Hayami *et al.*, Phys. Rev. B **95**, 224424 (2017).
[9] A. Neubauer *et al.*, Phys. Rev. Lett., **110**, 209902 (2013).
[10] M. Hirschberger *et al.*, Nat. Commun. **10**, 5831 (2019).
[11] T. Kurumaji *et al.*, Science **365**, 914 (2019).
[12] N. D. Khanh *et al.*, Nat. Nanotech. **15**, 444 (2020).

M. Hirschberger[1], T. Nakajima[1], S. Gao[1], L. Peng[1], A. Kikkawa[1], T. Kurumaji[1], M. Kriener[1], Y. Yamasaki[2,3], H. Sagayama[4], H. Nakao[4], K. Ohishi[5], K. Kakurai[1,5], Y. Taguchi[1], X. Z. Yu[1], T. Arima[1,6], and Y. Tokura[1,7]

[1]RIKEN Center for Emergent Matter Science (CEMS); [2]Research and Services Division of Materials Data and Integrated System (MaDIS); National Institute for Materials Science (NIMS); [3]PRESTO, Japan Science and Technology Agency (JST); [4]Institute of Materials Structure Science, High Energy Accelerator Research Organization; [5]Neutron Science and Technology Center, Comprehensive Research Organization for Science and Society (CROSS); [6]Department of Advanced Materials Science, University of Tokyo; [7]Department of Applied Physics and Tokyo College, University of Tokyo

Multiple Structural Level Morphology of Sulfonated sPS Membranes Resolved by SANS

1. Introduction

The proton exchange membrane (PEM) fuel cells (PEMFC) are considered an attractive energy conversion technology with a potential to become an alternative to the current fossil fuel technologies in light-duty transportation. The PEM separates the anode from the cathode and conducts at very high rates the protons emerging from the catalyst facilitated hydrogen oxidation in the anode chamber. PEM materials are characterized by a nanoscale phase separation into hydrophilic domains and hydrophobic regions, a combination that enables high-proton conductivity and provides a good chemical and mechanical stability of the membrane. The proton conduction in PEMs depends on water and is governed by the water behavior at different length scales [1]. However, due to the membrane swelling, there is always a trade-off between reaching optimal conductivity and mechanical stability. Moreover, the membrane durability is affected by chemical decomposition caused by the free radicals produced during the PEMFC operation. The design of new PEM materials is thus a prerequisite to understanding the morphology of hydrated domains at different length scales and the behavior of the hydrophobic domains under PEMFC operation conditions.

Nafion (Du Pont™) is the best-known PEM material and although it has been established as a benchmark for such applications, it presents several drawbacks, such as the high cost, lack of safety during manufacturing and use, need of supporting equipment and temperature related limitations. As alternatives, different crystalline-amorphous polymeric architectures with similar conductive and chemo-mechanical properties as Nafion have been extensively studied in recent years.

2. The syndiotactic-polystyrene as model PEM

Given the recent developments, which enable a controlled functionalization by sulfonation of only the amorphous phase, thus preserving the crystallinity of the material [2], and an improved resistance to oxidation decomposition when fullerenes are added [3], the sulfonated syndiotactic polystyrene (s-sPS) in its β-form may become a good PEM material candidate, as it displays high proton conductivity, comparable to Nafion, high chemical and thermo-mechanical stability and a low cost. Starting from the δ-form (clathrate with guest molecules), which enables a homogeneous sulfonation of the amorphous regions, the membrane can be subsequently transformed by annealing into the thermodynamically stable β-form.

3. Micro-structural characterization of s-sPS

In a preliminary study [4], highly sulfonated s-sPS membranes with δ-clathrate co-crystalline form were explored at different relative humidity (RH) levels by small-angle neutron scattering (SANS). Besides the structural characterization of the crystalline lamellar stacks and the water cluster morphologies, the preservation of crystallinity was assumed only indirectly from the SANS data.

In the current study, membranes with different sulfonation degrees and crystallinity (pre-characterized conditions) were systematically investigated at room temperature in controlled hydrated states by using the extended *Q*-range available at the TAIKAN (BL-15) SANS diffractometer [5]. A *Q*-range from 0.005 to 2 $Å^{-1}$ was covered, which enabled a structural investigation over a wide-length scale, from the crystalline structure to the mesoscale size. The deuterated s–sPS films (ca. 100 μm), used to assure a low incoherent background, were doped with different guest molecules: with fullerenes - in the amorphous regions, to reproduce the conditions that prevent the membrane's chemical decomposition [3], and with protonated toluene – in the crystalline regions, to provide the right contrast at the local scale. A humidity chamber (Anton Paar, Graz, Austria) was used to control the RH between 5% and 85%. To understand the nature of the hydrated domains, contrast variation SANS was done using different H_2O/D_2O mixtures.

Figure 1 presents a selection of one-dimensional scattering data from a stretched s-sPS film with a low degree of sulfonation (S = 19.3%) and low crystallinity (22%) that was loaded with C60 fullerenes and hydrated at RH = 80% using different H_2O/D_2O mixtures. The use of uniaxially deformed film samples allowed the clear separation of scattering contributions from different morphologies and structural levels on different detection sectors (equatorial or meridional), depending on their size and orientation. Thus, the scattering features from the crystalline regions – the inter-lamellar correlation peak and the crystalline structure peaks – are anisotropic due to the orientation of structures as a

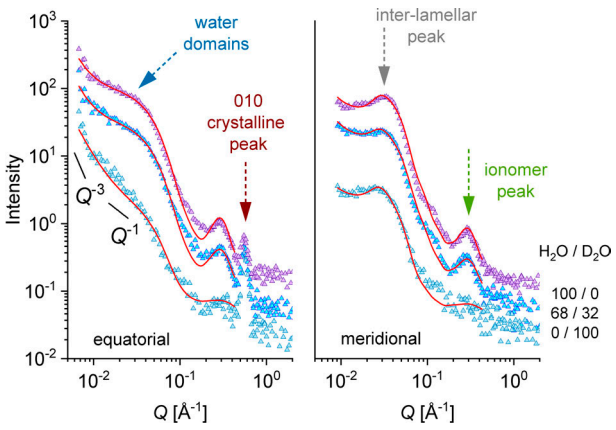

Figure 1. SANS patterns from a s-sPS film hydrated at RH = 80% using different H_2O/D_2O ratios. Symbols denote the experimental data, while the red lines correspond to the model interpretation of the data, as reported in [5].

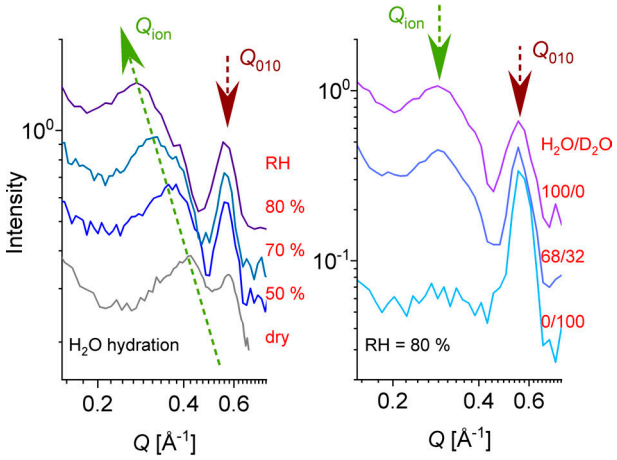

Figure 2. The high-*Q* range of the SANS patterns on the equatorial direction measured for different hydration levels with H_2O (left) and at RH = 80% using different H_2O/D_2O mixtures.

consequence of the film stretching, while the hydrated domains that are randomly distributed in the amorphous region yield isotropic scattering features.

The scattering patterns present three distinct peak-like features, which are also visible for all RH conditions (a selection of high-*Q* range data is shown in Fig. 2). These features are indicative of structural correlations occurring at different length scales in the complex morphology of the polymer films. The 010 crystalline peak visible in equatorial sectors at high *Q* values may be ascribed to the mean repeating distance between the sPS sheets and appears due to the neutron contrast provided by the protonated guest loaded in the cavities between deuterated host helices. The peak does not change its profile with the increase of RH or the variation of the SLD of hydrated water, which indicates the preservation of the membrane crystallinity, hence stability, during hydration-drying processes.

The ionomer peak, which occurs due to correlations between the ionic clusters, represents a scattering feature characteristic of the sulfonation and hydration in the amorphous regions, and is thus isotropic distributed on the detection area. The peak intensity is sensitive to the contrast between the hydration water and hydrophilic polymer segments, while the peak position Q_{ion} depends on the RH (Fig. 2), i.e. the correlation length ξ increases when the water cluster grows in size. No matching of scattering features characteristic of hydrated clusters was observed for the 70/30 H_2O/D_2O contrast condition corresponding to the SLD of sulfonic group, only the global intensity was lower, due to the lower contrast achieved between the hydrated and non-hydrated components of the film morphology. For hydration with 100% D_2O the ionomer peak vanishes, which indicates that the matching of the scattering properties of ionic clusters and surrounding water renders the correlation between the ionic clusters no longer visible. We concluded that the ionic clusters promoting the water uptake by the membrane consist of associations of larger sections of neighboring s-sPS chains in the region of the benzene ring and the sulfonic acid terminal group, which are correlated over the distance $2\pi/Q_{ion}$.

In the low *Q* region, the inter-lamellar peak characteristic of the oriented lamellar stacks can be observed in the meridian scattering patterns, with a stronger profile for the 100% H_2O contrast condition. The peak position remains almost unchanged with increasing RH, even in the case of samples with higher crystalline degree. The equatorial scattering pattern exhibits towards low *Q* a kind of plateau when hydration is achieved with 100% H_2O, which resembles characteristics of a spherical form factor, while a Q^{-1} power law behavior of the scattered intensity may be observed when 100% D_2O is used. Apparently, the water accumulates in clusters along groups of elongated s-sPS chains (SLD similar to that of D_2O) and highlights in this case the hydrated regions as one-dimensional arrangements against the hydrophobic environment (SLD lower than that of s-SPS). The upturn of intensity at low *Q*, which appears stronger on the equator direction due to the stretching of a sample on the vertical axis, arises from the large-scale fractal-like character of the membranes (Q^{-3} power law behavior).

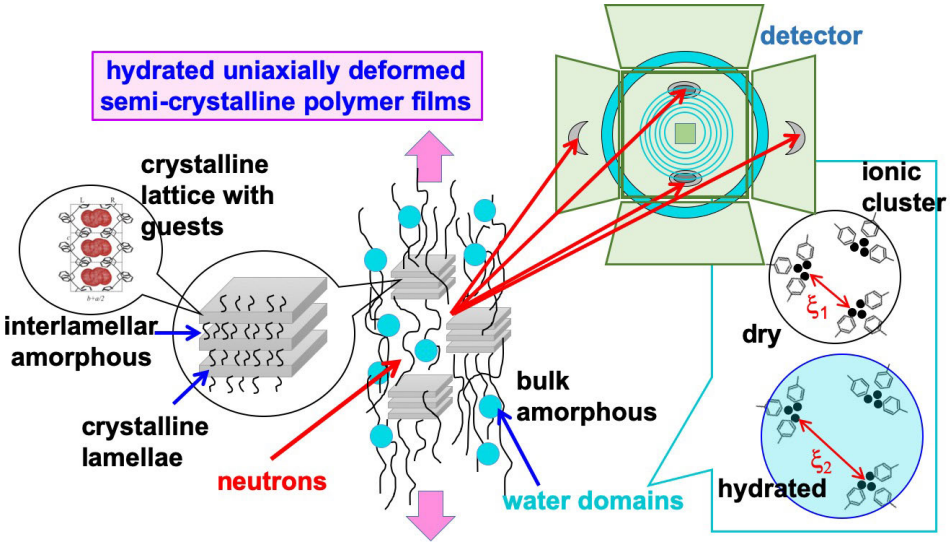

Figure 3. Schematic view of the experimental approach used to study the multiple structural level of the s-sPS morphology.

According to our qualitative and quantitative analysis of SANS data in terms of structural models [5], water is taken-up in clusters and is distributed to the same extent in the inter-lamellar and bulk amorphous regions at low hydration levels, whereas with increasing the hydration level the water accumulates predominantly in the bulk amorphous region favored by the increased flexibility of the sPS chains in these domains. At a very high RH cylindrical channel morphologies are yielded when the water clusters in the bulk amorphous regions grow and interconnect with each other [4].

Figure 3 shows the global picture of the multiple structural level character of the membrane as resolved using this specific SANS setup.

References

[1] A. Kusoglu, A.Z. Weber, Chem. Rev. **117**, 987 (2017).
[2] G. Fasano, et al., Int. J. Hydrog. Energy **36**, 8038 (2011).
[3] S. Saga, et al., J. Power Sources **176**, 16 (2018).
[4] M-M. Schiavone, et al., Solid State Ionics **320**, 392, (2018).
[5] M-M. Schiavone et al., Membranes **9**, 136, (2019).

M-M. Schiavone[1], H. Iwase[2], S. Takata[3], and A. Radulescu[1]
[1]Jülich Centre for Neutron Science, Forschungszentrum Jülich GmbH; [2]Neutron Science and Technology Center, CROSS; [3]Neutron Science Section, Materials and Life Science Division, J-PARC Center

Thickness of the Ethanol/Water Surface Layer

1. Introduction

The thickness of the surface layer of amphiphilic molecules is a crucial parameter for many physical processes. The essential processes involved in the interfacial layer include the evaporation rates and vapour/liquid equilibrium. Due to the thinness and fragile nature of the interface, such thickness remains improbable. The early studies (Li and co-authors, 1993) assumed the thickness is independent of concentration and equal to the length of the amphiphilic molecules. However, recent advances in the field have indicated that the interface layer is variable with the composition. Yet, the application of thermodynamic analysis leads to conflicting prediction. For the ethanol/water surface, which is important for many physical, chemical and biological processes, there are at least two contradicting predictions. One predicted that the thickness increases with ethanol concentration (Santos and Reis, 2018), whereas the other predicted a decreasing trend (Bagheri and co-authors, 2016).

2. New Method

We applied a new mathematical framework to relate the adsorption, composition and thickness. And the molar fraction at the surface is then:

$$x_e^s = \frac{\frac{\Gamma_e^{(w)}}{\delta} + \frac{x_e^b}{1-x_e^b} N_w^s}{\left(\frac{\Gamma_e^{(w)}}{\delta} + \frac{x_e^b}{1-x_e^b} N_w^s\right) + N_w^s} \quad (1)$$

The above equation links the surface concentration to the Gibbs excess, $\Gamma_e^{(w)}$, at any given x_e^b and δ. The thickness, δ, cannot be determined experimentally. As mentioned above, the assumption of constant thickness is no longer valid. In this study, x_e^s is determined via simulation as a function of x_e^b. The surface adsorption, $\Gamma_e^{(w)}$, is determined experimentally from neutron reflectometry. The combined NR and simulation results, x_e^s and $\Gamma_e^{(w)}$, are then applied to Eq.(1) to determine δ via numerical iterations. The results are used to verify, or otherwise, the proposed relationship between the interfacial thickness and bulk concentration.

The experimental work was carried out at BL16 in the MLF facility (Fig. 1). The mixture of H_2O, D_2O and deuterated ethanol C_2D_6O were used to get the scattering and serves as input for calculation. The NR data was analysed using the software *MOTOFIT*.

Figure 1. Neutron reflectometer SOFIA at BL16 in J-PARC MLF.

3. Results and Interpretation

The vacuum/solution (d-ethanol and water) interface was simulated. From the density profiles, the bulk and interfacial composition were calculated (Fig. 2).

The simulation and NR data were combined to calculate the surface composition (Fig. 3). Reconciliation between neutron reflectometry data and simulated x_e^s for each solution indicated a decreasing trend of δ as the solution concentration increased. The following equation relating the interfacial thickness to the bulk concentration is proposed:

$$\delta = \delta_0 \exp(\lambda\, x_e^b) + \delta_{inf} \quad (2)$$

where δ_0 and δ_{inf} are the theoretical limits at $x_e^b = 0$ and $x_e^b = 1$, respectively, and λ is the rate of decay.

The consistent results show (Fig. 4) that the thickness decays and reach a plateau around 8 Å.

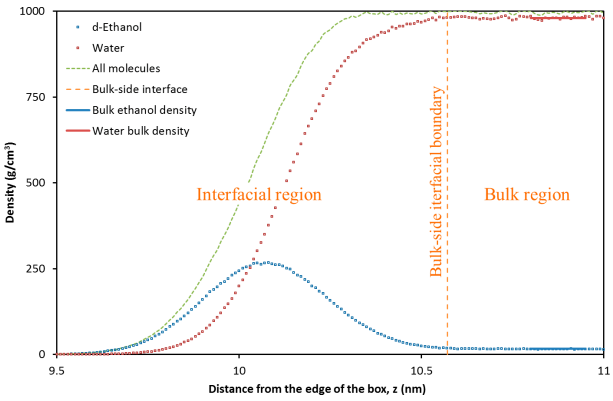

Figure 2. Density of d-ethanol within air/water interfacial layer.

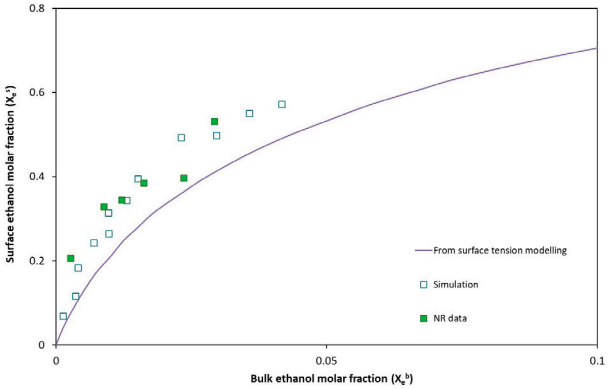

Figure 3. Ethanol surface composition surface tension, molecular simulation and NR experiments (this study).

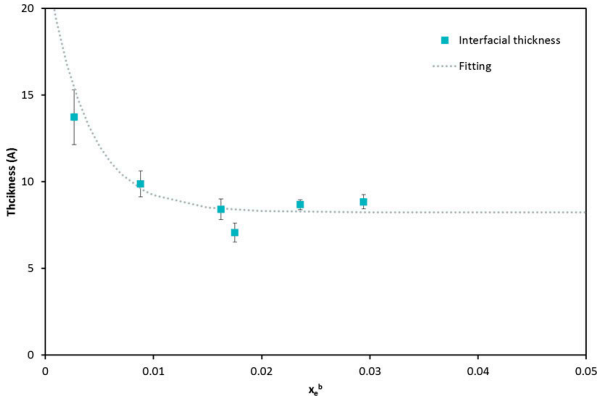

Figure 4. Surface thickness as a function of ethanol composition.

4. Implication and Future Plans

The combination of NR, molecular dynamics and theoretical analysis provides an objective determination of the interfacial thickness. The decreasing behaviour was reported for the first time.

The findings confirm that the interfacial thickness is not constant and instead decreases with increasing ethanol concentration. The result is consistent with a recent thermodynamic analysis and demonstrated the limitation of the conventional theory, which oversimplified the interfacial layer. The new insights provide a theoretical framework to describe the interfacial layer of water/alcohol mixtures. Our next step is to cooperate the results with thermodynamic analysis to correctly calculate the surface activities and related parameters from the molecular structure of alcohols.

References

[1] Li, Z.X., et al., Mol. Phys., **80** 925 (1993).
[2] A. Bagheri, M. Fazli, M. Bakhshaei, J. Mol. Liq., **224** 442 (2016).
[3] M.S.C.S. Santos, J.C.R. Reis, J. Mol. Liq., **255** 419 (2018).
[4] A.E. Hyde, M. Ohshio, C.V. Nguyen, S. Yusa, N.L. Yamada, C.M. Phan, J. Mol. Liq., **290** 111005 (2019).

C. Phan[1] and N. Yamada[2]
[1]*Chemical Engineering, Curtin University, Australia;* [2]*Neutron Science Section, Materials and Life Science Division, J-PARC Center, Institute of Materials Structure Science, KEK*

Development of Spin-Contrast-Variation Neutron Reflectometry

1. Introduction

Neutron reflectivity (NR) is used to determine the nanostructure of surfaces and interfaces of thin film samples. Because of the relatively high transmittance of neutron beams, NR has an advantage over X-ray reflectivity for measuring deeply-buried interface of materials. However, it is difficult to determine the structure of complex multiple surface and interfaces of the thin film from a single reflectivity curve.

To overcome this problem, we developed a new technique called "spin-contrast-variation neutron reflectometry (SCV-NR)", which utilizes the property that coherent polarized-neutron scattering length of a proton remarkably varies as a function of the proton polarization, P_H, against the neutron polarization direction. As P_H increases, the scattering length density (SLD) of each layer proportionally increases with the number density of protons, resulting in the variation of NR curves. The structure of multiple surface and interfaces of a thin film specimen can be determined from the P_H-dependent multiple NR curves. Here, we report the results of a polystyrene (PS) monolayer film to demonstrate the ability and reliability of the SCV-NR technique [1].

Figure 1. DNP apparatus for SCV-NR measurements using the cryogen-free transverse magnetic field magnet of BL15 [2, 3].

2. Experiment

The PS thin film was prepared by spin-coating toluene solution containing 2 wt.% of PS and 0.016 wt.% of 4-methacryloyloxy-2,2,6,6-tetramethylpiperidine 1-oxyl free radical (TEMPO methacrylate) at 5000 rpm on a 20 mm × 20 mm × 0.5 mm single-crystalline Si substrate, and then annealed in a vacuum at 85°C for 4 days.

Protons in the PS thin film were polarized using a dynamic nuclear polarization (DNP) apparatus, which was built by setting a microwave device, a NMR circuit, and an insert to the cryogen-free split-pair transverse magnetic field magnet used as a sample environment equipment at BL15 (Fig. 1) [2, 3]. The protons in the thin film samples were dynamically polarized by irradiating 94 GHz and 600 mW microwaves from the Gunn oscillator (VCSS, GDO-10-9417F) and the amplifier (Keycom, MPA95GHz-01) at 3.36 T and 2.4 ± 0.1 K. Whereas the DNP condition was tuned by monitoring an enhancement of a NMR signal of a bulk reference sample near the thin film sample, the thin film sample is too thin to measure its NMR signal. Instead, P_H was determined from the analysis of the SCV-NR curves (see below).

The PS thin film in the DNP apparatus was set into BL17 (SHARAKU) to perform the SCV-NR measurement using pulsed neutrons with wavelength from 0.24 to 0.88 nm and polarization of 98.5%. The positive and negative polarization was switched by inverting the polarization of the incident neutrons every 30 s while maintaining the proton polarization of the samples.

3. Results and analysis

Figure 2 compares the NR curves of the positively-polarized (POS), unpolarized (UNP), and negatively-polarized (NEG) PS thin film. The following P_H-dependent behaviors were observed. First, the reflectivity of NEG is higher than that of UNP, but the reflectivity of POS is even higher than that of NEG in the whole Q range. Second, the oscillation amplitude of NEG is much smaller than that of the others, and the oscillation of POS is almost inverted as compared with those of the others. Third, the oscillation period of POS is slightly shorter than those of the others. Forth, the critical Q-value Q_c of the total reflection of POS is higher than those of the others.

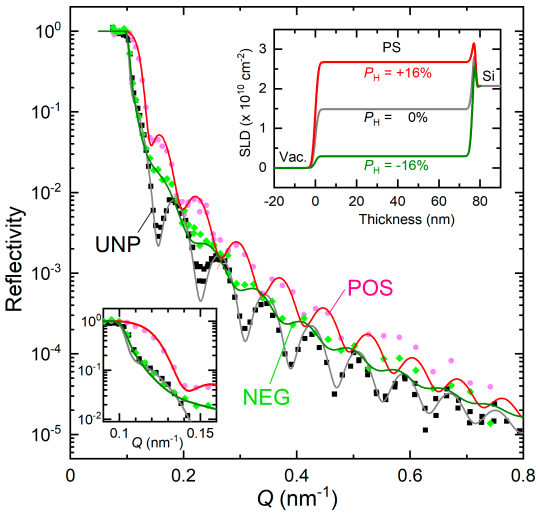

Figure 2. SCV-NR curves of the PS thin film. Solid lines depict the simulation curves using the SLD profiles in the right inset. The left inset shows the enlarged curves near Q_c [1].

The P_H-dependent NR curves, POS, UNP, and NEG, are reproduced by the simulation using a common set of structural parameters and SLD of PS at $P_H = +16$, 0, and −16% in the right inset, respectively. The variation of SLD across the free surface facing to vacuum at $P_H = +16\%$ is larger than any other variation across the surface and interface at $P_H = 0$ and −16%, which results in the largest reflectivity at $P_H = +16\%$. In contrast, the variation across the free surface at $P_H = -16\%$ is so small that the oscillation due to the interference between reflected neutrons from the free surface and the interface damps remarkably. The SLD of PS, ρ_{PS}, is higher than that of Si, ρ_{Si}, at $P_H = -16$ and 0% but smaller at +16%, which results in the inversion of the oscillation, i.e., the open reflection point at the interface becomes a fixed one. According to Snell's law, the angle of refracted neutrons inside the film decreases with increasing ρ_{PS}, resulting in shorter oscillation period at higher P_H. The total reflection occurs on the PS-Si interface at $P_H = -16$ and 0%, but on the free surface at +16%, because ρ_{PS} exceeds ρ_{Si}. In this case, ρ_{PS} is obtained from Q_c using the equation,

$$Q_c = 4\sqrt{\pi\rho_{PS}}. \quad (1)$$

P_H, which is a simple function of ρ_{PS}, is most reliably determined from the Q_c. As opposed to Q_c, the other P_H-dependent parameters, such as oscillation period and amplitude, are not always suited to determine P_H, because they are not a simple function of P_H, especially when reflection from many surfaces and interfaces are interfering.

4. Discussion

DNP is sensitive to many environmental factors, such as concentrations of the doped free radicals and O_2 impurity, which acts as a depolarizer. Thus, P_H could be considered inhomogeneous in the depth direction of the thin film sample due to localization of the TEMPO methacrylate and/or O_2 near the surface or interface. However, such a possibility can be ruled out due to the fact that all of the SCV-NR curves are reproduced by the simulation using homogeneous distribution of P_H in depth direction. It is well known that samples are homogeneously polarized at least in submicron length-scale due to the spin diffusion mechanism, in which the neighboring spins continually exchange through the energy conserving flip-flop transitions of the dipolar Hamiltonian [4, 5]. We demonstrated that poly (styrene-*b*-isoprene) (PSPI) samples were polarized almost homogeneously even when TEMPO radicals were selectively doped in the microphase-separated polystyrene or polyisoprene domains [6]. In this manner, the homogeneity of polarization in a submicron length scale is guaranteed by spin diffusion even if free radicals are more or less localized at a specific surface, interface, or layer. We can safely assume homogeneous polarization on analyses of SCV-NR curves of submicron-thick samples.

SCV-NR determines the structure of multiple surfaces and interfaces through the global fit of the P_H-dependent multiple curves, whereas multiple structural parameters have to be determined from a single curve in conventional NR. Thus, SCV-NR can exclude incorrect sets of structural parameters that accidentally reproduce a single curve of an unpolarized sample [1]. In particular, the SCV-NR curve can selectively pick up structural information of a specific surface or interface by matching out the SLDs of other surfaces and interfaces.

5. Future plans

Taking advantage of SCV-NR, we recently measured the structure of silica coating for plastic dishes. We will pick up the structural information of the silica–polymer interface, which is related to the peeling property of the coat. Very recently, $P_H \approx 40\%$ was achieved in the silica-polymer multilayer film using a cryogen-filled DNP system at 3.36 T and 1.2 K. Simultaneously, we are developing a 6.7 T higher-field DNP system to increase P_H further. We expect that the structural parameters of multilayer films will be determined more accurately and precisely by increasing P_H.

References

[1] T. Kumada et al., J. Appl. Cryst., **52**, 1054 (2019).
[2] T. Kumada et al., JPS Conf. Proc., **22**, 011015 (2018).
[3] T. Kumada et al., PoS, Proc. Sci. 324, 009 (2018).
[4] B. van den Brandt et al., Eur. Phys. J. B, **49**, 157 (2006).
[5] T. Kumada et al., J. Chem. Phys., **133**, 54504 (2010).
[6] Y. Noda et al., J. Appl. Cryst., **44**, 503 (2011).

T. Kumada[1], K. Akutsu[2], K. Ohishi[2], T. Morikawa[2], Y. Kawamura[2], M. Sahara[2], J. Suzuki[2], D. Miura[1,3], and N. Torikai[4]
[1]Materials Sciences Research Center, JAEA; [2]Neutron Science and Technology Center, CROSS; [3]Department of Physics, Yamagata University; [4]Graduate School of Engineering, Mie University

Magnetic Multilayer with Quasi Antiferromagnetic Layer Studied by Polarized Neutron Reflectometry

1. Introduction

Recently, antiferromagnetic (AFM) spintronics had attracted high attention because it has an advantage over ferromagnetic (FM) spintronics, *e. g.* high frequencies in spin torque oscillation (STO) and a zero-stray field [1, 2]. However, it is difficult to obtain the practical and obvious STO because of the strong exchange coupling between adjacent atoms. To realize STO without a stray field, we successfully created a new type of magnetic material, named quasi-AFM layer, whose magnetic domains are alternating antiparallel [3]. In simulation, STO was observed in the quasi-AFM layer because it exhibits FM coupling within one domain and each magnetic moment can oscillate simultaneously [4]. At the same time, a zero-stray field is expected owing to the alternating antiparallel magnetization in the next magnetic domains. Strictly speaking, however, even the native antiferromagnetic materials have a Néel vector made by deviation from perfect antiparallel magnetic moments, which interacts with the external input, e.g. magnetic fields, electric currents, and spin torques. In order to investigate the Néel vector of the quasi-AFM layer, we carried out fine magnetic structure analyses for the quasi-AFM layer by means of Polarized Neutron Reflectivity (PNR) measurements.

2. Experimental

The quasi-AFM layer is realized by 90° magnetic coupling, which is an interlayer exchange interaction between two FM layers separated by a thin layer. The 90° coupling becomes obvious under compensation of FM and AFM coupling between two FM layers. Figure 1(a) shows a schematic film structure. When the magnetization of the CoFe (A) layer is pinned by exchange bias from IrMn, the CoFe (B) layer has the +/−90° magnetization to the exchange bias and that is the quasi-AFM layer. Here, we prepared two kinds of samples with different buffer layers, Ru and $NiFeCr_{40}$/CoFe. Since the Ta/$NiFeCr_{40}$ buffer makes the layers flat, there was difference in the roughness. The smaller roughness generally provides the stronger 90° coupling. We compared the roughness effect on the Néel component of quasi-AFM quantitively.

We measured PNR using a neutron wavelength of 0.24–0.88 nm at SHARAKU (BL17) in the Materials and Life Science Experimental Facility (MLF), Japan Proton Accelerator Research Complex (J-PARC) [5]. Both the crystal and the magnetic structures were analyzed by X-ray Reflectometry (XRR) and PNR simultaneously. The reflectivities were measured as a function of the wave-vector transfer in applied magnetic fields along the x-axis and we found their values to be +1000 Oe, +29 Oe,

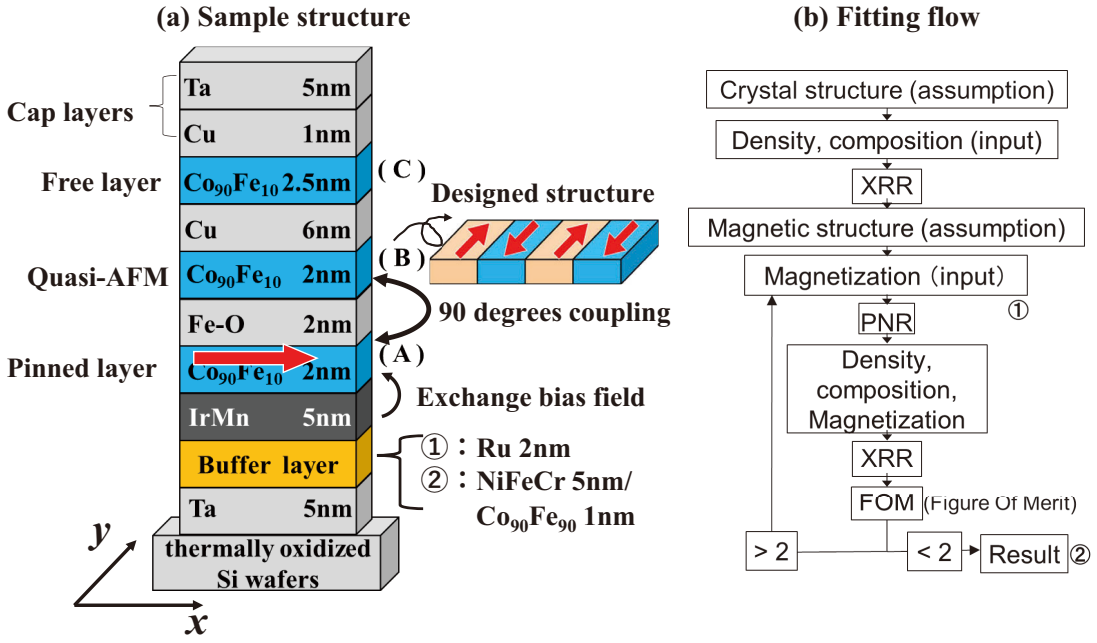

Figure 1. (a) Schematic image of the sputtered multilayer with the quasi-AFM layer made by 90° magnetic coupling. (b) Fitting flow of PNR and XRR profiles by using GenX.

and −28 Oe for the Ru buffer sample, and +1000 Oe, +32 Oe, and −45 Oe for the NiFeCr buffer sample at room temperature. The data reduction software Utsusemi [6] in BL17 was applied and GenX [7] was used for the PNR analysis. By repeating the XRR and PNR fitting as shown in Fig. 1 (b), we obtained sufficiently good agreement between the experimental data and the calculated data with the figure of merit less than $2e^{-1}$.

3. Results and discussion

Figers. 2(a) and (b) show the PNR profiles for the Ru and NiFeCr buffer samples, respectively, where the dots indicate the experimental data and the lines show the calculated results of fitting. By using the obtained magnetic parameters, *i. e.* the magnitude and direction of magnetization in quasi-AFM, the magnetization orientation can be described and compared with the magnetization curves in Fig. 3. Here, the focus is on the magnetization of the quasi-AFM layer though the magnetizations of the other layers were also obtained. As a result, it became clear that the Néel vector was 1.35 μ_B and 1.00 μ_B for the Ru and NiFeCr buffer samples, respectively, when the tilted angle was 1° in low applied fields, such as several tens Oe. It was noted that, according to the magnetization curves, the magnetization configuration in the applied field of several tens Oe was close to that in a nonmagnetic field.

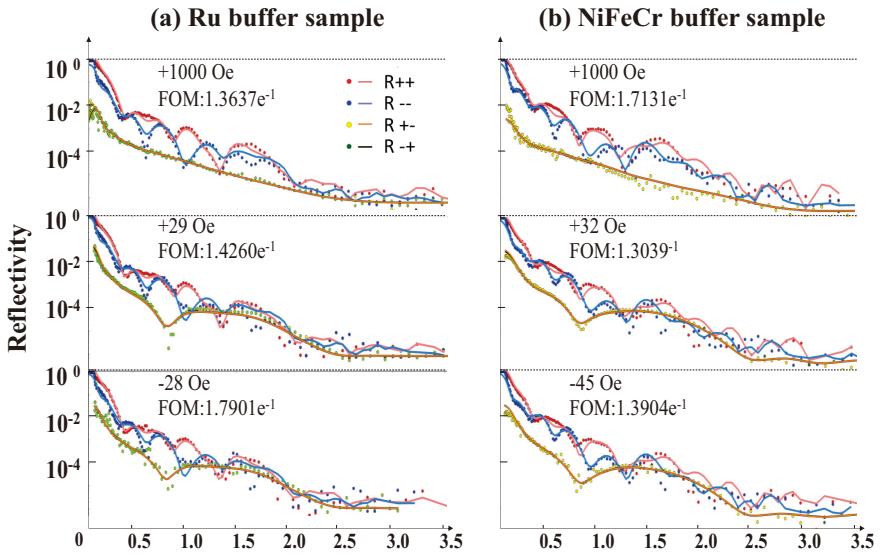

Figure 2. PNR profiles and fitting curves; (a) Ru buffer sample in +1000 Oe, +29 Oe, −28 Oe and, (b) NiFeCr buffer sample in +1000 Oe, +32 Oe, −45 Oe.

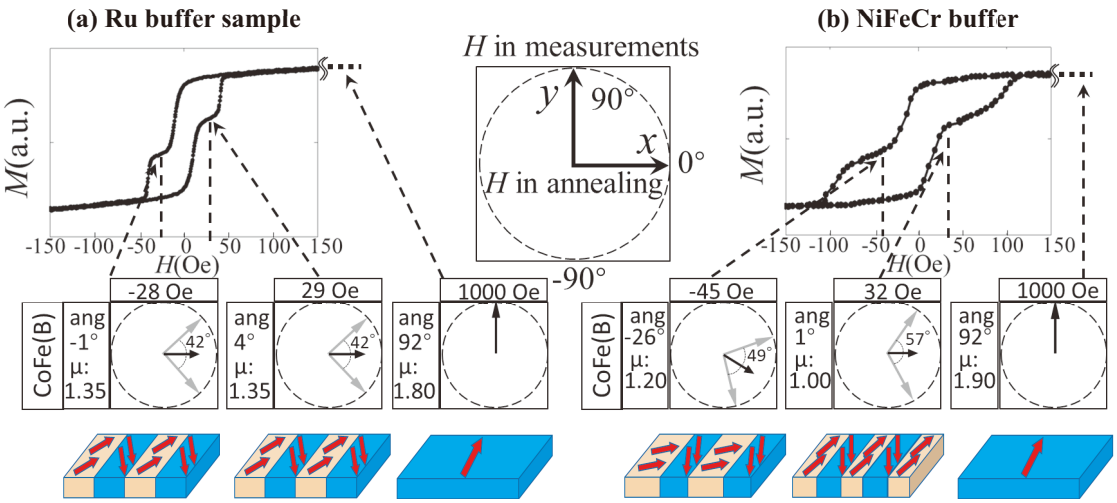

Figure 3. Comparison between magnetization curves and schematic images of the magnetization for $Co_{90}Fe_{10}$ (B) estimated from PNR analysis for (a) Ru and (b) NiFeCr buffer samples.

4. Future plans

The quantitative Néel vector, which we obtained successfully in the quasi-AFM layer, can be controlled by the buffer layer selection. The value of the Néel vector is useful to calculate the magnetization dynamics by micromagnetic simulation. From now on, the suitable magnetic structure will be estimated by simulation, and the spin torque of the quasi-AFM layer will be realized by direct electric current flows through the fine elements.

References

[1] A. H. MacDonald and M. Tsoi, Phil. Trans., R. Soc. A **369** 3098 (2011).
[2] R. Khymyn et al., Sci. Rep. **7** 43705 (2017).
[3] G. Nagashima et al., J. Appl. Phys. **126** 093901 (2019).
[4] S. Horiike et al., Jpn. J. Appl. Phys. **59** SGGI02-1~6 (2020).
[5] M. Takeda et al., Chin. J. Phys. **50** 161 (2012).
[6] Y. Inamura et al., J. Phys. Soc. Jpn. **82** SA031 (2013).
[7] M. Björck and G. Andersson, J. Appl. Cryst. **40** 1174 (2007).

H. Yuasa[1], Y. Zhong[1], Y. Kurokawa[1], and T. Hanashima[2]
[1]*Faculty of Information Science and Electrical Engineering, Kyushu University;* [2]*Neutron Science and Technology Center, CROSS*

Nonlinear Piezomagnetoelectric Effect in $CuFeO_2$

1. Introduction

Cross-correlated phenomena in solids are not only useful for electronic device applications, but also have promoted fundamental studies in condensed matter physics to understand a coupling mechanism between several degrees of freedom. In particular, recent progress in research on spin-driven ferroelectricity or magnetoelectric effects has revealed a nonlinear cross correlation between ferroic order parameters and nonconjugated external fields, i.e., a ferroelectric polarization (a spontaneous magnetization) can be controlled by a magnetic field (an electric field) [1]. One of the key factors governing the emergence of the spin-driven ferroelectricity is the complex spin texture breaking inversion symmetry in the systems. Owing to a tendency to exhibit such a magnetic structure, geometrically frustrated magnets have been recognized as one of the candidates for spin-driven ferroelectric materials. Following this strategy, many spin-driven ferroelectric materials have been found during the past two decades. On the other hand, several frustrated magnets are often spin-lattice coupled systems, in which a magnetic phase transition is accompanied by a lattice distortion to partially relieve the frustration between spins. Therefore, several degrees of freedom in the geometrically frustrated magnets, such as charge, spin, orbital, and lattice are potentially related to each other, and novel phenomena correlated with multiple degrees of freedom are expected beyond 'cross' correlation.

Recently, we discovered phenomena correlated with multiple degrees of freedom in a geometrically frustrated magnet, $CuFeO_2$, by applying uniaxial pressure p and magnetic field H [2]. As shown in Fig. 1(b), a ferroelectric polarization P is induced, only when both p and H are simultaneously applied in a specific sinusoidally amplitude-modulated magnetic structure phase (we refer to this phase as the PD phase, see Fig. 1(a)). Significantly, for the case of $H \parallel [110]$ or [1-10] (Fig. 1(c)), P is not observed even under applied p, although the magnetization measurements at ambient pressure showed that the PD magnetic ordering persists up to 20 T, except for the spin canting toward the H direction.

In order to determine whether or not the crystal and/or magnetic structure in the PD phase is changed by the application of p and H, we performed neutron diffraction experiments under applied p and H.

2. Experiments

A single crystal of $CuFeO_2$ synthesized by the floating zone technique, was cut into a rectangular shape with typical dimensions of $1.64 \times 1.37 \times 1.20$ mm^3, in which three axes are along the [110], [1-10], and [001] directions. Uniaxial pressure p was applied along the [1-10] direction, which is the conjugate direction to the spontaneous lattice distortion in $CuFeO_2$. To investigate wide reciprocal space, neutron diffraction experiments under applied p and $H \parallel c$ were performed using a time-of-flight neutron diffractometer SENJU (BL18) installed at MLF, J-PARC.

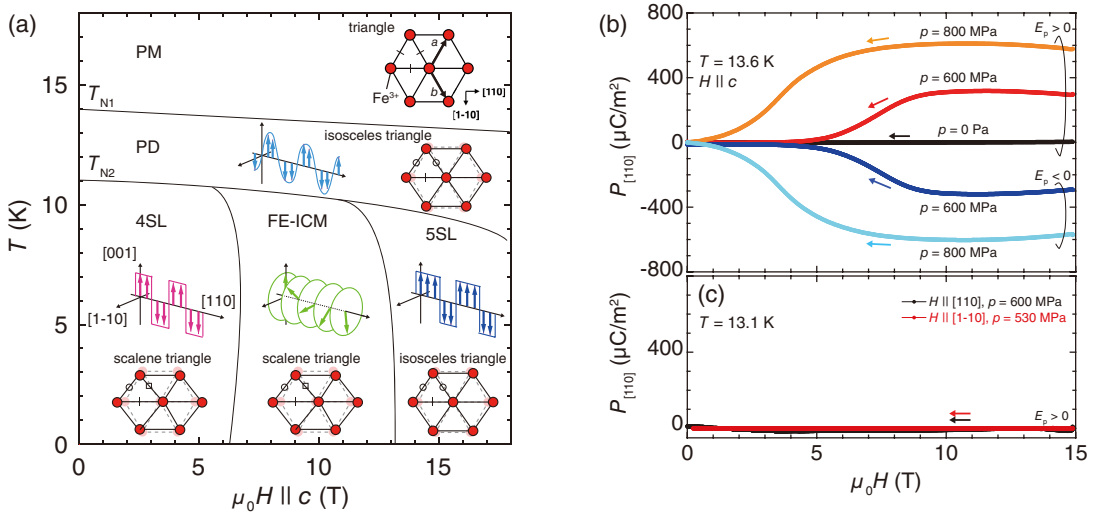

Figure 1. (a) Schematic magnetic phase diagram for $CuFeO_2$ under zero applied pressure. Schematics of magnetic structures and the magnetic Fe^{3+} triangular lattices in each phase are also shown. (b) Magnetic field dependence of P under applied p. H was applied along (a) the c axis, and along (b) the [110] and [1-10] axes. A poling electric field E_p was applied at 15 T before the measurements.

3. Results and discussion

Figure 2 shows *H* dependence of the integrated intensities of both the nuclear and magnetic reflections under *p* of 745 MPa [2]. Because of the complex geometry of experimental components in these measurements, such as a pressure device composed of Al and ZrO_2 pistons and a superconducting magnet, attenuation and absorption of the scattered neutrons could not be corrected for; therefore, the accuracy of the integrated intensities is rather limited in spite of the small error bars. Nevertheless, the integrated intensities of both the nuclear and magnetic reflections exhibit almost no change under applied *H*. This result clearly indicates that the modification of the PD crystal/magnetic structures by application of *p* and *H* is quite small, if it exists.

Taking into account that the PD magnetic structure does not break the inversion symmetry in this system, this result suggests that *P* induced by the application of *p* and *H* is not purely spin driven. Because the *P* certainly has relationship to the sinusoidal magnetic structure, as mentioned above, our result sharply contrasts with the conventional spin-driven ferroelectricity.

Induction of an electric polarization using two external fields, a strain σ and *H*, is known as the piezomagnetoelectric (PME) effect, which is described as $P_i = \pi_{ijkl} H_j \sigma_{kl}$, where π_{ijkl} is the piezomagnetoelectric tensor [3]. However, the phenomenon observed in the present work should not be the PME effect. Indeed, the *H* dependence of the *p*-induced *P* is not linear (a *p* dependence of *P* at a fixed temperature and *H* are also not linear [2]). Moreover, π_{ijkl} must vanish when the magnetic point group contains space inversion or time inversion *1′* [3]. The magnetic point group in the PD phase of $CuFeO_2$ is reported as *2/m1′* [4], which makes π_{ijkl} vanish. Therefore, to classify *P* induced by the combined application of *p* and *H*, we propose that the phenomenon in this work is a nonlinear PME effect. This means that this phenomenon would be explained by an additional coupled term in a free energy in this system, not higher order terms of $\pi_{ijkl} H_j \sigma_{kl}$, by analogy with spin-driven ferroelectricity as a nonlinear ME effect.

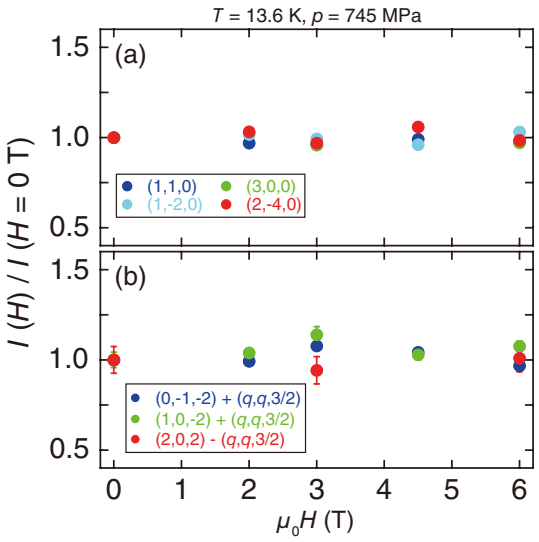

Figure 2. Relative integrated intensities $I(H)/I(H = 0\ \mathrm{T})$ of neutron diffraction from (a) nuclear reflections and (b) magnetic reflections as a function of $H \parallel c$. Measurements were performed at 13.6 K under an applied *p* of 745 MPa.

4. Conclusion

We have searched for phenomena correlated with multiple degrees of freedom in the geometrically frustrated magnet $CuFeO_2$, by applying p and H. Ferroelectric polarization is induced in the original PD phase by the application of *p* together with *H*. The crystal and magnetic structures seem to be unchanged by the application of *p* and *H*, which suggests that this phenomenon differs from conventional spin-driven ferroelectricy. We propose that the induction of ferroelectric polarization in $CuFeO_2$ by the combined application of *p* and *H* can be regarded as a nonlinear PME effect.

References

[1] Y. Tokura et al., Rep. Prog. Phys., **77**, 076501 (2014).
[2] H. Tamatsukuri, et al., Phys. Rev. B, **100** 201105(R) (2019).
[3] J. P. Rivera, et al., Ferroelectrics, **161** 91 (1994).
[4] N. Terada, et al., Nat. Commun., **9** 4368 (2018).

H. Tamatsukuri[1], S. Mitsuda[1], T. Shimizu[1], M. Fujihala[1], H. Yokota[1], K. Takehana[2], Y. Imanaka[2], A. Nakao[3], and K. Munakata[3]
[1]Faculty of Science, Tokyo University of Science; [2]Nano Physics Group, NIMS; [3]Neutron Science and Technology Center, CROSS

In-situ Neutron Diffraction Analysis on Dynamic Ferrite Transformation in Steels

1. Introduction

Over the last fifty years, thermomechanical processing, which involves deformation and heat treatment, has been practically used to manufacture commercial large steel products. Recently, several researchers have found that grain size of ferrite (BCC phase in steel) decreases down to approximately 1 μm through thermomechanical processing at a relatively low temperature [1-3]. In this process, phase transformation might occur during the deformation of the parent austenite (FCC phase in steel), because transformation kinetics is greatly accelerated by a large amount of lattice defects introduced into austenite. To distinguish it from the normal ferrite transformation, i.e., static ferrite transformation, which occurs during cooling or static holding, the ferrite transformation occurring during deformation of austenite has been termed as "dynamic ferrite transformation".

In order to study deformation and phase transformation behaviors at elevated temperature, we have recently developed a novel thermomechanical processing simulator for *in-situ* neutron diffraction analysis (Fig. 1), which is applicable to the BL19 "TAKUMI" in the MLF at J-PARC. The incident direction of a pulsed neutron beam is perpendicular to the compression axis, and two neutron detectors (time-of-flight detectors) are located at the positions perpendicular to the incident neutron beam. As a result, the lattice planes that contribute to the diffraction intensity in these detectors are parallel to the compression axis. We reported recently on the nature of dynamic ferrite transformation revealed by *in-situ* neutron diffraction using the newly developed thermomechanical processing simulator [4], and this report is based on our previous paper.

2. Experimental procedure

An Fe-2Mn-0.1C, an Fe-3Mn-2Si-0.1C, and an Fe-10Ni-0.1C alloys were used in the present study. Cylindrical specimens 11 mm in height and 6.6 mm in diameter were prepared and subjected to *in-situ* neutron diffraction experiment at BL19. Each specimen was firstly austenitized at 1000°C for 300 s, then cooled by N_2 gas at a cooling rate of 30°C s^{-1} to the deformation temperatures ranging from 480°C to 700°C. After holding for 10 s at the deformation temperature, a uniaxial compressive deformation of at most 60% reduction in height was applied at strain rates of 10^{-2} s^{-1}, 10^{-3} s^{-1}, and 5×10^{-4} s^{-1}. The compressed specimen was subsequently held at the same temperature for 600 s without loading. The neutron diffraction data were obtained during the whole thermomechanical processing. To evaluate the phase fraction and the lattice parameter, the neutron diffraction profile was analyzed by Rietveld method using Z-Rietveld software. The dislocation density was estimated by convolutional multiple whole profile fitting (CMWP) method [5, 6].

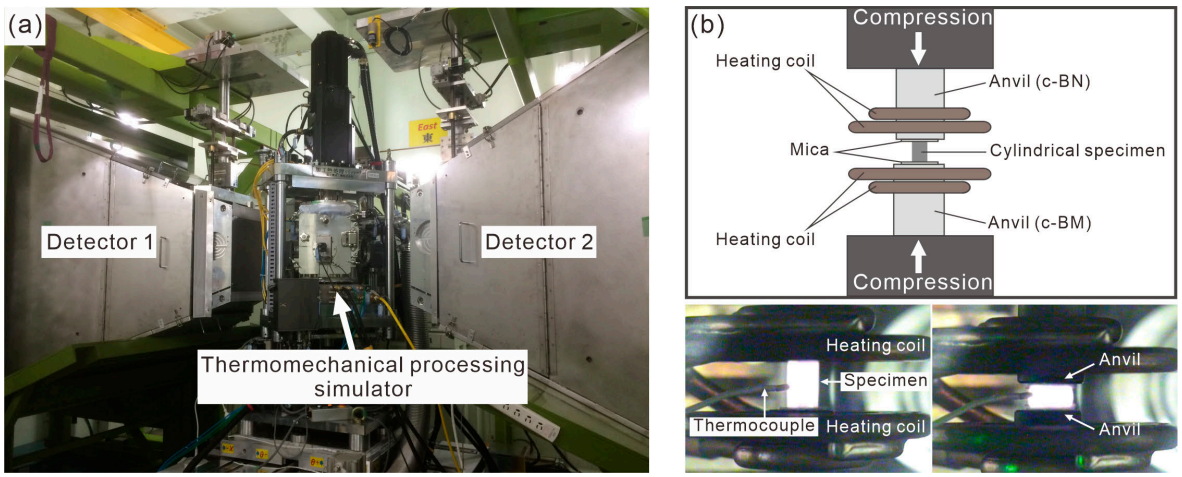

Figure 1. (a) The thermomechanical processing simulator installed at the BL 19 "TAKUMI" in the MLF at J-PARC, (b) schematic illustration and snap shots during the compression experiment of the testing part of the simulator. Adapted from Ref. [4]. Reproduced with permission from Elsevier.

3. Results and discussion

Figure 2(a) shows a plane-view neutron diffraction profile (enlarged region around the peaks of {011}α and {111}γ) during the thermomechanical processing (Fe-2Mn-0.1C, deformation temperature: 700°C, strain rate: 10^{-2} s^{-1}). We found that the ferrite peak started to appear during compression, indicating that the dynamic ferrite transformation definitely occurred during the compression, not after it. Changes in the volume fraction of ferrite with different strain rates are shown in Fig. 2(b) (Fe-3Mn-2Si-0.1C, deformation temperature: 675°C). It is clear that the kinetics of dynamic ferrite transformation was much faster than that of static ferrite transformation. When comparing the volume fraction of ferrite at the later transformation stage, the ferrite fraction increased with decreasing the strain rate. This suggests that the period when stress was applied affected the kinetics of the dynamic ferrite transformation.

Changes in the lattice constants of ferrite during the thermomechanical processing are shown in Fig. 3 (Fe-2Mn-0.1C, strain rate: 10^{-2} s^{-1}). We found that the lattice constant of dynamically transformed ferrite increased and then decreased significantly. During the static holding after the compression, the lattice constant kept almost the same value. The changes in the lattice constants of ferrite confirmed in Fig. 3 could be attributed to the fact that the partitioning behavior changed from para- to ortho-equilibrium during dynamic ferrite transformation.

By utilizing the CMWP method [5, 6], we analyzed dislocation density of the parent austenite phase during thermomechanical processing (Fe-10Ni-0.1C, strain rate: 10^{-3} s^{-1}), as shown in Fig. 4. In the present alloy system, austenite usually transforms to martensite during quenching so that it is nearly impossible to measure dislocation density of the parent austenite phase. On the contrary, the *in-situ* neutron diffraction technique can directly measure the change in dislocation density of the parent austenite phase during thermomechanical processing. We also confirmed that dynamic ferrite transformation occurred by deformation at 520°C and 480°C, but almost never at 560°C. For the compression at 560°C, the dislocation density of austenite increased

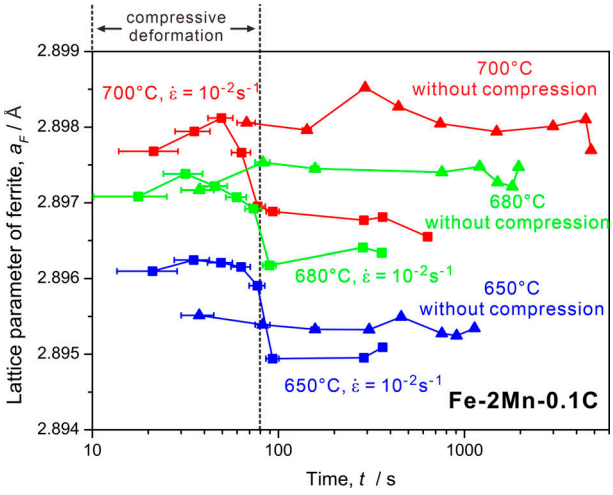

Figure 3. Change in lattice constants of ferrite during the thermomechanical processing (Fe-2Mn-0.1C, strain rate: 10^{-2} s^{-1}). Adapted from Ref. [4]. Reproduced with permission from Elsevier.

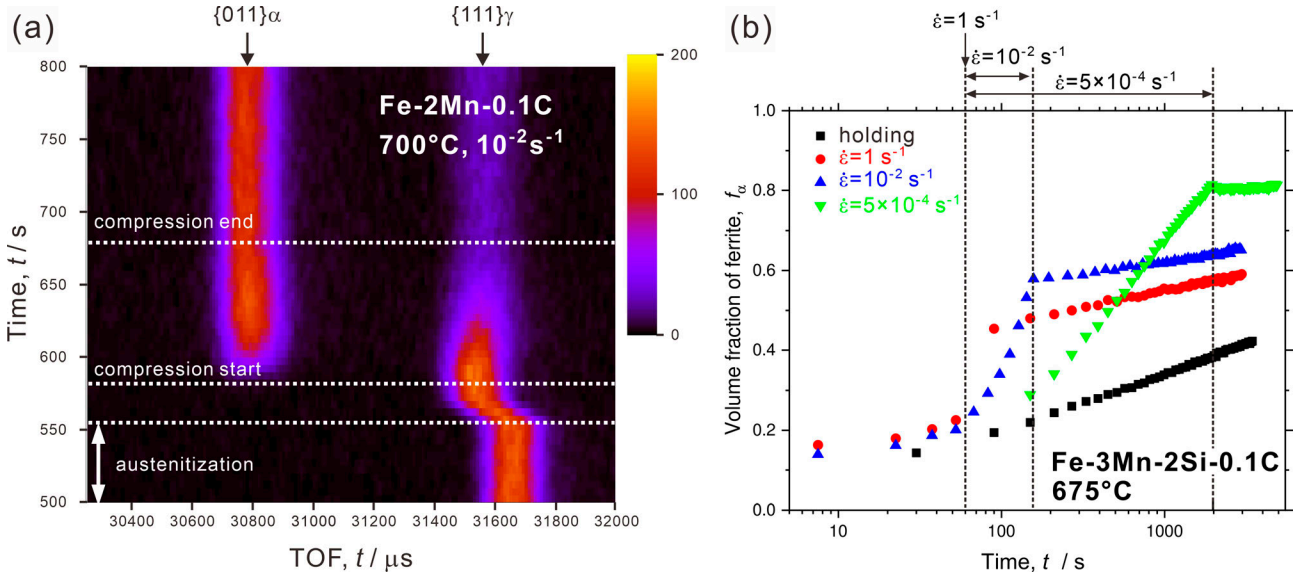

Figure 2. (a) Neutron diffraction profile (enlarged region around {011}α and {111}γ) during the thermomechanical processing (Fe-2Mn-0.1C, deformation temperature: 700°C, strain rate: 10^{-2} s^{-1}), (b) changes in volume fraction of ferrite with different strain rates during the thermomechanical processing (Fe-3Mn-2Si-0.1C, deformation temperature: 675°C).

gradually with increasing the strain, indicating that dynamic recrystallization (DRX) of austenite did not occur. At 520°C and 480°C, on the other hand, the dislocation density increased initially and then decreased with the strain increase. The decreases of the dislocation density observed at 520°C and 480°C were not due to DRX of austenite, because DRX of austenite did not occur even at 560°C (higher than 520°C and 480°C). The results suggest that significant strain concentration occurred in the dynamically transformed ferrite. Usually, the necessary amount of strain for the occurrence of DRX in ferrite is very large [3]. However, the accumulation of strain in the dynamically transformed ferrite could induce DRX even when the nominal applied strain was relatively small. Consequently, we propose that DRX of dynamically transformed ferrite led to the formation of ultrafine-grained structure.

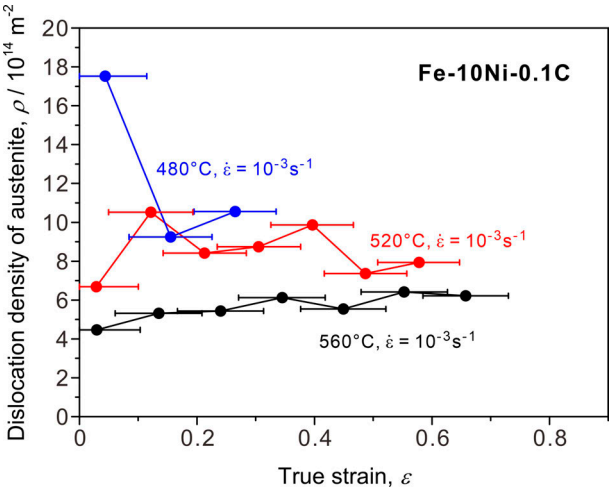

Figure 4. Change in dislocation density of the parent austenite phase during the thermomechanical processing (Fe-10Ni-0.1C, strain rate: 10^{-3} s^{-1}). Adapted from Ref. [4]. Reproduced with permission from Elsevier.

Acknowledgement

This study was financially supported by JSPS KAKEHI Grant Number JP15H05767 and JP15K14163, and the Elements Strategy Initiative for Structural Materials (ESISM). The *in-situ* neutron diffraction experiments were performed through proposals no. 2014E0003, 2014B0280, 2015A0069, 2015E0001, 2016E0003 and 2018L0401 at MLF at J-PARC. The authors sincerely thank the members of Tsuji-lab in Kyoto University for helping with the experiments.

References

[1] Y. Matsuyama et al., ISIJ Int., **27** 492 (1987).
[2] P.D. Hodgson et al., Scripta Mater., **40** 1179 (1999).
[3] H. Beladi et al., Int. Mater. Rev., **52** 14 (2007).
[4] A. Shibata et al., Scripta Mater., **165** 44 (2019).
[5] T. Ungár et al., Metall. Mater. Trans. A, **41A** 1202 (2010).
[6] T. Ungár et al., Acta Mater., **66** 251 (2014).

A. Shibata[1–3], Y. Takeda[2], N. Park[2,4], L. Zhao[2,5], S. Harjo[6], T. Kawasaki[6], W. Gong[3,6], and N. Tsuji[2,3]

[1]*Research Center for Structural Materials, National Institute for Materials Science;* [2]*Department of Materials Science and Engineering, Kyoto University;* [3]*Elements Strategy for Structural Materials (ESISM), Kyoto University;* [4]*School of Materials Science and Engineering, Yeungnam University;* [5]*Advanced Steel Processing and Products Research Center, Colorado School of Mines;* [6]*Neutron Science Section, Materials and Life Science Division, J-PARC Center*

Phase Stress Evolution under Cryogenic Tensile Loading

1. Introduction

It is known that deformation-induced martensitic transformation, which is regarded as a displace transformation of a metastable parent phase into deformation-induced martensite, results in a drastic increase in plasticity, the so-called transformation-induced plasticity (TRIP) effect [1]. Also, the formation of martensite plays an important role in the significant increase in strain hardening, and hence, its simultaneously enhanced strength and ductility [2].

Quantitative analyses on the evolutions of phase fractions, phase stresses in a ferrous medium-entropy alloy during deformation at cryogenic temperature, and the contributions of each phase to the flow stress were conducted at BL19 TAKUMI [3].

2. New release

When the microstructure consists of a single-phase crystalline structure and deformation-induced martensitic transformation occurs, it is not possible (in principle) to obtain the material parameter of stress-free reference martensite phase because the martensite is formed from the deformed parent phase. This results in only a qualitative understanding of the role of martensitic transformation in the strain hardening behavior.

For the phase stress calculation, Young's modulus of the parent phase was obtained from the neutron diffraction (ND) analysis, while that of the martensite phase was derived based on the stress equilibrium approach in the unloaded state after plastic deformation. This was done to provide a quantitative interpretation of the role of deformation-induced martensite phase on the strain hardening.

3. Quantitative analysis on phase stress

Here, to derive the phase stress, we obtained the average phase lattice strain of each phase by simply averaging three different (*hkl*) lattice strains and the phase fraction of each phase by using the Z-Rietveld software [4]. During elastic deformation, the parent phase deformed elastically and lattice strain increased linearly with a constant slope until yielding, and the slope was regarded as Young's modulus of the parent phase. Moreover, the deformation-induced martensite phase appeared due to the occurrence of the martensitic transformation after the elasto-plastic transition of the parent phase. Since the martensite phase was formed from a plastically deformed parent phase, it was not possible to obtain Young's modulus of the martensite phase because the initial microstructure was composed of a single phase.

Here, we used the stress equilibrium approach to determine Young's modulus of the martensite phase [5]. In this regard, the sum of residual stresses of each phase must be zero when weighted by their volume fraction in the unloaded state. Figure 1 shows the residual lattice strain of each (hkl) plane and residual phase stress of the parent phase in the unloaded state. Since we have already obtained the phase fraction, stress values of each phase, and lattice strain of the martensite phase, Young's modulus of the martensite phase could be obtained.

Finally, the strain hardening behavior and contributions of each phase during tensile loading can be analyzed by the evolution of each phase, as shown in Fig. 2. After yielding the parent phase, the stress contribution from the parent phase began to decrease. On the other hand, the stress contribution from the martensite

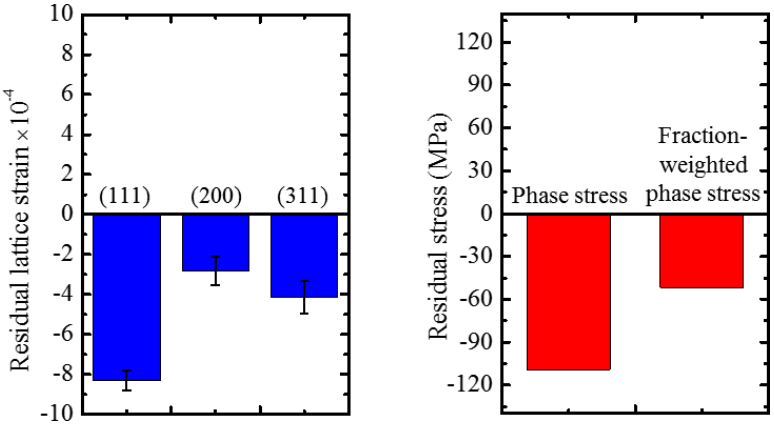

Figure 1. Residual phase lattice strain and stress in the unloaded state.

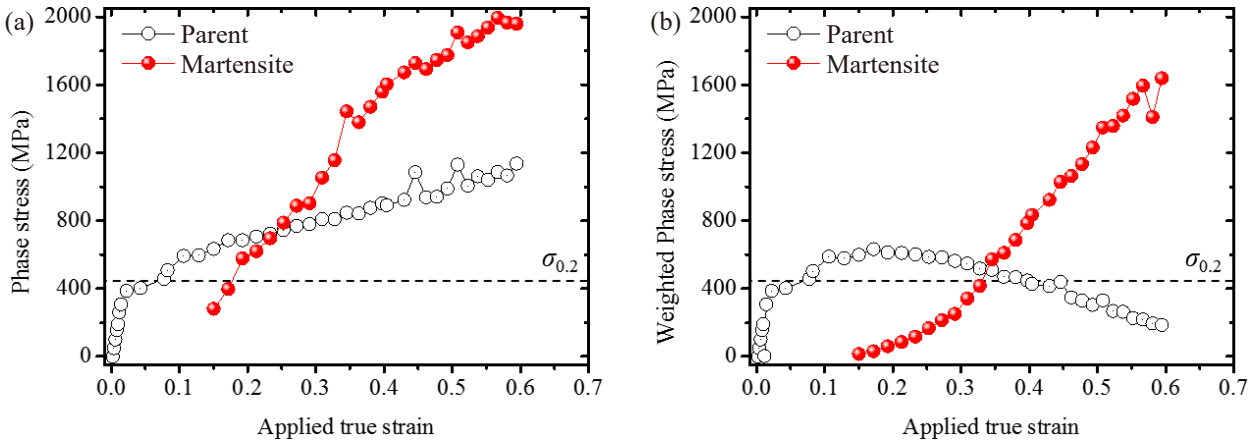

Figure 2. The evolution of phase and fraction-weighted phase stresses with respect to the applied strain, where FCC is parent face-centered cubic phase and BCC is body-centered cubic martensite.

phase continuously increased and became higher than that from the parent phase. The increase in the stress contribution of the martensite phase was attributed to the increase of both the fraction and phase stress. Finally, we obtained a comprehensive understanding of the quantitative contribution of each phase to the strain hardening and flow stress during a low-temperature tensile test.

4. Future plans

The phase stress evolution of the martensite phase measured using the ND analysis may represent the sum of contributions from a series of martensite phases formed at various strain levels. Furthermore, the results provide no direct access to the plastic strain in either of the phases. These issues will be the next focus of our future research to obtain a better understanding of the deformation characteristics in each phase of metastable alloys at low temperatures. In this regard, concurrent analysis of the quantitative estimation of dislocation density, twin probability, etc. using ND analysis and numerical simulations can provide a better understanding of the deformation behavior.

References

[1] F. D. Fischer et al., Int. J. Plast., **723** 16 (2000).
[2] J. W. Bae et al., Acta Mater., **388** 161 (2018).
[3] J. W. Bae et al., Scripta Mater., **165** 60 (2019).
[4] R. Oishi et al., Nucl. Inst. Methods, **94** 600 (2009).
[5] R. A. Winholtz, in: M. T. Hutchings, A. D. Krawitz (Eds.), Measurement of residual and applied stress using neutron diffraction, Kluwer Academic, London 1992, pp. 131–145.

J. W. Bae[1,2], J. G. Kim[3], J. M. Park[2], W. Woo[4], S. Harjo[5], and H. S. Kim[2]
[1]Max-Planck-Institut für Eisenforschung; [2]Department of Materials Science and Engineering, POSTECH; [3]Department of Metallurgical and Materials Engineering, Gyeongsan National University; [4]Korea Atomic Energy Research Institute; [5]Neutron Science Section, Materials and Life Science Division, J-PARC Center

Ferroelectric Polarization in Tetragonal $(Bi_{1/2}K_{1/2})TiO_3$–$(Bi_{1/2}Na_{1/2})TiO_3$ Single Crystals

1. Introduction

In perovskite oxides, a combination of Bi with alkali metals on the A-site enables to accommodate higher-valent cations such as Ti^{4+} on the B site. Bismuth potassium titanate $(Bi_{1/2}K_{1/2})TiO_3$ [BKT] has ferroelectricity in a tetragonal structure (space group *P*4*mm*) at room temperature, which has attracted much attention as a lead-free piezoelectric material. The solid solution with rhombohedral $(Bi_{1/2}Na_{1/2})TiO_3$ [BNT; space group *R*3*c*], i.e., the (1–*x*)BKT–*x*BNT system, displays a morphotropic phase boundary, where the ferroelectric structure changes dramatically and the piezoelectric activity is maximal.

By contrast, few studies on BKT-based single crystals have been performed to date because of the difficulty in growing high-quality samples; the crystals reported suffer from the problems arising from point defects. Owing to a high vapor pressure, Bi is apt to evaporate from the lattice leaving a vacancy of Bi (V_{Bi}'''), which is accompanied by the formation of oxygen vacancy ($V_O^{\bullet\bullet}$) [1–3]. $V_O^{\bullet\bullet}$ tends to accumulate at ferroelastic domain walls, which are strongly pinned and eventually clamped even under high fields [4–6]. For revealing the ferroelectric nature, it is desirable to develop a high-quality single crystal with a low concentration of V_{Bi}''' where external fields can switch spontaneous polarization (P_s).

2. Neutron diffraction analysis

Neutron powder diffraction (NPD) data were collected [8] using iMATERIA (BL20) for (1–*x*)BNT–*x*BKT powders (*x* = 30–35%) prepared by solid-state reaction, and the powders were found to have a tetragonal *P*4*mm* structure. The refined crystal structure with the atomic displacements is illustrated in Fig. 1(a). Figure 1(a) shows the displacements of the constituent atoms along the *c* (polar [001]) axis. The displacement of the A-site atoms $(Bi_{0.50}Na_{0.35}K_{0.15})$ is as large as 0.034 nm, which is about twice that of the B-site atom (Ti). Figure 1(b) depicts the electric dipole moments of the constituent atoms estimated from the off-center displacements and the averaged effective charges obtained by the DFT calculations. The cooperative displacements of the A- and B-site atoms lead to the parallel dipole moments of p_A = 23.0 μC/cm² for the A-site atoms and p_B = 36.1 μC/cm² for the B-site one. This dipole configuration provides a large P_s of 55.8 μC/cm².

3. Polarization of high-quality single crystals

Figure 2 shows the polarization (*P*) properties at 298 K. The crystal (Po_2 = 0.02 MPa) [Fig. 2(a)] exhibits a remanent polarization (P_r) of 32 μC/cm² and a coercive field (E_c) of 23 kV/cm. By contrast, the crystal (Po_2 = 0.9 MPa) [Fig. 2(b)] features a well-saturated loop with a large P_r of 48 μC/cm² and a low E_c of 18 kV/cm (*E* // [111]). The blue line in Fig. 2(b) indicates the *P*-*E* loop along [111] with a P_r of 30 μC/cm². Our measurements along [111] and [001] lead to a P_s of 50–52 μC/cm², which is in good agreement with that (55.8 μC/cm²) determined by the NPD analysis with the DFT calculations.

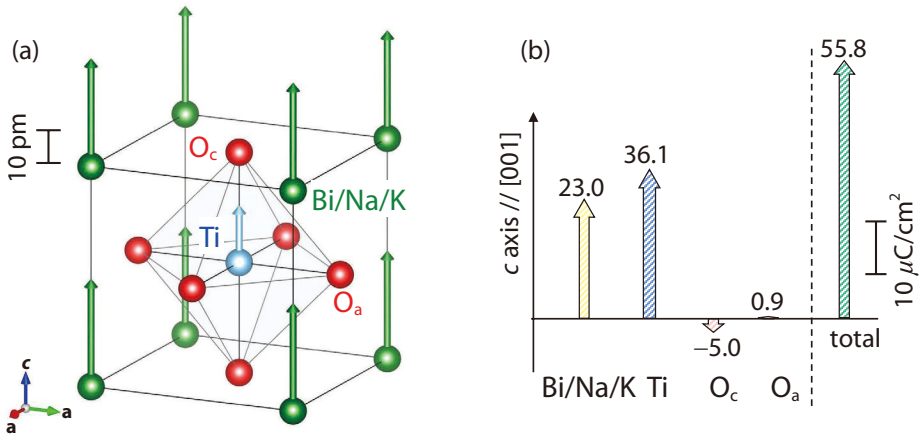

Figure 1. Ferroelectric displacements and polarizations of the refined tetragonal *P*4mm phase of BNT-BKT (*x* = 30%): (a) refined crystal structure with off-center displacements and (b) dipole moments of the constituent atoms along the *c* axis [7].

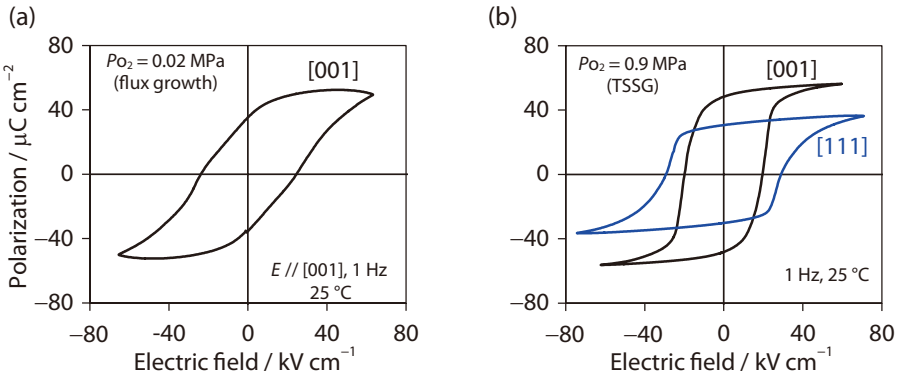

Figure 2. Polarization properties. Polarization-electric-field properties of BNT-BKT (x = 33%) single crystals grown at (a) P_{O_2} = 0.02 MPa and (b) P_{O_2} = 0.9 MPa. The index beside each curve indicates the crystallographic direction of the polarization measurements [7].

4. Origin of ferroelectricity

We investigate the electronic structures at p ~ 13.4 GPa and –2.3 GPa; the high p stabilizes the *R*3*c* structure (Figs. 3a–c) while the low p does the *P*4*mm* phase (Figs. 3d–f). We note that the marked density of states (DOS) of not only Ti-3*d* but also Bi-6*p* appears in the valence band; especially the hybridized states of Bi-6*p* and O-2*p* determine the bottom of the valence band.

At p ~ 13.4 GPa in the BNT cell, the *R*3*c* phase features a dominant contribution of the Bi-6*p* ($p_x + p_y$) derived states around the bottom with a minimum at –5.79 eV in the vicinity of the Γ point (the wavefunction is seen in Fig. 3c), which is lower by ~ 0.1 eV than the *P*4*mm* (not shown). We found that the stabilization of the *R*3*c* phase for BNT stems from the low-lying valence states arising from the Bi-6*p* and O-2*p* hybridization.

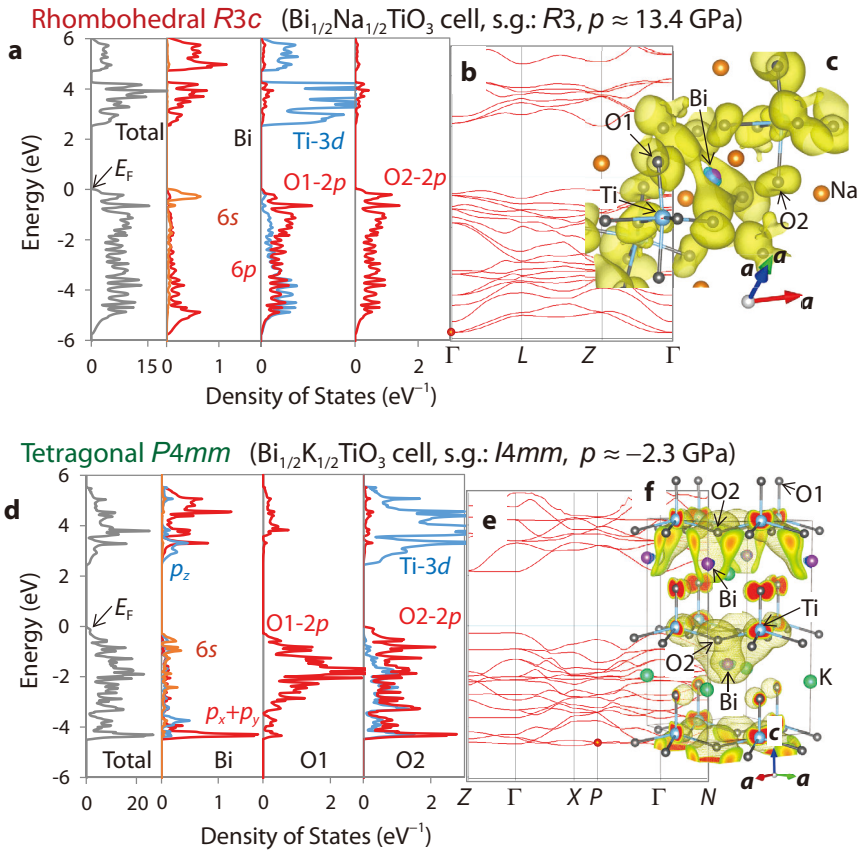

Figure 3. Density of states (DOS) calculations. DFT calculation results of (a–c) the *R*3*c* structure in the BNT cell at p = 13.4 GPa and (d–f) the *P*4*mm* structure in the BKT cell at p = –2.3 GPa; (a,d) partial DOS for Bi, O1 and O2 atom, (b,e) band structures, and (c,f) wave functions at the k points denoted by the dot marks in the band structures [7].

The similar feature is also seen in the BKT cell at $p \sim -2.3$ GPa; the mixed states of Bi-6*p* and O-2*p* dominate the bottom of the valence band. The maximal DOS of Bi-6*p* lies at ~ −4.3 eV for the *P*4*mm* phase, which is higher than that (~ −4.5 eV) for the *R*3*c* phase (not shown). However, the *P*4*mm* phase exhibits a markedly large DOS arising from the Bi-6*p* ($p_x + p_y$) and O-2*p* in-plane hybridization (see the wavefunction shown in Fig. 3f), which is due to a small band dispersion in the entire Brillouin zone. Indeed, the atomic partial charge of Bi-6*p* is 0.89 for the *P*4*mm* phase, which is larger than 0.85 for the *R*3*c* phase. We found that the *P*4*mm* phase of BKT is stabilized by a large DOS of the Bi-6*p* ($p_x + p_y$) states derived from the orbital interaction with O-2*p*.

5. Summary and Future Plans

We uncover the ferroelectric polarization and piezoelectric strain constant in the BKT-based single crystals grown by the high-P_{O2} TSSG (top-seeded solution growth) process. These properties originate from a P_s of ~56 μC/cm^2 with a *c*/*a* of ~1.6%; this P_s rivals that of $PbTiO_3$ (70 μC/cm^2). Our theoretical calculations show that the Bi-6*p* and O-2*p* hybridization at a moderately negative chemical pressure stabilizes the ferroelectric distortion in tetragonal symmetry. We could apply the high-P_{O2} process to other functional materials including Bi and/or K in bulk and film forms, here that we have developed high-quality BKT-based crystals by suppressing a defect formation reaction.

References

[1] H. Matsuo, Y. Noguchi, and M. Miyayama, Nat. Commun., **8** 207 (2017).
[2] Y. Noguchi, H. Matsuo, Y. Kitanaka, and M. Miyayama, Sci. Rep., **9** 1 (2019).
[3] Y. Noguchi, Y. Taniguchi, R. Inoue, and M. Miyayama, Nat. Commun., **11** 1 (2020).
[4] Y. Kitanaka, K. Yanai, Y. Noguchi, M. Miyayama, Y. Kagawa, C. Moriyoshi, and Y. Kuroiwa, Phys. Rev. B, **89** 104104 (2014).
[5] K. Yamamoto, Y. Kitanaka, M. Suzuki, M. Miyayama, Y. Noguchi, C. Moriyoshi, and Y. Kuroiwa, Appl. Phys. Lett., **91** 162909 (2007).
[6] Y. Kitanaka, K. Hirano, M. Ogino, Y. Noguchi, M. Miyayama, C. Moriyoshi, and Y. Kuroiwa, Sci. Rep., **6** 32216 (2016).
[7] Y. Kitanaka, Y. Noguchi, and M. Miyayama, Sci. Rep., **9** 1 (2019).
[8] T. Ishigaki, A. Hoshikawa, M. Yonemura, T. Morishima, T. Kamiyama, R. Oishi, K. Aizawa, T. Sakuma, Y. Tomota, M. Arai, M. Hayashi, K. Ebata, Y. Takano, K. Komatsuzaki, H. Asano, Y. Takano, and T. Kasao, Nucl. Instruments Methods Phys. Res. Sect. A Accel. Spectrometers, Detect. Assoc. Equip., **600** 189 (2009).

Y. Noguchi[1,2]
[1]*School of Engineering, The University of Tokyo;* [2]*(Present) Faculty of Advanced Science and Technology, Kumamoto University*

Origin of the Mixed Alkali Effect in Silicate Glass

1. Introduction

Silicate glasses are some of the oldest materials in history and are commonly used in the modern glass industry. It is well known that alkali mixing causes several unusual phenomena in silicate glass, that is, when an alkali ion is gradually replaced by another one, some physical properties, for instance electrical conductivity [1], vary in an extremely nonlinear trend. A large number of studies investigating this "mixed alkali effect" have been reported. Nevertheless, the origin of the mixed alkali effect remains unclear because the previous studies did not visualize the alkali ion coordination around the non-bridging oxygen (NBO) atoms, which formed by introducing the alkali ions into SiO_2 glass, in the glass structure to be consistent with the multiple experimental dataset, e.g., diffraction and NMR.

In this work, we investigated the structure of three kinds of $22.7R_2O$-$77.3SiO_2$ glasses (R = Na, K) by using neutron diffraction (ND) and high-energy X-ray diffraction (HEXRD) to reveal the influence of alkali ions on the glass structure. As alkali ion components, single Na (Na100 glass), single K (K100 glass), and an equal mixture of Na and K ions (Na50K50 glass) were selected. To obtain clear insight into the mixed alkali effect, we performed a dedicated data driven structure modeling, employing combined reverse Monte Carlo (RMC) [2] and classical molecular dynamics (MD) simulations (RMC-MD simulations) in accordance with the ND, HEXRD, and NMR [3] data. Based on the atomistic models, we carried out advanced topological data analysis [4], which highlighted the origin of the mixed alkali effect from the behavior of alkali ions around the NBO atoms in the glasses [5].

2. Methods

Alkali silicate glasses were prepared by a conventional melt quenching method from mixtures of reagent grade SiO_2, Na_2CO_3, and K_2CO_3 powders.

The ND experiments were performed on a high intensity total diffractometer, NOVA [6], installed at BL21 beamline in the Materials and Life Science Experimental Facility (MLF) of the J-PARC. The HEXRD experiments were conducted on a two-axis diffractometer, which is dedicated for disordered materials, at the BL04B2 beamline [7] of the SPring-8 synchrotron radiation facility.

For details about RMC-MD simulations, please refer to our original paper [5]. The starting configurations were created using hard-sphere Monte Carlo (HSMC) simulations with constraints to reproduce the Q^n ratio (where, n is a number of bridging oxygen atom in a SiO_4 tetrahedron) of the three glasses obtained by the NMR study [3]. After the HSMC simulations, the RMC simulations were carried out to reproduce the neutron $S(Q)$ and X-ray $S(Q)$ data. Following the RMC simulations, the atomic configurations were optimized by the MD simulations. After the MD simulations, all configurations were refined by additional RMC simulations while constraining the coordination number of silicon, the bond angle distribution for O-Si-O, and the partial pair distribution functions within the first coordination distance to avoid the formation of an unfavorable disordered structure. The RMC simulations were performed using RMC++ code [8]. The MD simulations were performed using the LAMMPS package [9].

The persistent homology analyses [4] were performed using the HomCloud package [10]. Given a set of points in space, persistent homology captures the topological multiscale structures and those identified are compactly expressed in a persistence diagram. The detailed process of the construction of the persistence diagram is described elsewhere [4, 5].

3. Results and discussion

We confirmed the mixed alkali effect in the electrical properties of the alkali silicate glasses by measuring the dielectric constants, ε_r. Indeed, the ε_r exhibits a nonlinear trend as a function of the K_2O amount and has a minimum value in the Na50K50 glass [5].

Figure 1 compares the neutron and X-ray total structure factors, $S^{N,X}(Q)$. The final results of the RMC-MD simulations are plotted in Fig. 1 as solid colored curves. A good agreement between the RMC-MD model and experimental data (black solid curves) has been obtained. It is worth mentioning that an average of the diffraction patterns of the Na100 and K100 glasses (black broken curves) is almost identical to the experimental data for the Na50K50 glass for both $S^N(Q)$ and $S^X(Q)$, implying that the mixed alkali effect cannot be detected easily in the 1-dimensional diffraction data.

To obtain more clear insight to reconcile the mixed alkali effect, we applied the persistent homology analysis to the RMC-MD models. First, we obtained the alkali-centric persistence diagrams for three alkali glasses. However, distinguishable differences among the three glasses are not observed in the data. On the other hand, the alkali-centric persistence diagrams of Na50K50 glass

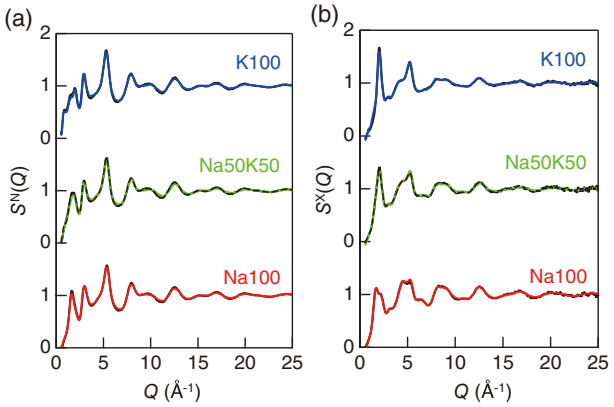

Figure 1. (a) Neutron total structure factor $S^N(Q)$ and (b) X-ray total structure factor $S^X(Q)$ for the alkali silicate glasses [5]. The black solid curve depicts the experimental data; the colored curve represents the RMC-MD model. The average experimental $S^{N,X}(Q)$ for the Na50K50 glass is calculated using the Na100 glass and the K100 glass data are plotted as a dashed black curve.

for Na-centric, Na/K-centric, and K-centric data shown in Fig. 2(a)–(c) exhibit a striking difference. We can observe profiles along the diagonal for all the data. It is known that the profile with a very short lifetime represents three-body correlations, as shown in Fig. 2(d)–(f). Both the Na-centric (Fig. 2(d)) and K-centric data (Fig. 2(f)) do not have any characteristic profiles, while only the Na/K-centric persistence diagram (Fig. 2(e)) has two profiles at d_k ~5 and ~10 Å^2. These profiles demonstrate that Na and K are highly correlated in Na50K50 glass, similar to Na-O-K. We can clearly observe the formation of specific correlations between Na and K ions as mentioned above. Thus, the persistent diagram enables us to extract the characteristic topology in the glasses. To obtain more crucial structural features to uncover the origin of the mixed alkali effect, alkali-oxygen polyhedra with the formation of edge-sharing NBO atoms in Na50K50 glass are visualized in Fig. 2(g). The K-O polyhedra that

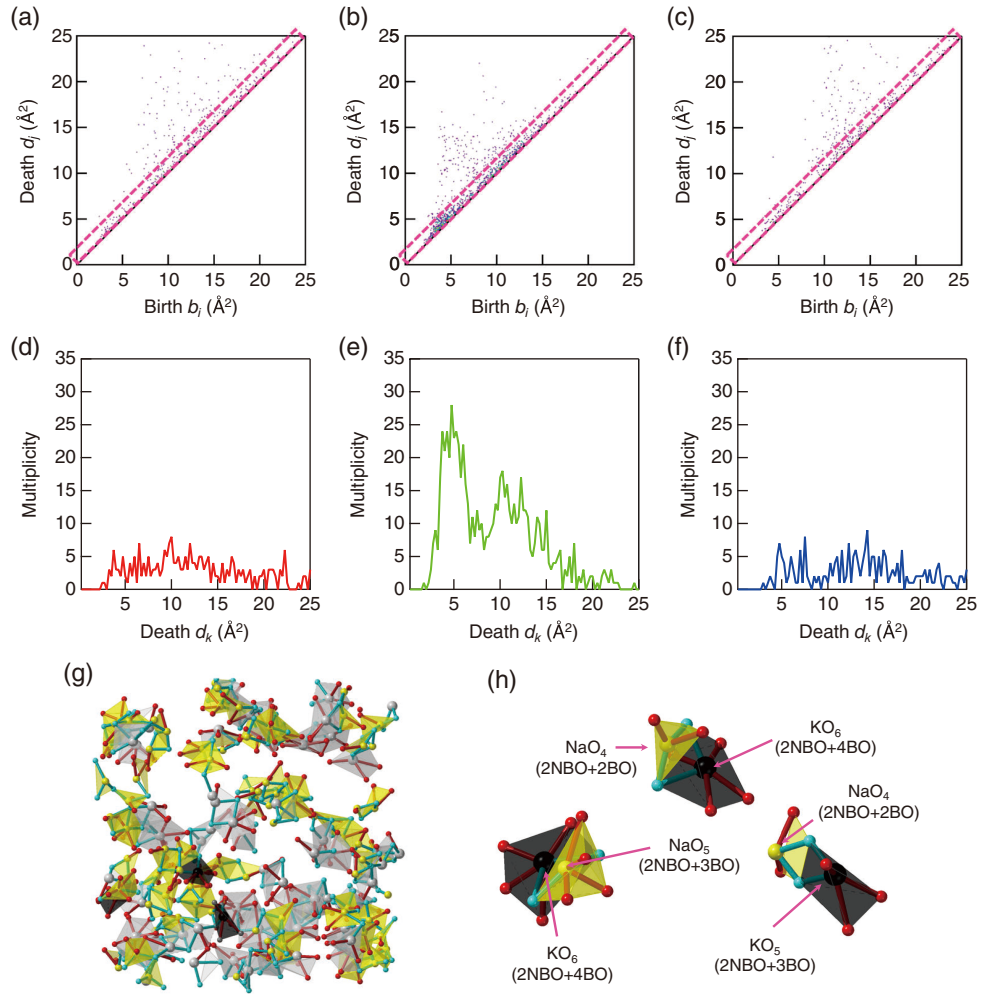

Figure 2. (a) Na-centric, (b) Na/K-centric, (c) K-centric persistence diagrams for the Na50K50 glass. The boxed regions follow the diagonal, and the associated profiles are plotted in (d), (e), (f). Visualization of the alkali-oxygen polyhedra around the non-bridging oxygen atoms in the Na50K50 glass (g) and the typical bottle neck structures consist of Na-O and K-O polyhedra (h) [5].

are highly coordinated with the bridging oxygen (BO) and Na-O polyhedra are highlighted in black, where the potassium ion is trapped by a large number of BO atoms (see Fig. 2(h)). It is likely that these specific configurations involving NBO atoms are a bottleneck in ionic conduction because the trapped potassium ions disturb the ionic migration.

References

[1] J. O. Isard, J. Non-Cryst. Solids, **1** 235 (1969).
[2] R. L. McGreevy and L. Pusztai, Mol. Simul., **1** 359 (1988).
[3] H. Maekawa *et al.*, J. Non-Cryst. Solids, **127** 53 (1991).
[4] Y. Hiraoka *et al.*, Proc. Natl. Acad. Sci. USA, **113** 7035 (2016).
[5] Y. Onodera *et al.*, NPG Asia Mater., **11** 75 (2019).
[6] T. Otomo *et al.*, KENS Rep., **17** 28 (2011).
[7] S. Kohara *et al.*, J. Phys. Condens. Matter, **19** 506101 (2007).
[8] O. Gereben *et al.*, J. Optelectron. Adv. Mater., **9** 3021 (2007).
[9] S. Plimpton, J. Comput. Phys., **117** 1 (1995).
[10] http://www.wpi-aimr.tohoku.ac.jp/hiraoka_labo/homcloud/.

Y. Onodera[1,2], Y. Takimoto[3], H. Hijiya[4], T. Taniguchi[3], S. Urata[3], S. Inaba[4], S. Fujita[3], I. Obayashi[5,6,7], Y. Hiraoka[8,5,6], and S. Kohara[9,2,10,11]

[1]Institute for Integrated Radiation and Nuclear Science, Kyoto University; [2]Center for Materials Research by Information Integration (CMI2), Research and Services Division of Materials Data and Integrated System (MaDIS), National Institute for Materials Science (NIMS); [3]Innovative Technology Laboratories, AGC Inc.; [4]Materials Integration Laboratories, AGC Inc.; [5]Center for Advanced Intelligence Project, RIKEN; [6]CREST, Japan Science and Technology Agency; [7]Kyoto University Institute for Advanced Study, Kyoto University; [8]Kyoto University Institute for Advanced Study, WPI-ASHBi, Kyoto University; [9]Research Center for Advanced Measurement and Characterization, NIMS; [10]PRESTO, Japan Science and Technology Agency,; [11]Diffraction and Scattering Division, Japan Synchrotron Radiation Research Institute

Neutron CT to Investigate Relationship between the Phase Separation Structures and Melt Convection during Solidification in Cu-Co Alloys

1. Introduction

The binary Cu-Co system exhibits a metastable miscibility gap in the undercooled state. In that state, the homogeneous Cu-Co melt separates into two liquid phases, i.e. Co-rich and Cu-rich phases, once the melt is undercooled below the binodal line. The solidified Cu-Co alloys have attracted attention because the alloys take on various electrical and magnetic characteristics depending on the phase separation structures.

The phase separation structures are generally controlled by the composition, the cooling rate and the degree of undercooling. In contrast, we have focused on and investigated the correlation between the phase separation structures and convection in molten Cu-Co alloys before solidification by using an electromagnetic levitator (EML) superimposed with a static magnetic field [1, 2]. This is because the static magnetic field is capable of controlling melt convection (e.g., Magnetohydrodynamic, MHD convection) in the levitated molten sample. Nevertheless, in the previous studies, only the cross-section of the solidified sample cut into two pieces has been observed using a scanning electron microscope (SEM). Therefore, neutron computed tomography (CT) to observe the 3D phase separation structures of Cu-Co alloys was performed.

2. Experiment

Cu with nominal purity 99.99% and Co with purity 99.9998% were used as raw substances and Cu-Co alloy samples with compositions of $Cu_{80}Co_{20}$ and $Cu_{58}Co_{42}$ were prepared. The alloy samples were melted and solidified using the EML superimposed with a static magnetic field. Figure 1 shows the schematic of the EML system. The procedure for undercooling and solidification of the molten Cu-Co samples was the same as in our previous studies [1, 2]. The static magnetic field was generated by a superconducting magnet to control convection, particularly MHD convection, in the molten samples and herein ranged from 0 to 5 T. The size of the solidified alloy sample was approximately 5 mm.

Neutron CT experiments were performed by using the energy-resolved neutron imaging system RADEN, in the Material and Life Science Experimental Facility (MLF) of the Japan Proton Accelerator Research Complex (J-PARC). An Al pipe (aluminum alloy 1070; length: 200 mm; inner diameter: 7 mm; outer diameter: 10 mm) was used as a sample container because of the significantly lower attenuation coefficient of neutron beam for Al compared with those for Cu and Co. The sample container was irradiated with 3500 pulses of neutron beam per projection, and 300 projections were obtained every 0.6° over the span of 180°. The neutron beam passing through the sample was converted to visible light using a ^{6}LiF/ZnS scintillator with 50 μm thickness, and the visible light was captured by a Charge Coupled Device (CCD) camera with a resolution of 2048 × 2048 pixels. Although the spatial resolution of the reconstructed tomographic images was 25 μm/pixel, the substantive resolution might be approximately 200 μm.

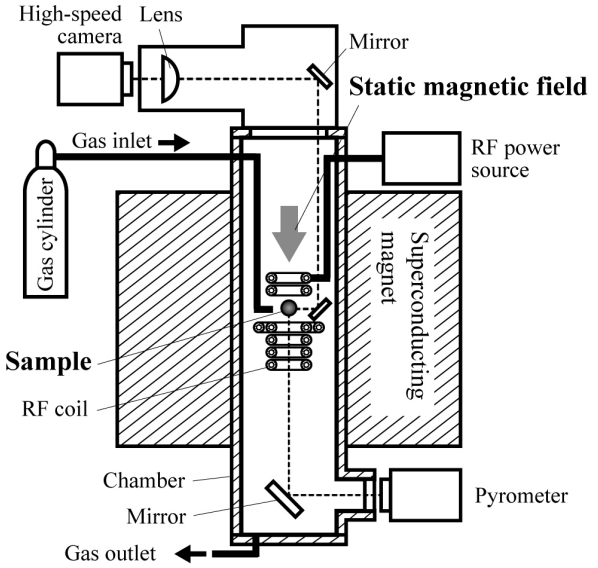

Figure 1. Electromagnetic levitator (EML) superim-posed with a static magnetic field to prepare solidified Cu-Co alloy samples with phase separation structures. Melt convection in molten alloy samples can be controlled by applying a static magnetic field. (Adapted from Ref. 3)

3. Results and discussion

Figure 2 shows the reconstructed images of $Cu_{80}Co_{20}$ and $Cu_{58}Co_{42}$ solidified under different strengths of the static magnetic field. In case of $Cu_{80}Co_{20}$, the Co-rich phases dispersed in the matrix of the Cu-rich phase at fields less than 1.0 T. In contrast, the Co-rich phases at

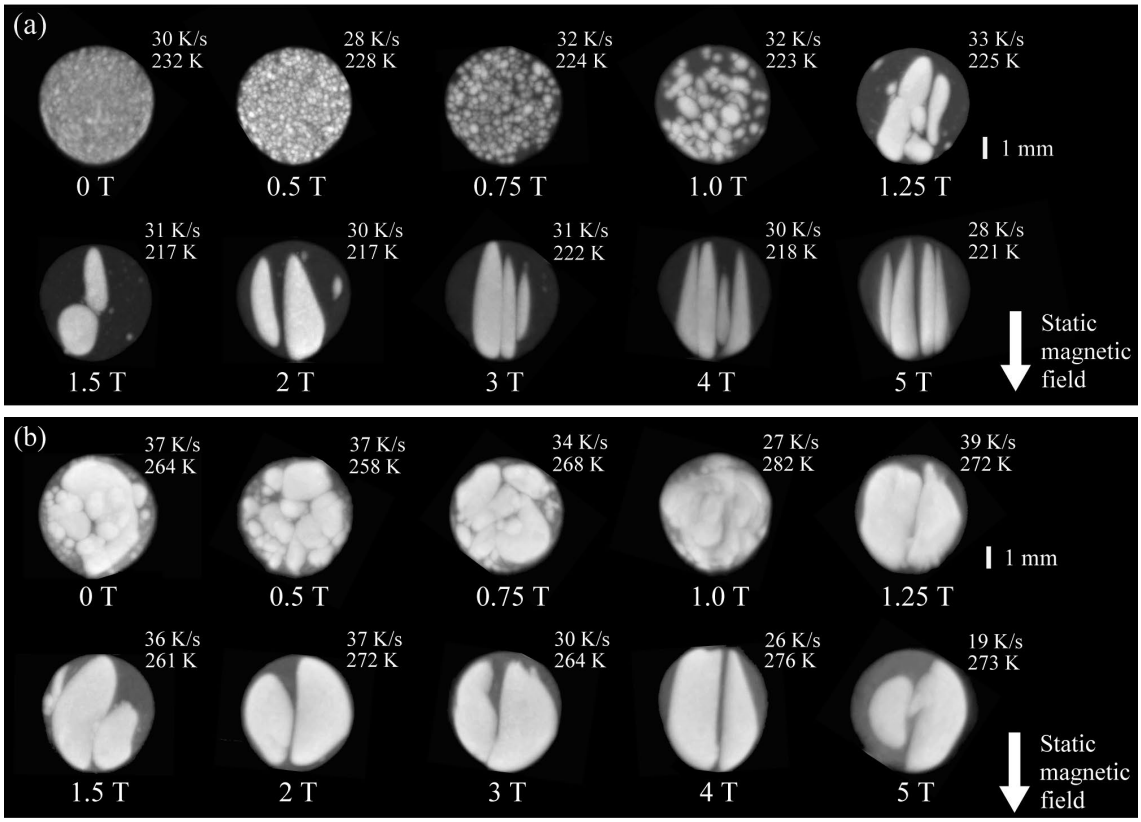

Figure 2. Phase separation structures in Cu-Co alloys solidified under different static magnetic fields obtained through neutron CT experiments. The brighter and darker regions indicate Co-rich and Cu-rich phases, respectively. The values in the upper right of each image represent the cooling rate and the degree of undercooling. (Adapted from Ref. 3)

the fields exceeding 1.25 T indicated the markedly large structures. The Cu-Co alloys at 1.25 T had a few Co-rich phases with different shapes and sizes, however, at fields greater than 2.0 T, all the Co-rich phases were elongated along the direction of the static magnetic field.

At the lower static magnetic fields, the phase separation structures of $Cu_{58}Co_{42}$ shown in Fig. 2(b) present more complex shapes compared with the $Cu_{80}Co_{20}$. At fields greater than 1.25 T, the Co-rich phases became elongated along the direction of the static magnetic field as well as the $Cu_{80}Co_{20}$.

4. Summary

Neutron CT to investigate 3D phase separation structures in Cu-Co alloys solidified using the EML technique superimposed with a static magnetic field was performed using the neutron imaging apparatus RADEN in J-PARC MLF. The neutron CT results showed that the 3D phase separation structures markedly changed depending on the applied static magnetic field, namely, melt convection. We are now performing the computational fluid dynamics (CFD) simulation to predict the details of a flow field in an electromagnetically levitated droplet. In the future, the detailed correlation between melt convection and phase separation structures in molten Cu-based binary alloys can be obtained by comparing these experimental and numerical studies.

References

[1] K. Sugioka et al., Metall. Mater. Trans. B, **45B** 1439 (2014).
[2] T. Kitahara et al., Metall. Mater. Trans. B, **46B** 2706 (2015).
[3] E. Shoji et al., Scr. Mater., **175** 29 (2020).

E. Shoji[1], S. Isogai[1], R. Suzuki[1], M. Kubo[1], T. Tsukada[1], T. Kai[2], T. Shinohara[2], Y. Matsumoto[3], and H. Fukuyama[4]
[1]Department of Chemical Engineering, Tohoku University; [2]Neutron Science Section, Materials and Life Science Division, J-PARC Center; [3]Neutron Science and Technology Center, CROSS; [4]Institute of Multidisciplinary Research for Advanced Materials, Tohoku University

Electronic Structure of Hydrogen in In-Ga-Zn-O Semiconductor Simulated by Muon

1. Introduction

In-Ga-Zn oxide, widely known as IGZO, is a semiconductor used as channel material in transparent thin-film transistors (TFTs) for display applications. IGZO has properties superior to the conventional Si TFTs such as relatively high electron mobility, low-temperature fabrication over a large area, uniformity and stability. However, there is a serious problem in the amorphous IGZO (a-IGZO) known as negative bias illumination stress (NBIS) instability, i.e., a negative shift of the threshold voltage in the normal operation condition that TFTs are always illuminated by the backlight under a negative bias voltage, whose microscopic mechanism is still under debate.

It is known that various electronic properties of IGZO are influenced by hydrogen (H) impurity. For instance, water vapor annealing improves the carrier mobility and the *S*-value (sharpness of the TFT switching as a function of gate-source voltage), *n*-type conductivity appears by H treatment. Recent infrared transmission spectroscopy has revealed the subgap state near the valence band maximum arising from two hydride ions at oxygen vacancy ($2H^-$ at V_O) [1, 2]. It is argued that this subgap state is associated with the NBIS mechanism, thus, understanding the microscopic mechanisms of these processes would be of crucial importance in controlling and stabilizing the electronic properties of IGZO.

We were thus motivated to investigate the local electronic structure of interstitial H in IGZO by the muon spin rotation (μSR) technique [3]. We have proposed the designation "muogen" (Mu) as the elemental name, where charge states of muogen, Mu^+, Mu^0, Mu^- correspond to that of hydrogen H^+, H^0 and H^-, respectively.

2. Experiment

Conventional μSR measurements on the crystalline IGZO (c-IGZO) were performed using ARTEMIS at MUSE of the MLF J-PARC. Meanwhile, μSR measurements on a-IGZO and hydrogenated a-IGZO (a-IGZO:H) thin films were performed using the low-energy muon (LEM) beam at Paul Scherrer Institute, Switzerland. Muon stopping profiles for c-IGZO films (5.97 g/cm^3) are shown in Fig. 1(d), where most of the LEM measurements were performed at 11 keV LEM.

3. Results and discussion

Figuers 1 (a) and (b) show typical zero field (ZF) spectra of c-IGZO and as-deposited a-IGZO, respectively. Each ZF-spectrum exhibits slow Gaussian damping with the partial recovery of polarization at a later time domain ($t \geq 10$ μs). The spectra were analyzed by the following equations:

$$A_0 P_\mu(t) = A_s G_{KT}(\Delta, t) + A_{BG}$$

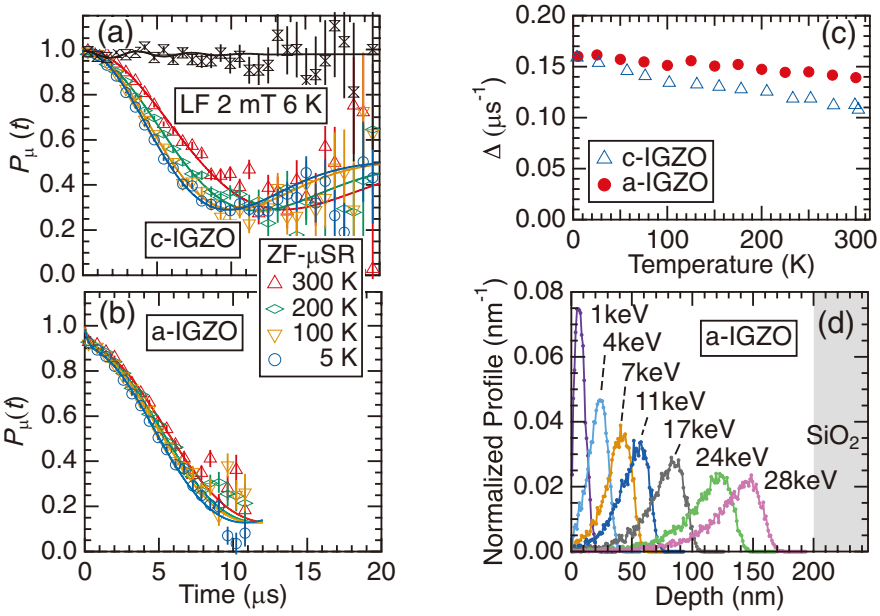

Figure 1. μSR time spectra for (a) c-IGZO and (b) as deposited a-IGZO [3]. (c) Temperature dependence of Δ. (d) Muon stopping profiles for respective implantation energies.

$$G_{KT}(\Delta, t) = \frac{1}{3} + \frac{2}{3}(1-\Delta^2 t^2)\, exp\left(-\frac{\Delta^2 t^2}{2}\right),$$

where $P_\mu(t)$ represents the time evolution of the muon spin polarization in the sample and the sample-holder with their respective partial asymmetry being A_s and A_{BG} ($A_0 = A_s + A_{BG}$). $G_{KT}(\Delta, t)$ is the static Kubo-Toyabe relaxation function, with the term Δ representing the local field distribution caused by nuclear magnetic moments around muon site(s). As shown by solid curves in Fig. 1(a), the spectra were perfectly reproduced by Eq. (1), indicating that the muon is entirely in the diamagnetic state (Mu^+ and/or Mu^-). It is apparent from the longitudinal field (LF) spectra in c-IGZO that Mu senses the quasistatic field distribution. Temperature dependence of Δ obtained by curve-fit is shown in Fig. 1(c).

Candidate Mu sites were narrowed down by simulation: (1) DFT calculation for H (to mimic Mu) using the VASP code to estimate the structural relaxation around H and the formation energy E_f with some initial structures around H due to the random occupation of Ga and Zn in their crystallographically equivalent sites. (2) calculation of Δ at the H site in their converged structure. The calculated E_f and Δ are shown in Fig. 2. It is noticeable that Δ tends to be reduced by the decrease in E_f, and the tendency is that the higher E_f, the more Ga and In ions group around Mu. These indicate that H prefers the Ga/Zn-O layer to the InO_2 layer and that H sites are stabilized by the Zn-rich structure.

The inset in Fig. 2 represents the local structure around H for Zn^4O^4. Structural similarity to ZnO suggests that the local electronic structure of Mu/H is similar to that in ZnO where Mu^0 is presumed to be localized at the bond center of Zn-O.

ZF spectra in a-IGZO:H are represented in Fig. 3(a). The initial muon polarization disappears at lower temperatures [$P_\mu(t{=}0) < 1$], and the remaining components exhibit a slow exponential-like relaxation. Transverse field (TF) and LF spectra, shown in Fig. 3(b), reveal that this slow relaxation comes from diamagnetic state probing the static field distribution due to the nuclear magnetic moments. These features strongly suggest that the distance between Mu and the nuclear magnetic moments is not uniform. This leads to the presumption that another H atom may locate around the Mu site in a-IGZO:H, which also invokes a model of $2H^-$ at V_O proposed by the recent studies [1, 2].

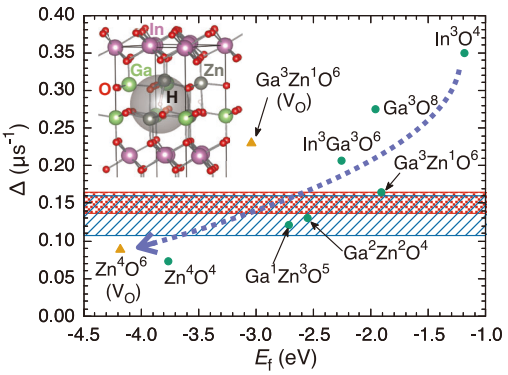

Figure 2. E_f and Δ for the candidate Mu sites, where label $A^iB^jC^k$ indicates the element name and number of atoms located within 0.3 nm from Mu. V_O means Mu at oxygen vacancy site. The hatched areas represent the range of Δ for c-IGZO (blue) and a-IGZO (red). Inset shows the local structure around H for Zn^4O^4. Large gray sphere represents the region of 0.3 nm from H.

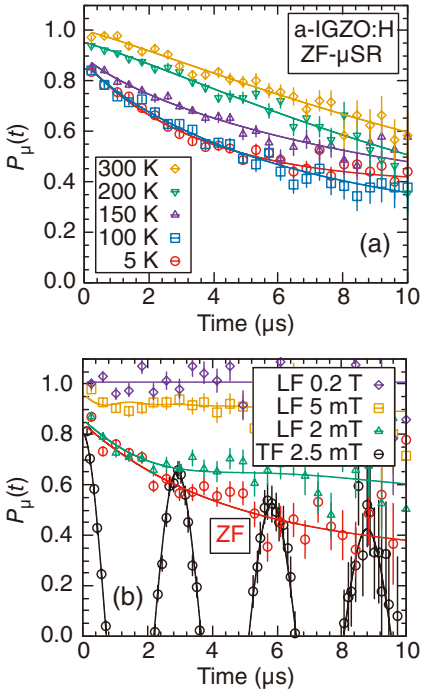

Figure 3. Temperature dependence of the ZF spectra in a-IGZO:H. (b) TF, ZF, and LF spectra measured at 5 K. TF spectra is partially represented for clarity.

References

[1] J. Bang, S. Matsuishi, and H. Hosono, Appl. Phys. Lett. **110** 232105 (2017).
[2] H. Li, Y. Guo, and J. Robertson, Sci. Rep. **7** 16858 (2017).
[3] K. M. Kojima, *et. al.*, Appl. Phys. Lett. **115** 122194 (2019).

M. Hiraishi[1], K. M. Kojima[1,2], H. Okabe[1], A. Koda[1,2], R. Kadono[1,2], K. Ide[3], S. Matsuishi[4], H. Kumomi[4], T. Kamiya[3,4], and H. Hosono[3,4]
[1]Muon Science Section, Materials and Life Science Division, J-PARC Center; [2]Institute of Materials Structure Science, KEK; [3]Laboratory for Materials and Structures, Institute of Innovative Research; [4]Materials Research Center for Element Strategy. Tokyo Institute of Technology (MCES)

Neutron Source

Neutron Source Section

The neutron source continued its stable operation in fiscal year 2019. The beam operation of mercury target #9, which had the same design as the preceding target #8, started in late October 2018 and ended in early July 2019 with a beam power of 500 kW during almost the entire operation time. The 8-month run of the program with such a high power was achieved for the first time, which demonstrated the durability of the mercury target used for the 500-kW power. After the user program was closed, a high-power operation study was held for 10.5 hours at 930 kW on July 3. This made it possible to obtain significant operation data, which normally would require long time to reach a stable value. Also, the validity of the system design with regard to the ultimate power goal was reconfirmed.

The most important challenge to achieve 1-MW stable operation is to mitigate the pitting damages on the inner surface of the target vessel that are caused by pressure waves in mercury. This is achieved by two different technologies, which are micro-bubbles injection of helium gas into mercury by a bubble generator and formation of a narrow mercury channel with a 2-mm gap and high-speed mercury flow in it by adding an inner wall at the forefront of the mercury vessel, shown schematically in Fig. 1. Micro-bubbles in mercury attenuate the pressure wave intensity and the efficiency is monitored by measuring sound signals with a microphone. Figure 2 shows the dependency of the sound signal magnitude on the beam power. The sound signal was normalized with that in the case of 340 kW without micro-bubble injection. The broad scatterings of target #9 data from 300 kW to 600 kW are due to the change in the amount of the micro-bubble injection and proton beam profiles. All in all, the sound data of targets #8 and #9 showed a consistent trend, which confirmed the efficiency of the micro-bubble injection to reduce pressure waves.

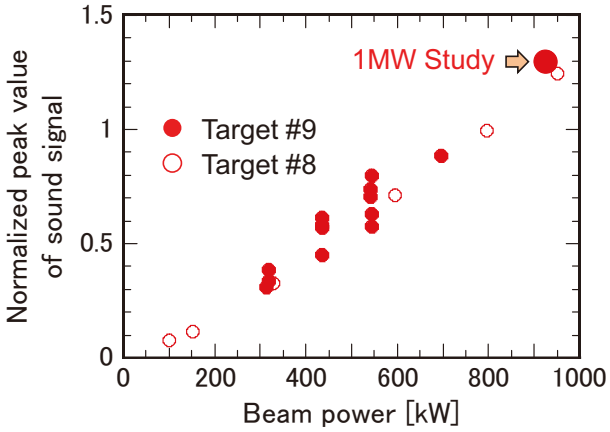

Figure 2. Sound signal data of the target vessels at the beam study.

Specimens were cut out from the forefront wall of target vessel #9 to see the pitting damages inside. Figure 3 shows that the pitting damages on the outer wall that is the boundary of mercury containment were negligibly small, even after the long run of the 500-kW operation. This fact showed that the high-speed mercury flow and the narrow channel structure were effective to mitigate pitting damages. On the other hand, the maximum damage depth on the inner wall, which was protected by micro-bubbles, was 3.3 mm. R&D for a technology to intensify the bubbling effect to mitigate pitting damages will be continued.

Target vessel #9 was replaced to a target vessel with a new design shown in Fig. 4, in which the coupling-free structure between the inner mercury vessel and the surrounding outer water shroud removes the structural cause of generating high thermal stress on the target. The stable operation of this new type of target vessel with over 500 kW demonstrated the successful design improvement after the target vessel failure in 2015 and was one of the major milestones to achieve 1 MW power.

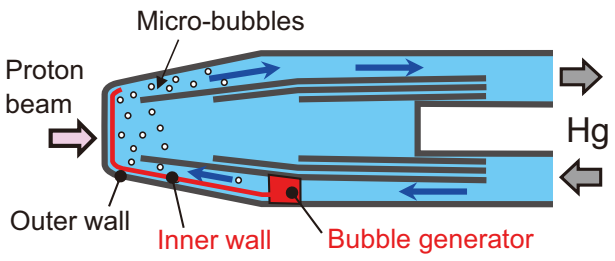

Figure 1. Technologies to mitigate pitting damages mounted in the mercury vessel.

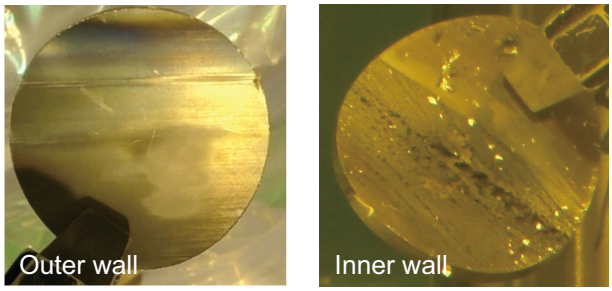

Figure 3. Target vessel specimens of the outer and inner walls.

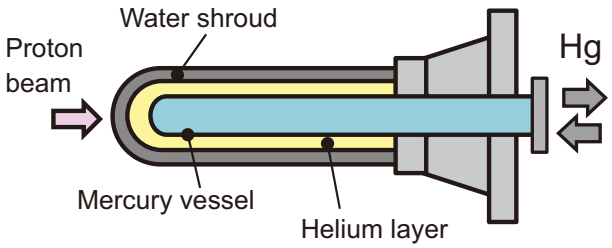

Figure 4. Vertical cross-section of the mercury target vessel consisting of the mercury vessel and the outer water shroud.

After the summer outage period, the restart of the beam operation was delayed for about a month since the gas processing system, which plays an important role in the target replacement procedure, took longer than expected to secure its operation with sufficient radiation safety. These operation experiences will result in a more robust and reliable system improvements.

The international collaboration with major foreign institutes of spallation neutron source continues. In-situ measurement of ortho/para liquid hydrogen ratio was carried out at the cryogenic hydrogen loop of MLF as a collaboration with the ESS (European Spallation Source) team in July 2019, which will be discussed in other chapter of this report. Technical workshop with SNS (Spallation Neutron Source) of Oak Ridge National Laboratory was held in December 2019 and many collaboration items, including R&D for the pitting damage mitigation technology, material fatigue experiments, and cryogenic moderator system operation, were confirmed.

K. Haga
Neutron Source Section, Materials and Life Science Division, J-PARC Center

Improvement of Gas Supply System for Mitigation of Pitting Damage in Mercury Target Vessel

1. Introduction

In the mercury target for a neutron source, the pulsed proton beam injection causes rapid thermal expansion of the mercury, which generates pressure waves in it. And those waves overload the mercury target vessel which contains the liquid mercury. In addition, the cavitation damage caused by the interaction between the pressure waves and the deformation of the target vessel degrades the structural integrity of the vessel. Since the vessel is made of 316L stainless steel with a 3 mm thickness at the beam entrance portion (beam window), the cavitation damage is a crucial factor to determine the lifetime of the target vessel and to schedule the ramping-up of the proton beam power. To reduce the cavitation damage, we have applied gas microbubble injection technique into the mercury to reduce the pressure waves by absorption of the thermal expansion due to the gas microbubbles [1]. In addition, to reduce the possibility of a mercury leak from the vessel, a double-walled structure at the beam window was applied to make a narrow channel of mercury by installing an inner wall with 5 mm in thickness and 2 mm in a gap between the target vessel and the inner wall. The narrow channel is expected to disturb the growth of cavitation bubbles by high-speed flow and narrow gap and mitigate the cavitation damage [2].

We have demonstrated the effect of microbubbles on pressure wave reduction by monitoring the vibration of the target vessel during the operation [3] and so far, observed the cavitation damage after the designed lifetime of target vessel [4]. Based on the observed result, we estimated the effect of the microbubbles and the narrow channel and ramped-up beam power to 500 kW in FY2018. After the 3680-h operation with the 500-kW beam, we observed cavitation damage in 2019. It was clear that the cavitation damage facing the narrow channel was very shallow, but the depth of the damage facing the bulk side exceeded 3 mm.

The reason why the damage on the bulk side was so deep is described in this report and we propose countermeasures to mitigate it.

2. Operation of the gas supply system

Figure 1 shows the schematic of the mercury target system. The mercury target vessel and mercury circulation system are mounted on a target trolley. The main components of the mercury circulation system are mercury pump, heat exchanger and surge tank. Bubble generator to inject microbubbles into the mercury is installed in the target vessel. The cover gas of helium in the surge tank is supplied to the bubble generator through the gas supply system which mounted on the back of the target trolley. Figure 2 shows the helium-gas-flow diagram of the gas supply system. The main components of the gas supply system are a bellows compressor, needle valves, and a buffer tank. The compressor sucks in helium cover gas in the surge tank of the mercury circulation system and pressurizes it. A return line with a pressure-control needle-valve is set between the suction and discharge sides of the compressor to control the pressure in the buffer tank. The helium gas stored in the buffer tank is supplied to the bubbler via the flow-control needle-valve.

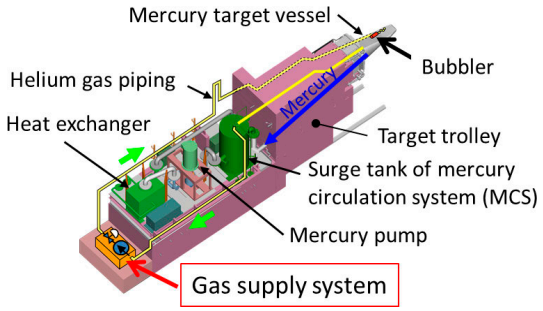

Figure 1. Mercury target system.

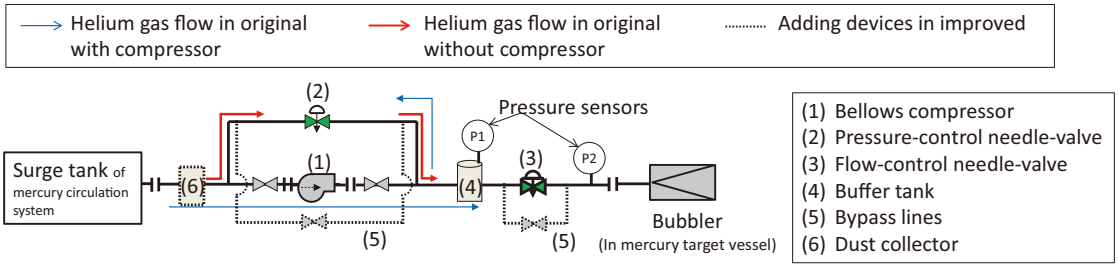

Figure 2. Diagram of the gas supply system.

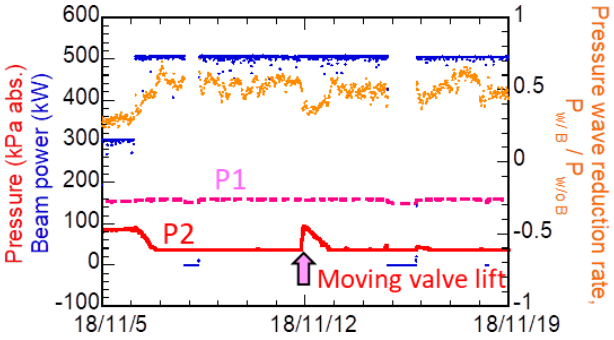

Figure 3. History of P1, P2 and pressure-wave reduction by using the original gas supply system without compressor.

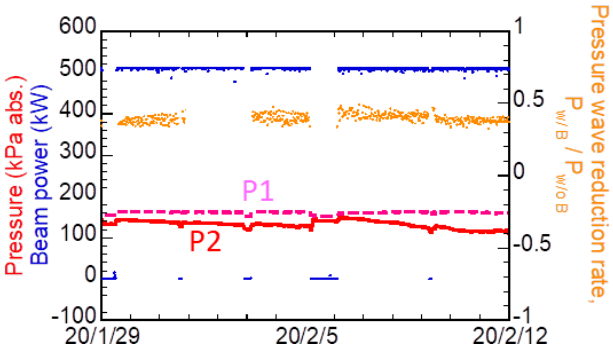

Figure 4. History of P1, P2 and pressure-wave reduction by using an improved gas supply system.

Two pressure sensors are set at the inlet (buffer tank) and outlet of the flow-control needle-valve. The flow rate of the helium gas under standard condition could be calculated by using the opening area and pressures at the inlet and outlet of the flow-control needle-valve.

In the initial operation, we used the compressor. However, we stopped to using it due to potential fatigue fail of its bellows, which could release into the atmosphere the radioactive materials mixed with the helium gas. To do so, we improved the bubbler to be able to suck helium gas by itself without the compressor. When the system is operated without the compressor, the helium gas flows through the pressure-control needle valve instead of through the compressor, as shown in Fig. 2.

Figure 3 shows history of pressure at the inlet and outlet of the needle valve, P1 and P2, respectively, and the pressure-wave reduction rate, which is defined as that the peak amplitude of vibration under the case with bubbles, is divided by that without bubbles. In the 300-kW beam operation, P1 and P2 were almost constant; 155 kPa abs. and 100 – 120 kPa abs, respectively. However, at 500 kW, P2 was decreased to the lower limit of the sensor (36 kPa abs.), even though the P1 was not decreased. And the effect of pressure wave reduction became worse; the pressure wave reduction rate exceeded 0.6. The pressure wave reduction rate increased with the decrease of the amount of helium gas bubbles [3]. On the other hand, P2 and the pressure wave reduction rate were recovered after moving the valve lift of the flow-control needle-valve. From these results, we suspected that something had clogged and the effect of the microbubbles became worse; the depth of the damage facing the bulk side exceeded 3 mm.

3. Improvement of the gas supply system

To prevent the clogging of the needle valve, we improved the gas supply system in FY2018. The diagram of the improved one is shown in Fig. 2. The pressure-control valve in the original system was also a needle valve but it was not clogged since its opening area was wider than the flow-control one. Therefore, the flow-control needle-valve was changed to the same type with the pressure-control needle-valve. And the lift of the flow-control needle valve was modified to move remotely to remove the clogging even during the beam operation. At the inlet of the gas supply system, we installed a cyclone-type dust collector to catch the clogging material. Furthermore, bypass lines for the needle valves were prepared as the countermeasure if the needle valve was completely clogged.

Figure 4 shows the history of the pressures and pressure wave reduction rate under the 500-kW operation by using the improved gas supply system. Although clogging was still occurred, the decrease rate of P2 slowed down. And by moving the valve lift, the pressure wave reduction rate could be kept below 0.45.

In FY2020, we will increase the beam power up to 600 kW and will still monitor the clogging situation at the gas supply system while taking measures to eliminate it.

References

[1] H. Kogawa, et al., J. Nucl. Sci. Technol., **52** 1461 (2015).
[2] T. Naoe, et al., J. Nucl. Mater., **506** 35 (2018).
[3] H. Kogawa et al., J. Nucl. Sci. Technol., **54** 733 (2017).
[4] T. Noe, et al., JPS Conf. Proc., 081004 (2020).

H. Kogawa, T. Naoe, T. Wakui, and K. Haga
Neutron Source Section, Materials and Life Science Division, J-PARC Center

Nuclide Analysis of the Irradiated Target Vessel

1. Introduction

Since FY2018, we have periodically measured the spectral intensity of gamma rays emitted by radioactive nuclides produced in the irradiated mercury target vessels. This measurement has three objectives:

1) Benchmark for the calculation of radioactive nuclide production in the target vessel.
2) Basic data for the storage, volume reduction, and disposal plan for radioactive waste.
3) Basic data of dose evaluation in disposal and volume reduction operation.

We measured by teletector only the dose distribution data. We obtained the data on the dose contribution of each nuclide.

2. Experimental method

In this measurement, the gamma rays were measured by a portable Ge semiconductor detector (ORTEC) cooled by liquid nitrogen. The 2.4-m thick hatch of the irradiated components storage room on the first basement floor of the MLF was opened, and the used mercury target vessel stored in the storage container, which was temporarily placed in the irradiated components handling room on the first floor of the MLF, was lifted and lowered into the irradiated components handling room using a 20 t crane. The distance from the center of the 2.4-m hatch to the measurement position of the detector was 13.2 m. The detector was shielded by surrounding and stacking of the Pb blocks 150 mm in thickness in front of the detector. And the two 5 mm thick Pb plates were put with 100 mm interspace at the center of the front side the detector. The multi-channel analyzer (MCA) and the measurement PC were connected by cables laid between the irradiated components storage room and the second manipulator operation room across the concrete wall through a through-bore. Figure 1 shows the measurement setup.

3. Result

In FY2019, we measured the irradiated mercury target vessels No. 3, 5, 2, and 8. The ground position at the head of the target was at 0 m from the floor, and the crane was used to measure the 1-m and 2-m positions. Figure 2 shows pictures from the measurement of mercury target vessel No. 8. Table 1 shows the duration of use, cooling time and accumulated beam power of each of the used target vessels.

Figure 3 shows the measured gamma ray spectra of each target vessel at the ground position. We confirmed that the major radioactive nuclides emitting gamma rays were Mn-54 (835 keV) and Co-60 (1173 keV and 1333 keV). These nuclides are produced by irradiation

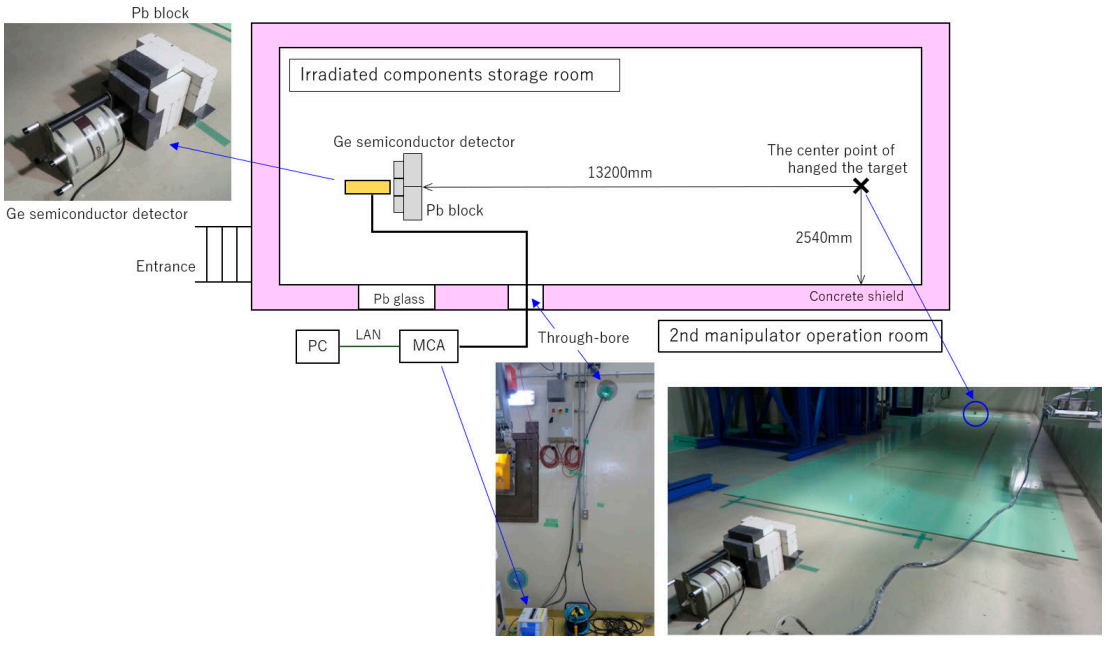

Figure 1. The measurement setup. The photo at the upper left is the Ge semiconductor detector and the Pb blocks. The two 5 mm thick Pb plates were put with 100 mm interspace at the center of detector. The lower photo in the center shows the second manipulator operation room. The lower one on the right is the view from the side of the entrance of the hot cell below the 2.4-m hatch.

to the stainless steel. Then, it was confirmed that the main contributors to the dose rate of the target vessel were the activation nuclides of the stainless steel rather than the mercury in the spallation products. As the half-life of Co-60 (5.3 years) is longer than that of Mn-54 (312 days), after long cooling times (as it is the case with target vessels No. 3 and 5), the contribution of Co-60 is dominant and that of Mn-54 is relatively negligible. On the other hand, the contribution of Mn-54 is dominant after a short cooling time (target vessels No. 2 and 8). Since, in the simulation, Mn-54 produced in the vessel at the end of the operation is 10 times more than Co-60, it is important to consider the Mn-54 contribution to the dose rate when replacing or storing the target vessel. However, the contribution of Co-60 is important during long-term storage and disposal.

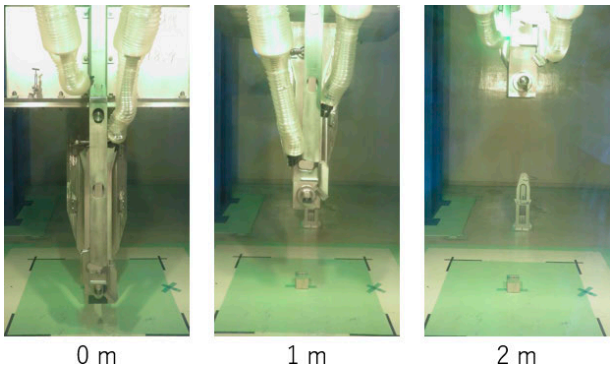

Figure 2. Pictures from the measurement of mercury target vessel No.8. The height of the target was determined by the z-coordinate of the crane.

Next, Figure 4 shows the spectra of target vessel No. 8 at each height. Compared to the ground position, the peak intensity gradually decreased with the increase of the height. It was assumed that most of the target vessel was within the measurement range at the ground position but when it was raised to 2 m, only the tip was within the measurement range because the latter was narrowed by the shielding. Taking the ratio of the Mn-54 and Co-60 intensities, the ratio of Mn-54 was higher at the tip. This is because Mn-54 was more likely to be generated at the tip of the vessel than Co-60. The reason for this can be explained by the difference in the reaction process. Since Mn-54 is produced mainly by the ^{54}Fe (n, p) ^{54}Mn reaction of iron, which is the main component of stainless steel, it is likely to be generated in a high-energy neutron field near the target head. On the other hand, Co-60 is mainly generated by ^{59}Co (n, γ) ^{60}Co of cobalt, which is an impurity in stainless steel, so it is easily generated in a thermal neutron field, and is widely produced, especially near moderators and reflectors.

Table 1. Data for each components at ground position. The target numbering is in the order of production.

	Duration of use	Cooling time (year)	Accumulated power (MWh)
Target No.3	2011/12~2014/6	5.1	2050
Target No.5	2014/10~2015/4	4.3	670
Target No.2	2016/2~2017/7	2.0	1048
Target No.8	2017/10~2018/7	1.0	1812

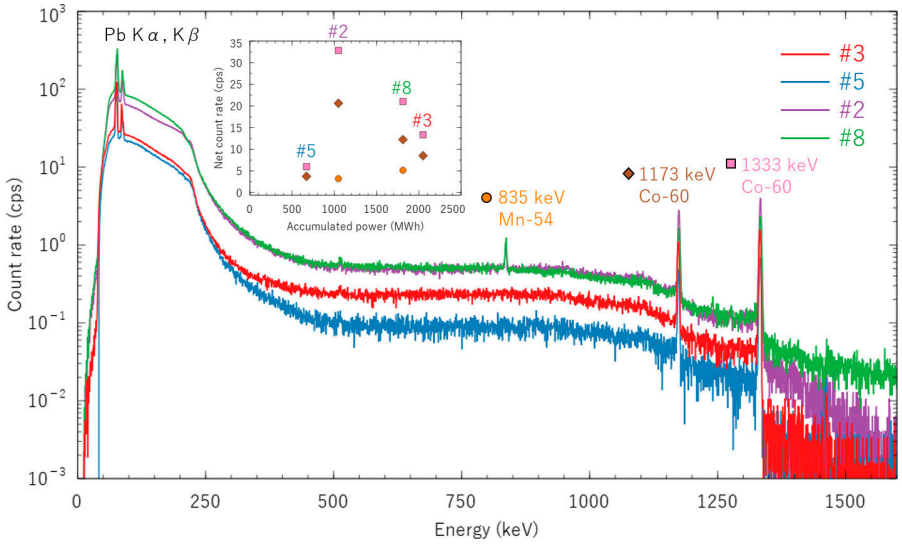

Figure 3. The gamma spectra of the mercury target vessels at ground position. Inset: accumulated power vs. net count rate of the peaks of Mn-54 and Co-60.

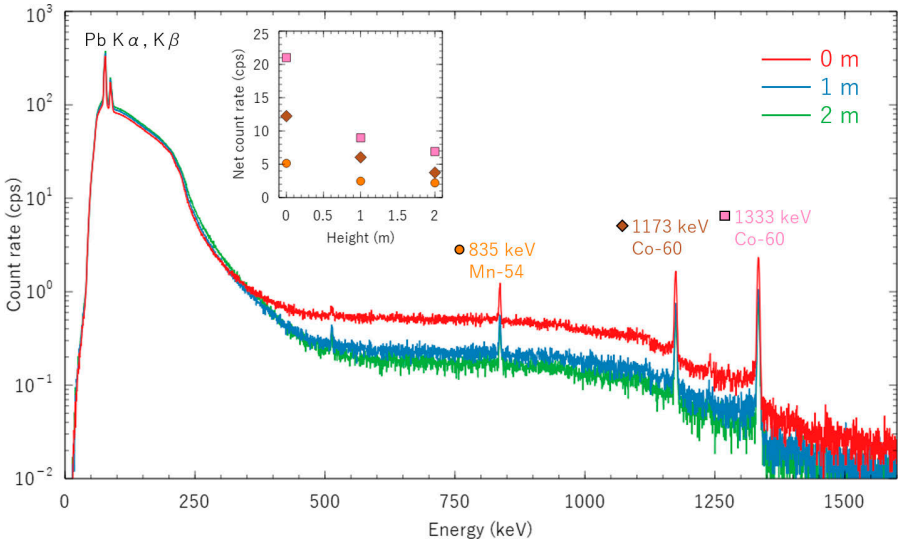

Figure 4. The gamma spectra of mercury target vessel No.8. Inset: height from ground position vs. net count rate of the peaks of Mn-54 and Co-60.

4. Summary

Using the portable Ge semiconductor detector, gamma rays emitted by the used mercury target vessel were measured.

1) Co-60 and Mn-54 were the main nuclides.
2) Mn-54 appeared in those with a short cooling time but disappeared in those with a long cooling time.
3) As the height was changed, the ratio of Mn-54 and Co-60 intensities increased, which was thought to indicate that Mn-54 was generated at the tip.

Acknowledgement

We would like to thank the target group and the remote handling group for helping us with this measurement.

S. Masuda, M. Harada, and H. Nemoto
Neutron Source Section, Materials and Life Science Division, J-PARC Center

The Status of the Cryogenic Hydrogen System

1. Introduction

The cryogenic hydrogen system consists of a helium refrigerator (Brayton cycle, 6 kW refrigeration power, 17 K, 1.5 MPaG and 270 g/s helium flow rate) to produce the liquid para-hydrogen and a hydrogen circulation loop (18 K, 1.4 MPaG, and 185 g/s hydrogen flow rate) to remove the heat deposition in the moderators as shown in Fig. 1.

Since the beginning of 2015, a pressure drop between heat exchangers (HXs) and an adsorber (2nd ADS) in the helium refrigerator gradually increased during every operation, causing degradation of refrigerator's performance [1]. By cleaning the inside of the HXs and replacing an adsorber with a new one (3rd ADS), which was the same as the 2nd one, during the 2016 summer outage, the refrigerator performance was restored [2]. We found out that the local accumulation of oil in membranous form on the felt at the helium entrance side of the 2nd ADS could have caused the pressure drop. The felt material in the 2nd ADS was changed from rock wool to high siliceous glass fiber. In FY2018, we improved the design of the felt material of the 4th ADS in order to prevent oil accumulation [3].

A high-power test with 1-MW beam power, which is the final goal of our facility, was carried out to validate the design values, such as response between heater and accumulator, etc. We also tried to perform an in-situ para-ortho hydrogen fraction measurement for high-power condition under the collaboration with the European Spallation Source (ESS).

2. Exchanging of the ADS

We reapplied rock wool at the helium entrance side for the 4th ADS as felt material, because we also found out that rock wool did not accumulate oil on the felt surface. The piping connection of ADS with the helium refrigerator was changed from welding to flange to make the future replacement easy.

It took about two weeks in September 2019 to replace the 4th ADS in the cold box, as shown in Fig. 2. Then, the activated charcoal in the ADS was regenerated by supplying heated nitrogen gas for one week to prepare for the operation.

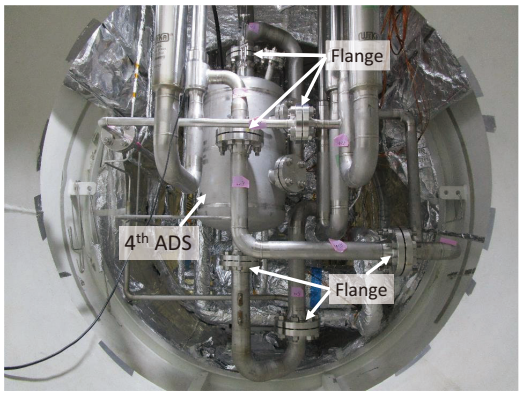

Figure 2. Installed 4th ADS in the cold box.

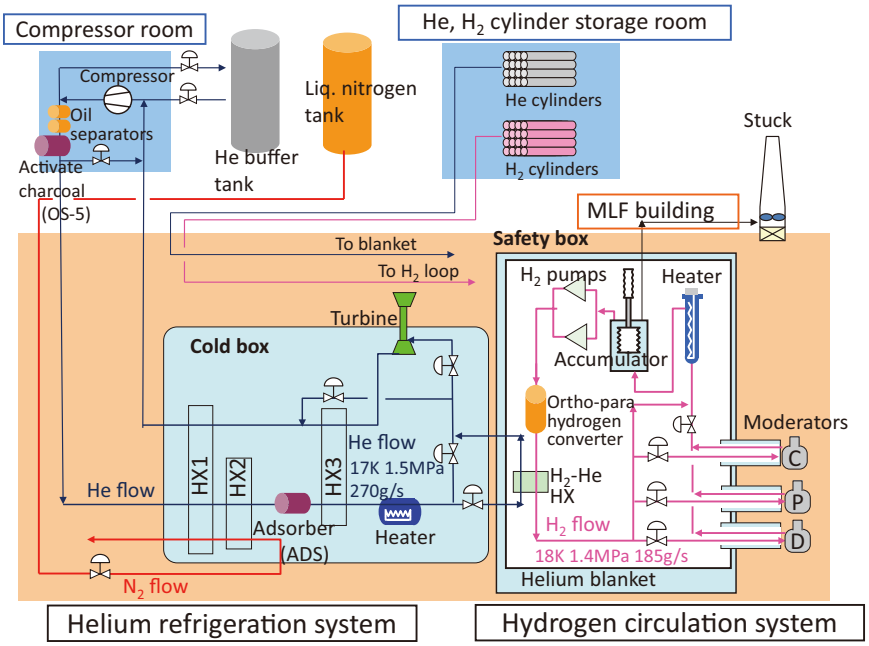

Figure 1. The cryogenic hydrogen system.

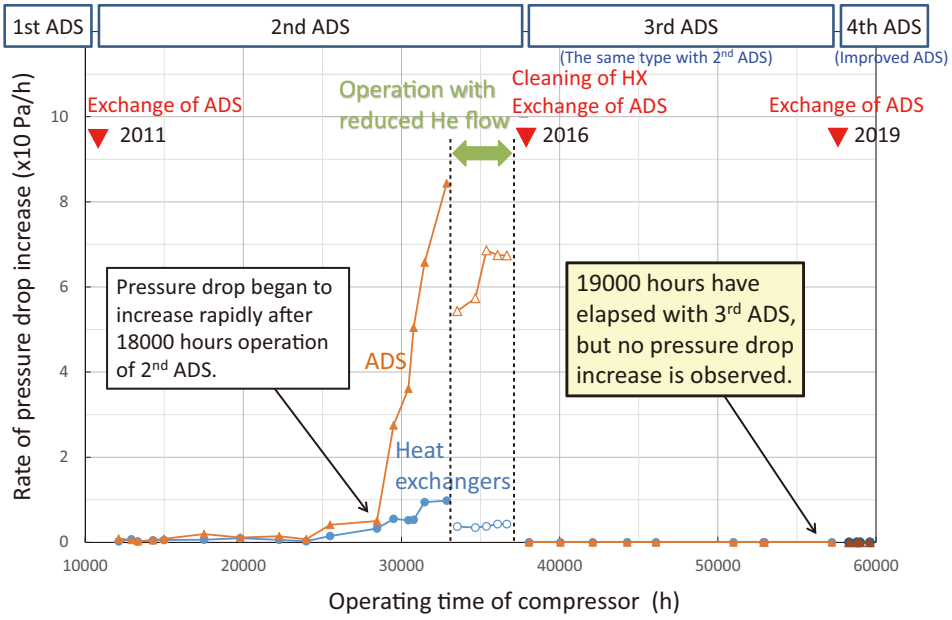

Figure 3. Rate of pressure drop at each operation.

3. Pressure drop trend

The 2nd ADS caused a pressure drop after 18,000 hours of operation, resulting in performance degradation, as shown in Fig. 3. However, the 3rd ADS did not cause a similar problem, even after 19,000 hours of operation until the end of June 2019.

Further pressure drop increase was not observed and the good performance of the refrigerator continued during the operation in the 4th ADS, except for the New Year's holidays.

4. Disassembling of the 3rd ADS

The used 3rd ADS was disassembled to observe the inside contents (felt and active charcoal) and analyze the oil accumulation on them. The surface of the inlet felt in the 2nd ADS had changed to yellowed oil color, as shown in Fig. 4(a), however, the one of the inlet felt in the 3rd ADS was not changed (Fig. 4(b)).

The oil concentration in the felt and charcoal was analyzed by solvent extraction and infrared spectroscopy. The distribution of oil concentration was almost flat in the depth of the inlet felt, showing a difference, compared to that of the 2nd ADS. The total amount of oil was about 5.5 g which was about 1/10 of that of the 2nd ADS. The distribution of oil was also different from that of the 2nd ADS.

These results gave beyond our expectation from previous 2nd ADS results. The details are still under investigation.

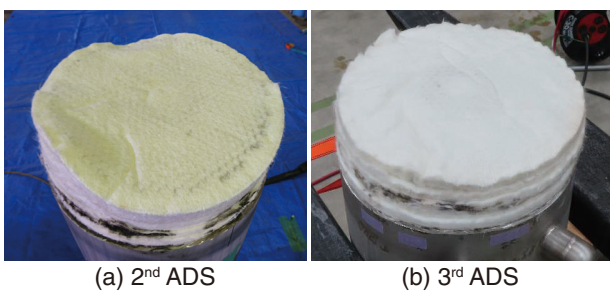

(a) 2nd ADS (b) 3rd ADS

Figure 4. Condition of the inlet felt of the dismantled ADS.

5. Measurement of Para-hydrogen concentration

5.1 1 MW beam injection test

In July 2019, proton beam power equivalent to 1 MW was injected into the spallation neutron source for about 10 hours to validate the original design.

The cryogenic hydrogen system worked well as designed and was able to continue its stable operation. Figure 4 shows the trend of the major parameters of the system at 928-kW operation. In order to compensate the temperature rise and pressure change of the liquid hydrogen caused by the high-power injection, a heater and an accumulator were installed in the cryogenic hydrogen system, as shown in Fig. 1. When the moderator outlet temperature rose with the 1-MW power injection, the heater power at the downstream of the moderators was decreased to counteract the temperature rise and the accumulator absorbed simultaneously the pressure change, as shown in Fig. 5.

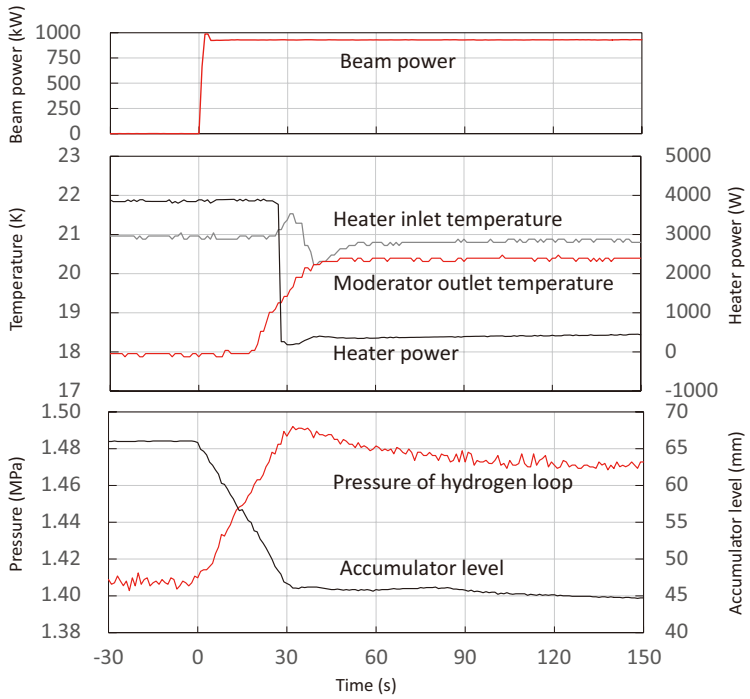

Figure 5. Fluctuation in the hydrogen circulation system at the 928-kW beam injection.

5.2 In-situ measurement of Para-hydrogen fraction

The hydrogen circulation system has an Ortho-para hydrogen converter in order to keep the para-hydrogen fraction of more than 99% at the inlet of the moderator to provide an excellent neutronic performance. It is considered that para to ortho back conversion caused by high neutron irradiation would get worse in the neutronic performance.

One of the urgent issues is to develop a moderator for a high intensity source with MW class power. In order to investigate the para to ortho back conversion due to neutron irradiation, we set up conditions without flowing para hydrogen converter using bypass flow in the hydrogen circulation system. We tried to measure para hydrogen fraction by introducing In-situ Raman spectroscopy measurement in addition to hydrogen gas sampling method (Fig. 6). Finally, we managed to measure the Raman spectroscopy under the condition of 2.4 MW-hour beam operation and without a flowing converter. This was conducted under the collaboration with ESS.

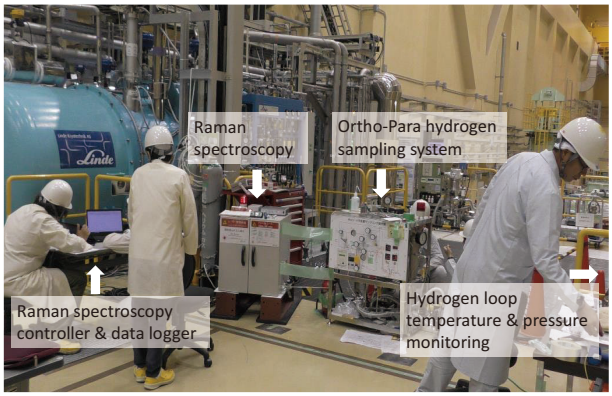

Figure 6. Measurement of the Para-hydrogen fraction.

References

[1] T. Aso et al., MLF Annual Report 2015, 57–58 (2016).
[2] T. Aso et al., MLF Annual Report 2016, 72–73 (2017).
[3] T. Aso et al., Abstracts of CSSJ Conf., Vol.97 47 (2018).

T. Aso, M. Teshigawara, H. Muto, and S. Tanaka
Neutron Source Section, Materials and Life Science Division, J-PARC Center

Neutron Science

Neutron Science Section

1. Introduction

Materials and Life Science Experimental Facility (MLF), one of the leading user facilities in the world, expands gradually its activities [1–4]. Stable 500 kW beam power is being continuously supplied for the user program. And the beam test with the full power of 1 MW to be used in the future operation was performed successfully. The applied proposals have increased to a record number in the proposal round 2019B. A total of 16,204 person-day visitors was recorded in JFY2019.

To continue the constant expansion of the activities in the Neutron Science Section (NSS) and the MLF, we continue our efforts to collaborate not only with domestic, but also with foreign scientific facilities in the fields of personnel, techniques, and research exchange. The first collaboration meeting on neutron instrumentation between China Spallation Neutron Source and the MLF was held at J-PARC in July, 2019. Instrumental collaboration, including researcher exchange, was established between EMU at ANSTO (the Australian Nuclear Science and Technology Organisation) and DNA's two backscattering spectrometers under the arrangement between ANSTO and J-PARC. AMATERAS accepted an AONSA Young Research Fellow (YRF) from Korea. However, the YRF had to suspend his stay at J-PARC due to the COVID-19.

Also, we made significant efforts to communicate with the neutron society through the annual meeting at the MLF about industrial applications (282 participants), the J-PARC symposium (909), the 4th Neutron-Muon School (MIRAI PhD School) (41), and the CROSSroads Workshop (70).

2. Instrumentation

Currently, 21 neutron instruments are under operation. POLANO is the youngest instrument, which just opened for the user program [5–7]. POLANO combines inelastic neutron spectroscopy with polarization analysis and is one of the most complicated but desired instruments, particularly for researches of systems where multiple physical degrees of freedom are entangled. Since the polarization devices on the POLANO are still under commissioning, the proposal with unpolarized neutrons can be currently accommodated (Fig. 1). The polarization system (polarizer, spin flippers, analyzer and guide fields) in the POLANO is an essential set of devices and is continuously developed. We expect that the on-beam polarization tests can be commissioned within the next year.

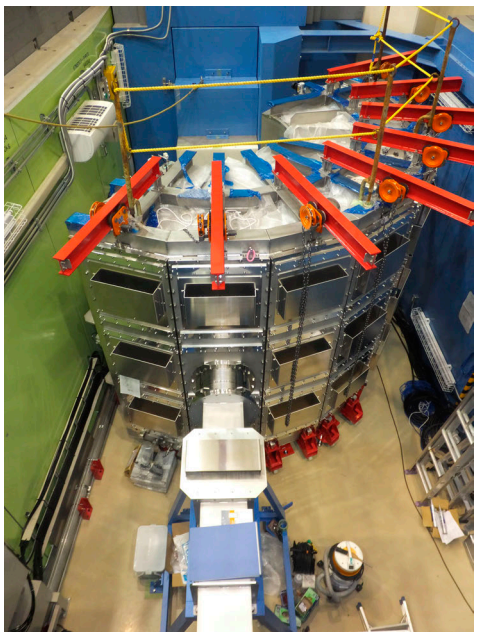

Figure 1. Back view of POLANO (BL23) vacuum chamber right after installation. The spectrometer started a part of user program from 2019.

A brand new T0 chopper developed by the Technology Development Section of the MLF debuted in the 4SEASONS spectrometer (Fig. 2). A T0 chopper is a rotating device that can eliminate unwanted gamma flash and fast neutrons from the target source. For a weak signal experiment, like inelastic scattering, this type of device is indispensable for accomplishing reasonable signal-to-noise ratio. After several years of design and development, the first prototype was installed and used for real beam experiments.

We have many achievements even in the neutron device development. Neutron detectors, sample environment devices, and computing are of great importance for realizing effective and sophisticated experiments; neutron optical devices such as neutron supermirrors and lenses are also essential devices. As shown in Fig. 3, we have successfully developed and installed the focusing mirrors for neutron reflectometer SOFIA (BL16) [8]. This mirror surface was designed as elliptically curved, focusing on the sample position. The peak intensity at the sample position has almost doubled and a much sharper peak profile can be obtained. In addition, new focusing mirrors for GI-SANS have been tested in SHARAKU (BL17), and magnetic lens systems for focusing SANS measurements were tested in TAIKAN (BL15).

Figure 2. Brand new T0 chopper installed into the beamline of 4SEASONS (BL01).

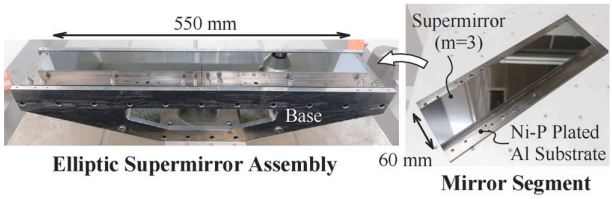

Figure 3. Newly manufactured focusing mirror for neutron reflectometry at SOFIA (BL16).

Thus, we keep upgrading the whole complex, including devices, beam lines, instruments, and even the facility itself to provide the best opportunities for the best science.

3. User program

In fiscal year 2019, the MLF received 326 proposals for 2019A and 444 for 2019B, of which 222 and 224 were approved, respectively. Also, 4 long-term proposals (LTP) were newly adjusted from 9 submissions and totally 17 LTPs were being executed in 2019B. Due to a one-month interruption of the beam delivery after the summer maintenance, all experiments scheduled in this term were carried over to 2020A. In the end of JFY2019, another disaster, the COVID-19 pandemic badly affected the users. Since March, 2020, the government decision of two-week isolation for the travelers from the outbreak nations has strongly reduced the number of foreign users. Even some domestic users could not get a permit to travel to J-PARC from their affiliations, which affected of course the ability of university students to get a degree. Some of those experiments were conducted by the NSS instrument groups and the rest were carried over.

4. Scientific outcome

The research activities in neutron science at the MLF resulted in more than 150 papers and 12 press releases. Inelastic and quasielastic neutron scattering measurements using AMATERAS revealed pressure-induced large entropy changes associated with the molecular order-disorder phase transition in plastic crystals [9]. These findings can be applied to the novel refrigeration technology.

References

[1] H. Takada et al., Quantum Beam Sci., **1** 8 (2017).
[2] K. Nakajima et al., Quantum Beam Sci., **1** 9 (2017).
[3] K. Sakasai et al., Quantum Beam Sci., **1** 10 (2017).
[4] W. Higemoto et al., Quantum Beam Sci., **1** 11 (2017).
[5] T. Yokoo et al., AIP Conf. Proc.,**1969** 050001 (2018).
[6] T. Yokoo et al., EPJ Web Conf., **83** 03018 (2015).
[7] also, see the related articles in this volume
[8] T. Hosobata et al., Optics Express, **27** 26807 (2019).
[9] B. Li et al., Nature, **567** 506 (2019).

Y. Kawakita[1], T. Yokoo[1,2], M. Nakamura[1], S. Itoh[1,2], K. Nakajima[1], and T. Otomo[1,2]
[1]*Neutron Science Section, Materials and Life Science Division, J-PARC Center;* [2]*Institute of Materials Structure Science, KEK*

BL01: 4D-Space Access Neutron Spectrometer 4SEASONS

1. Introduction and statistics

4SEASONS is a direct-geometry time-of-flight neutron spectrometer for thermal neutrons, and one of the Public Beamlines in the MLF [1]. The momentum-energy region for this spectrometer occupies the middle of the momentum-energy space covered by all the MLF spectrometers [2]. In 2019, 24 General Use (short-term) proposals, 1 New User Promotion proposal, and 1 Instrument Group Use proposal, were approved for 4SEASONS. The large number of international users is a characteristic of the user group of 4SEASONS, and they were about a half of the number of users in 2019. Unfortunately, part of the approved proposals was postponed to 2020 due to the COVID-19 pandemic. Conversely, 5 reserved (short-term) proposals were given beamtime to compensate the vacancy. About 60% of the submitted proposals were in the field of magnetism, while the rest of them targeted phonons and other atomic vibrations. The increased volume of research in the latter field is a notable trend at 4SEASONS. As for the outcomes from using the instrument, 10 peer-reviewed papers were published in 2019. 7 were papers about material science, while 3 papers were related to the instrumentation.

2. Instrument upgrade

T0 chopper: 4SEASONS utilizes the so-called T0 chopper to suppress the prompt pulse and high-energy neutron background generated by it. The required rotation speed of the T0 chopper is 50 Hz to accommodate the maximum designed neutron energy of ~300 meV [1], the maximum speed was 25 Hz so far, which degraded the neutron flux at high energies above ~100 meV. Recently, the Technology Development Section of the MLF succeeded in developing a compact T0 chopper running at a speed of 100 Hz. In 2019, 4SEASONS replaced the T0 chopper with this new one (Fig. 1). The new T0 chopper has been in operation since the 2019B round. We observed a significant recovery of the neutron flux at high energies (Fig. 2).

Detectors: 4SEASONS is equipped with a number of ϕ3/4 inch × 2.5 m ^{3}He position sensitive detectors. We have been increasing the number of detectors since the start of the instrument's operation. In 2019, we installed 7 detectors. As a result, the proposed detectors were installed fully except for ones being difficult to install due to physical constraints, and the designed angular coverage of −35° – +130° was achieved. In addition, part of the power supplies and preamplifiers for the detectors were repaired.

Figure 1. The new T0 chopper being installed on 4SEASONS.

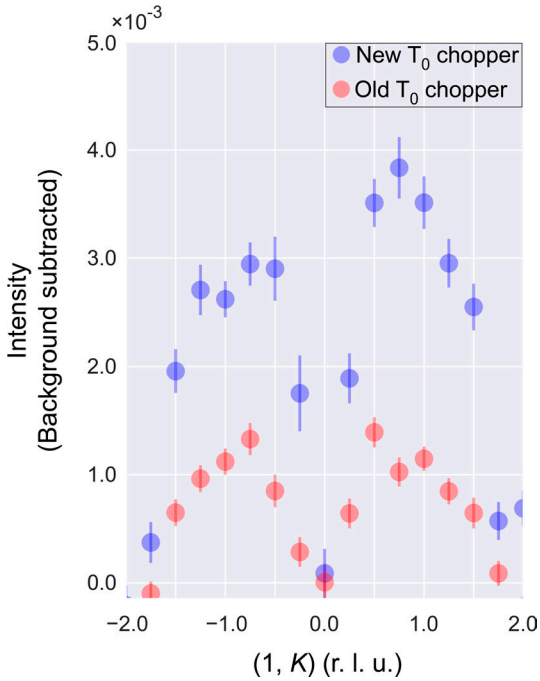

Figure 2. Comparison of the constant-energy profile of the magnetic excitation in $Ba_{0.75}K_{0.25}FeAs_2$ at the energy transfer of 200±10 meV with the old (red) and new (blue) T0 choppers which ran at 25 Hz and 50 Hz, respectively. The utilized incident energy was 500 meV. The intensity was normalized with proton counts and the background intensity was subtracted. The observed intensity was increased by a factor of 2 with the new T0 chopper.

Background suppression: In the vacuum scattering chamber of 4SEASONS, there is a square-shaped beam catcher made of B_4C resin in front of the detectors in the direct beam. The beam catcher was surrounded by an 80-mm long Cd frame to prevent neutrons scattered at the surface of the beam catcher from reaching any part of the detectors. However, we found that the

length of the frame was not sufficient to hide detectors recently added at high scattering angles. Then, in 2019, we extended the frame to 340 mm. We confirmed that the spurious scattering caused by the reflection at the beam catcher was successfully suppressed by this extended frame.

Re-investigation of energy resolution and flux: The energy resolution and flux of a direct-geometry time-of-flight spectrometer strongly depend on the incident energy and the rotation speed of the monochromating chopper. At 4SEASONS, the Fermi chopper was replaced with a new model in 2015, which has a short slit-package consisting of 0.4-mm wide and 20-mm long slits [3]. Although the resolution and flux have been analytically and numerically investigated with the new chopper, the systematic investigation has not been sufficient. Accordingly, in 2019, we re-investigated the energy resolution and intensity of the elastic scattering using incoherent scattering of vanadium. Based on the result, simple computing tools to calculate the energy resolution and intensities were developed, which should be useful for the users to decide about the experimental conditions [4].

Acknowledgements

We thank K. Inoue and W. Kambara for their support and advice. We also thank N. Murai for providing unpublished data. The instrumentation works described here were supported by the engineers of the Neutron Science Section and the Technology Development Section of the MLF.

References

[1] R. Kajimoto et al., J. Phys. Soc. Jpn. **80**, SB025 (2011).
[2] H. Seto et al., Biochim. Biophys. Acta, Gen. Subj. **1861**, 3651 (2017); K. Nakajima et al., Quantum Beam Sci. **1**, 9 (2017); R. Kajimoto et al., Physica B **562**, 148 (2019).
[3] M. Nakamura and R. Kajimoto, JPS Conf. Proc. **1** (2014); R. Kajimoto et al., J. Phys.: Conf. Ser. **1021**, 012030 (2018).
[4] R. Kajimoto et al., J. Neutron Res., pre-press, doi:10.3233/JNR-200146.

R. Kajimoto[1], M. Nakamura[1], K. Kamazawa[2], Y. Inamura[1], K. Iida[2], K. Ikeuchi[2], and M. Ishikado[2]
[1]Neutron Science Section, Materials and Life Science Division, J-PARC Center; [2]Neutron Science and Technology Center, CROSS

Current Status of BL02 DNA in 2019

1. Introduction

DNA is a TOF backscattering spectrometer designed to elucidate atomic and molecular dynamics [1]. DNA can provide micro-eV energy resolution measurements over a broad energy range of $-500\ \mu eV < E < 1500\ \mu eV$, thanks to the near-backscattering geometry of the instrument and its pulse-shaping options. In addition, back-coated Si analyzers with Gd or Gd_2O_3 neutron absorber provide an extra high signal-to-noise ratio of around 10^5, which enables the detection of small scattering amplitudes or signals from small quantities of samples. The accessible momentum transfer range is from 0.08 to 1.86 $Å^{-1}$ by using Si111 analyzer mirrors.

A hot topic in 2019 was the start of a close collaboration between the EMU back scattering spectrometer with a Doppler shifter at ANSTO and DNA. The DNA team conducted EMU experiments with less than 1 micro eV resolution in July and August for ten days. On the other hand, Dr. Nicola de Souza, an EMU instrument scientist, joined our commissioning work for two months, from October to November. Although he was supposed to perform his own experiments by using DNA, an unexpectedly prolonged summer maintenance term unfortunately prevented him from doing so.

The number of peer-reviewed papers from DNA was 8 in 2019, almost at the average yearly level since 2017.

2. User Program in the 2019A and 2019B periods

8 General Proposals (GP) and 10 GPs (including 3 New User Promotions (NUP)) were approved for 2019A and 2019B, respectively. The portion of approved beamtime from all requested beamtime was 59% for 2019A and 29% for 2019B. As in 2018, there was a tendency for the competition to be higher in the B-period (2.9) than in the A-period (1.5). Additionally, two reserved proposals were also conducted in 2019A. One Long-Term Proposal (LTP) has been newly adopted from 2019B. In total, four LTP's ran at BL02.

Due to delay of the beam delivery from November to December, the beam operation was canceled for a total of 32.5 days. The experiments scheduled for this term were carried over to 2020. Other than this unexpected beam delay, the users enjoyed a stable 500-kW beam in 2019. In March, the pandemic of COVID-19 started to affect the experiments at DNA.

The 4th Neutron and Muon School was held from October 28 to November 2 together with the MIRAI PhD School (MIRAI: the consortium between Swedish and Japanese universities). At DNA, 4 students studied sample installation into the cryo-furnace and data analysis on the molecular dynamics of water in Nafion membranes.

Figure 1. A photo of four students of the Neutron and Muon School & MIRAI PhD School together with four instrument scientists, including a visiting researcher, Dr Nicolas de Souza, from ANSTO.

3. Beamline activities

Beamline

Additional Si311 analyzer mirrors were installed at scattering angle (2θ) of $-126 < 2\theta < -90$, which extended the maximum momentum transfer range from 2.67 to 3.40 $Å^{-1}$. The designed energy resolution of 12 μeV for the Si311 analyzer was confirmed with a pulse shaping chopper rotating at 300 Hz. However, some spurious peaks were observed, presumably due to the scattering from the aluminum wall of the BL02 cryostat. We plan to install radial collimators in 2020 to suppress those scatterings.

When the MLF successfully achieved a continuous 10.5-hour operation at the designed largest beam power of approximately 1 MW on July 3, test measurements were carried out to demonstrate the performance of DNA at 1 MW. Figure 2 shows the temperature dependence of the elastic intensity and elastic incoherent structure factor (EISF) of gelatinized starch with cooling rate of 1.4 degree/min. Clear increases at about −4°C were observed for both parameters, which indicated the freezing of water. This suggests that the water in the starch is close to the properties of bulk water, despite the fact that it interacts with the starch. Quantitative analysis of QENS data is possible in even relatively rapid temperature scans. The 1-MW beam power is useful to analyze the QENS spectra to study the dynamics of non-equilibrium systems.

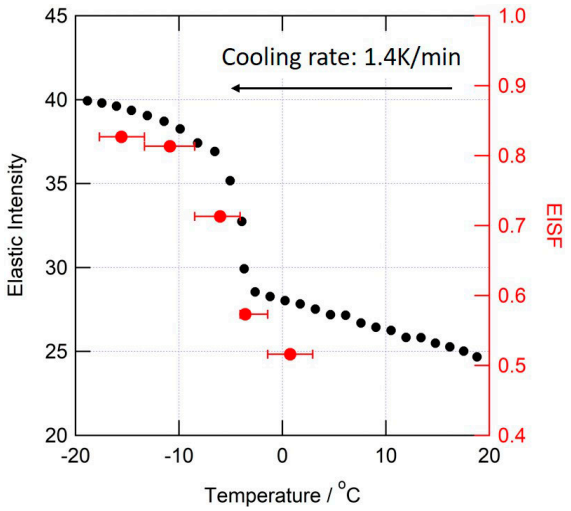

Figure 2. Temperature dependence of the elastic intensity and elastic incoherent structure factor (EISF) of gelatinized starch measured at a beam power of approximately 1 MW with cooling rate of 1.4 degree/min.

Development of sample environments

In addition to the standard sample environment of the cryo-furnaces, a dilution refrigerator, a sample changer with twenty samples, and a vapor-controlled system were under development and commissioning. Two brand new sample sticks for the cryo-furnaces were also developed. After the successful observation of a very weak QENS signal of Li self-diffusion [2], there has been strong demand for *in situ* measurements of Li conduction under electric field. With the help of Professor Kazuhiro Mori in Kyoto University, we developed a special sample stick which can make a battery in noble gas atmosphere and apply an electric field at 300°C. The other sample stick was designed to automate the sample change; it has three sample positions encoded and enables us to conduct fully automatic measurements by controlling it from IROHA2 [3].

Software

The software, which controls DAQ, choppers and sample environment equipment, was updated from IROHA to IROHA2 [3], developed by the computational team in the MLF. The update enables the automation of measurement and facilitates the integration of new devices into the control system.

4. Future plans

In addition to the further installation of Si311 analyzer mirrors extending the momentum transfer range to 3.8 $Å^{-1}$, new Si111 analyzer mirrors have been fabricated since some of the installed mirrors have been already damaged after being first installed in 2012. Correspondence against such an aging problem is essential to keep the world-class performance of DNA.

5. Outreach activities

There were several chances to advertise the DNA performance at international conferences, such as the 3rd J-PARC Symposium (J-PARC2019) held at Tsukuba Epochal on September 23–26, the 3rd Asian Oceanian Conference on Neutron Scattering (AOCNS2019) held in Kenting, Taiwan on November 16–21 and the Material Research Meeting (MRM2019) held in Yokohama on December 10–14.

At J-PARC2019, together with the current status of DNA, introducing its performance and future upgrade plan, the following topics in our research and development were presented: (1) water dynamics of double network polymers in a primally hierarchical structure, (2) position dependency of the scattered intensity of the DNA spectrometer, (3) Position-Encoded Automatic Cell Elevator for DNA, (4) commissioning for QENS experiments at pressures of up to 200 MPa (a new DNA sample environment for high pressures), (5) in-situ QENS of Nafion Membrane with water vapor pressure control system, (6) manufacturing a double-cylindrical quartz cell, and (7) determination of corrosion of aluminum-based containers.

6. Others

Mr. Makoto Kobayashi, an engineer of DNA, finished his contracted term in March 2020.

References

[1] K. Shibata et al., JPS Conference Proceedings, **8** 036022 (2015).
[2] K. Mori et al., Phys. Rev. Appl., **4** 054008 (2015).
[3] T. Nakatani and K. Moriyama, MLF Annual Report 2016, 130 (2017).

Y. Kawakita[1], M. Matsuura[2], T. Yamada[2], T. Tominaga[2], M. Kobayashi[2], and H. Nakagawa[1,3]
[1]Neutron Science Section, Materials and Life Science Division, J-PARC Center; [2]Neutron Science and Technology Center, CROSS; [3]Materials Sciences Research Center, JAEA

Current Status of iBIX (BL03) in 2019

1. Introduction

By the complementary use of neutron diffraction data, which include more information about hydrogen atoms, and X-ray diffraction data, which include more information about non-hydrogen atoms (such as C, O, N, and S), we can obtain the structure information of all atoms in the protein samples. This is particularly important, because understanding the enzyme chemistry of proteins at the atomic level requires the visualization of hydrogen atoms on active sites and water molecules. The IBARAKI biological crystal diffractometer called iBIX was constructed to realize high throughput single crystal neutron structure analysis for mainly biological macromolecules in various life processes [1, 2]. A new photon-counting two-dimensional detector system using scintillator sheets and wavelength-shifting fiber arrays for the X/Y axes was developed with the cooperation of JAEA to realize high measurement efficiency of the iBIX. In 2019, the iBIX diffractometer had 34 detectors and was available for user experiments on biological macromolecules and polymer samples, supported by the Frontier Research Center of Applied Atomic Sciences, Ibaraki University. The specifications of the iBIX are shown in Table 1.

Table 1. Specifications of iBIX.

Moderator	Coupled
Wavelength of incident neutron (Å)	0.7–4.0 (1st frame) 4.0–8.0 (2nd frame)
Neutron intensity (n/s/mm^2) (@1 MW)	0.7×10^6
L_1 (m)	40
L_2 (mm)	491
Solid angle of detectors (% for 4π)	22.0
Detector covered region (deg.)	15.5–168.5
Detector size (mm^2)	133 × 133
Detectors pixel size (mm^2)	0.52 × 0.52
No. of detectors	34

2. Current status

In 2019, J-PARC was operated regularly at an accelerator power of 500 kW. We were able to collect a full data set of biological macromolecules for neutron structure analysis with around 2.0 Å resolution in about 8 days by using the iBIX at the accelerator power of 500 kW. The typical crystal volume of the sample measured by the iBIX was 0.5–2.0 mm^3. If the accelerator power reaches 1 MW, the total measurement time of the sample size will be reduced to half of the previously necessary time or the sample size can be reduced to half size with the same measurement time.

In 2019, 9 test measurements for a proposal of an innovative research project of the Ibaraki Neutron Beamline (2019A: 3, 2019B: 6) and 5 test measurements for a proposal of a leading research project of the Ibaraki Neutron Beamline (2019A: 2, 2019B: 3) were performed using the iBIX. And then, 6 biological macromolecules and 2 polymer samples were provided to the full data collection for neutron structure analysis. 1 test measurement for a proposal of the MLF general use was performed but it carried over to the next year. Trouble of the air-conditioning equipment for the experimental hatch of the iBIX and a target trouble of the MLF occurred in 2019A and 2019B, respectively. So, the total amount of beam time for user experiments was reduced in both 2019A and B. If the accidents did not happen, 2 or 3 more protein samples could have been provided to the full data collection.

Figure 1. Data acquisition system.

3. Development

The current data acquisition (DAQ) system was installed in FY2013. The maintenance contract of all components of DAQ system has expired in the end of FY2019. A part of the DAQ system (storage, KVM drawer, uninterruptible power supply and network switch) was renewed in the end of FY2019. The new system should have faster data reading and writing function and higher capacity storage than the previous one because the iBIX needs to collect the diffraction data in the 1-MW operation of the accelerator in the near future. The large scale parallel access storage of the MLF advanced computational environment (MLF-ACE) was connected to the iBIX DAQ system as the main data storage for diffraction experiments by the iBIX, because the network, storage and connection of the MLF-ACE are redundant. To achieve high data redundancy, a large amount of event data is recorded on the storage of the MLF-ACE and local storage for 4 DAQ computers of the iBIX DAQ system at almost the same time using the newly developed components of DAQ-MW. By the end of March, we completed their installation and at the same time, the system became available for user experiments.

4. Future plans

It has been over 10 years since the instrument of the iBIX was installed on the beam line, some components need replacement due to age deterioration. Next year, 4 DAQ computers will be replaced and connected to the iBIX DAQ system and storage of the MLF-ACE. In the future, the accelerator power of J-PARC will increase to about 1 MW. The iBIX should be available regularly for full data-set measurement of samples with a volume of less than 1 mm^3. We will continue to develop the data reduction software and the beam line instruments to improve the measurement efficiency and the accuracy of intensity data obtained from small samples.

References

[1] I. Tanaka, K. Kusaka, T. Hosoya, N. Niimura, T. Ohhara, K. Kurihara, T. Yamada, Y. Ohnishi, K. Tomoyori and T. Yokoyama, Acta Cryst., D**66** 1194 (2010).

[2] K. Kusaka, T. Hosoya, T. Yamada, K. Tomoyori, T. Ohhara, M. Katagiri, K. Kurihara, I. Tanaka and N. Niimura, J. Synchrotron Rad., **20** 994 (2013).

K. Kusaka[1], T. Yamada[1], N. Yano[1], T. Hosoya[1], I. Tanaka[1], and T. Ohhara[2]

[1]Frontier Research Center for Applied Atomic Sciences, Ibaraki University; [2]Neutron Science Section, Materials and Life Science Division, J-PARC Center

Stellar Neutron Capture Cross Section of ^{191}Ir

1. Introduction

It is widely known that among various nucleosynthesis processes, the slow neutron capture process (*s*-process) involves the most stable isotopes. In addition to the stellar temperatures at energy levels of 25 keV and 30 keV, which have been proposed as the condition in the *s*-process, another recently suggested factor involves lower temperatures such as at the 8 keV level [1]. In order to experimentally evaluate the *s*-process models, neutron capture cross sections have been measured for a neutron energy of approximately 30 keV. The reliable nuclear data in wider neutron energy ranges, described above, are important to improve the accuracy of the *s*-process models. In particular, at branching points, where the neutron capture reaction competes with the β^- decay in the *s*-process, the neutron capture cross sections significantly affect the abundances of heavier nuclei. Iridium-192 is one of the branching point nuclei in the *s*-process and its daughter nuclide, ^{192}Pt, is the heaviest *s*-only isotope synthesized only in the *s*-process (Fig. 1). The abundant ^{192}Ir and ^{192}Pt play important roles as probes to verify the accuracy of the statistical calculation of neutron cross sections for heavier elements. Thus, the accurate neutron capture cross-section data for isotopes around ^{192}Pt have been required in the relevant neutron energy region.

Previously, Macklin and Koehler measured the neutron capture cross sections of ^{191}Ir in the stellar neutron energies from a few keV to about 30 keV using the time-of-flight (TOF) method [2, 3]. The discrepancies in their results, however, reached approximately 200% in the stellar neutron energies. Moreover, these uncertainties were not evaluated in Ref. 2 and were approximately 20% in Ref. 3. The impurities in the samples might have caused the discrepancies, although their experiments were not described in detail.

We, therefore, decided to measure the neutron capture cross section of ^{191}Ir using the TOF method in the range of the stellar neutron energies and an ^{191}Ir enriched sample.

2. Experiments

Pulsed neutrons were generated by the spallation reaction of a mercury target at Japan Proton Accelerator Research Complex (J-PARC). The proton pulses were shot at the target every 40 ms and the proton beam power was approximately 530 kW. The pulsed neutrons were slowed down in a liquid hydrogen moderator and extracted in the form of neutron beam to feed the Accurate Neutron Nucleus Reaction measurement Instrument (ANNRI) at the Materials and Life Science Experimental Facility of J-PARC. The present experiments used the TOF measurement system with NaI detectors located at a distance of 27.9 m from the moderator. All our samples had a shape of either a pellet or a foil and were wrapped with fluorinated ethylene propylene (FEP) film, which is neutron-insensitive.

^{191}Ir metal of 99.9% in purity and of 90.2 mg in weight was used as a sample. In addition, a ^{197}Au sample was used for energy calibration, and also carbon and ^{208}Pb samples for estimation of the neutron scattering influence, the FEP film (blank) sample for estimation of the background level.

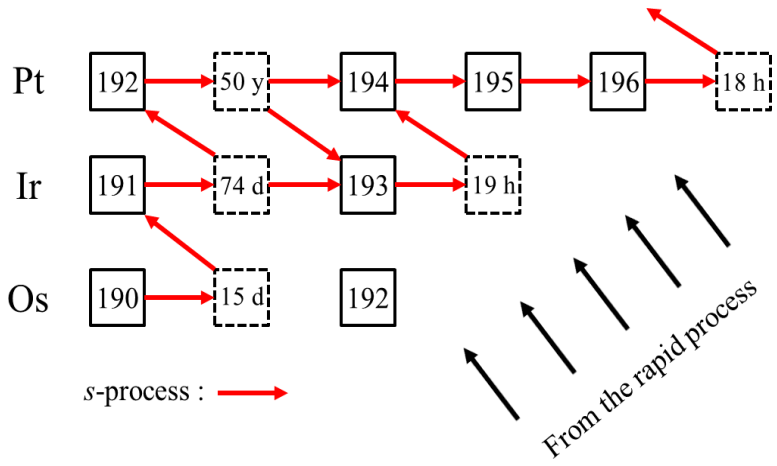

Figure 1. The *s*-process network around ^{192}Ir.

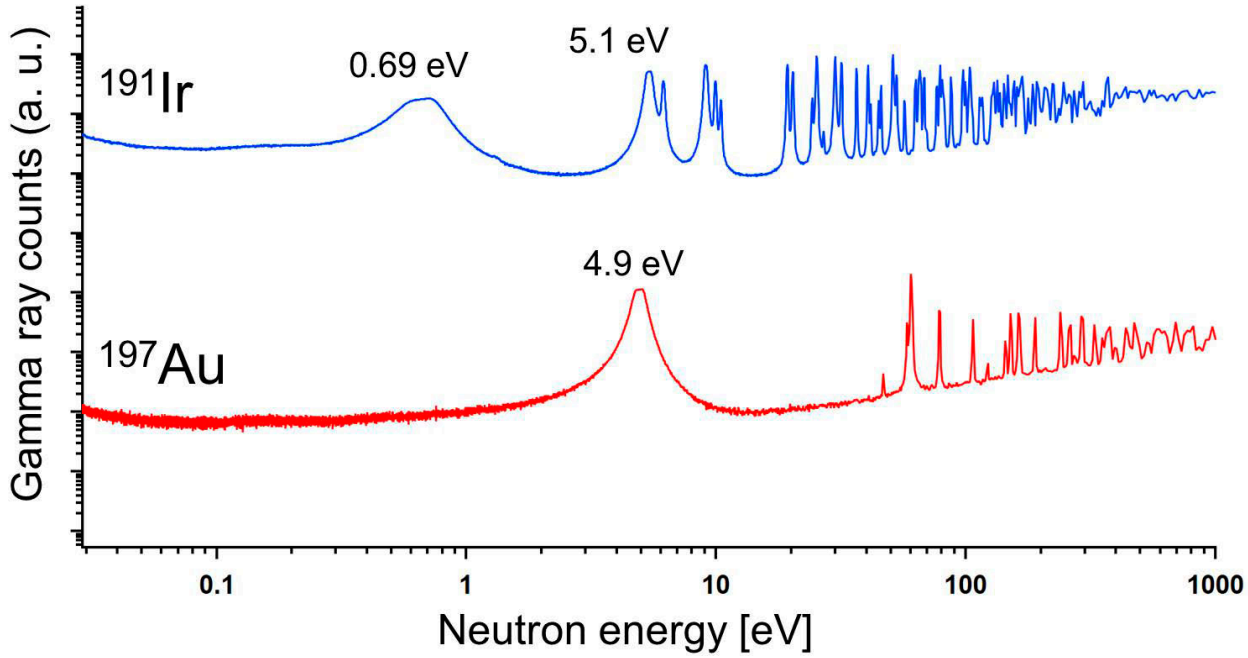

Figure 2. TOF spectra obtained with the NaI detectors equipped with the ANNRI.

3. Results

The obtained TOF spectra of the ^{191}Ir and ^{197}Au samples, corrected by the number of proton shots and the dead time, are shown in Fig. 2. After calibrating the incident neutron energies with the resonances of ^{197}Au, several resonance peaks of ^{191}Ir are clearly observed. The resonances of ^{191}Ir at neutron energies of 0.69 eV and 5.1 eV are consistent with these neutron energies on reported data [4]. The TOF spectra of the other samples were also successfully obtained.

4. Conclusions

We performed the TOF experiment in order to determine the neutron capture cross section of ^{191}Ir in the stellar neutron energy range. The TOF spectrum caused only by ^{191}Ir was obtained without the influence of impurities by using the ^{191}Ir enriched sample. Hereafter, the obtained data of the carbon, ^{208}Pb and the blank samples will be used to correct data as follows: the scattering component and the self-shielding effect in the samples. This analysis is now in progress.

This work was supported in part by Grants-in-Aid for Scientific Research (JP17H01076).

References

[1] R. Gallino et al., Astrophys. J., 497, 388 (1998).
[2] R.L. Macklin et al., Report LA-7479-MS, LOS Alamos Scientific Laboratory (1978).
[3] P.E. Koehler and F. Käppeler, Nuclei in the Cosmos III (Proceeding of American Institute of Physics1994).
[4] H.J. Stone et al., Nucl. Instrum. Methods Phys. Res. A, 547 601 (2005).

M. Tsuneyama[1,2], M. Segawa[2], S. Endo[2], S. Nakamura[2], M. Maeda[2], A. Kimura[2], and Y. Toh[2]
[1]Nihon Advanced Technology, Co. Ltd.; [2]Nuclear Science and Engineering Center, JAEA

Status of Fundamental Physics Beamline BL05 (NOP) in 2019

1. Introduction

"Neutron Optics and Physics (NOP/BL05)" at MLF in J-PARC is a beamline for studies in the field of fundamental physics. The beamline is divided at the upstream into three branches, the so-called Polarized, Unpolarized, and Low-Divergence branches, used in different experiments in a parallel way [1–2].

A neutron lifetime measurement is conducted at the Polarized beam branch with a spin flip chopper. Pulsed ultra-cold neutrons (UCNs) by a Doppler shifter are available at the Unpolarized beam branch. At the Low-Divergence beam branch, the search for an unknown intermediate force is performed by measuring neutron scattering with rare gases. The beamline is used also for R&D of optical elements and detectors.

2. Measurement of the neutron lifetime, and the cross section of ^{14}N(n,p)^{14}C reaction

A neutron decays into a proton, an electron, and an antineutrino. The decay lifetime is an important parameter for the unitarity of the CKM matrix and also for the primordial big bang nucleosynthesis. However, recently reported values for the neutron lifetime deviate significantly from the systematic uncertainties. An experiment to measure the neutron lifetime with a pulsed beam is ongoing at BL05 (NOP). The lifetime is measured as a ratio of the electron events of the neutron decay to the ^{3}He(n,p)^{3}H events caused by ^{3}He gas precisely doped in a time projection chamber (TPC). By analyzing the data, we obtained our first preliminary result of the neutron lifetime as $\tau_n = 898 \pm 10$ (stat.) $^{+15}_{-18}$ (sys.) [3] (Fig. 1).

The TPC was made for measurement of the neutron decay and ^{3}He(n,p)^{3}H. However, it is also applied for measurements of the other nuclear reactions. We measured the thermal neutron cross section of the ^{14}N(n,p)^{14}C reaction [5]. Nitrogen makes up 78% of the atmosphere and is essential for almost all living organisms because it is found in amino acids. The ^{14}N(n,p)^{14}C is a reaction, which absorbs thermal neutrons and emits protons. This reaction, which is produced by the absorption of atmospheric neutrons, is used for radiocarbon dating and is the main cause of the neutron dose equivalent in human bodies. It also plays an important role in the CNO cycle, which occurs during stellar evolution. This reaction is also used as a neutron flux monitor [6]. The cross section has been measured for a long time, but the accuracy of the cross sections has been limited to about 3% due to the number of targets. We measured the ^{14}N(n,p)^{14}C thermal neutron cross section with high precision using a gas-handling system, a spin flip-chopper, and the TPC developed for neutron lifetime experiments. The experiment was performed by mixing N^2 and ^{3}He gases with high accuracy and counting the reaction number ratios. Compared with the conventional solid target, the uncertainty of the target quantity was reduced by using a gas target, and the reaction cross section was successfully determined to be 1.868(7) barn with an uncertainty of 0.4%. This is about five times more accurate than the weighted mean of the previous measurements (Fig. 2).

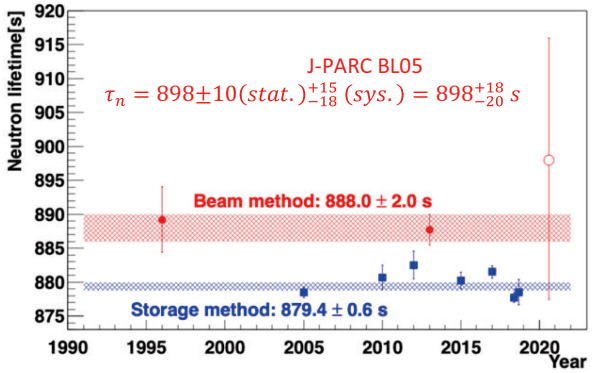

Figure 1. The neutron lifetime measurements in the 2018 PDG [4], the storage methods are denoted as blue squares, the beam method is shown as closed red circles. The J-PARC result is shown as a red open circle [3].

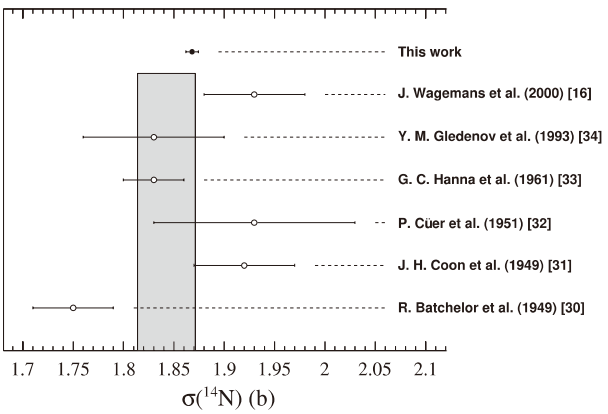

Figure 2. Experimental results of the cross section of the ^{14}N(n,p)^{14}C reaction at the neutron velocity of 2200 m/s. The weighted mean from the previous results (open circles) and gray band. The measurement result from this work (closed circle) [5].

3. Measurement of the total neutron scattering cross section of noble gases

The thermal neutron scattering cross sections are fundamental parameters for nuclear properties. In particular, the s-wave scattering length of n-^{4}He is important because it limits the three nuclear forces. In the present work, we have performed comprehensive measurements of neutron scattering by noble gases and derived the scattering cross section ratios for He, Ar, Kr, and Xe with respect to Ne [7]. The experiment was carried out using the unknown short-range force measurement system at BL05 [8]. Scattered neutrons from the noble gas encapsulated in a cell were detected with a position-sensitive neutron detector. The ratios of the scattering cross sections of Ar/Ne, Kr/Ne, and Xe/Ne were in agreement with the literature values [9] in the momentum transfer region of 1–7 nm^{-1}. However, the value for He/Ne was 11.3% (7.6σ) smaller from that obtained from the neutron interferometry (Fig. 3). The given results and their consistency with other n-^{4}He measurements suggested that there was an unaccounted systematic uncertainty in the scattering length of ^{4}He in the literature. It is notable that the newly obtained scattering length of ^{4}He by the neutron interferometry was close to our value [10].

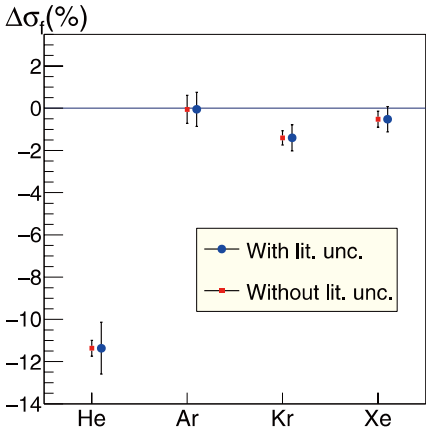

Figure 3. The percentage difference of the thermal neutron scattering cross sections of noble gases between the measured value at BL05 [7] and that in the literature [9].

References

[1] K. Mishima et al., "Design of neutron beamline for fundamental physics at J-PARC BL05", *Nucl. Instruments Methods Phys. Res. Sect. A*, vol. 600, no. 1 (2009) 342–345.

[2] K. Mishima, "J-PARC Neutron fundamental physics beamline (BL05/NOP)," *Hamon Neutron Netw. news*, vol. 25, no. 2 (2015) 156–160.

[3] K. Hirota et al., "Neutron lifetime measurement with pulsed cold neutrons", arXiv:2007.11293 (2020)

[4] M. Tanabashi et al. (Particle Data Group), Phys. Rev. D,98 (2018) 030001.

[5] R. Kitahara et al., "Improved determination of thermal cross section of ^{14}N(n,p)^{14}C for the neutron lifetime measurement", Progress of Theoretical and Experimental Physics (2019) 093C01.

[6] F. Issa et al., "Characterization of thermal neutron beam monitors." Physical Review Accelerators and Beams 20.9 (2017) 092801.

[7] C. C. Haddock et al., "Search for deviations from the inverse square law of gravity at nm range using a pulsed neutron beam", Phys. Rev. D 97 (2018) 062002.

[8] V. F. Sears, "Neutron scattering lengths and cross sections.", Neutron news 3.3 (1992) 26–37.

[9] C. C. Haddock et al., "Measurement of the total neutron-scattering cross-section ratios of noble gases of natural isotopic composition using a pulsed neutron beam", Phys. Rev. C 100 (2019) 064002.

[10] R. Haun et al., "Precision measurement of the neutron scattering length of ^{4}He using neutron interferometry", Phys. Rev. Lett. 124.1 (2020) 012501.

K. Mishima[1,2] on behalf of NOP collaboration

[1]*Neutron Science Section, Materials and Life Science Division, J-PARC Center;* [2]*Institute of Materials Structure Science, KEK*

BL06: Commissioning Status of Village of Neutron Resonance Spin Echo Spectrometers (VIN ROSE)

1. Introduction

BL06 consists of two types of resonance neutron spin echo (NSE) spectrometers, a modulated intensity by zero effort (MIEZE) instrument and a neutron resonance spin echo (NRSE) instrument. NSE is a variety of inelastic and quasi-elastic neutron scattering methods with fine energy resolution [1]. Because the energy resolution of the energy transfer measurement in the NSE technique is not limited by the energy spectrum of the incoming neutrons, a moderately (10–15% FWHM) mono-chromatic neutron beam can be acceptable. In addition, the intermediate scattering function can be directly derived by NSE, so the method is suitable for investigating slow-relaxation dynamics in condensed matter, and high-intensity and high-energy-resolution NSE spectrometers have been developed and built [2].

Since 2011, Kyoto University and The High Energy Accelerator Research Organization (KEK) have been working jointly on the beam line construction. The NSE spectrometers are equipped with neutron resonance spin flippers (RSFs), which enable us to replace large magnetic precession fields with low guide fields, thus making possible the downsizing and adjacence of the two spectrometers [3].

In this report, the status of the MIEZE and NRSE spectrometers at BL06 in FY2019 is presented.

2. Commissioning status at BL06 in FY2019

Since the 2017B proposal round, the user program has started partially with the MIEZE spectrometer, which will be described in detail in the following section. A two-dimensional neutron detector with a 32 × 32 cm detecting area is now under development for the MIEZE spectrometer, which is adopting a ZnS/^{6}LiF scintillator and multi-pixel photon counters (MPPC). Figure 1 displays a photograph of the detector mounted at the spectrometer (top), the measured pixel sensitivity (middle), and the scattering profile of a glassy carbon plate as a secondary standard (bottom). We plan to start using the detector from FY2020.

At the NRSE spectrometer, used for fine-energy resolution, commissioning of devices, such as RSFs and two-dimensional ellipsoidal neutron-focusing mirrors, were intensively conducted [4]. The NiC/Ti two-dimensional ellipsoidal neutron-focusing supermirrors are also under development in close collaboration with the RIKEN center for advanced photonics [5]. The optical design is 1250 mm semi-major axis and 65.4 mm semi-minor axis with 900 mm length. In Fig. 2, one example of on-beam tests is shown. More than $5Q_c$ reflection, where xQ_c means that the critical angle of Ni (Q_c = 0.22 Å^{-1}) is x times larger, can be achieved, and also, the beam can be focused properly with the mirror. This achievement will be utilized in the development of the NRSE spectrometer.

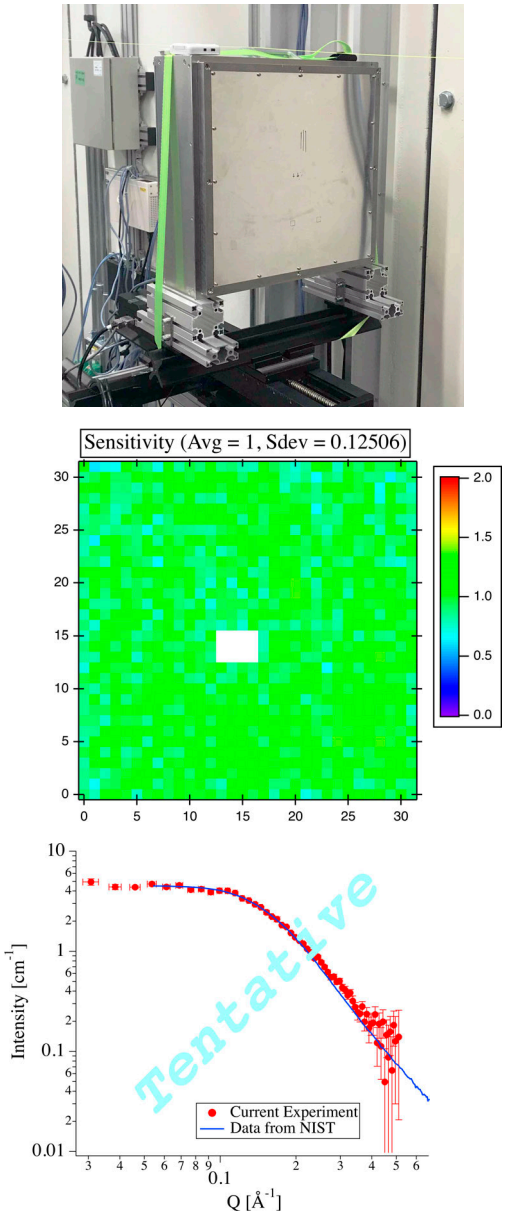

Figure 1. Top: a picture of the detector. Middle: the observed sensitivity of the detector. Bottom: the observed scattering profile of a grassy carbon as a standard sample compared with the data from NIST.

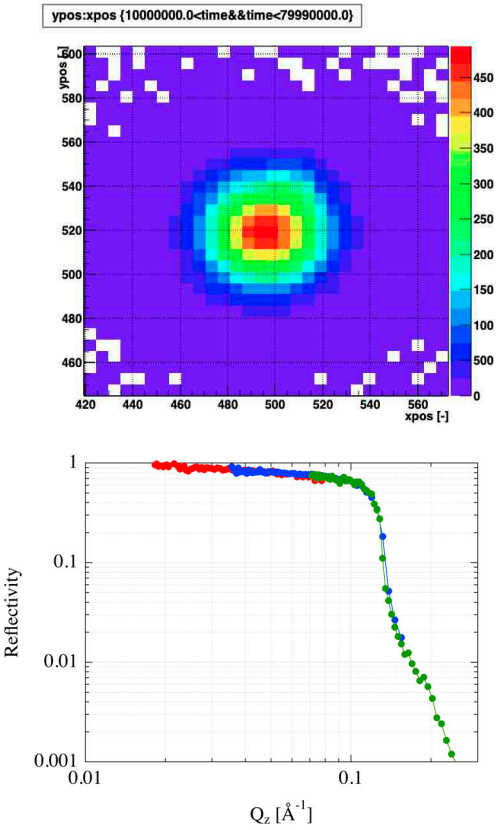

Figure 2. Top: a beam profile at the focal point, where 10 scales correspond to 1 mm. Bottom: the observed reflectivity of the mirror.

3. User Program

Currently, the MIEZE spectrometer can be opened for the public users. The great advantage of the instrument is that a relatively strong magnetic field in any direction can be added in the sample position, while such conditions are impossible in other types of NSE spectrometers with large solenoids generating strong precession magnetic fields. This advantage is very useful for studies of slow spin dynamics on magnetic properties, such as Skyrmion phase observed in magnetic substances. The instrument is equipped with a 4K GM cryostat and a very compact magnet, which can add a maximum of 0.2 T at the sample position. In addition, the combination between neutron reflectometry and MIEZE measurement was tested by using a KENS S-type project, and it will be made available to public users in FY2020.

4. Summary

In this report, the current status of BL06 VIN ROSE in FY2019 was briefly summarized. A new 2D detector with MPPC silicon photomultipliers was tested and will be operational soon. The public users can now use the MIEZE spectrometer, where a 4-K GM cryostat and a compact maximum 0.2 T permanent magnet are available as sample environments. At the NRSE spectrometer, the commissioning with two-dimensional ellipsoidal neutron-focusing supermirrors has progressed significantly, which is essential for the further development of NRSE to reach high-energy resolution.

References

[1] F. Mezei ed., Neutron Spin Echo, Lecture Notes in Physics, (Springer, Berlin) **128**, (1982).

[2] D. Richter, M. Monkenbusch, A. Arbe, J. Colmenero, *Adv. Polym. Sci.* **174**, (2005) 1–221.

[3] M. Hino, T. Oda, N. L. Yamada, H. Endo, H. Seto, M. Kitaguchi, M. Harada, Y. Kawabata, *J. Nucl. Sci. Tech.* **54**, (2017) 1223.

[4] F. Funama M. Hino, T. Oda, H. Endo, T. Hosobata, Y. Yamagata, S. Tasaki, *J. Surf. Invest.: X-ray, Synchrotron and Neutron Tech.*, **14**, Suppl. 1, (2020) S50–S55.

[5] T. Hosobata, M. Hino, H. Yoshinaga, T. Kawai, H. Endo, Y. Yamagata, N. L. Yamada, S. Takeda, *JPS Conf. Proc.* **22**, (2018) 011010.

H. Endo[1,2], M. Hino[3], T. Oda[3], N. L. Yamada[1,2], H. Seto[1,2], and Y. Kawabata[3]

[1]Neutron Science Division, Institute of Materials Structure Science, KEK; [2]Neutron Science Section, Materials and Life Science Division, J-PARC Center; [3]Institute for Integrated Radiation and Nuclear Science, Kyoto University

Commissioning of ^{3}He Cryostat on Super-HRPD

1. Introduction

Super-HRPD (BL08) is the highest resolution neutron powder diffractometer ($\Delta d/d = 0.037\%$) in the world [1]. Taking advantage of high resolution, we can detect symmetry lowering and distortion of crystal structure. In addition, it is possible to perform high quality structure analysis by extraction of many distinguishable diffraction peaks. Various sample environments (SE) (temperature range from 1.3 K to 1170 K, magnetic field up to 14 T, and gas environment) have been developed. We have done commissioning of a bottom-loading cryostat at FY2017 [2]. It can reach up to 4 K in about 2 hours and perform relatively quick heating. Until now, many users have used that cryostat without trouble. On the other hand, measurement at an even lower temperature was requested by specific users for magnetic studies. Using our 14 T magnet system, we can perform measurement down to 1.3 K. But if we do not need a magnetic field, it is unreasonable to use our magnet because its preparation involves significant labor and time. Moreover, the signal decreases at the back scatter (BS) and the low angle (LA) detector bank by the narrow scattering window and we cannot make available the 90-degree (QA) detector bank because of the lack of a window. So, we need the other cryostat that is easier to handle and can reach temperatures below 2.6 K. In this report, we introduce about the commissioning of the bottom loading type of the ^{3}He cryostat.

2. Spec and off-beam test

Our ^{3}He cryostat consists of a GM refrigerator and a ^{3}He gas circulation system. Below 30 K, the cold head of the GM refrigerator and the 1-K pot are separated thermally by H_2 gas heat switch to keep the temperature of the sample. On the neutron beam pass, there are an outer chamber with a vanadium window of 0.1 mm thickness, and two radiation shields, located at 40 K and 4 K stages respectively, with a vanadium window of 0.04 mm thickness.

Figure 1 shows the cooling and heating tests of the cryostat. The starting time is defined as the time of turning on the compressor. Before it starts to cool, it takes several hours to vacuum the inner space of the outer vacuum chamber (OVC). Unfortunately, the cooling rate is very slow, so about 40 hours are needed for the sample mount to measurement at base temperature. On the other hand, the temperature stability below 5 K is good. We controlled the temperature increase from

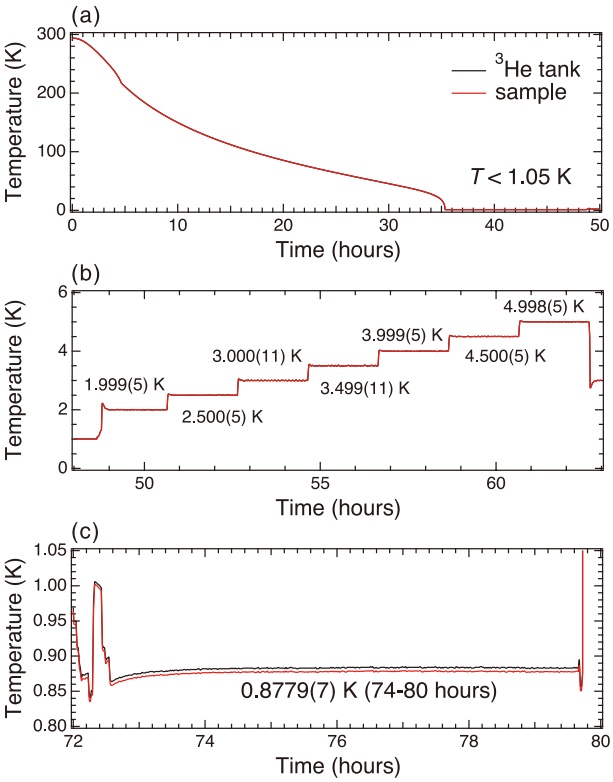

Figure 1. The off-beam test on our 1K cryostat, cooling, (b) heating, and (c) approaching the lowest temperature.

2 K to 5 K with 0.5 K steps. Although the temperature is slightly unstable near the boiling point of ^{3}He, we think it is acceptable for general use. The base temperature is about 1.05 K with no control. When the ^{3}He gas flow rate is limited by controlling the needle bulb, we can ensure availability to 0.87 K. At the initial tests, we could not keep the temperature for a long time because of an occurring stack on the narrow part of the ^{3}He line. After fixing the leakage, we could keep the temperature below 0.9 K for at least 2 days.

3. On-beam test

In order to check the actual sample temperature, we measured polycrystalline ErF_3. The sample was loaded to our conventional vanadium cell (6 mm diameter) and the height of sample was 40 mm. It has been reported that ErF_3 behaves antiferromagnetic transition at $T_N = 1.05(3)$ K and its magnetic structure is represented with $\boldsymbol{k} = \mathbf{0}$ [3]. Our result showed $T_N = 1.04(1)$ K (Fig.2), consistent with that of the reference, so the sample was cooled down to at least 1 K. Neutron powder diffraction profiles were collected at 1.10 K and 1.00 K to confirm the magnetic structure. The collected data were based on three hours

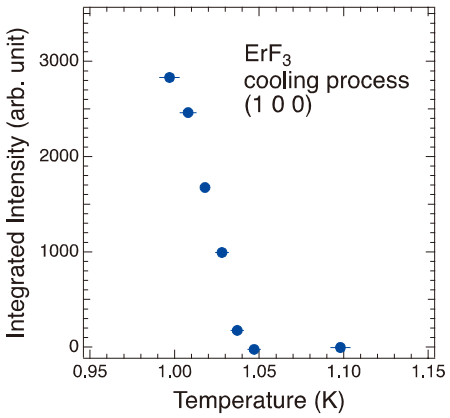

Figure 2. The temperature dependence of the magnetic peak intensity of ErF_3.

per one profile with 500 kW proton beam of the MLF. The profile looked good, so it appeared that the reduction of intensity by the OVC and the other shield had no effect. Our sample included a small amount of unidentified impurities. So, the profile on which the intensities of 1.00 K were subtracted from those of 1.10 K was used for analysis. We performed Rietveld refinement using Z-Rietveld software [3]. For accuracy, two profiles collected at the LA and the QA detector banks were used. We could fit the profiles adopting the model of the reference. The strength of the magnetic moment was 4.303(8) μ_B per Er^{3+}. The value was smaller than the reported one because the magnetic moment was not saturated at 1.00 K.

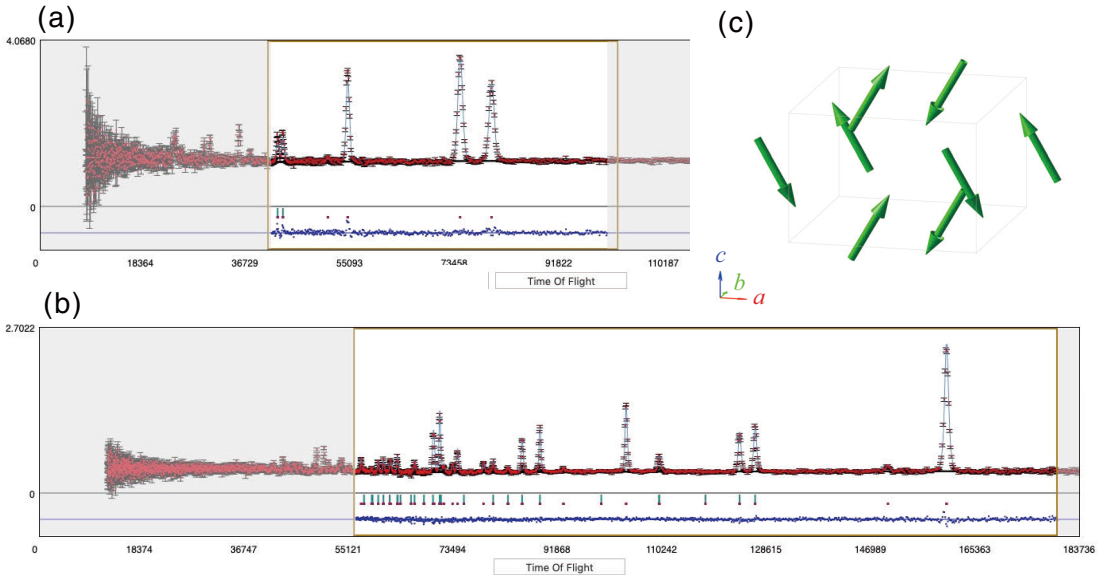

Figure 3. The fitting result of the subtracted profiles of (a) the LA bank and (b) the QA bank. The χ^2 were (a) 1.39 and (b) 1.26. (c) The refined magnetic structure of ErF_3. It was yielded that the component of magnetic moment on (0.3674, 1/4, 0.0619) site was (2.182, 0, 3.708) with bore magnet units.

4. Future plans

It was decided that the ^{3}He cryostat will be made available to users from the 2020B cycle. The cooling rate of the ^{3}He cryostat is very slow, it is impossible to measure two or more samples without time lag. To solve the problem, we will perform off-beam cooling and will arrange the beam time flexibly.

References

[1] S. Torii et. al., J. Phys. Soc. Jpn. SB020 SB020-1-4 (2011).
[2] M. Hagihala et. al., MLF Annual Report 2017 p.81 (2018).
[3] K. Krämer et. al., Europ. J of Sol. Sta. and Inorg. Chem. 33, 273–283 (1996).
[4] R. Oishi-Tomiyasu et. al., J. Appl. Crystallogr. 45 a299–308 (2012).

M. Hagihala[1,2], K. Cho[2], S. Torii[1,2], and T. Kamiyama[1,2]
[1]*Neutron Science Section, Materials and Life Science Division, J-PARC Center;* [2]*Neutron Science Division, Institute of Materials Structure Science, KEK*

Current Status of BL09 (SPICA) in 2019

1. Introduction

The rechargeable battery is a key component of mobile devices and electric vehicles, and the development of new generation batteries is essential to meet the requirements for batteries in the future. The Special Environment Powder Diffractometer (SPICA) installed at BL09 is a time-of-flight neutron powder diffractometer dedicated to new generation battery studies. Its design is optimized for conducting various types of measurement for observing active materials from operating battery devices, i.e. it is a high intensity and high-resolution diffractometer, with flexible sample environment setup. It is also equipped with an automatic sample changer for conventional powder diffraction measurements, as well as off-beam charge/discharge equipment for conducting long-term deterioration tests, and a chemical lab of its own, to provide flexible environment for handling highly reactive battery materials.

SPICA has demonstrated its ability for operando-measurements of the charge/discharge process of working Li-ion batteries, as well as for precise crystal structure analyses of various battery related materials by the conventional powder diffraction method [1, 2]. In fiscal year 2019, several sample environments were commissioned, and became open for general users.

2. Cryostat and cryofurnace

In fiscal year 2019, a new top-loading cryostat and cryofurnace have been commissioned, and both of them became available for general users.

The sample temperatures of the new cryostat and cryofurnace range from 4 K to 300 K, and from 20 K to 600 K, respectively (Fig. 1). The sample temperatures were measured at sample positions for each apparatus. It took about 3 hours (6 hours) to reach the base temperature from 300 K for the cryostat (cryofurnace). For the cryofurnace, the sample temperature can be controlled from low temperatures (below 300 K) to high temperatures (above 300 K) continuously, without taking out the sample. Figure 2 shows the temperature dependent diffraction data for $BaTiO_3$, which demonstrates the observation of the sequential structural phase transition of $BaTiO_3$ on heating. Phase transitions varying as rhombo. → ortho. → tetra. → cubic were clearly observed as the temperature was increased monotonically throughout the temperature range. (The horizontal blue line around 240 K corresponds to the beam stop which occurred during that period.)

Figure 3 shows the normalized diffraction patterns of the standard sample (NIST Si) collected at the backward bank using cryostat, cryofurnace and without sample environment apparatuses. The contribution from the cryostat or cryofurnace in the raw data is corrected, and there are no extra signals or backgrounds due to these apparatuses.

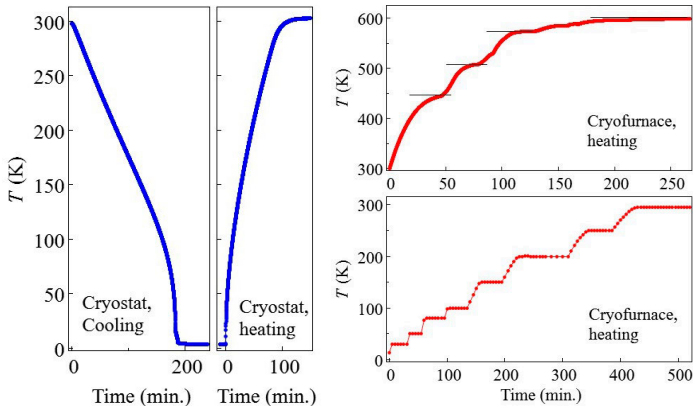

Figure 1. Time dependence of the temperature for the cryostat (left) and cryofurnace (right). The temperatures were measured at the sample positions for each apparatus.

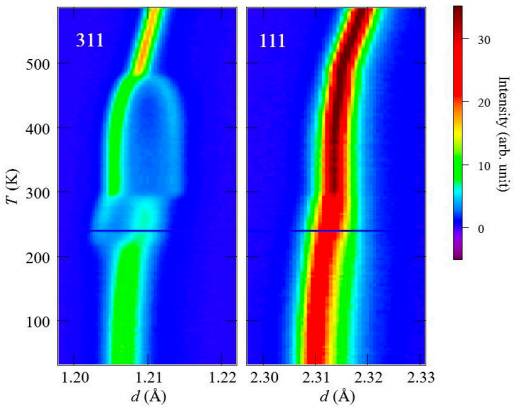

Figure 2. Temperature dependent neutron powder diffraction patterns for $BaTiO_3$ near 311 (left) and 111 (right) reflections. The left axis represents the control temperature, which is somewhat higher than the actual sample temperature.

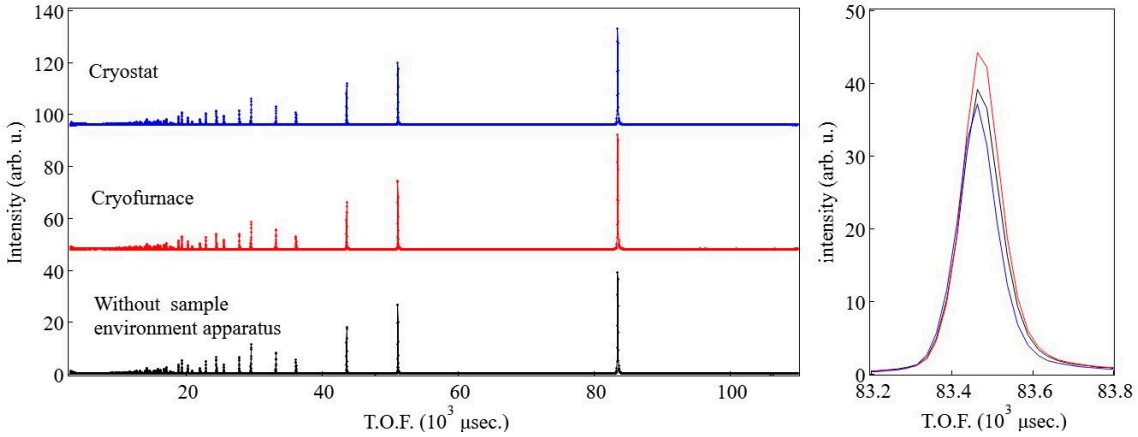

Figure 3. Neutron powder diffraction patterns collected with the cryostat (blue), cryofurnace (red), and without sample environment apparatus (black).

3. Fluoride shuttle battery standard cell

The fluoride shuttle battery (FSB) is one of the promising candidates for beyond–lithium–ion, innovative, rechargeable battery. FSBs work on the principle of the reversible redox transformation between a metal and its fluoride counterpart at both the negative and positive electrode, under fluoride–ion shuttling.

We have studied in detail the crystal structures of solid electrolyte materials for FSBs using SPICA and unveiled the fluoride ion conduction mechanism in these materials [3, 4]. For the forthcoming operando neutron powder diffraction experiment of all-solid-state FSBs using these solid electrolytes, we developed a standard battery cell system for such experiments, in cooperation with Kyoto University. Figure 4 illustrates the cell set up. We expect to start the operando neutron powder diffraction experiments in fiscal year 2020.

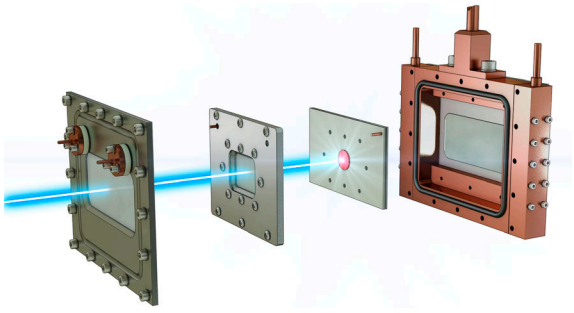

Figure 4. Schematic view of the newly developed all-solid-state fluoride shuttle battery standard cell.

4. Future plans

We will continue with the development of the cryostat/cryofurnace. The measurement control software will be upgraded for automatic temperature control, and efforts are being made to improve the maximum sample temperature for the cryofurnace. The commissioning of the FSB standard cell will continue as well.

Acknowledgements

The development of the FSB standard cell was done in collaboration with Prof. K. Mori and Assis. Prof. F. Fujisaki at the Institute for Integrated Radiation and Nuclear Science, Kyoto University. We would like to thank Mr. Shioya and Mr. Namba for their technical support in operating SPICA. This work was supported by the Research and Development Initiative for Scientific Innovation for New Generation Batteries 2 (RISING2) project of the New Energy and Industrial Technology Development Organization (NEDO).

References

[1] N. Yabuuchi, *et al.*, *Nat. Commun.*, **7** 13814 (2016).
[2] S. Taminato, *et al.*, *Sci. Rep.*, **6** 28843 (2016).
[3] K. Mori, *et al.*, *ACS Appl. Energy Mater.*, **3** 2873 (2020).
[4] K. Mori, *et al.*, *J. Phys. Chem. C*, **124** 18452 (2020).

T. Saito[1,2], T. Kamiyama[1,2], and S. Torii[1,2]
[1]*Neutron Science Section, Materials and Life Science Division, J-PARC Center;* [2]*Institute of Materials Structure Science, KEK*

BL10: NOBORU

1. Introduction

In FY 2019, sixteen general-use proposals and three project-use proposals were carried out at NOBORU. Two general-use proposals were postponed due to a delay in restarting the facility operation after the summer shutdown.

This year, the MLF successfully performed a 1-MW test operation for 10.5 hours on July 3, and we accordingly conducted the neutron source diagnostics measurements at NOBORU. In the following sections, we briefly describe the measurement methods and obtained results.

2. Fixed-point observation of thermal-cold neutron spectrum and its intensity

The neutron intensities of thermal and cold neutrons from the moderator were measured at BL10 by the foil-activation method using gold foils. The foils were located at the beam line center, 13.0 m from the moderator surface. Each measurement at different proton beam power was done with and without a Cd cover to derive the thermal neutron intensity. The optical device conditions, such as collimator size and slit setting, were kept the same for all measurements for easy comparison. Figure 1 shows the thermal neutron intensities measured by the foil activation method with the calculations. We confirmed that the neutron intensity depends almost linearly on the proton beam power.

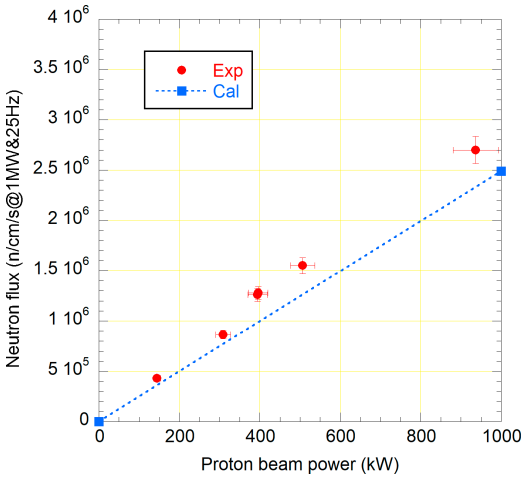

Figure 1. Thermal neutron intensities measured by the foil activation method using gold foils.

3. Pulse shape measurement of thermal-cold neutrons

The pulse shapes of the thermal and cold neutrons were measured by a conventional diffraction method, where the sample and experimental setup were almost the same as in the previous work done at NOBORU. We confirmed that the observed Bragg peaks of the decoupled moderator below 300 kW were in good agreement with those calculated using the PHITS simulation code [1]. Here, we compare the mica Bragg peaks at beam powers of 150 kW and 1 MW measured in 2017 and 2019, respectively. As shown in Fig. 2, we can expect that the pulse shape does not change even in the steady operation of 1 MW.

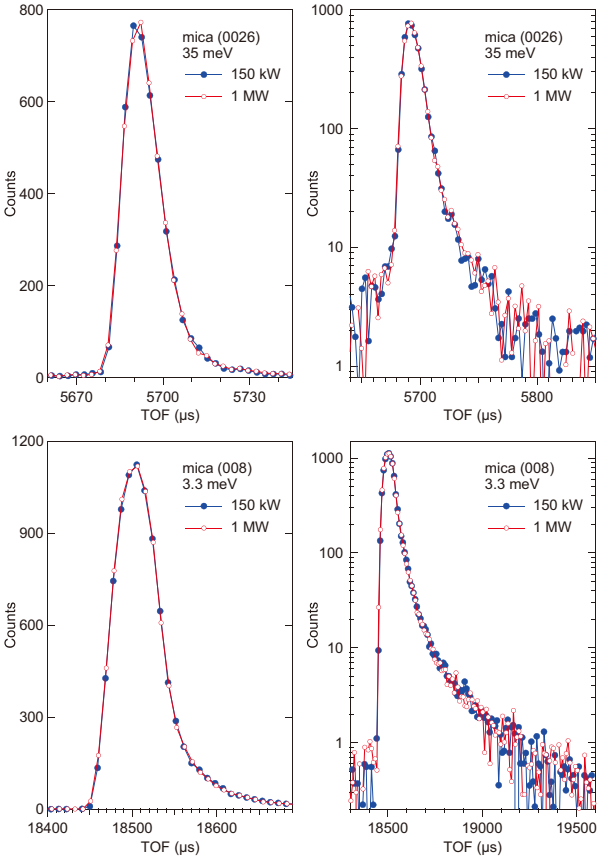

Figure 2. Examples of pulse shapes for thermal and cold neutrons. Bragg peaks of (0026) and (008) of mica are represented in linear and log scale.

Reference

[1] K. Oikawa et al., JPS Conf. Proc. 1, 014012 (2014).

K. Oikawa[1] and M. Harada[2]

[1]Neutron Science Section Materials and Life Science Division, J-PARC Center; [2]Neutron Source Section Materials and Life Science Division, J-PARC Center

Recent Developments in High-*PT* Experiments Using the Multi-Anvil Press "ATSUHIME" at BL11

1. Introduction

To conduct neutron diffraction experiments under high-pressure and high-temperature (high-*PT*) conditions, the PLANET [1] is equipped with the large volume 6-axis multi-anvil press "ATSUHIME" [2] that has six independently controlled hydraulic rams. The use of multi-anvil assembly 6-6 (MA6-6) [3], which compresses a cubic pressure medium with six second-stage anvils, enables us to generate high-*PT* stably. However, the maximum pressure was limited below 10 GPa so far. To extend the available pressure range, we modified the anvil shape and tested its feasibility. In addition, the MA6-8 (or Kawai-type 6-8 cell assembly) which has the potential to extend the available pressure was also tested.

2. MA6-6

Figure 1 shows MA6-6 used in this study. The sample assembly is compressed by six tungsten carbide (WC) anvils that are shrink-fitted into steel outer jackets [3]. The use of large anvils and the shrink-fitting increase the maximum applicable load compared with the conventional anvils with 26 mm square base. Anvils with different truncation edge lengths (TELs) of 3.5, 5, 7, 10 mm were tested. A step is made on each anvil facet to increase signal intensity from the sample by reducing the blind angle.

To check the pressure-load performance, diffraction profiles of NaCl were obtained at several loads during compression (Fig. 2). The performance improves as the TEL is reduced: the maximum pressure reached was 15.3 GPa at 1000 kN when using anvils with TEL of 5 mm, whereas the anvils with TEL = 3.5 mm could not exceed the performance of TEL = 5 mm. Further optimization of the sample assembly and the gasket that seals pressure is necessary for TEL = 3.5 mm in the future.

As the achievable pressure increases, a problem in heating with graphite heater arises from the transformation to diamond above approximately 12 GPa and 1400 K. To achieve stable heating, we replaced the graphite by TiC/Al_2O_3 composite (Nippon Tungsten, NPA-2). An off-line test with this heater confirmed the stable heating up to 2000 K. The developed cells are now offered for general user experiments.

3. MA6-8

The MA6-6 generated successfully pressures up to 15 GPa, but further increase of pressure while maintaining the sample volume is difficult because of the limitation of the anvil strength. To extend the pressure range to 20 GPa, we tested MA6-8. In this assembly, the applicable load is higher than in MA6-6. Several anvils with

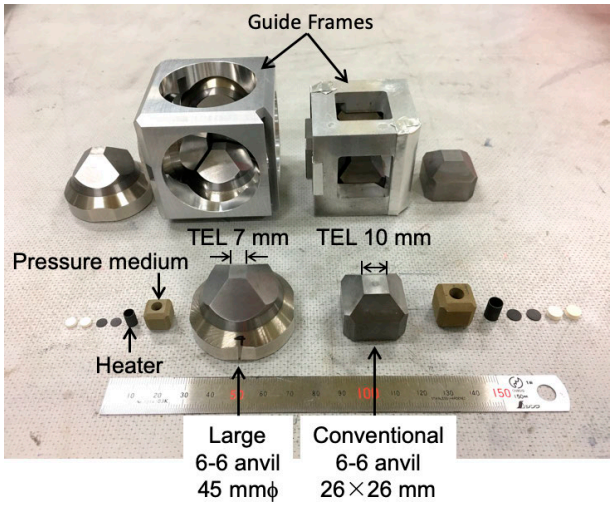

Figure 1. Conventional 6-6 anvils and large 6-6 anvils with shrink-fitted jackets. Guide frames and cell assemblies are also shown.

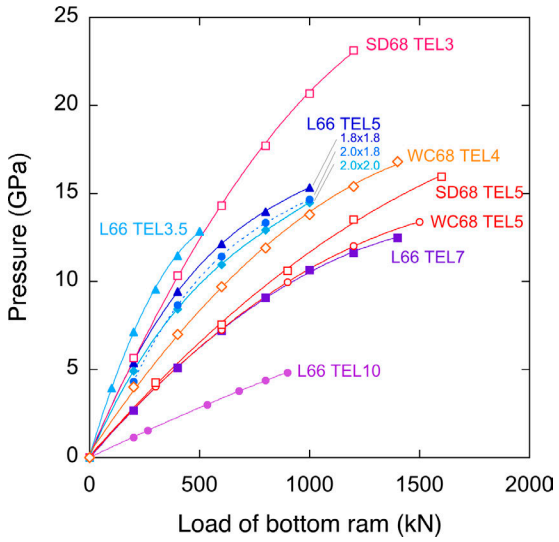

Figure 2. Pressure generation curves of a large 6-6 cell (L66) and 6-8 cells (SD68 and WC68) with various TELs. Pressures are calculated from lattice parameters of NaCl on the basis of the equation of state [4]. Numbers for L66 TEL5 indicate dimensions of the gaskets. Units of TELs and gaskets are in mm.

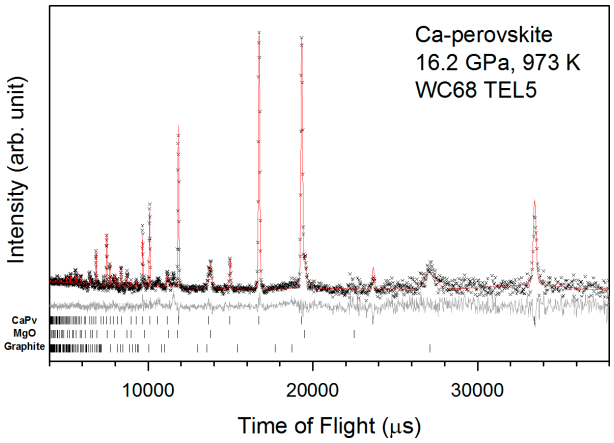

Figure 3. Observed (cross), calculated (red line) and difference (gray) for the profile of Ca-perovskite. Vertical bars indicate calculated positions for reflections of Ca-perovskite, MgO endcap and graphite capsule. The binning width of the data is $\Delta t/t = 0.001$.

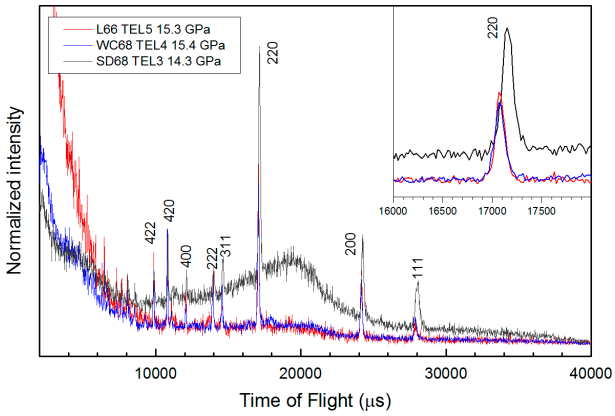

Figure 4. Comparison of normalized diffraction patterns of NaCl obtained with MA6-6 (L66) and MA6-8 using SD and WC anvils (SD68 and WC68) at ca. 15 GPa. The radial collimators with diffraction gauge length of 3 mm and 1.5 mm were used for the experiments with MA6-6 and MA6-8, respectively. The binning width of the data is $\Delta t = 20$ μs. Inset shows enlarged area of NaCl 220 reflection.

different materials and shapes were tested, including SiC-sintered diamond (SD) and tungsten carbide (WC) anvils with TELs of 3, 4 and 5 mm. To gain the diffraction intensity by maintaining a window for scattered neutrons, tapers and slits are made on the facets of the first stage anvils.

The generated pressures are plotted in Fig. 2. The pressure reached 23.1 GPa at 1200 kN using SD anvils with TEL = 3 mm and it reached 16.0 GPa at 1500 kN using WC anvils with TEL = 5 mm.

A test for high-T generation and the diffraction data collection was conducted using WC68 anvils with TEL = 5 mm. The sample of wollastonite ($CaSiO_3$) was compressed to 1800 kN, then heated up using a $LaCrO_3$ heater. After reaching 973 K at 16.2 GPa, the peaks of Ca-Perovskite appeared. The patterns were contaminated by small peaks from the sample surroundings, such as end caps and a sample capsule (Fig. 3). High quality data that is refineable by Rietveld method were obtained by 24 h exposure.

4. Comparison of signal intensities

To evaluate efficiency in data acquisition, peak intensities of NaCl are compared at around 15 GPa among various cell assemblies (Fig. 4). The intensity for MA6-8 using WC anvils with TEL = 4 mm is almost comparable to that of MA6-6 using WC anvils with TEL = 5 mm. Thanks to the high neutron transparency of the sintered diamond, MA6-8 with SD anvils provides the highest intensity. These results demonstrate the feasibility of MA6-8 to expand the pressure range while maintaining sufficient signal intensity.

5. Summary

We have developed a technique for high-temperature experiments above 10 GPa with MA6-6 and MA6-8. The MA6-6 with TEL5 anvils and MA6-8 with TEL3 anvils extended the pressure range to 15 GPa and 23.1 GPa, respectively. This technique is useful in a wide range of fields, including Earth science and material science.

References

[1] T. Hattori et al., Nucl. Inst. and Meth. Phys. Res. A, **780** 55 (2015).
[2] A. Sano-Furukawa, et al., Rev. Sci. Instrum., **85** 113905 (2014).
[3] A. Yamada et al., Rev. High Press. Sci. Tech. **26** 99 (2016).
[4] J.M. Brown, J. Appl. Phys. **86**, 5801 (1999).

A. Sano-Furukawa[1,2], T. Hattori[1], K. Funakoshi[3], J. Abe[3], and S. Machida[3]
[1]Neutron Science Section, Materials and Life Science Division, J-PARC Center; [2]Institute of Materials Structure Science, KEK; [3]Neutron Science and Technology Center, CROSS

High Resolution Chopper Spectrometer HRC

1. Introduction

The High Resolution Chopper Spectrometer (HRC) is being operated at BL12 in the MLF under the S type project, in order to study dynamics in condensed matter, especially in a wide range of correlated electron systems. The activities of the HRC in FY2019 are summarized in this report.

2. Maintenance of the T0 chopper

A T0 chopper was installed at the beginning of the operation of the HRC in May 2010 [1], and this T0 chopper (T0#1) was in operation until the Hadron incident in May 2013. After the earthquake in 2011, a spare T0 chopper was manufactured, T0#1 was replaced by the spare one (T0#2) during the recovery work from the Hadron incident, and T0#2 was in operation since February 2014. Maintenance work was performed on T0#1 in November 2015, where the components damaged during the operation, such as the rotor bearings, the magnetic seals, the timing belt, the vacuum seals, and the motor, were replaced with new ones, and a trial operation was performed for 200 hours rotating at 100 Hz to ensure smooth rotation. T0#2 was replaced with T0#1 in July 2017, at the time the water couplers for both T0 choppers were improved to avoid water leaks [2]. T0#1 is currently in operation.

In May 2016, during the operation of T0#2, the fluctuations of the rotational period suddenly increased to ±50 μs, whereas they are normally less than ±3 μs for a good phasing to the repetition of the neutron production. The fluctuation increase was caused by the decrease of the output voltage (V) of the rotational signal of the rotor and the noisy part of the signal being comparable to the reference level (V_R) (Fig. 1(a)). The same phenomena occurred in July 2017 and December 2018. The light source is mounted in the controller, the light is transferred though an optical fiber to the marker on the rotational axis of the T0 chopper rotor, where the light is shut or transmitted, and the light returns to the controller through an optical fiber for return [3]. The rotational phase is determined from the time when $V > V_R$. The voltage in the initial installation of the T0 chopper was V = 600 mV, and the V_R value was set in the electronic circuit in the controller. The fluctuation increase occurred when the difference became $V - V_R < 150$ mV, and recovered by reducing V_R to $V - V_R > 200$ mV (Fig. 1(b)). These phenomena occurred more frequently with the increase of the beam power and the decrease of V was proportional to the integrated beam power. Therefore, we concluded that the fluctuation increase was caused by the radiation damage to the optical fibers.

Since V decreased to 400 mV in December 2018, V_R changed once to 200 mV. In order to estimate the lifetime of the optical fibers and extend it, we set V = 500 mV by changing the parameters of the circuit to increase the light intensity, and V_R = 150 mV, which is the limit in the circuit, and started the operation in January 2019 with the beam power of 500 kW. We found that V decreased at the rate of 6.5 mV/month until July 2019 (the solid line in Fig. 1(c)). We can estimate that the fluctuation increase will occur 30 months later from January 2019, when V = 300 mV and $V - V_R$ = 150 mV.

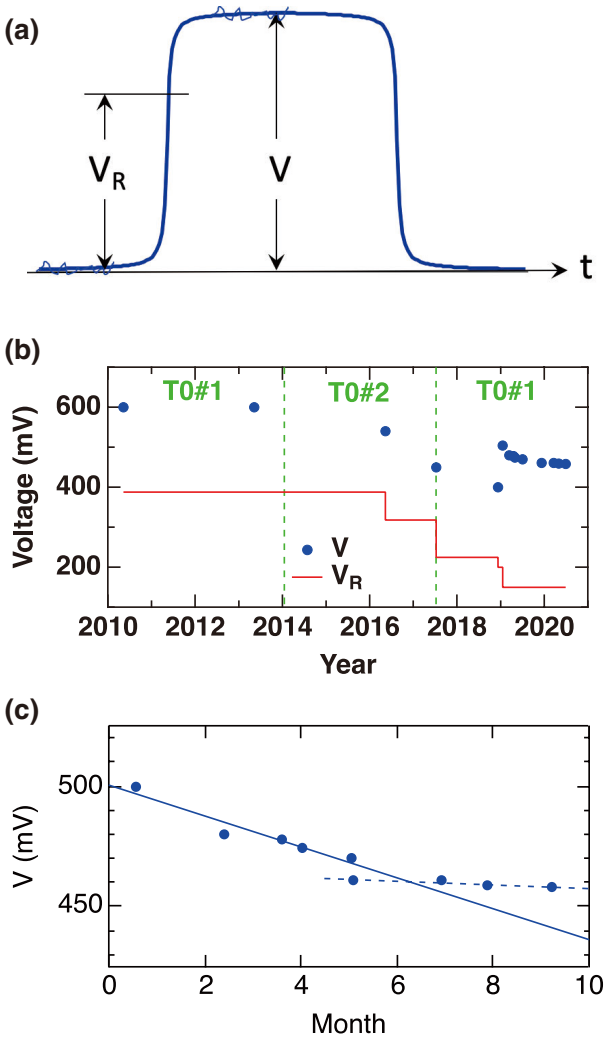

Figure 1. (a) Schematic drawing of the output voltage of the rotational signal as a function of time (t). (b)Variations of V and V_R. The T0 chopper in operation at the time is indicated. (b) Variation of V since January 1, 2019 (Month = 0) indicated by removing the beam off period.

We decided to perform the maintenance work on T0#2 in 2019 and to exchange it with T0#2 in the summer of 2020. In fact, the maintenance work for T0#2, which is the same as that for T0#1 performed in 2015, was performed in November 2019. Note that the initial voltage in this circuit condition was 750 mV and the time when V drops by a half is estimated to be 3 years for a continuous period and 5 years if the beam off period at 1-MW beam power is included. The lifetime was roughly estimated to be 19 years in the initial design [3].

Due to a different reason, fluctuation increase of the rotational period sometimes occurred in T0#1. Since the fluctuation increase sometimes calms down in several days, a heating in the circuit was assumed to be the reason, so we took the following measures. In the controller, there is a module, where signals generated in a synthesizer are transformed to TTL and then transferred to the servo amplifier of the motor [1]. First, this module was replaced with an improved one, where the heating in an operational amplifier is minimized by reducing the voltage ratio of the operational amplifier to the resistor connected to the amplifier increasing the resistor value. Next, this module was replaced with a more advanced one, where the heating in the operational amplifier is further reduced by transforming the synthesizer signal to TTL using a comparator. The servo amplifier was exchanged with a spare one and so was the motor. We found that the tension of the timing belt was reduced from the value applied during the maintenance. The tension increased back to the maintenance value. All these measures failed to reduce the fluctuations. Finally, we found that the fluctuations were caused by the noise in the electric power during the operation of the main ring. By resurveying the control parameters of the servo amplifier, the optimum values were found, and they were different from those determined during the maintenance, so the fluctuations were reduced to a certain degree. We found that the control parameters of the servo amplifier and the tension of the timing belt had changed after the long-time operation. The correction works were performed from March 2019 to January 2020. Although V decreased by removing and reinstalling T0#1 for the exchange of the motor, fortunately, the decrease rate of V was slightly reduced even at 600-kW beam power. Therefore, V will not be reduced by much by the summer of 2020, as shown with the dashed line in Fig. 1(c).

3. Other instrumentations

The superconducting magnet is operated properly, based on the decision to apply a maximum magnetic field of 5 T. The magnet can be controlled with the control program YUI. A distribution version of the data analysis and visualization program HANA was released, where the vanadium correction can be done for an efficiency normalization of PSDs and the par file can be created for data analysis using Horace. A Windows PC was installed for data analysis by Windows users. We discussed the maintenance of the chopper controller, then, the details of the descriptions of the controllers were collected and a test environment for the Fermi chopper was equipped for maintenance and development work.

4. Scientific results

We have some publications: a review article for neutron Brillouin scattering on the HRC [4], a discovery of novel excitations in a frustrated magnet $CsFeCl_3$ [5] and some instrumentations [6–8].

References

[1] S. Itoh et al., Nucl. Insrt. Meth. A **661** 86 (2012).
[2] S. Itoh et al., MLF Annual Report 2017, pp. 94–95.
[3] S. Itoh et al., Nucl. Insrt. Meth. A **654** 527 (2011).
[4] S. Itoh and Y. Endoh, J. Phys. Soc. Jpn. **88** 081004 (2019).
[5] S. Hayashida et al., Sci. Adv. **5** eaaw5639 (2019).
[6] S. Itoh et al., Physica B **568** 76 (2019).
[7] S. Itoh et al., JPS Conf. Proc. accepted.
[8] M. Watanabe et al., JPS Conf. Proc. **25** 011024 (2019).

S. Itoh[1,2], T. Masuda[2,3], T. Yokoo[1,2], T. Nakajima[3], S. Asai[3], H. Saito[1,2], D. Kawana[3], R. Sugiura[3], T. Asami[3], Y. Ihata[4], and H. Tanino[1,2]
[1]Neutron Science Section, Materials and Life Science Division, J-PARC Center; [2]Institute of Materials Structure Science, KEK; [3]The Institute for Solid State Physics, The University of Tokyo; [4]Technology Development Section, Materials and Life Science Division, J-PARC Center

BL14 AMATERAS

1. Introduction

AMATERAS is a cold-neutron disk-chopper spectrometer for studies on the dynamical properties in atomic, molecular and magnetic systems from cold to sub-thermal energy range with high efficiency and flexible resolution. Experiments of 23 general user applications and two JAEA project research applications have been carried out. On the other hand, we encountered some mechanical problems, one of which was serious and interrupted the user program. A new member, Dr. Naoki Murai, joined the AMATERAS team in April.

2. User program, outreach activities and outcomes

The numbers of general proposals (short-term) submitted in the 2019A and 2019B periods were 27 (accepted: 11, reserved: 15, not approved: 1) and 37 (accepted: 10, reserved: 25, not approved: 2), respectively. We also received one long-term general proposal (not approved) and two JAEA project research proposals (both approved). The research fields of the majority of the general proposals were magnetism and strongly correlated electron systems, as in the previous periods. The second major field was liquid and non-crystalline systems, and the third one was energy (functional) materials. Finally, in FY2019, 23 short-term general proposals and two JAEA project proposals were carried out on AMATERAS.

In FY2019, six refereed papers covering the works at AMATERAS were published. The topics included quantum spin systems, thermo-electric materials and others. Two of papers were subjects of press releases. One was study on triplon excitations with the topologically protected edge states in a two-dimensional (2D) dimer antiferromagnet (AF) done by Dr. Kazuhiro Nawa (Tohoku University) and his co-workers [3]. The other was a work on magnetic excitations in a perfectly frustrated 2D dimer AF done by a research group headed by Dr. Nobuyuki Kurita (Tokyo Institute of Technology) [4]. Dr. Nawa won the JSNS Young Researcher Prize in part due to this work.

In the 4th Neutron and Muon School and MIRAI PhD School 2019, three students conducted a hands-on experiment at AMATERAS and learned how to measure the magnetic excitations of a single crystal material.

Dr. Chi-Hung Lee visited AMATERAS as a guest researcher of AONSA Young Research Fellowship organized by the Asia-Oceania Neutron Scattering Association. Originally, he planned to stay at J-PARC for three months from February to April and to study a new-type of multiferroic material on AMATERAS. Unfortunately, however, due to the COVID-19 pandemic, he terminated his stay before carrying out his experiment. He is planning to come again in 2020 or later.

3. Instrument related issues

In FY2019, AMATERAS encountered several mechanical problems. The most serious one was the failure of the monochromating chopper. One of the resolvers failed (Fig. 1) which caused the suspension of the AMATERAS user program for twelve days. The details of the incident are mentioned elsewhere [5].

The work on maintaining and upgrading the spectrometer continued. The preparation for replacement of the vacuum system of the scattering chamber also continued. A jig for the installation and the control software was prepared. The installation will be completed in FY2020. We started the planned installation of the extended section of the beam-transport (0.5 m after the monochromating chopper). The jacket of the mirror for this section was purchased. The super-mirror will be delivered in FY2020.

In July, at the 1-MW test operation of the MLF, we carried out a demonstration measurement on the magnetic excitations in a low-dimensional magnet by omega-rotation scans. Even with a tiny (170 mg) single crystal sample, clear picture of the excitations in a four-dimensional space was obtained. The results will be reported in a future publication.

Figure 1. The monochromating disk-chopper under inspection. Inset shows a failed resolver.

References

[1] K. Nakajima *et al*., J. Phys. Soc. Jpn. **80**, SB028 (2011).
[2] K. Nakajima, RADIOISOTOPES **66**, 101 (2017).
[3] K. Nawa *et al*., Nat. Commun. **10**, 2096 (2019).
[4] N. Kurita *et al*., Phys. Rev. Lett. **123**, 027206 (2019).
[5] K. Nakajima *et al*., JPS Conf. Proc. *in press*.

K. Nakajima[1], S. Ohira-Kawamura[1], M. Kofu[1], N. Murai[1], Y. Inamura[1], D. Wakai[2], and T. Kikuchi[1, 3]
[1]Materials and Life Science Division, J-PARC center; [2]Nippon Advanced Technology Co., Ltd.; [3]Chemical Analysis Center, Research & Development HQ, Sumitomo Rubber Industries, Ltd.

Upgrading TAIKAN

1. Introduction

The small and wide angle neutron scattering instrument TAIKAN (BL15) has been developed and upgraded at J-PARC to analyze precisely and efficiently the microstructures or hierarchical structures of substances in various scientific fields with a 1-MW spallation neutron source [1]. In FY2019, it was upgraded further to perform efficient wide-*q* measurement and high precision low-*q* measurement.

2. Upgrading for wide-*q* measurement

The detector system of TAIKAN is composed of 5 detector banks: small-, middle-, high-, ultra-small-angle, and backward detector banks. On the middle-, high-angle, and backward detector banks, 128, 120, and 40 ^{3}He PSD tubes were additionally installed, respectively. The measurement efficiency of the middle-, high-angle, and backward detector banks increased by about 22, 60, and 200%, respectively. The number of ^{3}He tubes then increased to 912, 720, 320, and 80 for the small-, middle-, high-angle, and backward detector banks, respectively. The installation ratios of the ^{3}He tubes became 100, 100, 57, and 100% or the small-, middle-, high-angle, and backward detector banks, respectively. Figures 1 and 2 show photos of the small-, middle-, and high-angle detector banks and the backward detector bank after installing the ^{3}He tubes, respectively.

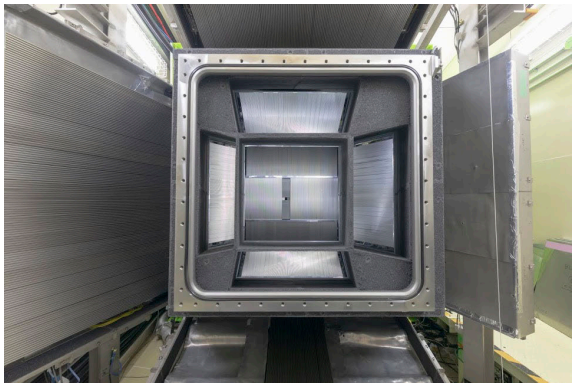

Figure 1. Small-, middle-, and high-angle detector banks.

Figure 2. Backward detector bank.

3. Upgrading for high precision low-*q* measurements

For high precision low-*q* measurements, an ultra-small-angle detector and beam focusing devices consisting of a quadrupole magnet to polarize a neutron beam, two sextupole magnets to focus the beam on the ultra-small-angle detector, and three spin flippers have been installed in TAIKAN. The performance of the system was evaluated with a sample of polystyrene spherical nanoparticles. The experimental data were well fitted with scattering functions using the hard sphere model with the averaged diameter of 496 nm in the *q*-range of 0.0007 – 0.003 A^{-1}. This result validated the assumption that the q_{min} of TAIKAN can be extended to 0.0007 A^{-1}.

4. Future prospects

The improvement of the measurement efficiency by the installation of middle-, high-angle, and backward detectors and the validation of the high precision low-*q* measurement make efficient wide-*q* measurement easier. TAIKAN is expected to contribute to the research of microstructures or hierarchical structures by authentic precise measurement in a wide-*q* range.

Reference

[1] S. Takata, J. Suzuki, T. Shinohara, T. Oku, T. Tominaga, K. Ohishi, H. Iwase, T. Nakatani, Y. Inamura, T. Ito, K. Suzuya, K. Aizawa, M. Arai, T. Otomo and M. Sugiyama, JPS Conf. Proc., **8** 036020 (2015).

J. Suzuki[1], S. Takata[2], K. Ohishi[1], H. Iwase[1], Y. Kawamura[1], K. Hiroi[2], T. Morikawa[1], and M. Sahara[1]
[1]Neutron Science and Technology Center, CROSS; [2]Neutron Science Section, Materials and Life Science Division, J-PARC Center

Neutron Reflectometry Using Focusing Mirror at BL16 SOFIA

1. Introduction

Neutron reflectometry (NR) is very useful for investigations of structures of surfaces and buried interfaces composed of soft materials. SOFIA is a horizontal-type neutron reflectometer constructed at Beamline 16 (BL16) of the Materials and Life Science Experimental Facility (MLF) of the Japan Proton Accelerator Research Complex (J-PARC) [1, 2]. Due to the high-flux beam of J-PARC, less than one hour is needed for taking full Q-range data and only a few seconds for a limited Q-range data in the case of a sample with 3 inches (76 mm) in diameter; even though the beam power is still one-third of the planned value, 1 MW. However, several hours are still needed for a small sample such as 10 mm × 10 mm, which is a typical size of a sample for X-ray reflectometry.

For the further upgrade of the SOFIA reflectometer, we have developed an elliptical focusing mirror to illuminate a sample with a neutron beam with a large beam divergence. In the case of conventional double slit collimation, the optimal beam divergence decreases according to the sample size. Hence, the focusing optics with the mirror is beneficial to the beam flux, especially for small samples. The planned specifications of the focusing mirror and detector are a beam size of 0.1 mm at a sample position with divergence of 2.5 mrad.

So far, we have developed several focusing supermirrors [3–5]. The latest mirror is capable of focusing neutrons with a width of 0.13 mm in full width at half maximum (FWHM), as reported last year. This mirror has been installed in the SOFIA already, and is available to users. This year, we report in detail the reflectivity data using the focusing mirror.

2. Beam width at sample position

We employed the focusing mirror to converge neutrons on the sample position. In this geometry, a focal point is on a slit working as a virtual source, and the other is on the sample position. As the image of the virtual source is projected on the sample position, the beam size at sample position can be controlled by changing the slit width. The actual size at the sample is dependent not only on the slit width but also on a figure error of the mirror limiting the minimum beam size. Hence, we evaluated the relation between the slit width and the actual beam size at the sample first. As shown in Fig. 1, the beam size at the sample decreased with the slit width monotonically, and saturated to be approximately 0.3 mm in the full width because of the figure error.

Next, we compared the beam intensity profiles at the sample position with the focusing optics and conventional double slit optics, which would be used later. The slit width for the focusing optics was adjusted to achieve a beam width of 0.42 mm at the sample position, and that for the double slit optics was to achieve the same beam width with the largest beam intensity. Whereas the profile for the slit optics exhibited triangular shapes, that for the focusing optics exhibited Gaussian-like shape, as shown in Fig. 2. Remarkably, the peak intensity of the focusing optics was higher than that of the slit optics, and the gain factor was estimated to be 1.97 by integrating the intensities over the full width.

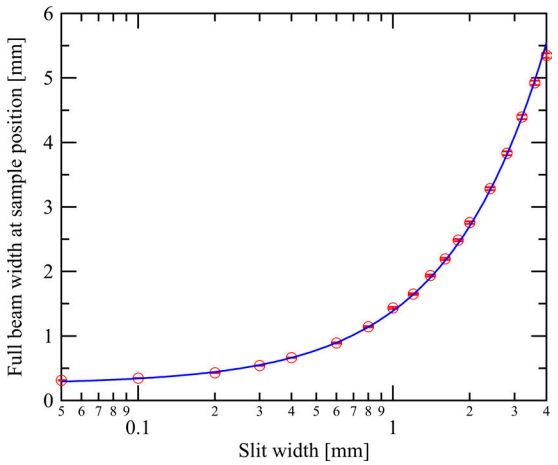

Figure 1. Full width of beam at sample position depending on slit aperture.

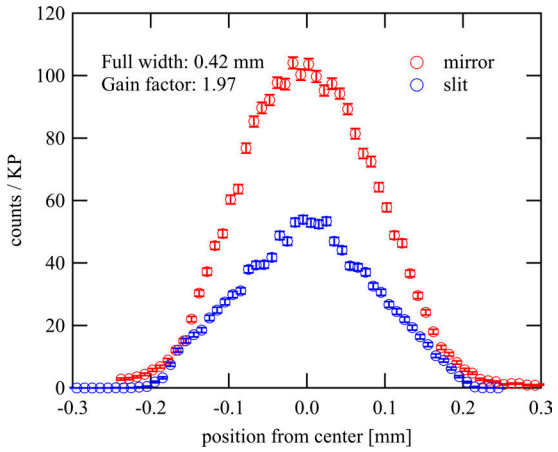

Figure 2. Comparison of beam profiles between focusing optics and slit optics at sample position.

3. Neutron reflectivity data

Next, we performed in-situ measurements of an LIB with the focusing optics and compared the results with those of the conventional slit optics. A cathode made of $LiCoO_2$ on $SrRuO_3$ was fabricated on a $SrTiO_3$ substrate with an area of 20 mm × 20 mm. This was packed with a custom-made electrochemical cell [6] and soaked in an electrolyte $LiPF_6$ solution of deuterated organic solvents, with a counter-electrode made of Li metal. The neutrons were introduced from the substrate side, the electrode in contact with the electrolyte with an area of 15 mm × 15 mm was illuminated. The reflection intensity was normalized by the direct beam intensity through the substrate to evaluate the reflectivity.

Figure 3 presents the reflectivity profiles with the two optics at the incident angle θ of 1.6°. The focusing optics could not be applied for lower angles to cover the low-Q_z region, $\theta = 0.3°$ and 0.7°, owing to the limitation of the beam size. The same data at the lower angles obtained with the double slit optics were used for both sets of data at $\theta = 1.6°$ to be merged into one set of reflectivity data. The two data points at $\theta = 1.6°$ were consistent with one another despite a slight discrepancy. To evaluate the effect of the latter on the data analysis, the two data sets were analyzed by least-squares fitting with the reflectivity. The profiles could be fitted effectively, except for the fringes around 0.25 nm^{-1}, with the model taking into account an interfacial layer on the electrode, in which the scattering length densities (SLDs) of the substrate materials and electrode were fixed to be the same as those of the bulk materials. The obtained SLD profiles along the direction normal to the substrate indicated in Fig. 4 were consistent with one another.

Note here that the accumulation time to obtain 20000 counts was reduced by a factor of 2.16 times: 258000 neutron pulses (equivalent to 10300 s) were required for the double slits, whereas 119000 (equivalent to 4760 s) were required for the focusing optics at $\theta = 1.6°$. Hence, we concluded that the interfacial layer related to the electrochemical reaction on the cathode was successfully observed with and without the focusing mirror, and the optics worked effectively to reduce the exposure time.

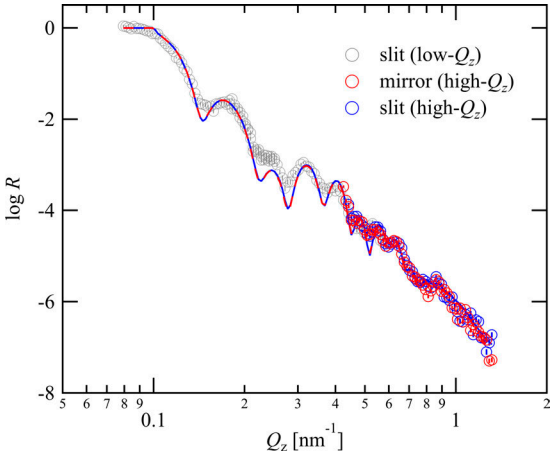

Figure 3. Reflectivity profiles obtained with double slits and focusing optics, and fitting results. As the focusing optics cannot be applied for low incident angles owing to the limitation of the beam size, the reflectivity data taken with double slits at low-Q_z values are shared for two data sets on the fitting.

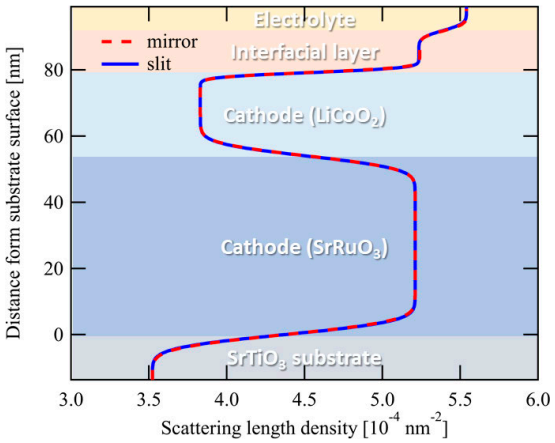

Figure 4. Scattering length density of the electrode evaluated by fitting the reflectivity data in Fig. 3.

References

[1] N. L. Yamada et. al., Euro. Phys. J. Plus, **44** (2011) 9424.
[2] K. Mitamura et. al., Polymer J., **45** (2013) 100.
[3] S. Takeda et. al., Opt. Express, **24**, (2016) 12478–12488.
[4] T. Hosobata et. al., Opt. Express, **25**, (2017) 20012–20024.
[5] T. Hosobata et. al., Opt. Express, **27**, (2019) 26807–26820.
[6] M. Yonemura et. al., IOP Conf. Ser., **502**, (2014) 012054.

N. L. Yamada[1,2], T. Hosobata[3], M. Hino[4], K. Hori[2,5], F. Nemoto[1,2,#], J. Izumi[6], K. Suzuki[6,7], M. Hirayama[6,7], R. Kanno[6,7], and Y. Yamagata[3]
[1]Neutron Science Section, Materials and Life Science Division, J-PARC Center; [2]Institute of Materials Structure Science, KEK; [3]RIKEN Center for Advanced Photonics; [4]Institute for Integrated Radiation and Nuclear Science, Kyoto University; [5]Sumitomo Rubber Industory; [6]Interdisciplinary Graduate School of Science and Engineering, Tokyo Institute of Technology; [7]Institute of Innovation Research, Tokyo Institute of Technology; [#]Present affiliation: National Defense Academy

Current Status of SHARAKU: Polarized Neutron Reflectometer

1. Introduction

The neutron reflectometer SHARAKU installed at BL17 in the Materials and Life Science Facility of J-PARC has been used for structure analysis of the surface and interfaces in a sample. Because it can perform spin-polarization analysis of the reflected neutrons using polarizing mirrors and spin flippers, it can be used for analysis of the magnetic structure. Various kinds of sample environments are available: strong magnetic field up to 7 T, refrigerator, temperature/humidity chamber, and so on. Therefore, SHARAKU has been used for structure analysis in a wide variety of research fields: polymers [1, 2], ionic liquids [3], and magnetic thin films [4, 5]. Moreover, novel methodologies for neutron reflectometry are being developed [6, 7]. In this fiscal year, we introduced a new sample environment for the measurement of a liquid/solid interface and the virtual server systems.

2. Development of sample environments

The surface/interface in an immersed condition in a liquid has been extensively studied by neutron reflectometry. A liquid immersion cell has been used in SHARAKU; however, the liquid injection needs to be performed manually by a syringe in a wet lab. Therefore, the time-resolved measurement of the structure change induced by the liquid immersion cannot be carried out. This year, we designed a new liquid cell shown in Fig. 1. It has a liquid reservoir tank equipped with a solenoid valve. Because the operation of the valve is controlled by the measurement software, the liquid injection and data acquisition can be synchronized.

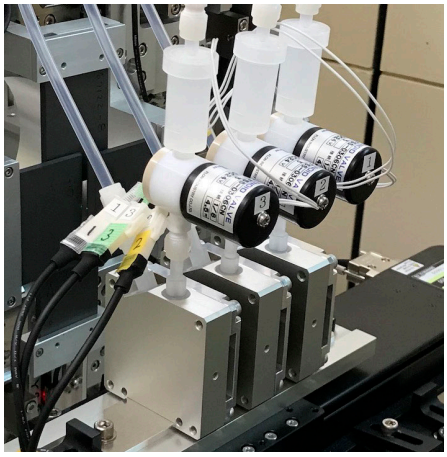

Figure 1. Liquid immersion cells.

3. Upgrade of the computer systems

In SHARAKU, eighteen server machines are used to control the B_4C slit devices, sample stage, polarizing optics, data acquisition, and sample environments. SHARAKU was installed at the MLF eight years ago; therefore, the server machines and the operating system are obsolete. Therefore, in recent years, the old server computers have been replaced with new ones. In this replacement process, we apply the virtualization of the server systems. One physical machine can run several virtual computer systems for the operation of SHARAKU, as shown schematically in Fig. 2. This year, the server systems for the device control, data analysis, and the document archive have been migrated to a single host computer. The important merit of the virtualization of the server system is redundancy. Each virtual system installed in the host system is backed up to a storage system in a different physical server machine. Therefore, in case of a fatal failure of the computer system, the system will be recovered with minimal

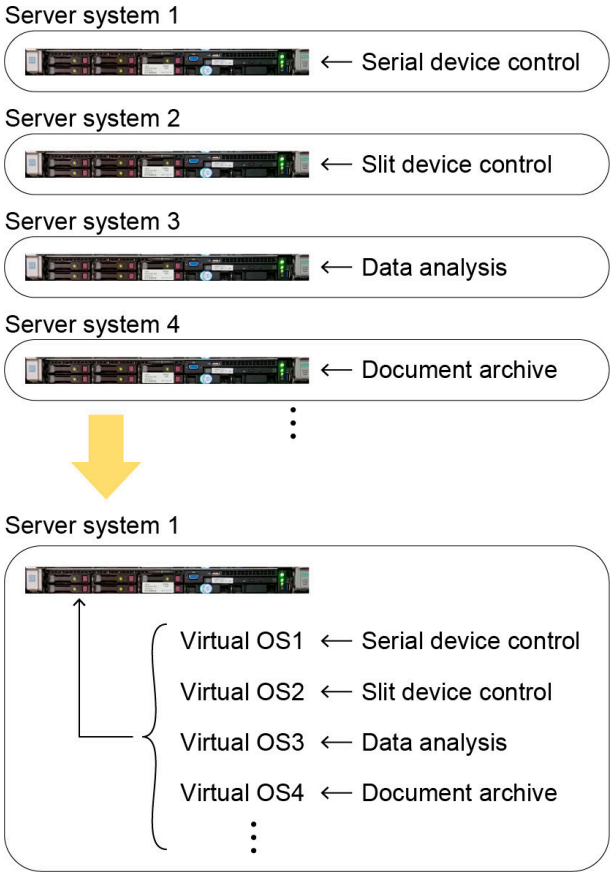

Figure 2. Virtualization of the server systems.

down-time by running the backed-up system on the other computer. Another advantage of the virtual system is the safety in the development of the software. In the tuning and optimizing process of the device operation, an error in the program code would sometimes cause a serious failure in the server. In that case, the whole system can be easily rolled back to the original state before the failure.

References

[1] H. Aoki, Polym. J., **51** 611 (2019).
[2] T. Miyazak et al., Langmuir, **35** 11099 (2019).
[3] K. Akutsu-Suyama et al., Phys. Chem. Chem. Phys., **21** 17512 (2019).
[4] M. Mogi et al., Phys. Rev. Lett., **123** 016804 (2019).
[5] Y. Zhong et al., AIP Advances, **10** 015323 (2019).
[6] K. Sakurai et al., Sci. Rep., **9** 571 (2019).
[7] T. Kumada et al., J. Appl. Cryst., **52** 1054 (2019).

H. Aoki[1,2], K. Soyama[3], D. Yamazaki[4], N. Miyata[5], K. Akutsu[5], T. Hanashima[5], and S. Kasai[5]
[1]Neutron Science Section, Materials and Life Science Division, J-PARC Center; [2]Institute of Materials Structure Science, KEK; [3]Materials and Life Science Division, J-PARC Center; [4]Neutron Instrumentation Section, Materials and Life Science Division, J-PARC Center; [5]Neutron Science and Technology Center, CROSS

Status of SENJU 2019

1. Introduction

SENJU is a TOF single-crystal neutron diffractometer designed for precise crystal and magnetic structure analyses under multiple extreme environments, such as low-temperature, high-pressure and high-magnetic field, as well as for taking diffraction intensities of small single crystals with a volume of less than 1.0 mm^3 down to 0.1 mm^3 [1]. Ever since SENJU was launched in 2012, continuous commissioning and upgrading operations have been carried out.

In 2019, we installed four new additional detectors at the obliquely downward direction of the sample position and developed a remote-access version of the data processing and visualization software for SENJU, STARGazer-Online. In addition, we also report on the purposes, for which the instrument beam-time for SENJU was used.

2. Installation of additional area detectors

The detector arrangement of SENJU was almost cylindrical, 36 detectors were arranged cylindrically around the sample position and only one was positioned at its bottom. Consequently, the obliquely downward direction of the sample position was not covered by the detector and the reciprocal space around the azimuth region of the ϕ-axis was not measured without pulling out the goniometer and changing the sample orientation. To solve this problem, we have added four area detectors at the obliquely downward direction of the sample position. The additional detectors were newly developed for SENJU. The detector thickness is 17 cm, 13 cm thicker than its previous version. The slimness made it possible to put the new detectors at the obliquely downward direction of the sample position. The arrangement of the additional detectors is shown in Fig. 1.

The positional parameters of the additional detectors were accurately fixed by diffraction images of a standard single crystal, C12A7. The calibration procedure is almost the same as that described in the MLF Annual Report 2018 [2]. After the calibration, structure analysis of a ruby single crystal was performed by using all detectors, including the additional four detectors. The obtained structural parameters were reasonable and the final R-factor ($I > 5\sigma(I)$) was 5.19%. Those results showed that the new detectors worked correctly.

3. Development of STARGazer-Online

Both the data processing software, which creates a reflection file (called "HKLF file") from raw data, and the data visualization software, which visualizes and analyzes the diffraction pattern in the real-space or reciprocal-space, are essential components of a single crystal diffractometer. For SENJU, a software suite called "STARGazer for SENJU" is used for data processing and visualization. Although STARGazer for SENJU is an indispensable software for SENJU data, it inconveniences the SENJU users because it works on CentOS, not Windows or Macintosh, and the size of the raw data is very large (~50 GB). Consequently, it becomes a hurdle for the

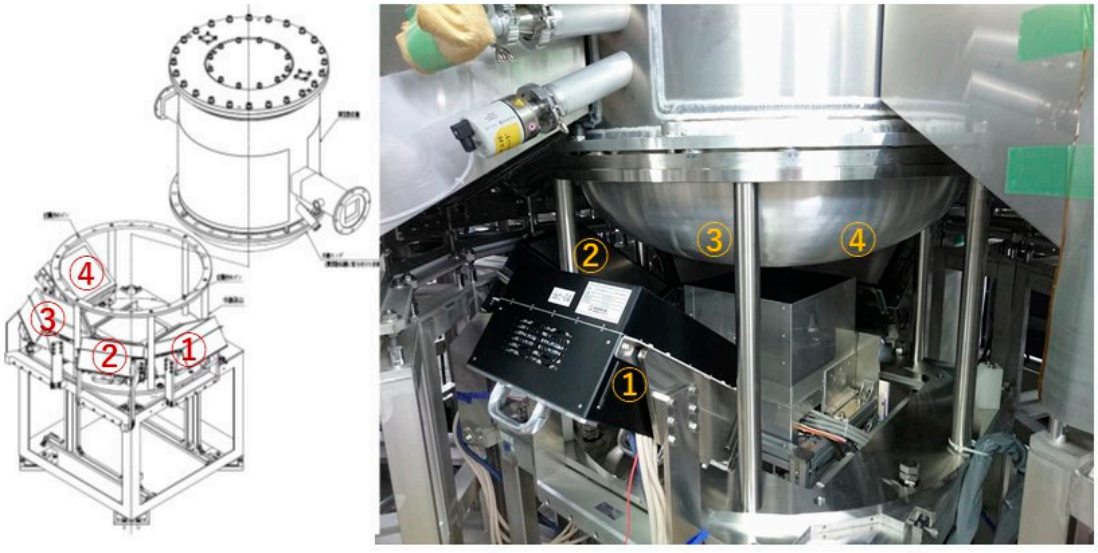

Figure 1. Arrangement of the additional area detectors (①~④ in the figure).

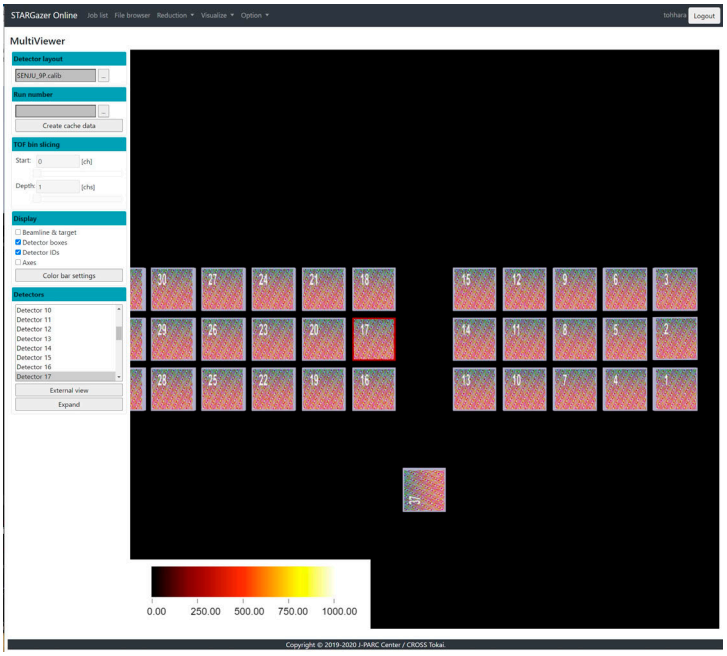

Figure 2. Screenshots of the data visualization component of STARGazer Online.

SENJU users to process and visualize their data at their local laboratory sites. To solve this problem, we have developed a remote-access version of the STARGazer for SENJU, named STARGazer Online.

STARGazer Online is a web application that works on the Google Chrome browser. The core components for data processing and data storage work on a cloud computing service, Amazon Web Service (AWS). SENJU users' access AWS by a web browser and process their raw data at their local laboratories. The user information and raw data are managed by the User-ID and password.

Figure 2 shows a screenshot of STARGazer Online working on Google Chrome. Almost all data processing and data visualization functions of STARGazer for SENJU work on STARGazer Online. Because of COVID-19, such a remote data processing software becomes more and more important.

4. Use of the instrument beam time

In 2019, the instrument beam time was used mainly for measurements of standard samples, and a vanadium-nickel alloy for calibration of the detector efficiency.

References

[1] T. Ohhara et al., J. Appl. Cryst., **49** 120 (2016).
[2] T. Ohhara et al., MLF Annual Report 2018, 102 (2019).

T. Ohhara[1], R. Kiyanagi[1], A. Nakao[2], K. Munakata[2], Y. Ishikawa[2], K. Moriyama[2], I. Tamura[1], and K. Kaneko[1]
[1]Neutron Science Section, Materials and Life Science Division, J-PARC Center; [2]Neutron Science and Technology Center, CROSS

Engineering Material Diffractometer TAKUMI

1. Introduction

TAKUMI is a neutron diffractometer dedicated for research in engineering materials sciences, which was installed at Beamline 19 in the MLF of J-PARC. Careful analysis of the Bragg peaks in a neutron diffraction pattern can reveal important structural details of a sample material, such as internal stresses, phase conditions, dislocations, texture, etc. Experiments in TAKUMI vary from internal strain mapping in engineering components, microstructural evolutions during deformations of structural or functional materials at various temperatures, microstructural evolutions during manufacturing (thermo-mechanical) processes, to texture analyses of engineering materials.

2. User program and publications

In FY2019, 25 general-use programs, 2 long-term programs and 1 project-use program were successfully conducted on TAKUMI. However, due to the consequences of COVID-19, one general-use program has not yet been conducted. The ratio of approved experiments versus proposed experiments was 75% (12/16) for 2019A and 58% (14/24) for 2019B. The statistics about the experimental types and the sample materials of conducted experiments during FY2019 are summarized in Fig. 1. More than half of the beamtime was occupied by in-situ measurement during a loading test, the same as every year. In particular, the demand for low-temperature environment has been increasing in the past few years due to the expanding research of the deformation properties of high-entropy alloys. As of the high-temperature environment, the demands are growing for in-situ measurements during thermo-mechanical controlled processes, which include rapid heating, cooling and deformation. Currently, the instrument "thermec-mastor" [1] is often used for this kind of experiments. After the next year (FY2020), the new loading machine equipped with an induction heating system will be opened for users. On the other hand, 14% of the beamtime was used for strain mapping experiments for internal strain (stress) analysis of mechanical parts. Most of this kind of experiments were proposed by industrial users. They involved measuring of iron- or aluminum-based objects. Reflecting the importance of iron and steel as structural materials, the percentage of these materials in all the samples was 35%. Summarizing the percentages for light metals (Al-, Mg- and Ti-based alloys, 19%) and metals and alloys (Ni-based superalloy, high-entropy alloys and other alloys, 32%), it becomes clear that 86% of the beamtime was used for experiments with metallic material samples. In contrast, the percentage of experiments with non-metallic samples (rocks and ceramics) was only 4%. Further utilization promotion of TAKUMI to the researchers in this field would be effective to enhance the research field around TAKUMI.

Thanks to the users and the collaborators, 18 papers and 2 proceedings papers using the data measured at TAKUMI have been published in FY2019. In addition, the data were also used in 2 doctoral theses. Some of highlighted papers are introduced below:

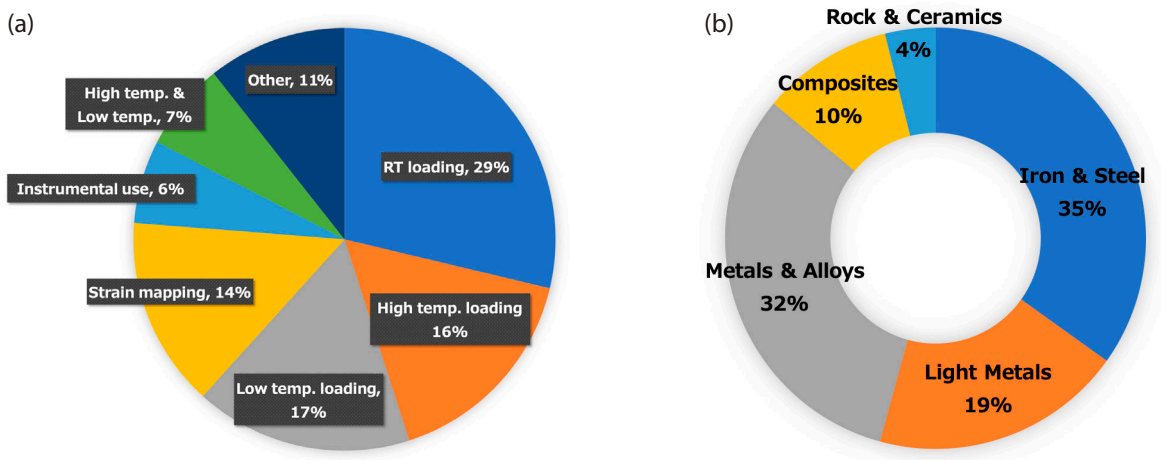

Figure 1. The statistics of (a) the kinds of experiments conducted at TAKUMI and (b) the kinds of materials used in these experiments in FY2019. The percentages are shown for the beamtime (days).

(a) "**Cooperative deformation in high-entropy alloys at ultralow temperatures**", by Naeem Muhammad et al., [2]. The interaction of a rich variety of deformation mechanisms in high-entropy alloys at 15 K, which began with dislocation slip, followed by stacking faults and twinning, was demonstrated using in-situ neutron diffraction.

(b) "**Real time observation of martensite transformation for a 0.4 C low alloyed steel by neutron diffraction**", by Wang Yanxu et al., [3]. In-situ neutron diffraction with a thermomechanically controlled processing simulator was employed to investigate martensitic transformation behavior with and without ausforming for a medium-carbon low-alloy steel. Cutting-edge operant quantitative measurements with neutron diffraction for steel production were demonstrated.

(c) "**Plastic anisotropy and deformation-induced phase transformation of additive manufactured stainless steel**", by Chae Hobyung et al., [4]. Plastic anisotropy and deformation-induced phase transformation of additively manufactured stainless steels were investigated. Different onsets of strain nonlinearity between different manufactured directions were closely related to martensitic transformation.

(d) "**In-situ investigation of the microstructure evolution in long-period-stacking-ordered (LPSO) magnesium alloys as a function of the temperature**", by Máthis Kristián et al., [5]. Deformation behavior of two Mg–Zn–Y alloys, with a different fraction of the long-period-stacking-ordered (LPSO) phase, was investigated by a combination of in-situ neutron diffraction and acoustic emission. The results indicated that the twinning in the magnesium matrix and the kinking in the LPSO phase strongly depend on the composition of the material and the testing temperature.

(e) "**Study on formation mechanism of {332} <113> deformation twinning in metastable β-type Ti alloy focusing on stress-induced α" martensite phase**", by Ken Cho et al. [6]. Deformation behavior of Ti–12Mo alloy which is primarily deformed by {332}<113> deformation twinning was studied. The formation of stress-induced α" martensite, which is acting as a nucleation site for the {332}<113> twins at the initial stage of the plastic deformation, was directly observed.

3. Future plans

To make TAKUMI more user-friendly, several upgrades on the sample environment devices and the software are scheduled after FY2020, as follows:

(1) Development of the new sample chamber for low-temperature deformation tests. The sample change and the temperature control are expected to be more convenient with this chamber.

(2) Installation of the large tilting stage for strain mapping. Alignment of large samples (< 150 kg) will become easier to do using this stage.

(3) Upgrades of the real-time monitoring software for the diffraction patterns and the device control software.

References

[1] A. Shibata et al., Scripta Mater., **165** 44 (2019).
[2] M. Naeem et al., Sci. Adv., **6** eaax4002 (2020).
[3] Y.X. Wang et al., Acta Mater., **184** 30 (2020).
[4] H. Chae et al., Mater. Sci. Eng. A, **762** 138065 (2019).
[5] K. Máthis et al., Front. Mater., **6** 270 (2019).
[6] K. Cho et al., Scripta Mater., **177** 106 (2020).

T. Kawasaki[1], S. Harjo[1], and K. Aizawa[2]
[1]Neutron Science Section, Materials and Life Science Division, J-PARC Center; [2]Materials and Life Science Division, J-PARC Center

The Current Status of the Versatile Neutron Diffractometer, iMATERIA

1. Introduction

Ibaraki Prefecture, local government of Japan's area where the J-PARC sites are located, has decided to build a versatile neutron diffractometer (IBARAKI Materials Design Diffractometer, iMATERIA [1]) to promote industrial applications for the neutron beam in J-PARC. iMATERIA is planned to be a high-throughput diffractometer that could be used by materials engineers and scientists in their materials development work, including chemical analytical instruments.

The applications of neutron diffraction in materials science are (1) to do structural analyses of newly developed materials, (2) to clarify the correlation between structures and properties (functions), and (3) to clarify the relation between structural changes and improvements of functions, especially for practical materials. A diffractometer with super high resolution is not required to achieve those goals. The match of features like intermediate resolution around $\Delta d/d = 0.15\%$, high intensity and wide d coverage is more important.

This diffractometer is designed to look at a decoupled-poisoned liquid hydrogen moderator (36 mm, off-centered) (BL20), and it has an incident flight path (L1) of 26.5 m, with three wavelength selection disk-choppers and straight neutron guides with a total length of 14.0 m. The instrumental parameters are listed in Table 1. There are four detector banks, including a low-angle and small-angle scattering detector bank. The angular coverage of each detector bank is also shown in Table 1. The rotation speeds for the disk-choppers are the same, with a pulse repetition rate of 25 Hz for the most applications (SF mode). In this case, the diffractometer covers $0.18 < d$ (Å) < 2.5 with $\Delta d/d = 0.16\%$ and covers $2.5 < d$ (Å) < 800 at three detector banks of 90-degree, low-angle and small-angle with gradually changing resolution. When the speed of the wavelength selection disk-choppers is reduced to 12.5 Hz (DF mode), we can access a wider d-range, $0.18 < d$ (Å) < 5 with $\Delta d/d = 0.16\%$, and $5 < d$ (Å) < 800 with gradually changing resolution with doubled measurement time compared to the SF mode.

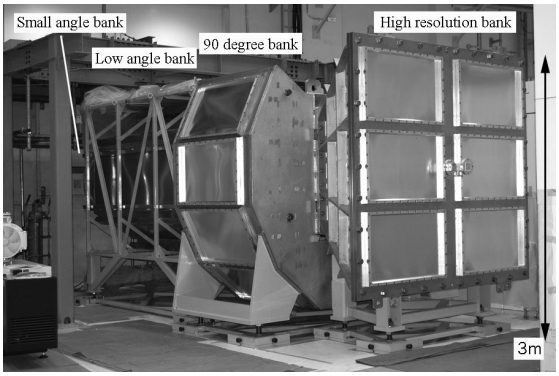

Figure 1. IBARAKI Materials Design Diffractometer, iMATERIA without detector for each bank and instrument shielding. The high-resolution bank, special environment bank (90-degree bank), and low-angle bank, can be seen from right to left. The small-angle detector bank, which is not shown in the picture, is situated in the low-angle vacuum chamber (left-hand side of the picture).

Table 1. Instrumental parameters of iMATERIA. L2 is the scattered flight path. The d-range (q-range) for each bank is the maximum value for 2-measurement mode.

L1	26.5 m	
Guide length		Total 14 m (3section)
Position of Disk choppers		7.5 m (double) 11.25 m (single) 18.75 m (single)
High Resolution Bank	2θ L2 d-range	$150° \le 2\theta \le 175$ 2.0 - 2.3 m $0.09 \le$ d (Å) ≤ 5.0
Special Environment Bank	2θ L2 d-range	$80° \le 2\theta \le 100°$ 1.5 m $0.127 \le$ d (Å) ≤ 7.2
Low Angle Bank	2θ L2 d-range	$10° \le 2\theta \le 40°$ 1.2 - 4.5 m $0.37 \le$ d (Å) ≤ 58
Small Angle Bank	2θ L2 q-range	$0.7° \le 2\theta \le 5°$ 4.5 m $0.007 \le$ q ($Å^{-1}$) ≤ 0.6

2. Current status

All of the four banks, high-resolution bank (BS bank), special environment bank (90-degree bank), low-angle bank and small-angle bank, are operational. It takes about 5 minutes (in DF mode) to obtain a 'Rietveld-quality' data in the high-resolution bank at 600 kW beam power for about 1 g of standard oxide samples.

Figure 2 shows a typical Rietveld refinement pattern for $LiCoO_2$ sample, cathode material for lithium ion battery (LIB), at the high-resolution (BS) bank by the multi-bank analysis function of Z-Rietveld [2]. It takes 20 min in DF mode to collect the available Rietveld data, due to the high neutron absorption cross section for natural Li ($\sigma_s^{Nat} = 70$ barn).

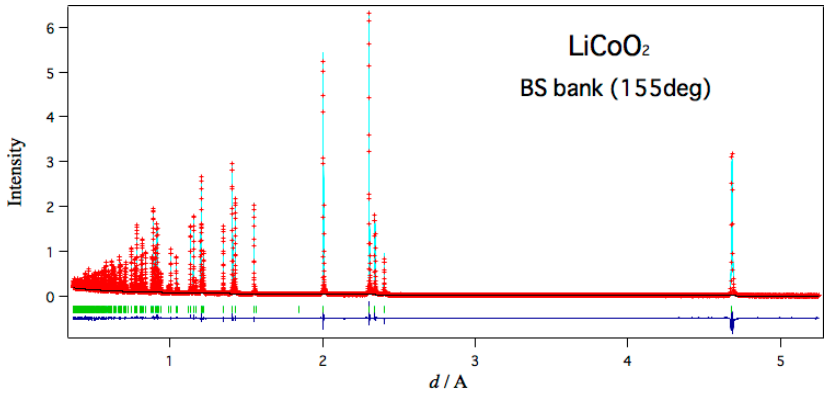

Figure 2. Rietveld refinement pattern for $LiCoO_2$ at the high-resolution bank of iMATERIA.

3. Sample Environments

The automatic sample changer is the most important sample environment for high-throughput experiments. Our automatic sample changer [3] consists of a sample storage, elevating system of two lines, two sets of pre-vacuum chambers and a sample sorting system. We can handle more than 600 samples continuously at room temperature without breaking the vacuum of the sample chamber.

The V-furnace (~900°C), the gas flow furnace (~1000°C), the cryo-furnace (4K) and the 1K cryo are ready for experiments. The in-operando charge and discharge measurement system for LIB with a sample changer is available in cylindrical, coin, and laminated types of batteries.

The rapid heating/quenching furnace with an automatic sample changer (RT – 1273 K with heating speed 10 K/s and cooling speed > 20 K/s) [4] and the universal deformation testing machine (maximum loading 50 kN with RT – 1273 K) [5] are available for texture measurements.

References

[1] T. Ishigaki et al., Nucl. Instr. Meth. Phys. Res. A, **600** 189 (2009).
[2] R. Oishi et al., Nucl. Instr. Meth. Phys. Res. A, **600** 94 (2009).
[3] A. Hoshikawa et al., J. Phys.: Conf. Ser., **251** 012083 (2010).
[4] Y. Onuki et al., Metall. Mat. Trans. A., **50** 4977 (2019).
[5] Y. Onuki et al., Quantum Beam Sci., **4** 31 (2020).

T. Ishigaki, A. Hoshikawa, T. Matsukawa, and Y. Onuki
Frontier Research Center for Applied Atomic Sciences, Ibaraki University

Status of the High Intensity Total Diffractometer (BL21, NOVA)

1. Introduction

Total scattering is a powerful technique to analyze disordered structure in materials with atomic Pair Distribution Function (PDF). NOVA was designed to perform total scattering and is the most intense powder diffractometer with reasonable resolution ($\Delta d/d \sim 0.5\%$) in J-PARC. It is easy to adapt NOVA to a very wide area of fields: liquids, glasses, local disordered crystalline materials, magnetic structures, and so on.

The development of NOVA has three main objectives: small amount of the sample, short time measurement, and precise analysis. So far, the diffraction pattern of only 1-mg complex hydride ($YLiFeH_6$) [1] and 0.3 μ_B magnetic moment of a superconductor ($LaFeAsO_{0.55}H_{0.45}$) [2] have been measured. In addition, Pd to PdD_2 time-transient measurement in 10 seconds was reported [3]. On the other hand, it is necessary to evaluate the convergence for the measurement time to provide a method for high throughput experiments. Hence, Rietveld refinement of diffraction patterns and PDF analysis for standard materials were carried out.

2. Performance evaluation

Si powder (NIST standard reference material 640d) was measured from 1 sec to 3 h. The structure factor $S(Q)$ was refined by Z-Rietveld [4, 5] (Fig. 1). It is possible to analyze even a 1-sec measurement pattern. The atomic pair distribution function $G(r)$ was obtained by the Fourier transformation of $S(Q)$ and analyzed by PDFgui [6] (Fig. 2). A measurement longer than 1 min is necessary to get PDF with sufficient statistics. The Rietveld refinements were evaluated by reliability factors;

$$R_{wp} = \left\{ \frac{\sum w_i [y_i - f_i(x)]^2}{\sum w_i y_i^2} \right\}^{1/2} \quad (1)$$

$$R_e = \left(\frac{N-P}{\sum w_i y_i^2} \right)^{1/2} \quad (2)$$

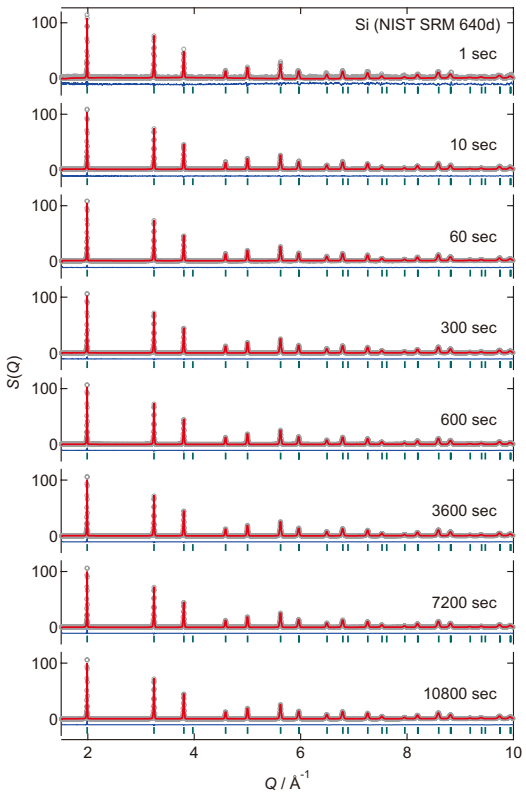

Figure 1. $S(Q)$ and Rietveld refinement results of Si powder (NIST SRM 640d) measured from 1 sec to 3 h at 500 kW. The observed, calculated and difference patterns are indicated as gray circles, red and blue lines, respectively.

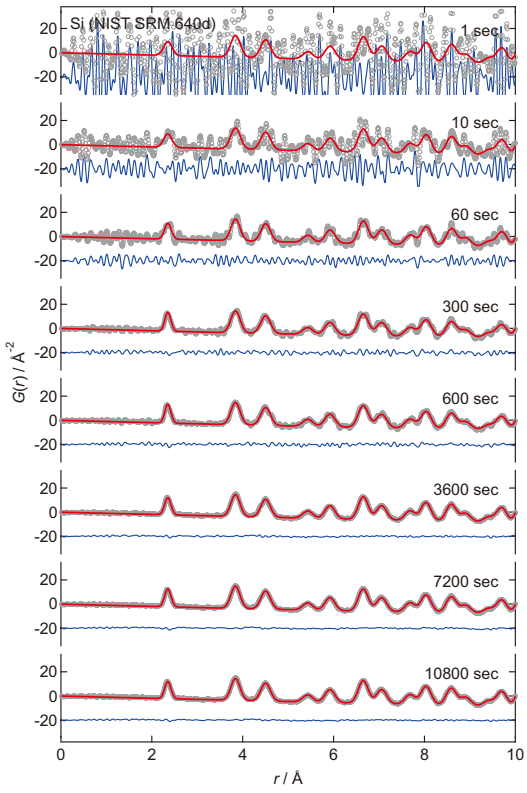

Figure 2. $G(r)$ and PDF analysis results of Si powder (NIST SRM 640d) measured from 1 sec to 3 h at 500 kW. The observed, calculated and difference patterns are indicated as gray circles, red and blue lines, respectively.

where, w_i is statistic weight, y_i is observed intensity, $f_i(x)$ is theoretical intensity, N is data point number, P is parameter point number, respectively. R_e is statistically the smallest value of R_{wp} that monotonically decreased depending on measuring time, but R_{wp} reaches a plateau at a certain time (Fig. 3). This means that about 5-min measurement of Si powder at 900 kW operation is enough to refine the diffraction pattern. On the other hand, PDF analysis needs a 1-h measurement according to the reliability factor R_w similar to R_{wp} in the Rietveld refinements. Also, Figure 3 shows that the required measuring time is reduced by enhancing the beam power of the MLF at J-PARC.

In addition, $S(Q)$ of SiO_2 glass rod was obtained and the Radial Distribution Function $RDF(r)$ was evaluated for several measuring time periods (Fig. 4). The coordination numbers deduced by Gaussian fitting of RDF were sufficiently converged for a measuring time of 200 sec or more at 900 kW (Fig. 5). Since these evaluations depend on the statistics of background data, a comprehensive procedure to estimate the required measuring time during experiments needs to be introduced.

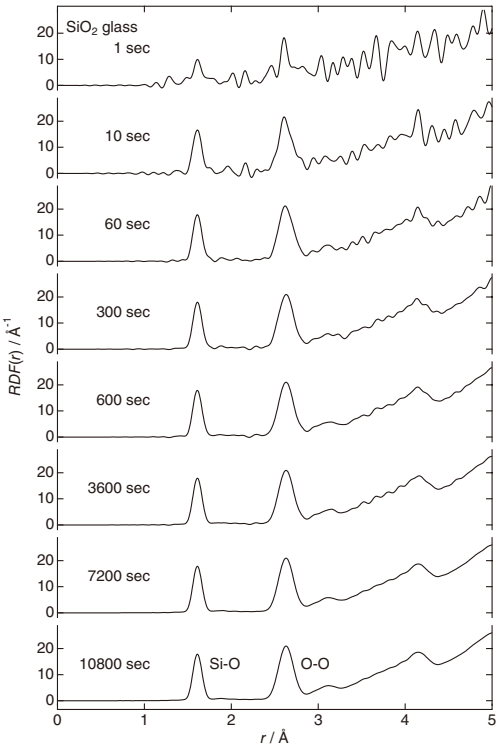

Figure 4. *RDF*(*r*) of SiO_2 glass rod measured from 1 sec to 3 h at 900 kW.

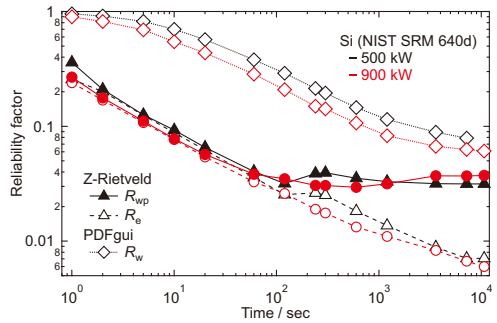

Figure 3. Reliability factors of Rietveld refinement and PDF analysis of Si powder.

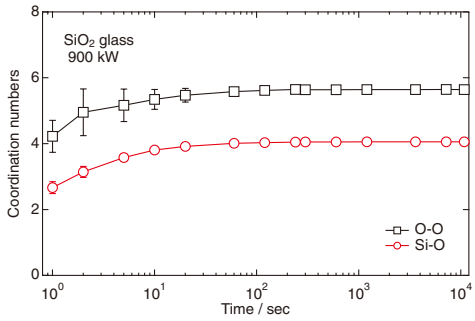

Figure 5. Coordination numbers obtained by Gaussian fitting to *RDF*(*r*) of SiO_2 glass.

Acknowledgement

The operation and developments of NOVA was performed under the S1-type program (2019S06) approved by the Neutron Scattering Program Advisory Committee of IMSS, KEK.

References

[1] T. Otomo et al., MLF Annual Report 2012, 114 (2013).
[2] M. Hiraishi et al., Nature Phys., **10** 300–303 (2014).
[3] T. Otomo et al., MLF Annual Report 2013, 113 (2014).
[4] R. Oishi et al., Nucl. Instrum. Methods Phys. Res. A, **600** 94–96 (2009).
[5] R. Oishi-Tomiyasu et al., J. Appl. Cryst., **45** 299–308 (2012).
[6] C.L. Farrow, P. Luhás, J.W. Liu, D. Bryndin, E.S. Božin, J. Bloch, Th. Proffen and S.J.L. Billinge: J. Phys.: Condens. Matter, **19** 335219 (2007).

K. Ikeda[1,2,3], T. Otomo[1,2,3,4], T. Honda[1,2,3], H. Ohshita[1,2], Y. Onodera[5], T. Hawai[1], K. Ono[1], S. Sashida[3], and M. Tsunoda[4]

[1]*Institute of Materials Structure Science, KEK;* [2]*Neutron Science Section, Materials and Life Science Division, J-PARC Center;* [3]*Department Materials Structure Science, The Graduate University for Advanced Studies;* [4]*Graduate School of Science and Engineering, Ibaraki University;* [5]*Institute for Integrated Radiation and Nuclear Science, Kyoto University*

Status of the Energy-Resolved Neutron Imaging System RADEN

1. Introduction

The energy-resolved neutron imaging system "RADEN", installed at beamline BL22 in the Materials and Life Science Experimental Facility (MLF) of J-PARC, is a dedicated instrument for wavelength/energy-dependent neutron imaging experiments, which fully utilizes the nature of the short-pulsed neutron [1]. Then, variety of imaging experiments have been conducted, such as, the Bragg-edge imaging for crystallographic structure information, the neutron resonance absorption imaging for elemental or thermal information, and the polarized pulsed neutron imaging for magnetic field information. After the beam line construction was completed, RADEN now accepts about 30 user programs every year, from broad academic to industrial fields. In this report, we will explain the current status of RADEN's activities, including technical developments and application studies.

2. Technical development of the neutron imaging

To conduct high-spatial resolution imaging, we tested three thin scintillator screens (^{6}LiF/ZnS with 50 μm-thickness, GdOx with 50 μm-thickness, and GdOx with 30 μm-thickness) and evaluated their resolution performance by means of the Modulation Transfer Function (MTF) method using neutron transmission images of test patterns [2, 3]. The obtained spatial resolution values were 58.3, 42.4, and 35.9 μm for ^{6}LiF/ZnS (50 μm), GdOx (50 μm), and GdOx (30 μm), respectively. Although these numbers were slightly larger than the visually recognized spatial resolution, we could achieve fine spatial resolution imaging of less than 50 μm by means of GdOx scintillator screens (Fig. 1). Similarly, we also studied the performance of high-resolution CT experiments using a simple sample composed of several metallic cylinders, and spatial resolution of 115 μm was evaluated by using the same method of analysis as in normal radiography.

Next, the neutron phase imaging apparatus based on the Talbot-Lau interferometer for RADEN was replaced with a new one with an optimized design. Previously, the apparatus was designed with a central wavelength of 5 Å to fully cover the RADEN's neutron spectrum for achieving precise differential phase imaging. However, since the weak neutron intensity in the longer wavelength neutron range made the measurement time longer, the central wavelength was changed to 2.7 Å to utilize effectively the peak intensity of the spectrum (Fig. 2). As a result of the new design, the available wavelength range became narrower than the previous one, but the measurement time was reduced by more than half and the scanning range of auto-correlation length by visibility contrast image, which can be obtained together with the differential phase contrast images, became wider. The obtained visibility of the new system was about 60% at the central wavelength with a wavelength resolution of 50%, and demonstration

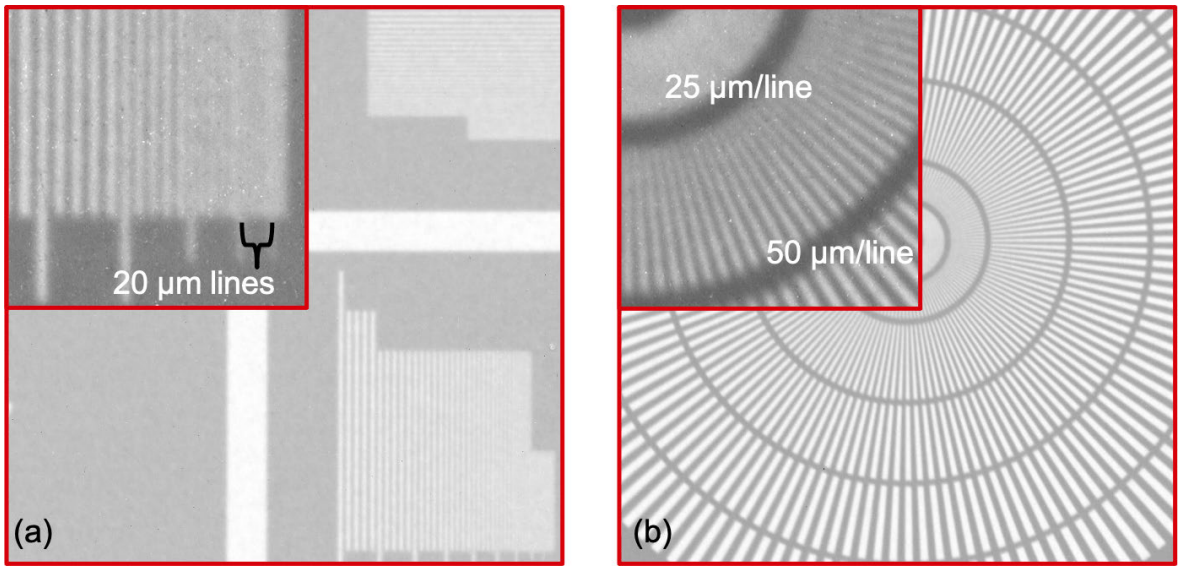

Figure 1. Images of test patterns obtained using 30 μm-thick GdOx scintillator. (a): line pattern [2], (b) Siemens star pattern [3].

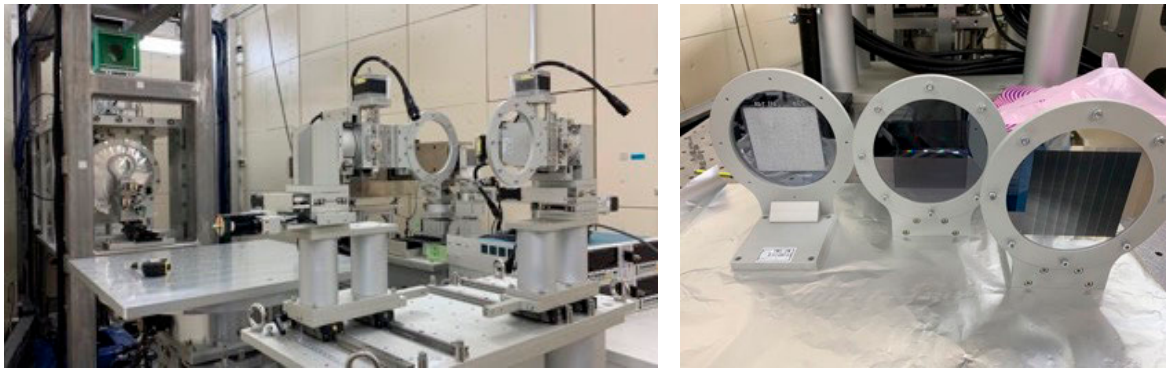

Figure 2. Photographs of the new phase imaging apparatus. Left: neutron Talbot-Lau interferometer installed at RADEN. Right: newly fabricated gratings.

studies using a permanent magnet sample and additively manufactured metallic samples were conducted. In the study, using a permanent magnet, partially demagnetized by local heating treatment, the magnetization direction and the diminishment of magnetic domain size could be analyzed by the directional analysis of the correlation length dependence of the visibility.

3. Application studies

Recently, neutron imaging studies on the distinction of the water and the ice have been conducted using energy selection of the pulsed neutron beam. Because the total neutron cross section of water in the low neutron energy region differs between liquid and iced state, it is possible to identify the water and the ice from the energy-dependent neutron transmission measurements. This technique has already been applied to the fuel cell study [4], but by using pulsed neutrons, scanning broad energy range can compensate for the difference of molecular density between water and ice using the neutron transmission at the high-energy region, where their cross sections are similar, and can distinguish the state of water using that at a low-energy region, where their cross sections are different. Hence, it is possible to recognize their states accurately free from the influence of the density change. With this technique, we succeeded in visualizing the thawing process of ice in a metallic narrow capillary [5].

As another application of neutron imaging, the demands for visualizing spatial distribution of large-neutron absorbing elements like Boron are increasing. The epithermal neutron radiography and tomography are suitable technique for this, but we are also developing a technique combining the epithermal neutron imaging and the prompt gamma-ray analysis, which enables us to conduct quantitative analysis of such elements in the sample with spatial resolution.

4. Summary and future plans

Now, RADEN is under user operation and its application spreads widely in various fields, both scientific and industrial. In addition to the user programs, RADEN's improvement as an instrument and the development of neutron imaging techniques continue.

References

[1] T. Shinohara et al., Rev. Sci. Instrum., **91**, 043302 (2020).
[2] M. Segawa, et al., JPS Conf. Proc. **22**, 011028 (2018).
[3] C. Grünzweig, et al., Rev. Sci. Instrum. **78**, 053708 (2007).
[4] M. Siegwart, et al., Rev. Sci. Instrum., **90**, 103705 (2019).
[5] Y. Higuchi, et al., Phys. Chem. Chem. Phys. (accepted).

T. Shinohara[1], T. Kai[1], K. Oikawa[1], Y. Tsuchikawa[1], K. Isegawa[1], K. Hiroi[1], T. Nakatani[2], Y. Su[2], H. Hayashida[3], J. D. Parker[3], Y. Matsumoto[3], and Y. Kiyanagi[4]

[1]Neutron Science Section, Materials and Life Science Division, J-PARC Center; [2]Technology Development Section, Materials and Life Science Division, J-PARC Center; [3]Neutron Science and Technology Center, CROSS; [4]Graduate School of Engineering, Nagoya University

Polarized Neutron Spectrometer POLANO

1. Introduction

POLANO is a direct geometry spectrometer with middle energy and spatial resolution. In combination with the SEOP ^{3}He gas spin filter and the 5.5 Qc bending mirror analyzer, the POLANO makes it possible the higher-energy polarization analysis [1–3]. The construction of the spectrometer started in 2012 and was mostly completed by 2016. Following beam commissioning and many mechanical tests, a part of the user program with an unpolarized neutron beam has finally started. The neutron polarization technique with the time-of-flight (tof) method was introduced in recent years, and the devices had to be re-designed to conform to the tof method. Many of technical or mechanical restrictions and difficulties arising out of a new concept of new technique, have been kept making much effort to overcome and to realize better polarization analysis in the tof method in the world neutron facilities.

By 2019, some of those neutron facilities put into practice the tof polarization technique, but all of them are focusing on polarization analysis with low-energy region of the transfer energy up to several tens of meV. However, these energy ranges of polarization analysis have been actually done so far with reactor-based neutrons. In the research of the dynamical properties of atoms, spins, charges, orbitals, and so on, the energy scale could reach over 100 meV. The POLANO was designed to realize much higher-energy polarization analysis through the combination of a SEOP ^{3}He spin filter and an analyzer mirror as the first step. This enables us to reach higher transfer energy (Ef ~ 42 meV). As the second step, we plan to use the wide angle SEOP/MEOP system as an analyzer. In this second step, we are targeting polarization analysis with neutron energy (transfer energy) of up to 100 meV, covering an absolutely wide momentum and energy region in the reciprocal space.

2. Polarization devices

As we reported in the last year's annual report, a set of a SEOP polarization system, Helmholtz coils for applying both vertical and horizontal magnetic fields on the measurement sample, and a guide field to maintain the neutron spin polarization including a supermirror analyzer will be stationed in the beamline as depicted in Fig. 1. This magnetic system is indispensable to control the spin direction, to apply the appropriate magnetic fields, and to maintain the neutron spin direction. The system is composed of several magnetic devices, namely,

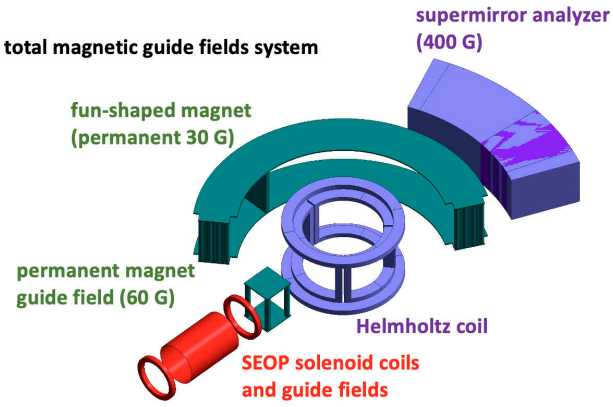

Figure 1. The suite of magnets including SEOP ^{3}He polarizer, Helmholtz coils, analyzer mirror, and guide fields.

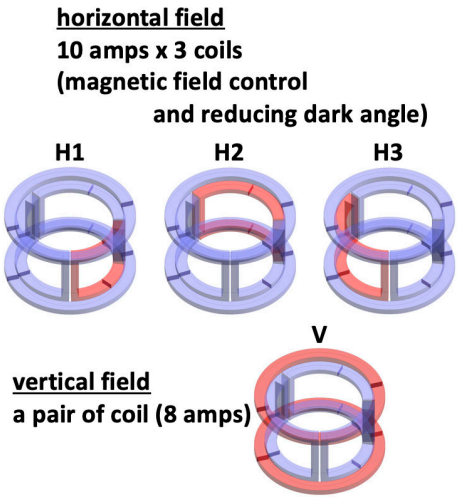

Figure 2. Asymmetric Helmholtz coils applying flexible magnetic fields on the sample.

guide field systems that combine permanent magnets, a pair of SEOP solenoid coils, asymmetric Helmholtz coils at the sample position, and a magnetic analyzer mirror. Other magnetic devices, such as spin flippers or a field controlling system at the sample position, will be developed in the future. We made much effort to research, design, and manufacture the above magnetic devices, in particular the Helmholtz coil, which was one of the most significant but also complicated devices (Fig. 2). There are three coils for applying horizontal fields to any 360° direction in the scattering plane. And there is a pair of coils for the vertical field. All these four coils need about 10 Amps each, yielding almost 200°C of high temperature in specific part of the coils. So, we developed a highly efficient water-cooling system for this Helmholtz coil keeping the magnet temperature below 100°C.

The cooling system can be effective even in the vacuum using high performance "heat pipes" for heat removal. The heat test was very successful, we got up to 80°C at maximum.

The SEOP polarizer system is almost ready to debut [4]. We are now trying to assemble glass cell with a much more efficient gas mixture. Also, the laser and device safety assessment has been done before installing it in the beam line.

3. New sample environment

As mentioned in the introduction, POLANO started user experiments with an unpolarized neutron beam. For those users, low-temperature experiments are the main subject of research. We equipped a new refrigerator (cryostat) to cool down the sample. The cryostat is a top-loading (TL) 4K type, with sample rotating (ω-rotation) capability. It is mounted on the vacuum chamber flange directory as shown in Fig. 3. All this saves time in the experimental preparation process, such as sample set-up, evacuation of the vacuum chamber, and temperature control, which is particularly important for long-counting experiments. We are going to provide much convenient experiment for the best sciences.

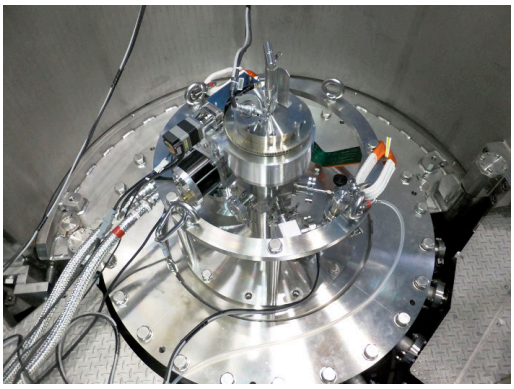

Figure 3. Newly manufactured top-loading type refrigerator.

4. Outcomes of the unpolarized experiment

POLANO finally started user experiments in addition to on-beam commissioning. As shown in Fig. 4, the neutron inelastic signals of the dynamical atom and spin motions were clearly observed. These data were some of the references measured on 1-dimensional quantum spin chain material with the new TL refrigerator mentioned above. At the same time, we had some amount of noise that did not originate from the sample. These were possibly consequences from placing several devices in the vacuum chamber. A much higher signal to noise ratio is crucial to detect a weak signal of inelastic, particularly polarized signals. We may need to figure out where those unwilling noise signals are coming from.

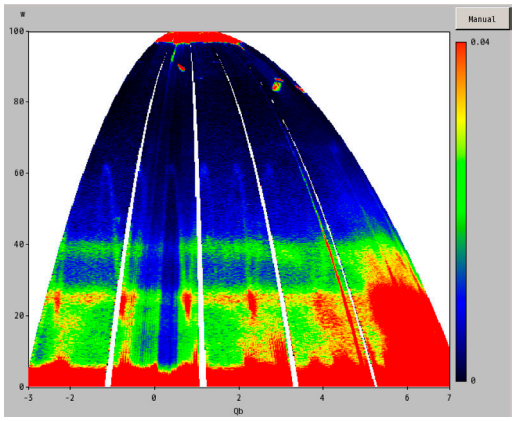

Figure 4. Energy spectra measured at POLANO with unpolarized neutrons.

References

[1] T. Yokoo, et al., EPJ Web of Conferences, **83** 03018 (2015).
[2] T. Yokoo, et al., AIP conference proceedings, **1969** 050001 (2018).
[3] MDPI Books, Quantum Beam Science 162 (2019).
[4] T. Ino, et al., *ibid.*

T. Yokoo[1,2], N. Kaneko[1,2], S. Itoh[1,2], K. Hayashi[1], M. Ohkawara[3], Y. Ikeda[3], and M. Fujita[3]
[1]Institute of Materials Structure Science, KEK; [2]Neutron Science Section, Materials and Life Science Division, J-PARC Center; [3]Institute for Materials Research, Tohoku University

AFP NMR Amplifier for ^{3}He Neutron Spin Filter

1. Introduction

Adiabatic fast passage (AFP) is a technique of nuclear magnetic resonance (NMR) that manipulates magnetic moments to rotate by 180 degrees, or in other words, it reverses the nuclear spin direction [1]. AFP NMR is often used in ^{3}He neutron spin filters (NSF) to flip ^{3}He nuclear spins, and accordingly the neutron spin direction [2–7].

Polarized ^{3}He nuclear spins are maintained in a static magnetic field. By applying an oscillating field perpendicular to the static field and sweeping the frequency so that it passes through the Larmor resonance, the ^{3}He spins are adiabatically reversed. The oscillating field strength B_1 should meet the so-called adiabatic condition $d\omega/dt \ll |\gamma B_1/2|^2$ to minimize the polarization loss during the spin flip. Here, γ is the gyromagnetic ratio of the magnetic moment, and ω represents the angular frequency of the oscillating field. The frequency sweep speed $d\omega/dt$ is limited by another factor, the transverse relaxation rate of the spins under the oscillating magnetic field [8]. Generally, in ^{3}He AFP NMR with the frequency sweep, $d\omega/dt > 10^6$ rad/s and $B_1 >$ 0.01 mT. To generate an oscillating magnetic field with this strength, a radio frequency (RF) amplifier is usually used to provide sufficient oscillating current to the B_1 coil. Such RF amplifiers are commercially available, but almost all of them are large and heavy, as well as expensive, since they are made for a wide use, covering a wide frequency range, capable of a continuous operation, etc. However, for AFP NMR of ^{3}He NSF, the frequency range is limited, and the continuous operation is not necessary, since ^{3}He spins are only flipped once in several to tens of minutes. Moreover, the sweep time, which corresponds to the duration of the RF amplifier operation, is usually far less than one second, and the corresponding duty cycle becomes virtually zero.

We have developed several types of compact and low-cost RF amplifiers specifically for AFP NMR of ^{3}He NSF, and one of them, with a very simple design, is presented in the next section.

2. RF amplifiers for AFP NMR of ^{3}He NSF

An important requirement for the RF amplifier is the linearity. Any spurious emissions including noises may cause unwanted polarization loss [3], and thus a class A or AB amplifier is ideal for the purpose. Other requirements, such as the output power, voltage, current, and frequency range, depend on B_1 coils and resonance circuits. In our AFP NMR systems, however, no resonance circuits are used as they interfere with the AFP NMR measurement or the phase-sensitive detection of the AFP NMR signal [2]. For this reason, our RF amplifiers are designed to drive B_1 coils without resonance circuits. Typical sweep frequency ranges, impedances, voltage, and current values of our B_1 coils are 60–90 kHz, 100–500 Ω, 70–180 V, and 0.3–0.5 A in amplitude, respectively.

RF amplifiers can be built using discrete transistors, but the circuit will be much simpler and more stable if operational amplifiers (op-amps) are used instead. We used power op-amps PA96 [9] for RF amplifiers. Some relevant parameters of PA96 are listed in Table 1, and the RF amplifier circuit is presented in Fig. 1. The power supply circuit can provide positive and negative DC voltages whose absolute values are over 135 V for the amplifier part with a limited power consumption. Two single-stage amplifiers with normal (non-inverting) and inverting outputs are as simple as Electronics 101. The amplifier gains are both set to twenty assuming that the input signal is fed from a common function generator. The maximum output voltage of each amplifier is $> 250\ V_{PP}$ (peek-to-peek), and it can be doubled by the bridge-tied load (BTL) connection, where a B_1 coil is connected between the normal and inverted outputs.

Pictures of the RF amplifier are shown in Fig. 2. The power supply circuit occupies more than half of the space. The op-amps are attached to heat sinks for convection cooling as the self-heating of an op-amp is ~ 8 W due to the PA96 quiescent current of 30 mA and the supply voltage of ~ 280 V. The heating during the signal amplification is negligible as the duty cycle is essentially zero.

Table 1. Some relevant specifications of PA96.

Supply voltage (maximum)	300 V (±150 V)
Output voltage swing (typical)	–Vs + 10 V to +Vs – 5.6 V
Output current (minimum)	1.5 A
Slew rate (typical)	250 V/μs
Gain band product (typical)	175 MHz
Quiescent current (typical)	30 mA

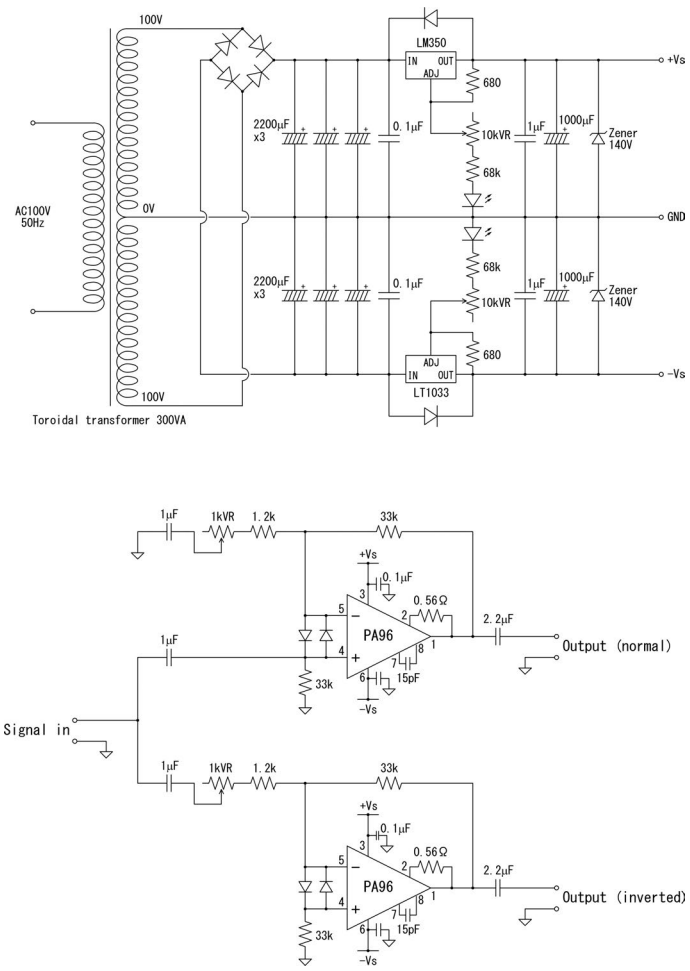

Figure 1. Circuit diagram of an RF amplifier. The power supply part (top) and the amplifier part (bottom). Normal (non-inverting) and inverting amplifiers are configured to enable the BTL connection.

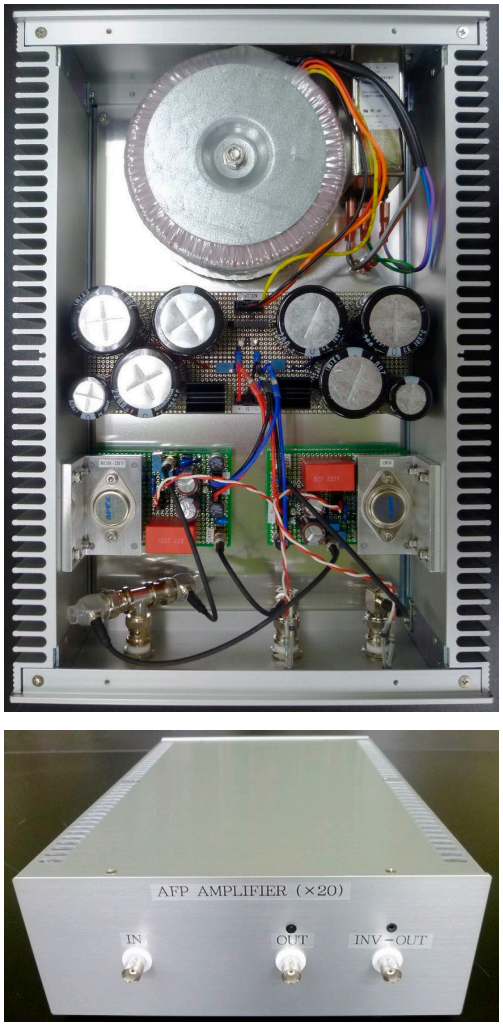

Figure 2. An RF amplifier developed for AFP NMR of ^{3}He NSF.

3. Conclusions

We have developed compact, lightweight, and low-cost RF amplifiers for AFP NMR of ^{3}He NSF. Examples are presented in Figs. 1 and 2. The instantaneous output power of this RF amplifier can be > 150 W using the BLT connection. Despite the high output power, the dimensions, weight, and cost are all far less than those of a commercial RF amplifier with similar specifications due to the limited band width and low duty cycle.

References

[1] A. Abragam, The Principles of Nuclear Magnetism, Clarendon, Oxford, 1961.
[2] T. Ino, JPS Conf. Proc. **22**, 011016 (2018).
[3] E. Babcock et al., Physica B **397**, 172 (2007).
[4] A. K. Petoukhov et al., Physica B **385–386**, 1146 (2006).
[5] T. J. McKetterick et al., Physica B **406**, 2436 (2011).
[6] W. C. Chen, et al., J. Phys. Conf. Ser. **528**, 012014 (2014).
[7] J. Baer, "SEE YOU ON THE FLIPPED SIDE – The construction and testing of RF Coils used to flip ^{3}He polarization," https://www.ncnr.nist.gov/programs/CHRNS/pdf/SURF/2014_Baer.pdf
[8] C. L. Bohler and D. D. McGregor, Phys. Rev. A **49**, 2755 (1994).
[9] PA96U data sheet, rev J, Apex Microtechnology, Inc., 2017, https://www.apexanalog.com/resources/products/pa96u.pdf

T. Ino[1,2], M. Ohkawara[3], N. Kaneko[1,2], T. Yokoo[1,2], S. Itoh[1,2], Y. Ikeda[3], and M. Fujita[3]
[1]Neutron Science Section, Materials and Life Science Division, J-PARC Center; [2]Institute of Materials Structure Science, KEK; [3]Institute for Materials Research, Tohoku University

Sample Environment at MLF

1. Introduction

The MLF sample environment (SE) team provides the sample environment equipment commonly used among several beamlines, and is also responsible for upgrading that equipment. The MLF SE team develops "cutting-edge" equipment that can function even under extreme sample conditions and also fulfills the growing users' needs. Our activities in JFY2019 are described below.

2. Cryogenics and magnets

We have supported users' experiments using several devices. In JFY2019, the superconducting magnet was operated for 10 experiments, the ^{4}He cryostat for 9 experiments, the ^{3}He cryostat for 5 experiments, the dilution refrigerator insert for 9 experiments, the Gifford-McMahon (GM) cryostat for 4 experiments and the GM cryofurnace for 1 experiment, including instrument proposals.

As the number of devices to handle increases, our load of user support is also growing. Specially, the superconducting magnet and the ^{4}He cryostat are wet-type cryostats, which need liquid cryogens for operation, and users have to refill them once a day or every two days. In order to reduce the load and improve the efficiency of the experiments, we are considering introducing closed-cycle cryostats, which are cryogen-free.

3. High temperature equipment

We have two furnaces as the BL-common equipment: a niobium furnace for inelastic and quasi-elastic neutron scattering measurements, and a furnace for small-angle neutron scattering (SANS) measurements. In JFY2019, the niobium furnace was used for three users' experiments on BL18. We prepare the SANS furnace to connect with the common monitoring system at the MLF, which enables users' unmanned operation of the furnace; as of now, according to the regulations of the MLF, the user should be present at all times to monitor the status whenever a high-temperature furnace is in operation. The hardware setup has been completed, and the preparation is in progress for realization of high-temperature experiments without monitoring by the user.

4. A pulsed magnet system

In JFY2018, we had already developed a new pulsed magnet system including a solenoid coil within the insert and a cryostat, using GM refrigerator to cool samples down to 3 K. In this system, even users who are not accustomed to LHe can use this system with convenience and practicality.

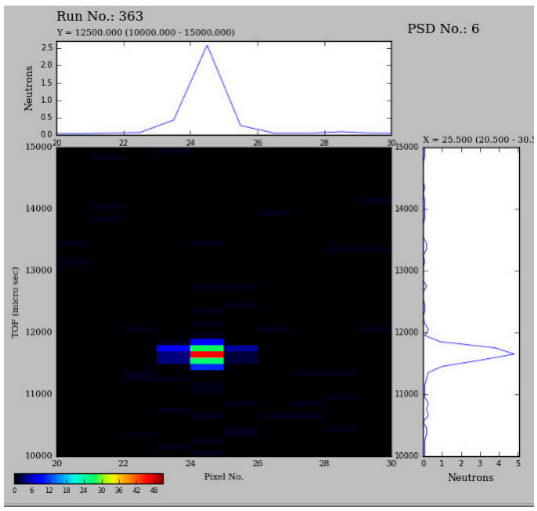

Figure 1. Diffraction spot of 29.2 T accumulating 40 shots.

In JFY2019, neutron scattering experiments using this system were performed at NOBORU (BL10) to study multiferroics $TbMnO_3$. This time, pulsed magnetic fields up to approximately 30 T were applied to the sample. Figure 1 shows the diffraction spot. This spot data was obtained by accumulating 40 shots of applied 29.2 T at neutron beam power of 500 kW. The data were reduced and visualized by the UTSUSEMI package [1]. Since the pulse interval length was 7 minutes, it took approximately 5 hours to accumulate the data. It was also confirmed that the pulsed magnet system operated properly.

5. High pressure

The control program of the automatic pressure pump has been modified. Now, it can refill the hydraulic oil while holding the load of the cell. The strain measurement system has been upgraded. Currently, it is possible to observe the ram's movement at low temperatures during off-line pressurization testing using a strain gauge attached to the test piece.

6. Light irradiation

In the light irradiation experiment, it is important to examine the light energy dependence on the photo-induced effect because it directly demonstrates the origin of the photo-induced change. To allow the experiment to examine such light energy dependence, we installed four high-power light emitting diode (LED) modules with different peak energies (3.38, 3.04, 2.81, 2.38 eV) [2].

Figure 2. LED light source system with four modules with different peak energies used on *SHARAKU* (BL17)

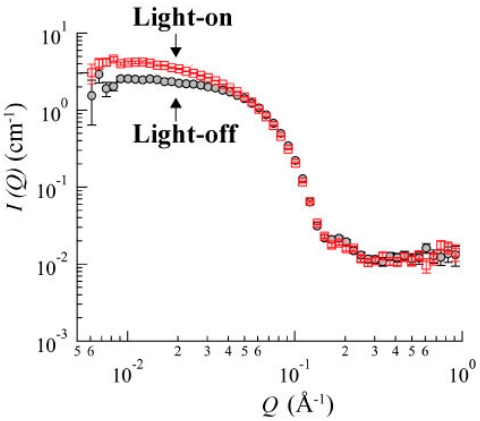

Figure 3. Photo-induced changes of the small-angle neutron scattering, suggesting the changes in the micellar shape of the light-sensitive surfactants [2].

The LED modules were used on SHARAKU (BL17) to observe the light energy dependence of the neutron reflectivity profiles of the light-sensitive films [3].

So far, the light sources of the MLF SE team has been used only on SHARAKU (BL17). In JFY 2019, the light irradiation experiment was performed on TAIKAN (BL15) using the Hg lamp of the MLF SE team to observe changes in the micellar shape of the light-sensitive surfactants, whose change appears at the small-angle region, collaborating with Dr. H. Iwase (CROSS), Dr. Y. Inamura (JAEA), Mr. S. Kasai (CROSS), Prof. H. Sakai and Dr. M. Akamatsu (Tokyo Univ. of Science) [2]. The experiment clearly demonstrates that the light irradiation system is available on TAIKAN (BL15) and applicable to many other light-sensitive surfactant systems.

7. SE training school and the domestic meeting on SE

Two of the SE team members (M. I. and H. A.) took part in the 3rd International Society for Sample Environment (ISSE) Training School held at Helmholtz-Zentrum Berlin (HZB) in Berlin, Germany, from October 27 to November 1, 2019. The sophisticated lectures and hands-on training on the sample environment's techniques were impressive and helpful for the future user support at the MLF.

Our SE team members, the SE staffs in JAEA, and the Institute for Solid State Physics, the University of Tokyo held the domestic meeting on SE at the "Quantum beam facilities" for the first time as the 23rd CROSSroads Workshop in Tokai on January 8 and 9, 2020. There were 75 participants who openly discussed various problems of SE, such as technical and financial issues, and human resources.

References

[1] Y. Inamura et al., J. Phys. Soc. Jpn., **82** SA031 (2013).
[2] Y. Sakaguchi et al., JPS Conf. Ser., to be published.
[3] Y. Sakaguchi et al., Eur. Phys. J AP, **90** 30101 (2020).

M. Watanabe[1], R. Takahashi[1], M. Ishikado[2], Y. Yamauchi[3], S. Ohira-Kawamura[1,4], M. Nakamura[3], H. Arima[2], S. Takata[1,4], Y. Su[1], S. Zhang[2], T. Morikawa[2], K. Ohuchi[2], Y. Sakaguchi[2], T. Oku[1], and K. Aizawa[1]
[1]*Technology Development Section, Materials and Life Science Division, J-PARC Center;* [2]*Neutron Science and Technology Center, CROSS;* [3]*Nippon Advanced Technology Co.;* [4]*Neutron Science Section, Materials and Life Science Division, J-PARC Center*

Development and Application of ^{3}He Spin Filter

1. Introduction

The development of a ^{3}He spin filter, a neutron polarization device which can polarize a neutron beam in a broad energy range and analyze neutron spins with a large solid angle, has been conducted at J-PARC. The fabrication of the ^{3}He spin filter and its utilization have started recently.

2. Development of the ^{3}He spin filter

A gas filling system for fabricating ^{3}He spin filters was completed in 2018, and 5 high quality ^{3}He spin filters using potassium and rubidium with a long relaxation time of ^{3}He polarization were fabricated in 2019 (Fig. 1). Also, a new ^{3}He pumping system using a 110-W fiber laser has been constructed at the J-PARC research building. The ^{3}He spin filter polarized by the new laser system at the J-PARC research building was installed on neutron beam line BL10, and a demonstration experiment was carried out. In the experiment, we achieved a long relaxation time of 170 h at the beamline and a high ^{3}He polarization of 85%, which was accomplished by using the high quality ^{3}He spin filter made in J-PARC and the new laser system. The neutron polarization and transmission passing through the ^{3}He spin filter is shown in Fig. 2. We can see that high neutron polarization is obtained for a broad energy range.

Figure 1. ^{3}He spin filter fabricated at J-PARC.

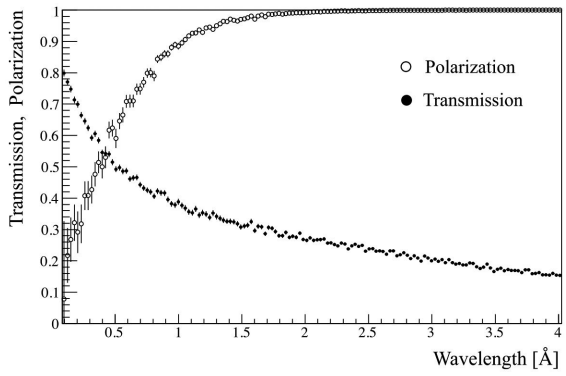

Figure 2. Neutron wavelength dependence of neutron polarization and neutron transmission using the ^{3}He spin filter at BL10.

3. Utilization of the ^{3}He spin filter

The utilization of the ^{3}He spin filters has also started at the MLF. In 2017, a ^{3}He spin filter was supplied for the first time to a user experiment. No user experiments were conducted in 2018, but four user experiments were performed in 2019 at BL04 and BL10. The ^{3}He spin filter was used as a neutron polarizer for those experiments to study nuclear reactions at BL04 and neutron holography at BL10.

Furthermore, our ^{3}He spin filter was applied to the MIEZE-type neutron spin echo experiment experiment as a spin analyzer to study ferrofluid at BL06 (Fig. 3). In this experiment, high ^{3}He polarization of 75% and a long relaxation time of 130 h was achieved at the beamline.

Experiments with the ^{3}He spin filter at BL15 and BL21 are also planned for isolating the incoherent scattering from hydrogen atoms and the magnetic scattering from a magnetic sample. A Helmholtz coil equipped with a sample changer to keep the ^{3}He polarization at the neutron beam lines has been prepared for BL15. Also, a coil, which can be installed at the vacuum changer at BL21, is now under construction. The experiments will be carried out in the next year.

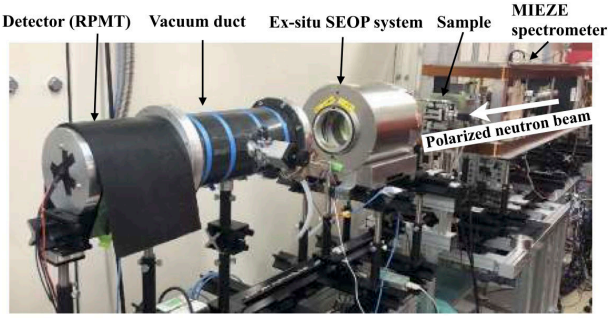

Figure 3. Experiment at BL06 using a ^{3}He spin filter. The ^{3}He spin filter was installed behind the sample, and the scattered neutron spins were analyzed by it.

T. Okudaira[1], T. Oku[1,2], S. Takahashi[2], T. Ino[3], K. Sakai[1], H. Hayashida[4], K. Hiroi[1], K. Kakurai[4], T. Oda[5], H. Endo[3], M. Hino[5], and K. Aizawa[1]

[1]Technology Development Section, Materials and Life Science Division, J-PARC Center; [2]Graduate School of Science and Engineering, Ibaraki University; [3]Neutron Science Section, Materials and Life Science Division, J-PARC Center, Institute of Materials Structure Science, KEK; [4]Neutron Science and Technology Center, CROSS; [5]Institute for Integrated Radiation and Nuclear Science, Kyoto University

Statistically Optimal Bin-widths Prediction to Histogram Experimental 4D Inelastic Neutron Scattering Intensity Distributions

1. Introduction

Although optimal bin-widths for a histogram of an INS (Inelastic Neutron Scattering) spectrum are usually intuitively set by each researcher, they can be determined objectively from the data's statistics.

In the field of neurophysiology, a method to estimate an optimal bin-width was developed based on the Poisson statistics of the number of the events recorded in equal intervals [1]. An extrapolation method was also reported, which estimated the optimal bin-width of the hypothetical data of m total count from the statistics on the actual data of n total count.

For the neutron data, Ref. [2] extended the optimization method to the simulated data sets of INS intensity distributions in a (**q**, E) space. However, thus far, the optimization method has not been applied to the actual neutron experimental data. Moreover, the extrapolation method has not been examined on any INS data. The extrapolation method may be used to terminate a measurement with necessary and sufficient resolutions. Alternatively, if we see a faint unknown spectral feature in a measured intensity distribution, the optimization method may be used to determine whether the feature is statistically significant. Thus, we work to introduce the bin-width optimization/extrapolation method to the INS experiment in the MLF.

2. Methodology

Optimal bin-widths minimizing MISE (mean integrated squared errors) between the histogram and the underlying probability density function are calculated as follows [1, 2]:

$$\Delta^*_{n,q_a}, \Delta^*_{n,q_b}, \Delta^*_{n,q_c}, \Delta^*_{n,E} = \mathrm{argmin} C_n$$

$$C_n = \frac{\langle k_n \rangle - \langle (k_n - \langle k_n \rangle)^2 \rangle}{n^2 (\Delta_{q_a} \Delta_{q_b} \Delta_{q_c} \Delta_E)^2}, \quad (1)$$

where $\Delta^*_{n,x}$ is the optimal bin-width along the x axis for data with a total neutron count n, k_n represents a neutron count in a bin, $\langle \cdot \rangle$ shows an average of $\cdot$ over the bins. From C_n and k_n, the cost function is extrapolated to the hypothetical data with a total neutron count $m \neq n$ as follows:

$$C_{m|n} = \left(\frac{1}{m} - \frac{1}{n} \right) \frac{1}{\Delta_{q_a} \Delta_{q_b} \Delta_{q_c} \Delta_E} \langle k_n \rangle - C_n \quad (2)$$

Extrapolated optimal bin-widths to the data with m is as follows:

$$\Delta^*_{m|n,q_a}, \Delta^*_{m|n,q_b}, \Delta^*_{m|n,q_c}, \Delta^*_{m|n,E} = \mathrm{argmin} C_{m|n} \quad (3)$$

Hereafter, we refer to quantities on the actual data and the hypothetical data by n and m, respectively.

In experimental INS with pulsed neutron source, the INS data array in a (**q**, E) coordinate space contains some "masked" spaces where a neutron cannot be detected due to the measurement geometry. In order to reduce the effect of these masked spaces on the optimization results, we made an option to choose whether the statistic procedure eliminates bins containing the masked spaces. Once this option is turned on, only the bins which satisfy the following condition are taken into account in the statistics:

$$\sum_{h \in A_i} m_h > \alpha \sum_{h \in A_i} \quad (4)$$

where h is an index of the data array element, $m_h = 0$ if the element h is masked and otherwise $m_h = 1$, A_i denotes the 4D space within a bin i, and α is a constant parameter in [0,1]. We prepared phantom data with a known probability density function and compared the results with the option on and off. The results with the option on and appropriate α were closer to the optimization results on the phantom data without the masked spaces. For a large α, anomalously large bin-widths had the minimum of the cost function, because the 4D space considered in the statistics depended on the bin-widths through Eq. (4). We heuristically increased α as much as possible before the minimum of the cost function located at anomalously large bin-widths.

3. Application to INS data in the MLF

The method was applied to the INS data acquired from an fcc single crystal Cu, with three different measurement conditions. The optimal bin-widths on each data set are summarized in each columns of Fig. 1. Firstly, to validate the overall behavior of the optimal bin-widths, we plot the inverse of the optimal bin-widths products (Δ^*_n or Δ^*_m) with the inverse of the total neutron counts (n or m). In the horizontal axis region of large $1/m$, $1/\Delta^*_m$ slightly increases as $1/m$ decreases. On the other hand, in the region of small $1/m$, $1/\Delta^*_m$

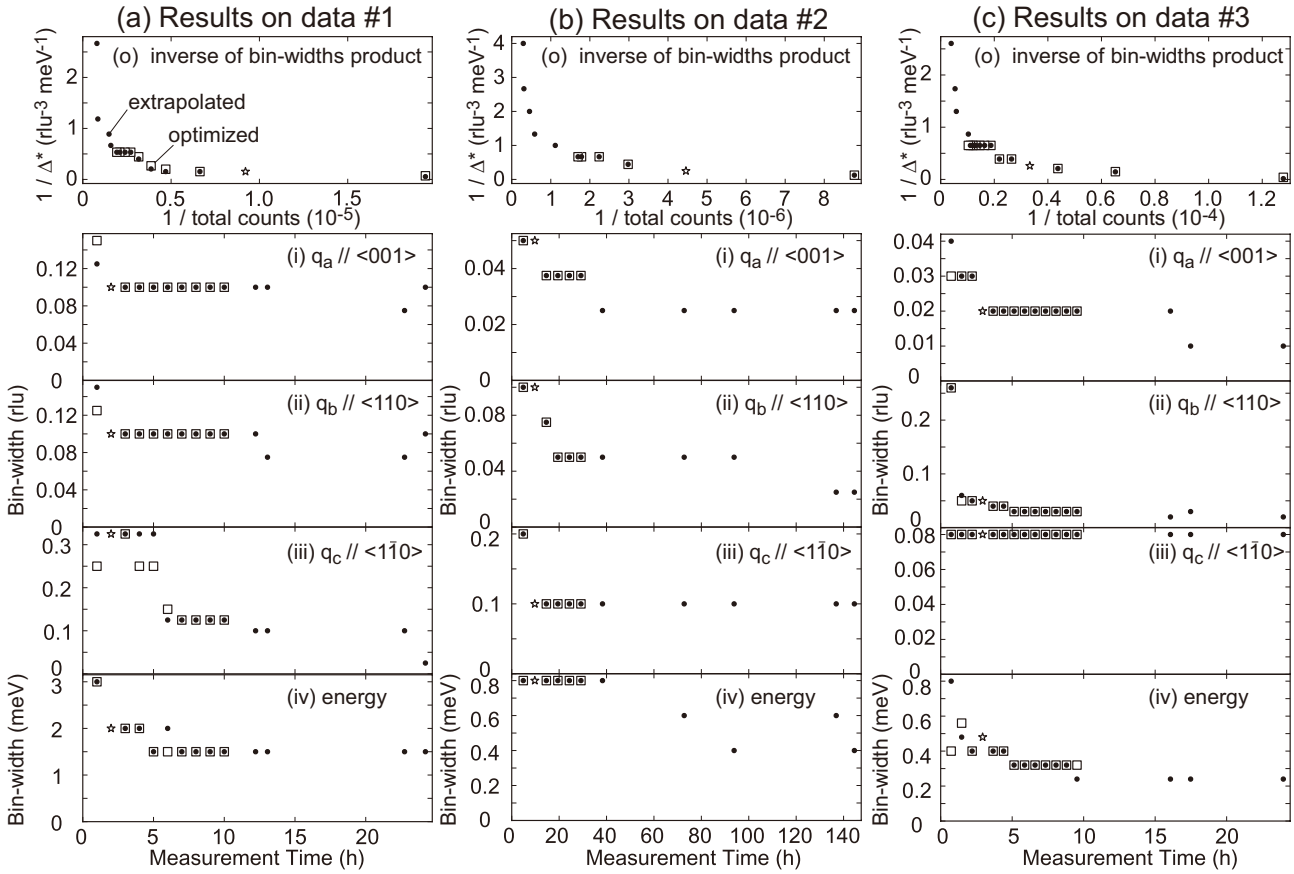

Figure 1. The inverses of the optimal bin-widths product and the total neutron count in the analyzed data arrays (o), and the optimal bin-widths with respect to the measurement time (i, ii, iii, iv): The data arrays were cumulatively obtained in a measurement session for each data of #1, #2, and #3. In (o) ((i, ii, iii, iv)), the extrapolation results from a data array with a specific total count (measurement time) are shown by dots, the optimization result on the data with this specific total count (measurement time) is shown by a star, and the optimization results on the data arrays with the other total counts (measurement times) are shown by squares.

increases noticeably with decreasing $1/m$. This behavior is qualitatively consistent with the following relationship approximately deduced on a 1D data set with a specific nature of a probability density function [1],

$$\frac{1}{\Delta^*_m} \propto -\left(\frac{1}{m}-\frac{1}{n}\right) \qquad \text{for } m > n_c$$
$$= +0 \qquad \text{otherwise} \qquad (5)$$

with a positive constant n_c. Secondly, in the second to fifth rows in Fig. 1 are shown the behaviors of the optimal bin-widths along the respective axes with respect to the measurement time. The extrapolated optimal bin-widths are consistent with the optimal bin-widths of the actual data. Therefore, the extrapolation method predicts well the optimal bin-widths at different times.

The analyzed data arrays contain the masked spaces. We present the results with $\alpha = 0.9$ for data #1 and #2, $\alpha = 0.7$ for data #3. For data with large measurement times, for example, 9 and 10 h for data #1 and 24 and 29 h for data #2, we confirmed that the optimal bin-widths were identical whether the mask option was turned on or not. Conversely, the results with and without the mask option are useful to see the robustness of the results.

The optimal energy bin-widths at the total measurement time are 1.5, 0.8 and 0.32 meV for data #1, #2 and #3, respectively. The energy resolutions were estimated from FWHM of a peak in an energy profile at a **q** where phonon branches are expected to have energy extrema: these FWHM values were 3 ± 0.4, 3 ± 0.2 and 0.5 ± 0.08 meV for data #2 and #3, respectively. The fact that the optimal energy bin-widths were not much larger than the FWHM values supports for the estimate of the energy resolution as FWHM values.

4. Outlook

The optimization/extrapolation method worked well on the three kinds of experimental INS data. By saving redundant preprocesses on the data arrays and preparing adequate computers with a fast network, we believe this method can be used during the experiment.

References

[1] H. Shimazaki and S. Shinomoto, Neural Computation, **19** 1503 (2007).

[2] K. Muto, H. Sakamoto, K. Matsuura, T. Arima, and M. Okada, J. Phys. Soc. Jpn., **88** 044002 (2019).

K. Tatsumi[1], Y. Inamura[2], M. Kofu[2], R. Kajimoto[2], and R. Kiyanagi[2]

[1]*Technology Development Section, Materials and Life Science Division, J-PARC Center;* [2]*Neutron Science Section, Materials and Life Science Division, J-PARC Center*

Real-Time Data Display and Storage Device with Simple Functions for Easy Adjustments of a Two-Dimensional Detector

1. Introduction

We have developed a two-dimensional gaseous neutron detector system for the Materials and Life Science Experimental Facility (MLF) at the Japan Proton Accelerator Research Complex (J-PARC) [1, 2]. The developed system can output time-resolved neutron position data with a time resolution of less than 1 μs. The experimental data are typically measured using a commercially available multipurpose data acquisition equipment. However, it is necessary to develop an alternative data acquisition device because the versatility of the commercially available equipment reduces the processing speed due to high-load multifunction processes, and the counting rate is less than a few hundred kilo counts per second (cps) when the two-dimensional neutron measurement is performed. Furthermore, a multipurpose equipment requires complex operations and is not user friendly to a researcher unfamiliar with neutron scattering experiments. Therefore, we developed a new data acquisition device with characteristics of real-time data display and storage for use at the MLF and used it subsequently to perform operation tests with signals that simulate the detector output signals.

2. Device design

The schematic diagram of the two-dimensional detector system and developed data acquisition device is shown in Fig. 1. The detector element contains 128 signal lines each for the X- and Y-axes. Charge signals from neutrons are collected by the lines and processed by the amplifier-shaper-discriminator electronics in each axis. The incident position of the neutrons is determined in the position encoder using a field programmable gate array (FPGA). The position encoder transfers the neutron position data as 16-bit low voltage differential signals to the developed data acquisition device. In the pulsed neutron irradiation facility, T0 signals that indicate the time when the pulsed neutron is generated are always generated and distributed to all experimental beamlines for the TOF experiments. The 25-Hz TTL signals with a time interval of 40 ms are used in the MLF.

The photograph of the developed data acquisition device is shown in Fig. 2. The developed device is fabricated as a one-unit VME module to operate in VME crates that are widely used at the MLF. A high-definition multimedia interface (HDMI) is adopted as a display connector to use a commercially available monitor. The developed device can display two-dimensional neutron images on the monitor through the HDMI connector with an update time of 800 ms. The experimental data are saved in the storage device that has a universal serial bus (USB) connector. The device has a 68-pin connector and ERA00-type connectors for receiving the position data from the position encoder and the T0 signal from the experimental facility, respectively. T0 signals and position data are entered into the FPGA in the developed device, and the TOF, i.e., the time interval between T0 and the following position data, is calculated in the FPGA. The calculated

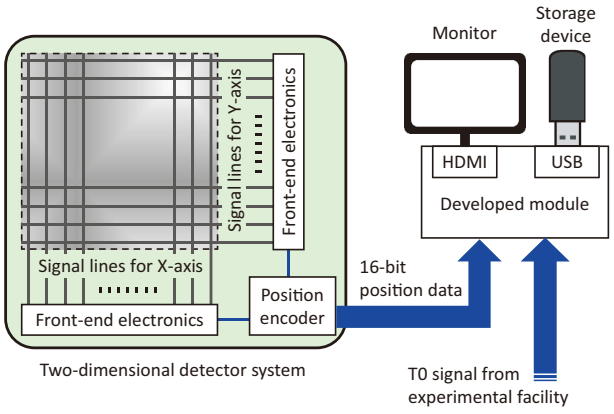

Figure 1. Schematic view of the neutron detector system and data acquisition device.

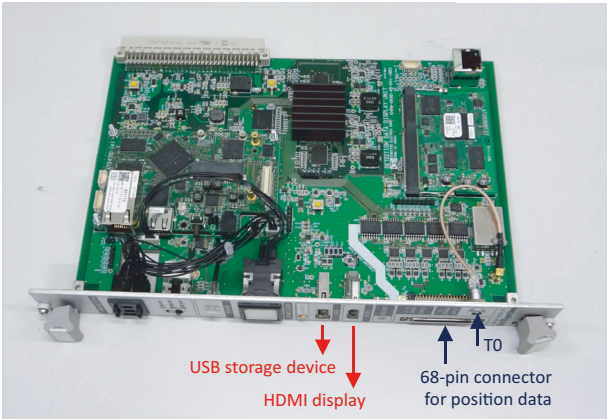

Figure 2. Photograph of developed real-time data display and storage device fabricated as a one-unit VME module.

TOF, and position data are saved in the USB storage device. Simple functions and operations are necessary for the device to demonstrate long-time stability, robustness, and a user-friendly interface. The device contains a thumbwheel switch for measuring the time and an on/off switch to start/stop the measurement.

3. Operation test

Performance tests for the developed device were performed using test signals that simulated the detector output signals. Double pulses of position signals with various time intervals were entered to evaluate the time response. Figure 3 shows the dependence of the counting loss of the measured signals on the time interval of the double pulse. The counting loss is zero when the time interval was more than 1 μs, and the loss became larger with decreasing the interval time. It was confirmed that the developed device could separate the signal pulses with a time interval of 1 μs. The counting loss of the double pulse was fitted based on the following single linear equation, $L_d = 54.6 - 56.5\ t$, where L_d represents the counting loss (%); t is the time interval (μs). It was found from the equation that the counting loss was zero until the time interval reached 0.97 μs.

The counting rate capability was evaluated using continuous test pulses. Figure 4 shows the measured signals plotted as functions of the frequency of the continuous test pulse. The measured signals increased with the frequency of the continuous pulse, and the signals were saturated beyond 1 MHz. The calculated counting loss and a fitting line with a single linear function are plotted in Fig. 4. The fitting equation of counting loss of the continuous pulse was expressed as $L_c = -102 + 100\ f$, where L_c represents the counting loss (%); f is frequency of the continuous pulse (MHz). It was found from the equation that the counting loss was zero until the frequency reached 1.02 MHz. We obtained a linear response over 1 MHz using the developed device, and the maximum counting rate was approximately 1 Mcps.

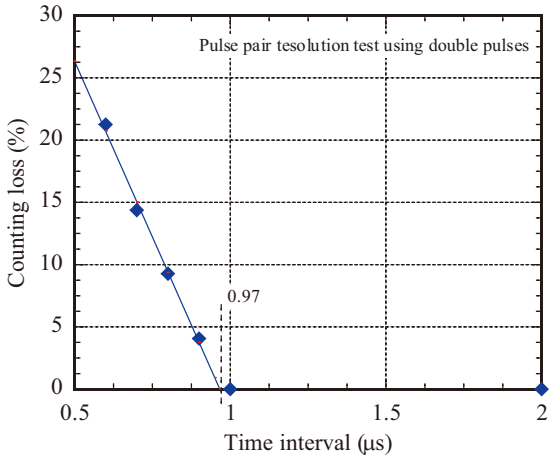

Figure 3. Counting losses of the developed device as a function of the time interval of double pulses.

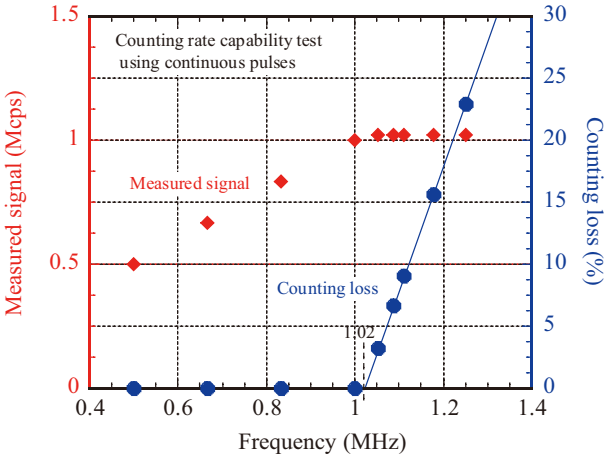

Figure 4. Measured signals of the developed device as a function of the frequency of the continuous test pulse, and calculated counting losses.

4. Summary

A real-time data display and storage device was developed for neutron scattering experiments using the TOF method. The developed device can determine the time-of-flight and time-resolved neutron position data with a time range from 0 to 40 ms using a beam of pulsed neutrons at 25 Hz. It was confirmed by an operation test using burst and continuous test pulses that the device exhibited a pulse pair resolution of less than 1 μs and a counting rate capability of more than 1 Mcps.

References

[1] K. Toh et al., Nucl. Inst. and Meth. Phys. Res. A, **726** 169 (2013).
[2] K. Toh et al., J. Instrum., **9** C11019 (2014).

K. Toh[1], T. Nakamura[1], K. Sakasai[1], and H. Yamagishi[2]
[1]*Neutron Instrumentation Section, Materials and Life Science Division, J-PARC Center;* [2]*Nippon Advanced Technology Co.*

Muon Science

MUSE Facility Overview

1. Electric power substation for the H-line completed

Among the muon beamlines envisioned in the original plan of the MLF, the H-line in experimental hall No.1 has been expecting funding from MEXT for years. Considering the situation, the J-PARC headquarters decided to provide partial support for realization of the plan. The support was primarily for the construction of a new electric power substation to cover the huge demand for electricity expected when the H-line becomes fully operational. Following the installation of cable racks, pitting of the MLF building wall, and outdoor structures in FY2017, the major civil engineering work for the substation site near the MLF building was completed by the end of March 2019 (see Fig. 1). Meanwhile, the work continued to ensure access to electricity at the substation site. During the last summer shutdown, a power panel was installed in hall No.1 at the MLF. The scaffoldings around the main carry-in door (where power cables pass through) was removed after the completion of cabling work from the new power substation to the interior of the MLF. Those who plan experiments on the H-line are now hoping to have electricity available sometime in FY2020.

Figure 1. Electric power substation constructed on the east side of the MLF building (left). The white wall in the back is that of the NU2 building (Photo taken in May 2019).

2. Muon rotating target replaced

As reported a year ago, potential damage of a flexible joint within the muon rotating target system was suspected during the summer maintenance in FY2018. After careful assessment of the risk expected in case of a joint breakdown, a multitude of safety measures were imposed to allow for a restricted operation of the target until the next summer shutdown. Fortunately, the target served for muon production without trouble for about seven months, and was finally replaced with a brand-new spare during the last summer shutdown. Actually, this was an unprecedented occasion for the muon target team to replace the whole system after a high-proton power operation, and utmost care was taken to minimize the risk of radiation hazard during the replacement work (Fig. 2). Now, the new target seems ready to be exposed to a 1-MW proton beam in the years to come.

Figure 2. A snapshot of the MUSE target team working on the target replacement assembly, where the radiation workers wearing airtight suites are in a temporary greenhouse to contain radioactive contaminants.

3. Updates from the S & U-lines

The Okayama University group received a JSPS Kakenhi grant for their research project "Precision test of electroweak theory and search for new physics beyond the Standard Model by laser spectroscopy of purely leptonic atoms". This led to the application of a new S1-type research proposal to use a high-flux surface muon beam provided by MUSE, which was approved at the recent PAC meeting. As a result of discussion with the MUSE staff on how to complete this project within the limited term of the grant, it was agreed that Okayama University group was going to assume full support for the construction of a new experimental area S2 in FY2020, so that they can secure a major portion of the beamtime without affecting other user programs.

At the U-Line, continued efforts for increasing ultra-slow muon intensity were in progress. For a muonium ionization laser system, a new crystal (YSAG) for amplification of 212 nm light was successfully fabricated and its implementation in the existing system started.

At U1B, a dedicated interference experimental setup was prepared as a part of the S1-type research project "Transmission Muon Microscopy" to verify the wave-particle duality of the muon.

R. Kadono[1,2], Y. Miyake[1,2], K. Shimomura[1,2], A. Koda[1,2], P. Strasser[1,2], T. Yamazaki[1,2], S. Kanda[1,2], H. Fujimori[1,2], Y. Ikedo[1,2], Y. Kobayashi[1,2], J. Nakamura[1,2], N. Kawamura[1,2], Y. Oishi[1,2], Y. Nagatani[1,2], S. Matoba[1,2], S. Takeshita[1,2], S. Nishimura[1,2], S. K. Dey[1,2], W. Higemoto[2,3], and T. U. Ito[2,3]

[1]*Institute of Materials Structure Science, KEK;* [2]*Muon Science Section, Materials and Life Science Division, J-PARC Center;* [3]*Advanced Science Research Center, JAEA*

Present Status of the Muon-Beam Source, M2 Tunnel

1. Introduction

The muon production target and the front-end part of each muon beamline are located in the M2 tunnel as well as the primary beamline, as shown in Fig. 1. This area is crucial for the stable and safe operation of the whole MLF facility containing not only MUSE but also JSNS. All the potential issues in this area are linked to the radiation generated by the muon production target and related devices like the beam scrapers, and thus the muon science section has a responsibility to deal with all accidents that may happen in this area in cooperation with the 3NBT group of the neutron source section. This engagement has been executed since the construction period of the MLF facility. We report the present status, selecting a few topics which was appeared in stepwise power upgrade of proton beam.

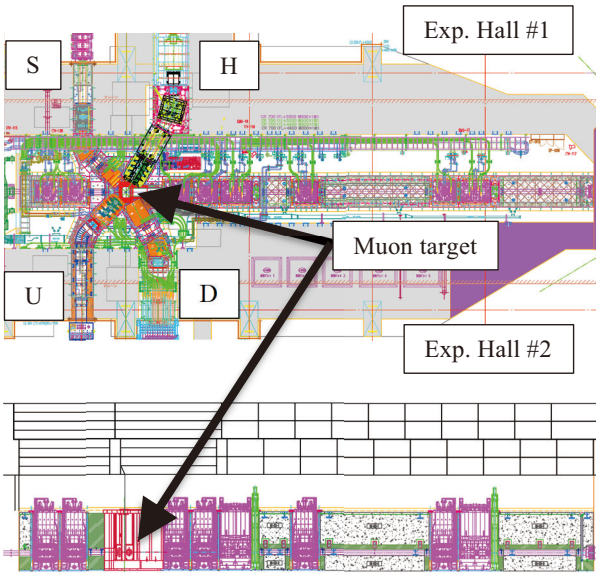

Figure 1. The horizontal (upper) and the vertical sectional view (lower) of the M2 tunnel. The proton beam is transported from the left to the right side of the neutron target through the tunnel.

2. Muon production target

In the last fiscal year, we found a defect in the target assembly. The coupling made of aluminum alloy connecting the rotating shaft of the target with the rotation motion feedthrough was damaged [1]. This was considered to be due to embrittlement caused by cyclic stress of the rotating motion, resulting in the breakage of one of two couplings during the periodical maintenance in the last fiscal year. The broken one was successfully replaced with a new one made of stainless steel. However, it turned out that the other coupling was impossible to replace manually, and even a visual inspection was difficult. Although there was no obvious evidence that the remaining coupling was damaged, this situation should not be left unresolved. However, the problem was found just a few weeks before resuming the facility operation and we did not have enough time to perform the replacement work that had to be well planned. Thus, we decided to continue to use the assembly. Before the operation, the rotational motion of the target wheel was confirmed visually from 10-m upstream of the primary beamline.

The worst conceivable trouble of the target is the sublimation of graphite in the case when the target rotation is stopped but the proton beam is still injecting into the same position of the target. To avoid such a problem, any abnormal situations in the target must be detected with monitors like thermometers, torque sensors, and so on. In addition, we introduced the quadrupole mass spectrometer (QMS) to monitor residual gas atoms/molecules. Especially tritium, which originates from the spallation process in the target, is expected to increase if the target temperature rises. It is hard to distinguish tritium from the other mass-number-3 particles like (HD), and thus basic data are accumulated to implement QMS into the interlock system. To establish layered safety, we introduced the buffer tank system [2]. Even in the worst case, the buffer tank stores the evaporated gas, and prevents the release of a huge number of radio-isotopes contained in the gas to the outside of the facility.

In this fiscal year, we decided to replace the whole target assembly rather than the remaining coupling. The new rotating target assembly, the 2nd target, has been operated since November 2019. Details are reported separately [3].

3. Buffer tank system

The buffer tank system, connected to the downstream of the existing vacuum exhaust line, was installed in the last fiscal year [2]. The system has two 100-liter tanks to be used exclusively by it. One of them stores the exhaust gas, while the gas stored in the other tank is evacuated after the radiation survey. This year, some of the valves were replaced, and remote-control capability was introduced. In the case of an emergency, the tank in use can be swapped without stopping the beam operation due to local valve operation. This gives redundancy to the buffer tank operation.

Table 1. Tritium release rate to the beamline vacuum stored in the buffer tank system. The amount of tritium is measured by the liquid scintillation counter (LSC [*1]) and ionization chamber (IC [*2]). LSC distinguishes between HTO and HT with pre-treatment. Because the differences between the values of LSC and IC are a few times, we adopted IC for the operation hereafter due to its quick response. The grey hatched line shows the off-beam data, and the values subtracting the off-beam component are also shown [*3].

Start Date	End Date	Tritium Release Rate [Bq/day]				Tritium Release Rate subtracting off-beam data [*3]		Beam Power [kW]	Target
		LSC [*1]			IC [*2]				
		HTO	HT	SUM		LSC	IC		
2019/5/22	2019/5/29	6.2E+05	5.2E+07	5.2E+07				500	#1
2019/5/29	2019/6/26	9.2E+05	2.9E+07	3.0E+07				500	#1
2019/6/26	2019/7/8	9.0E+05	8.4E+07	8.5E+07				500/1000	#1
2019/10/16	2019/11/20	7.1E+04	1.6E+06	1.7E+06	4.9E+05			0	#2
2019/12/6	2019/12/11	2.0E+05	1.0E+07	1.0E+07	5.3E+06	8.1E+06	4.6E+06	500	#2
2019/12/11	2019/12/24	5.3E+04	1.3E+06	1.3E+06	4.6E+06	-1.4E+06	3.8E+06	500	#2
2020/1/7	2020/2/12	5.4E+04	2.4E+06	2.4E+06	8.1E+06	1.2E+05	7.4E+06	500	#2
2020/2/12	2020/4/15				1.4E+07		1.3E+07	500	#2

The operation data have been accumulated. They are summarized in Table 1. Before starting the beam operation, the un-irradiated 2nd target's data were obtained. Even in the case of an un-irradiated target, the rate of tritium in the exhaust gas reaches around 1 MBq/day. This could be explained by the tritium release from the copper scrapers adjacent to the target.

The diffusivity of tritium in copper is evaluated to be $D = 2 \times 10^{-13}$ m^2/s at room temperature [4]. Thus, assuming tritium diffusion generated uniformly in a copper block, about 12% of the tritium in the 1-mm layer from the surface has a possibility to be released from the block per week, although in reality, the chemical reaction on the surface may decrease the release rate to the vacuum. The tritium yield is estimated to be 0.11 and 0.02 MBq/cc/week in the 1st and the 2nd scrapers, respectively, under the 1-MW beam operation, and the surface area of each scraper is 1.2×10^4 cm^2. Therefore, 9 MBq of tritium generated under the 500-kW operation is expected to be released to the beamline vacuum per week even during the off-beam periods. This rough estimation explains the observed value rather well.

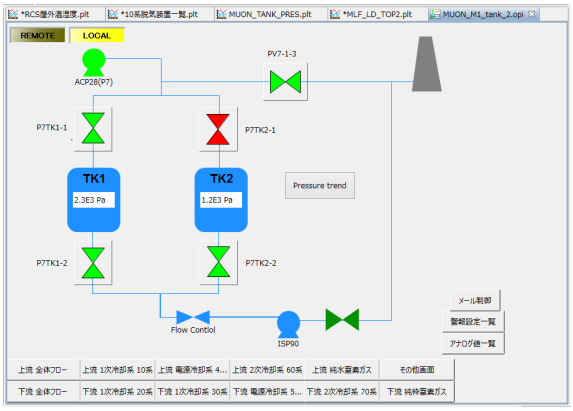

Figure 2. The control panel for the buffer tank system on the J-PARC control LAN.

References

[1] S. Makimura *et al.*, KEK-MSL report 2018.

[2] N. Kawamura *et al.*, KEK-MSL report 2018; proceedings of J-PARC2019 symposium.

[3] S. Matoba *et al.*, *ibid.*

[4] F. Reiter *et al.*, "A Compilation of Tritium-Meaterial Interaction Parameters in Fusion Reactor Materials" Commission of the European Communities (1993). The diffusivity used in the context is extrapolated to the room temperature in Fig. A.1

N. Kawamura[1,2], S. Matoba[1,2], Y. Kobayashi[1,2], and A. Koda[1,2]

[1]*Institute of Materials Structure Science, KEK;* [2]*Muon Science Section, Materials and Life Science Division, J-PARC Center*

Report of Rotating Target at MLF

The fixed target was replaced with a rotating target in September 2014 to extend the lifetime of the muon target. The rotating target has been successfully used for five years without replacement. Since 2018, a continuous and stable 500-kW proton beam operation has been successfully conducted. The accumulated operational period and the number of revolutions have reached 17000 hours and 16 million, respectively, in July 2019. Furthermore, on July 3, 2019, a 1-MW beam operation (Beam power, 935 kW: 1 MW equivalent to one pulse) was successfully conducted for 11 hours. Because the rotation axis and the graphite of the rotating target are moving, it is difficult to directly attach thermocouples for measurement. Therefore, the temperature variation of the thermocouples that are placed beside the axis and the graphite through the thermal radiation from the axis and the graphite is measured. Because the heat is not so strong, the temperature does not respond quickly. Nevertheless, it was confirmed that the temperature reached a thermal equilibrium state in the 1-MW beam operation for 11 hours. The maximum temperatures, to some extent, were in good agreement with the prediction. Figure 1 shows the temperature variation of the thermocouples.

Meanwhile, damage on the flexible coupling in the rotation system was found during the long shutdown in September 2018. It was decided to repair the target assembly by replacing only the damaged coupling in the long-term shutdown in 2019. If the replacement had been successfully completed, the target assembly would have been reused. As a backup plan, the replacement of the entire target assembly was planned. The used target assembly was transported from the beam line to a storage pod. For the replacement, it was necessary to assemble the greenhouse so as not to spread the pollution and to wear an air line suit to avoid internal radiation exposure.

A large amount of tritium is released from muon-producing targets and scrapers by proton beam irradiation. Tritium deposited on the inner wall of the proton beamline duct and on the surface of the muon target assembly is converted to HTO by substitution with H_2O molecules in the atmosphere when exposed to air. When the muon target assembly is pulled out into the air, HTO diffuses in the air. The concentration of HTO in the air causes the spread of radioactive contamination and internal exposure. We carried out decontamination of tritium in the proton beamline ducts before the replacement work. The beam duct was filled with nitrogen and about 5% air, and tritium-containing gas, which was transferred from the wall to the water in the air by the isotope reaction, was exhausted. Figure 2 shows the tritium concentration in the beam duct. The first purge (4.7 kPa, 25˚C, 70% humidity) took place on July 16, and the tritium concentration was 50 Bq/cc on the next day. The total amount of tritium in the air in the beam duct was estimated to be about 350 MBq. The contaminated air was exhausted on July 15 and a second purge (5.0 kPa, 25˚C, 67% humidity) was performed on July 16. The tritium concentration on July 22 was 26 Bq/cc, although the retention period was longer than the first time, the tritium concentration decreased, and the decontamination by this method was confirmed. The removal of the vacuum flange was carried out under the condition that the tritium concentration was reduced to about 1 Bq/cc by purging with pure nitrogen before the target extraction operation. The tritium concentration increased to a maximum of 26 Bq/cc after the vacuum flanges were removed, but it has been gradually decreasing as it continues to be released into the stack by the green house exhaust. As a result of the decontamination, the maximum concentration of tritiated water vapor was about 0.2 Bq/cc, which was lower

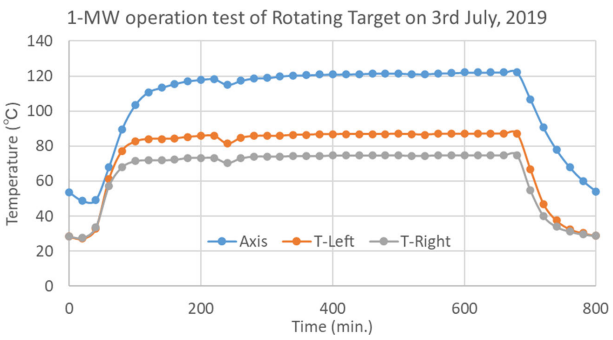

Figure 1. The temperature variation of the thermocouples.

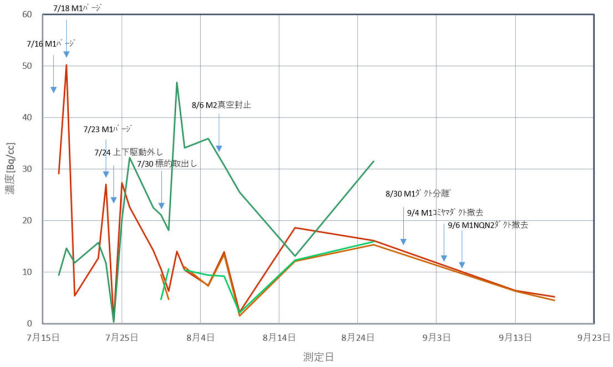

Figure 2. Daily trend of tritium contamination in the beam duct.

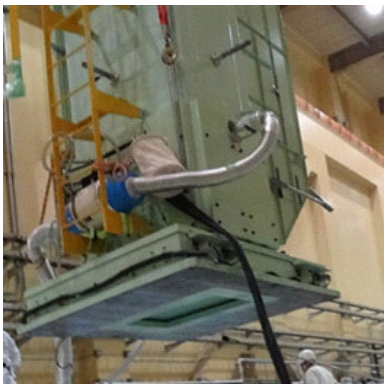

Figure 3. The cask with an exhaust fan.

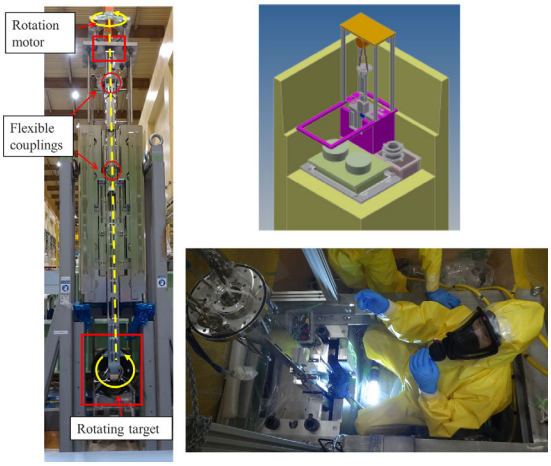

Figure 4. The pictures of the target assembly (left), the conceptual design of replacement jigs (right up), and the commissioning test by the spare target (right down).

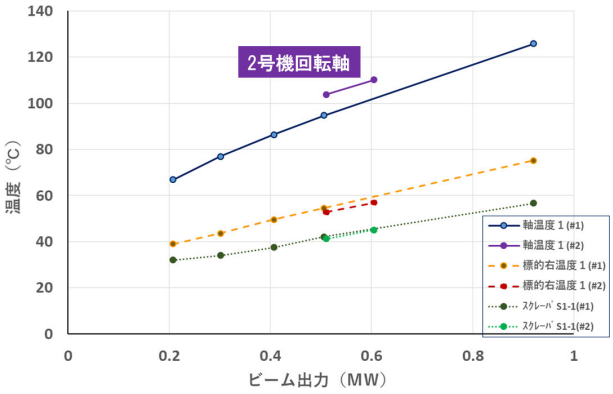

Figure 5. Beam power dependence of the temperatures of the rotating target system.

than 0.8 Bq/cc, the concentration limit of tritiated water vapor in the working area of the green house. The first rotational target was moved with a shielded cask as shown in Fig. 3.

The cask was maintained at a constant negative pressure by a blower connected to the stack to prevent the spread of tritium contaminations. The target assembly was inserted into the vertical hole in the storage pod because the rotating target was highly radioactive. Since it was necessary to access the screws in a narrow space of the target assembly for the replacement, the workers had to get close to the position of the coupling. So, the target assembly was placed at the position where the coupling was accessible. It was necessary to place a local shield to reduce external radiation exposure. Replacement jigs were carefully designed and manufactured. It had been confirmed that the coupling was successfully replaced using a mock assembly. Figure 4 showed the pictures of the target assembly, the conceptual design, and the commissioning test by a mock assembly. In the summer of 2019, the used target assembly was transported, and the radiation dose was measured. The radiation dose of the used rotating target at a distance of 10 cm was 500 mSv/h. Though the radiation dose at the working space was anticipated to be 50 μSv/h, the measured one was 500 μSv/h, therefore, it was decided to give up the replacement of the coupling. Finally, we decided to replace the entire target assembly.

The temperatures for the beam power of the second and first rotating targets are shown in Fig. 5. Although there is a slight difference in the axial temperature, there is almost no difference in the temperature during operation at the same beam power. Therefore, the second rotational target is working properly. The slight difference in the axial temperature is not due to the change in the beam orbit, but to the different heat transfer due to the difference in the thermocouple contact.

Since the second rotating target was installed, we are now forced to operate the beam without a spare target. We are planning to build a spare target as soon as possible.

S. Makimura[1,2], S. Matoba[1,2], and N. Kawamura[1,2]
[1]*Institute of Materials Structure Science, KEK;* [2]*Muon Science Section, Materials and Life Science Division, J-PARC Center*

Monitoring System for the Muon Rotating Target

It is important to measure the temperature of the muon-production rotating target (hereinafter referred to as "rotating target") in order to detect quickly its problems. The temperature of the rotating target cannot be measured by direct contact because it is not possible for thermometers to be attached to the rotating body. Thermocouples are attached to the cooling jacket to measure the temperature due to the thermal radiation from the rotating target. However, in the case of a significant temperature rise, this monitoring system cannot quickly stop the proton beam.

We are developing a real-time two-dimensional radiation thermometer to monitor the temperature of the rotating target. We installed a new proton beam duct for mounting an infrared camera. Figure 1 shows the infrared camera and a mirror attached to the duct port. The infrared camera (ULVVIPS-04171SL made by Vision-Sensing Co., Ltd.) is installed perpendicular to the beam axis at the bottom of the proton beam duct. Radiation from the muon target is reflected by a gold-deposited mirror placed at 45° in the proton beam duct and observed by a camera through a ZnSe infrared vacuum window. The infrared camera was installed 11 meters upstream from the rotating target for radiation protection. The focal length of the lens of the infrared camera was 150 mm and the target can be observed with a spatial resolution of about 2 mm. The infrared camera is expected to have resistance against 5 Gy or more irradiation that corresponds to more than a one-year operation under 1-MW beam power.

The temperature of the muon target during beam operation was successfully measured using the infrared camera as shown in Fig. 2. At the center, a high-temperature part, which is likely to be a beam spot with a diameter of about 1.5 cm, was observed. The temperature of the part of the target ring was observed to be high due to the radiation from the face. We are now analyzing the conversion from infrared radiance to absolute temperature and will analyze the change of thermal conductivity by proton beam irradiation.

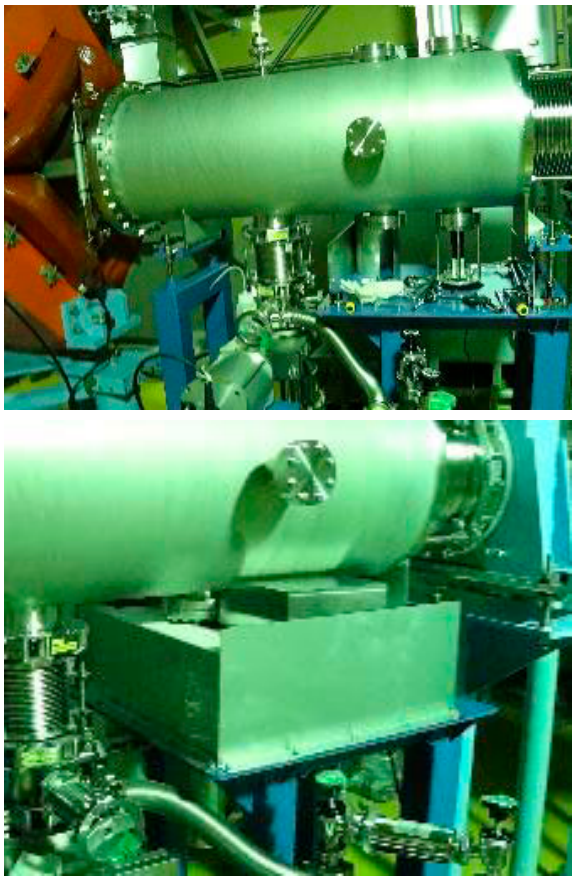

Figure 1. Infrared camera on the proton beam duct (upper) and a shielding made of polyethylene blocks containing lead and boron (lower).

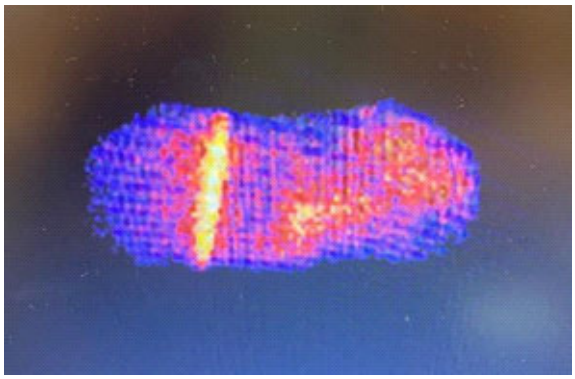

Figure 2. Infrared camera image of the rotating target during a beam operation.

S. Matoba[1,2], N. Kawamura[1,2], and S. Makimura[1,2]
[1]*Institute of Materials Structure Science, KEK;* [2]*Muon Science Section, Materials and Life Science Division, J-PARC Center*

Current Status of μSR Experiment at D1

1. Introduction

At the D-line, muons are delivered to D1 and/or D2. At the D1-area, a μSR spectrometer is installed as a main and fixed instrument. Since high-momentum muons, surface muons, and negatively charged muons are available at D1, all type of μSR measurement, except for ultra-slow μSR, can be carried out. In particular, unique sample environments, such as very low temperature by using the dilution refrigerator, high pressure, etc., were possible to carry out only at the D1. Recently, negative muon spin rotation/relaxation (μ^-SR) is also frequently performed. Figure 1 shows the μSR spectrometer with the dilution refrigerator and the fly-past chamber. Here, we report the recent development of D1.

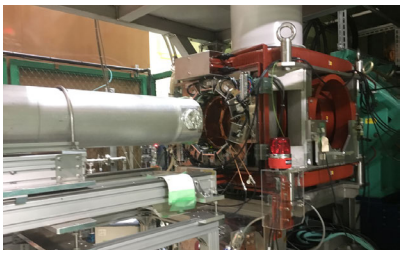

Figure 1. μSR spectrometer with the dilution refrigerator and the fly-past chamber at D1.

2. Origin of distortion of the μSR spectra

Often, the time dependence of a μSR spectrum is distorted for some reasons. One of the main reasons is "pile up" of μ-e decay positrons. The counters have finite dead time and if more than two positrons pass a counter within very short time, the counting system cannot distinguish the first and second positron, which causes a finite counting loss of μ-e decay positrons. This counting loss has been already adjusted and usually the corrected data are used for analysis. Another reason is due to contamination of positrons (or electrons) in the muon beam. In particular, a time-dependent positron is one of the issues for distortion of the spectra. To remove positrons from the muon beam, we use a "particle separator" which is installed at the upstream part of the septum magnet. This is a kind of "Wien filter" that can separate muons and positrons by applying electric field and magnetic field at the same time. However, if the muons stopped at the duct wall of downstream part of the beam line, the μ-e decay positrons of the same momentum as the muons could not be removed by using a positron separator and a finite amount of positrons with the decay time of 2.2 μs could reach the sample position. Such positrons could be scattered at the sample and hit the positron counters, which causes additional events. Usually, these additional events are contributed as a constant μSR signal. However, when we use a kicker to obtain a single pulse, beam trajectory depends on time dependence of the kicker operation and μSR spectra could be distorted.

Figure 2 shows the μSR spectra in several Cu plates with different thickness. When the thickness is less than ~1 mm, the spectra shows almost no distortion. However, significant distortions were seen in the time range of 0–1.5 μs in a thicker sample. Since the thickness of a Cu plate is enough to stop all surface muons, it is obvious that this distortion is due to scattered positrons. In addition, the distortion does not depend on the condition of the separator, it is clear that the positrons are coming from the downstream part of the beam line. The shape of the distortion is similar to the magnetic field profile of the kicker and we conclude that the distortion is owing to positrons whose trajectory is modified only when the kicker is working. Indeed, no distortion was found in the double pulse μSR spectra, in which the kicker was not working. We also tried to change the kicker operation mode to kick a second pulse to D1, however, the distortion still occurred. We note that the kicker at S1 is not magnetic but electric one and no distortion of the μSR spectra due to positrons is seen.

Unfortunately, we have not solved the distortion but we are working continuously to improve the situation.

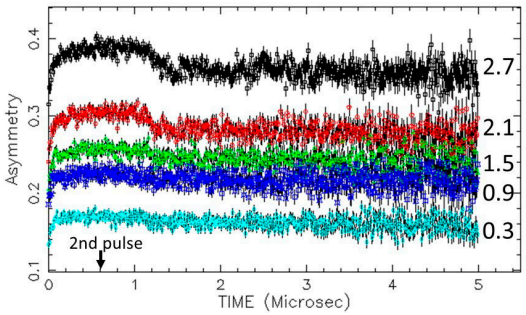

Figure 2. μSR spectra in several Cu plates with different thickness (~50 mm × 50 mm, room temperature) from 0.3 to 2.7 mm, which were obtained at D1. A surface muon beam was used. Kicker was used to remove the 2nd pulse. The Cu plates were placed in the air without any chamber or sample holder.

W. Higemoto[1,2,4] and A. Kota[1,3]

[1]Muon Science Section, Materials and Life Science Division, J-PARC Center; [2]Advanced Science Research Center, JAEA; [3]Institute of Materials Structure Science, KEK; [4]Department of Physics, Tokyo Institute of Technology

Negative Muon Commissioning at D1/D2 Areas

1. Introduction

The D-line, which is a beamline located at MUSE, MLF, has a long superconducting solenoid and, therefore, can supply positive and negative decay muons from several MeV/c to ~100 MeV/c in addition to surface muons. Since the energy of the primary proton beam of the MLF is as high as 3 GeV, the yield of negative muons is higher than at other muon facilities. In particular, because of the increment of power in recent years, the world's highest intensity negative muon beam is supplied. Using the high-intensity negative muons, applications for various experiments such as non-destructive elementary analysis using muonic X-rays, and negative muon spin relaxation, are being developed. In this report, we describe the current status of commissioning of the negative muon beam at the D-line.

In the D1 area, negative muon spin relaxation measurements can be performed using polarized high-intensity negative muons. Recently, some results have been obtained with negative muon spin relaxation methods [1]. However, further commissioning is required to perform experiments on a variety of samples. Here, we report recent commissioning results on spectral distortion reduction and momentum measurements.

2. Distortion in asymmetry and background component in μ^--decay spectra

Due to the low intensity of the beam, negative muon spin relaxation measurements have not been commissioned in the past. However, with the recent increase in the intensity of proton power at J-PARC, μ^-SR has become familiar to us, and simultaneously some problems have been found. One of them is spectral distortion. For example, as shown in Fig. 1, the asymmetry is distorted in the time domain, especially in the long-time region ($t > 10$ μs, in RUN 4554 (Red) in Fig. 1). As a result of the commissioning to improve this, the spectral distortion was significantly improved, as shown in RUN 6633 (Blue) in Fig. 1.

In order to investigate the cause of the distortion, we first investigated the muon decay spectrum (Fig. 2) and found that in addition to the muon-derived component with a lifetime of about two μs for graphite, there is a long-lived component with a lifetime of several tens of μs, which can be confirmed from the Fig. 2. Considering the muon lifetime, this is unlikely to originate from negative muon decay electrons. Compared with the asymmetry calculated from the histogram (red curve in Fig. 1), it was found that the asymmetry was distorted in the

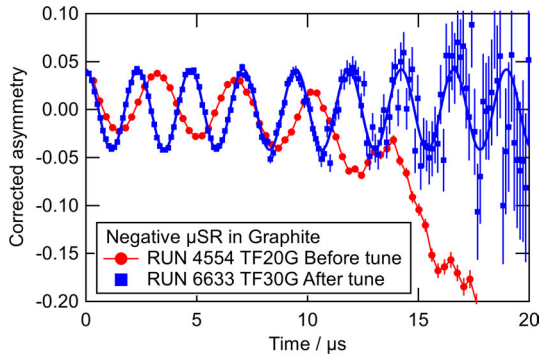

Figure 1. Time dependence of the asymmetry in a Graphite sample before and after beamline tuning.

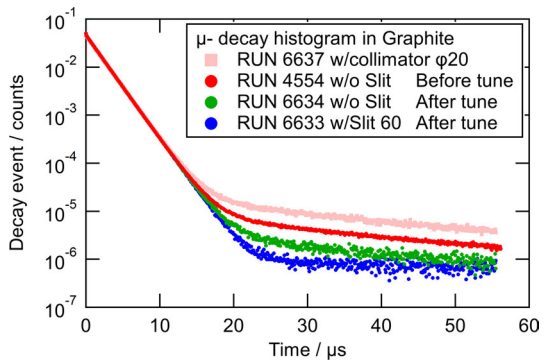

Figure 2. μ-e decay histograms before and after beamline tuning and some other conditions.

region of 15–20 μs, where the muon decay events are almost impossible to observe. These results suggest that this background component is responsible for the distortion of the spectra. This background component appears after the pulse timing of the muon, which is considered to be caused by neutrons, β- or γ-rays associated with the negative muon nuclear absorption. In particular, the contribution to the muon absorption rate is thought to be significant because of the use of large Z elements such as Pb and W in the collimator at the beam exit.

Therefore, beam tuning was performed in order to reduce this long-lived background component. The tuning was carried out under the condition that a 60 x 60 mm slit aperture restricted the beam path. As a result, the long-lived background component was reduced by one order of magnitude (Fig. 2). The resulting asymmetry is shown in Fig. 1 (blue curve). The spectral distortion after 10 μs was reduced. By optimizing the beamline slit aperture, the beam size at the collimator position was reduced, and the number of negative muons stopped at the collimator was decreased. As a result, the long lifetime component was also reduced significantly.

3. Beam momentum measurement at D1

The momentum value of the beam is an important information to determine the volume of the sample for the negative muon spin relaxation measurement. For this purpose, the actual momentum value of the beam and its distribution width were measured. By changing the thickness of the target, we measured how much of the negative muon beam passed through a target plate (the so-called range measurement). The central momentum and the distribution width of the beam were calculated by comparing them with a simulation. As a result, the central momentum was found to be a little higher than the nominal momentum, and the distribution width was very narrow.

Figure 3 shows a schematic diagram of the target used for the momentum measurement. The target was an Al target with a graphite plate overlaid on its downstream surface. Since the graphite plate was sufficiently thick, all the negative muons that passed through the Al plate stopped in the graphite plate. And because the nuclear absorption rate of negative muons differs depending on the atomic number Z of the material where the muons stopped, the number of total decay electron events observed depends on which side of each plate the negative muons stopped (the lifetime of negative muons in Al is about half of that in graphite). Therefore, the number of negative muon decay electron events counted by the detector was used as an indicator of how many muons passed through the Al plate.

The measurements were performed in the μSR experimental apparatus located in the D1 area. The target was placed in the center of the apparatus. A counter (Kalliope) installed in the apparatus was used to measure the number of decay electrons. The number of negative muon decay electron events was evaluated by calculating the number of decay electrons per unit of time after integrating the measured number of decay electrons. The beam condition was the same as that of RUN 6633 (slit aperture of 60 x 60 mm) in Fig. 2.

The number of decay electron events as a function of the aluminum thickness measured at 30 MeV/c is shown in Fig. 4. The decay electron rate decreases sharply with increasing thickness, indicating that with this method, the range measurement can be performed without any problem.

The fitting result of these data by an error function is shown as a blue line. From this fit, the central thickness

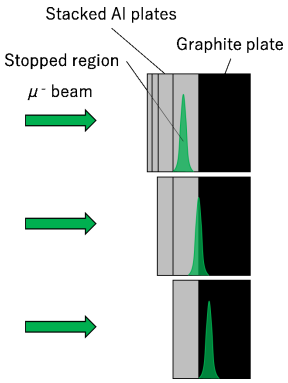

Figure 3. Schematic view of the beam momentum measurement. The more muons stop at the graphite, the longer the apparent muon lifetime is.

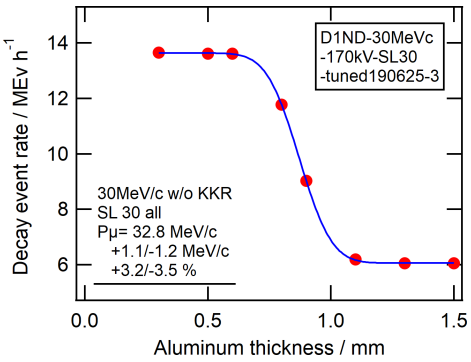

Figure 4. Aluminum thickness dependence of muon decay event rate under a nominal muon momentum of 30 MeV/c.

and its width were obtained. By comparing with simulations using SRIM/TRIM [2, 3], the central beam momentum and distribution width were deduced. The obtained values were estimated to be 32.8 MeV/c (nominal value +9.3%) for the center and +1.1/−1.2 MeV/c (+3.2/−3.5%) for the stopping spread.

For the condition of 60 × 60 mm slit aperture, the momentum width was about 3%, which indicated that a very narrow momentum distribution was obtained. The actual momentum value was slightly higher than the nominal value. We will investigate the cause in detail and resolve this discrepancy in the future.

References

[1] J. Sugiyama *et al.*, Phys. Rev. Lett. 121 (2018) 087202.
[2] J. P. Biersack and L. Haggmark, Nucl. Instr. and Meth., 174 (1980) 257.
[3] The Stopping and Range of Ions in Solids, Pergamon Press, New York, USA (1985).

S. Takeshita[1,2], P. Strasser[1,2], M. Tampo[1], S. Doiuchi[1], A. Hashimoto[1], I. Umegaki[3], N. Kawamura[1,2], K. Shimomura[1,2], and Y. Miyake[1,2]
[1]Institute of Materials Structure Science, KEK; [2]Muon Science Section, Materials and Life Science Division, J-PARC Center; [3]Toyota Central Research & Development Laboratories, Inc.

Development of Sample Environment at the S1 Area

A light-irradiating setup is required for the μSR sample environment. The light and the muon should irradiate the sample at the same area and time. At the S1 and D1 areas, a xenon flash lamp in a short-arc stroboscope package is used as a light source. Typical values in the manufacturer's data sheets of the lamp (SAX-100 lamp with SA-130A power supply, Nissin Electronic. Co., Ltd. [1]) show that the light power is 130 W and the pulse width is 18 μs (FWHM). The light power at the μSR sample does not only depend on the combination of a lamp and a power supply but also on repetition frequency and experimental setup. The pulse width also depends on the frequency. At the MLF, the muon beam is a 25-Hz pulsed beam, so synchronized 12.5 Hz light pulses can be used to conduct SR experiments in red-green mode, showing 12.5-Hz alternative data with light on and off. As of the setup, the vacuum chamber, flypast chamber for example, is used for the experiments. A 10-cm distance from the sample is a suitable position for the lamp housing, which is outside of the chamber. We report the results of the experimental examination of the light power and the pulse width within the conditions of the μSR experiments.

Firstly, we measured the precise pulse shape, using a slightly light-leaking scintillator of the μSR detector. Figure 1 shows the single histogram of the scintillator. An exponential curve shows a signal of decay positrons, and a gaussian curve shows a light pulse. This results clearly show that the pulse width (FWHM) was exactly 18 μs at our μSR experiments. Note that the light-leaked signal in a single histogram was eliminated in a coincided histogram and conventional experimental data, asymmetry.

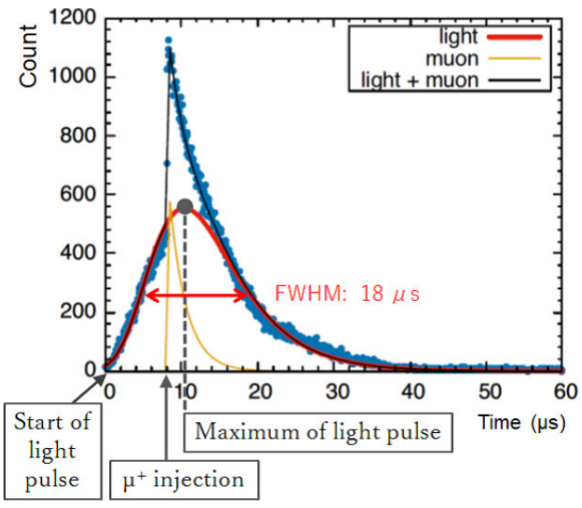

Figure 1. Histogram of the light-leaking scintillator.

Next, we examined the pulse energy of the light source. Figure 2(a) shows the setup for the measurements. The energy was measured by a pyroelectric power meter PE50-DEF-C (Ophir Optronics Solutions, Inc.), which can detect the light pulse thermally. The size of its light receiving surface is close to that of the SR sample (φ35 mm). The measured pulse energy was 7 mJ (=90 W, Table 1), which was consistent with the typical value.

Although the lamp housing has been replaced to non-magnetic materials, the longitude field (LF) prevents the lamp from lighting near the magnet. To conduct LF-μSR experiments with light source, we prepared a fiber light guide. The new light source can introduce light to a direction transverse to the muon beam direction (Fig. 3). In this setup, the same sample surface is irradiated by the muon and light pulse. This allows us to conduct LF-μSR experiments with side-windowed vacuum chamber, flypast chamber at the S1 area. The light is collimated to φ20 mm beam and the pulse energy is also examined to be 0.15 mJ (=2 W, Fig. 2(b)). As shown in Table 1, the light transmission caused the energy loss, which was larger than the value estimated by the technical data of the light guide. (Typical transmission rate shows 95% for white light and, < 90% for blue light (< 480 nm) [1].) Therefore, the energy loss should have been caused at the end of the light guide, which may be improved by further alignment or using another collimator lens.

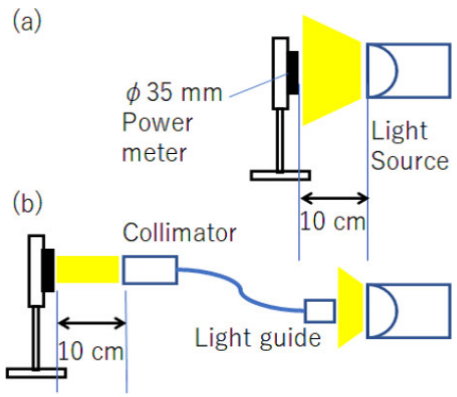

Figure 2. Setup for examining the pulse energy of the light source.

Table 1. Pulse energy of the light source.

	Pulse energy
(a) Light source	7 mJ (90 W)
(b) With light guide transmission	0.15 mJ (2 W)

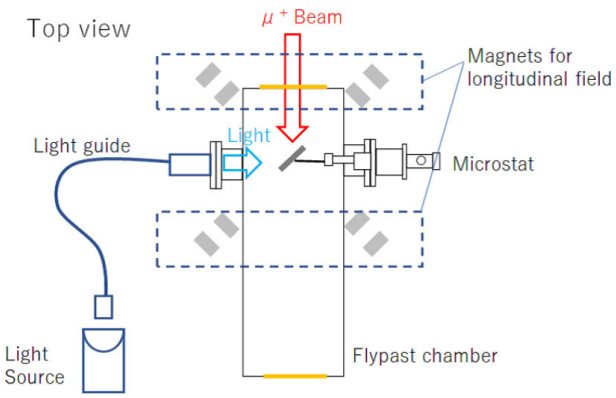

Figure 3. LF-μSR setup with light source.

In addition, we report on the ^{3}He cryostat, Heliox AC-V, which was installed to the ARTEMIS spectrometer in the S1 area. Its performance was examined in our previous report [2]. Next, we prepared temperature control of the cryostat from the IROHA sequence. The temperature-controlling sequence was safely operated at user experiments of 2019B and in the beamtime of the following 2020A.

References

[1] https://www.nissin-ele.co.jp/
[2] J. Nakamura *et. al.*, KEK Progress Report 2019-3 (2019) 23.

J. Nakamura[1,2], A. Koda[1,2], M. Hiraishi[1], S. Nishimura[1,2], H. Li[1], H. Okabe[1], and R. Kadono[1,2]
[1]*Institute of Materials Structure Science, KEK;* [2]*Muon Science Section, Materials and Life Science Division, J-PARC Center*

USM Commissioning at the U1B area

1. Introduction

We are developing a 5-MeV transmission muon microscopy at the U1B area. The goal of the microscopy is visualizing a thick object (> 10 μm) in nanometer resolution. The ultra-slow muon beam has quantum coherence, and its acceleration over 5 MeV energy gives it deep-penetration capability for thick specimens. A specially designed cyclotron is employed for the acceleration.

2. Diffraction Experiments of muons

We started an experiment of muon diffraction as the first demonstration of the transmission muon microscopy without reacceleration. The aim is to obtain a direct proof of the quantum interference of muons, by detecting diffraction patterns of the ultra-slow muon beam. The experiment will be the first direct proof of the wave-particle duality beyond the second generation of the Standard Model. The experiment uses the first prototype of the transmission muon microscopy constructed in the U1B area.

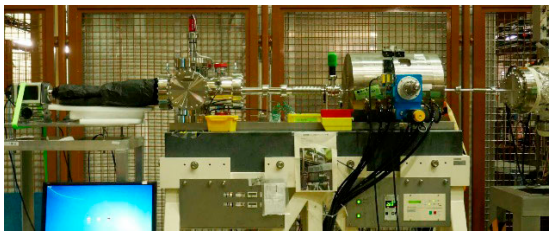

Figure 1. The prototype of the transmission muon microscopy for the diffraction experiment.

The prototype consists of an object lens, including a specimen-stage, and a camera-chamber, including a 2-dimensional image sensor. The object lens makes a small spot of the muon-beam on the image-sensor and forms a diffraction pattern of a specimen installed into the center of the object lens. A multi-channel plate (MCP) with a phosphor plate is employed as the image-sensor for ultra-slow muons. The image on the phosphor is taken by a CCD camera. We are using a single-layer graphene as the specimen. We have already taken data and are analyzing them.

3. Cyclotron for muons

We are constructing a 5-MeV cyclotron for muon with Sumitomo Heavy Industry Inc. The energy dispersion of the accelerated beam should be in the order of 10^{-5} for reducing effects of the chromatic aberration. We adopt a flat-top RF acceleration for the cyclotron to realize such a small energy dispersion. This year, we have designed the cyclotron in detail, and constructed a magnet for it.

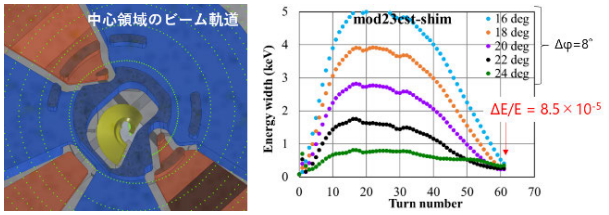

Figure 2. Beam trajectory at the center of the cyclotron and evolution of the energy dispersion.

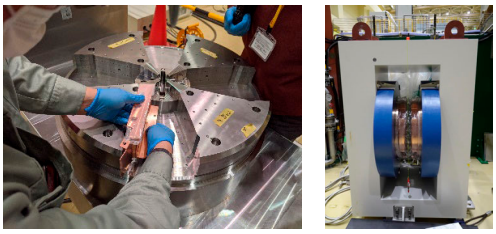

Figure 3. Sector pole (left) of the magnet, and the magnet (right) of the cyclotron.

We have also developed a 3-dimensional measurement device of the magnetic field of the cyclotron, which uses a search coil (see Fig. 4). To reduce the energy dispersion, precise (~10^{-5}) measurement of the magnet is required.

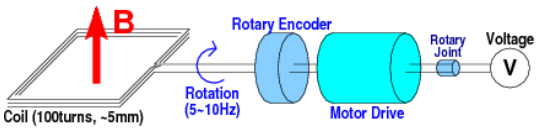

Figure 4. Concept of the search coil.

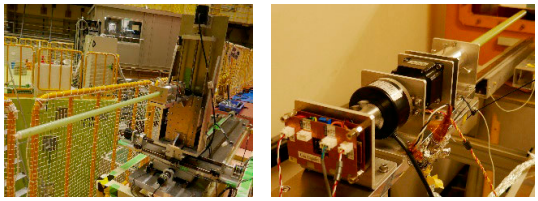

Figure 5. 3-dimensional magnetic field measurement device (left), and core part of the search-coil (right).

Next year, we will tune up the magnet by using this measurement device, install the RF-system into the cyclotron, and start beam tests of the cyclotron.

Y. Nagatani[1,2], T. Adachi[1,2], T. Yamazaki[1,2], S. K. Dey[1,2], Y. Ikedo[1,2], and Y. Miyake[1,2]
[1]Institute of Materials Structure Science, KEK; [2]Muon Science Section, Materials and Life Science Division, J-PARC Center

H-Line Construction – Recent Progress

A new beamline named H-line is under construction in the east #1 experimental hall of the MLF. Figure 1 is a layout drawing of the H-line. The H-line is a general-purpose beamline [1], which can generate both decay and surface muons, and has two branches named H1- and H2-area. Its large acceptance (108 mSr) capture solenoid and following beamline magnets with large apertures enable us to use high intensity muons for precise measurements, such as the MuSEUM experiment to measure the hyperfine splitting of muonium [2] and the muon g-2/EDM experiment [3]. The intense muon beam of the H-line is also suited to search for rare processes forbidden in the framework of the Standard Model of particle physics (DeeMe experiment [4]). In addition, a transmission muon microscope (TμM), which enables us to observe thick samples, such as living tissue, non-destructively, is planned to be installed at the H2 area.

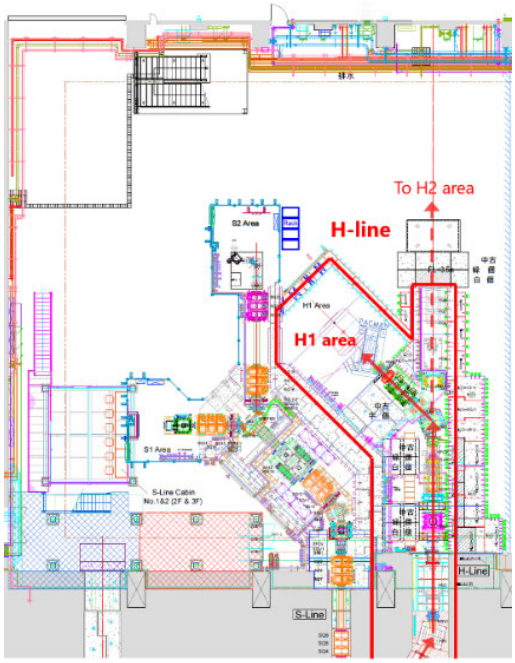

Figure 1. A layout drawing of the east #1 experimental hall of the MLF in the 1st phase of the H-line.

The H-line has been constructed step by step. First, its frontend devices, such as the capture solenoid and the first bending magnet, were installed during the summer shutdowns in FY2012 and FY2014. Then radiation shields and beam blockers were installed in FY2016.

Since FY2017, the construction of a new electric sub-station for the H-line started. This is because the H-line consumes a lot of electricity which cannot be provided by surplus electricity of the MLF. One of the reasons is that the capture solenoid of the H-line is a normal conducting magnet since it is located only 600 mm apart from the muon production target and is wound with radiation-resistant mineral insulation cables (MIC) [5].

The building work of the platform of the new electric sub-station was almost completed in FY2018, and then, in FY2019, the electrical construction was executed. High voltage receiving cubicles and voltage transformers from 6.6 kV to 400/200 V were installed. The cabling work from the new electric sub-station to the new experimental panelboards in the MLF was also finished, and the construction of the sub-station was finally completed in FY2019 (Fig. 2).

Figure 2. The construction of the new electric sub-station was completed in FY2019.

In FY2020, we plan to carry out installation of beamline apparatuses, electrical cabling and cooling water piping of some magnets, as well as an update of the safety interlock system to release the first beam in the H1 area.

Other important progress is made on an extension building for the H2 area. We have to build a new building for the H2 area in the east side of the MLF, currently occupied by a parking lot. This is because the muon g-2/EDM experiment planned at the H2 area needs very low emittance muon beam re-accelerated up to 212 MeV by linear accelerators of about 50 m. In FY2019, a J-PARC center task force was organized to consider many issues concerning the extension building, such as its exterior design, relocation of equipment, radiation control, utilities, and so on. Figure 3 shows one of its results, exterior design endorsed by the J-PARC center task force.

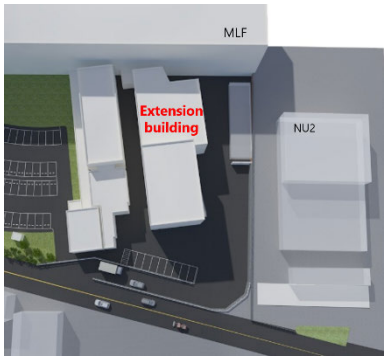

Figure 3. Exterior design of the extension building for the H2 area endorsed by the J-PARC center task force.

References

[1] N. Kawamura, *et al.*, Prog. Theor. Exp. Phys. **2018**, 113G01 (2018).
[2] K. Shimomura, AIP conf. proc. **1382**, 245 (2011).
[3] T. Mibe, *et al.*, Chin. Phys. C **34**, 745 (2010).
[4] H. Natori, *et al.*, Nucl. Phys. B (Proc. Suppl.) **248-250**, 52 (2014).
[5] H. Fujimori, *et al.*, Nucl. Instrum. Methods Phys. Res. Sect. A **600**, 170 (2009).

T. Yamazaki[1,2] and N. Nakamura[1,2]
[1]*Institute of Materials Structure Science, KEK;* [2]*Muon Science Section, Materials and Life Science Division, J-PARC Center*

MLF Safety

Research Safety

1. Radiation safety

Radiation safety for users

The low-surface contamination area that has been adopted at the MLF experimental halls from November 2016 is essential for avoiding surface-contamination problems caused by a sample, an environmental atmosphere, and so on. Several experiments with gaseous or liquid samples or atmospheres have been conducted at the MLF, showing that it was useful to expand the flexibility of the experiments.

The monitors for take-out articles allow to bring an article out from the controlled area without significant trouble. However, the troubles with hand-foot-clothe monitors (such as damage of the light shielding sheets), which check the radiation contamination in workers, have not decreased.

The MLF radiation team, in cooperation with CROSS, supports user experiments by measuring activated samples and devices with Ge detectors, and also supports rad-work, contamination and dose-rate surveys in each of the experiment devices, radiation safety checks for experiments, and so on. All monitors and all survey meters prepared by the MLF radiation team are inspected and calibrated annually.

Survey of the MLF facility for the 1-MW operation

On July 3, 2019, a 1-MW proton beam operation at the MLF was conducted for 10.5 hours. In the 1-MW operation, the MLF division and the Radiation Control section cooperatively measured the dose rates at all evaluation points inside and outside the MLF to check the shielding performance. The dose rate limitations specified in the law are 1 mSv/week (25 μSv/hour with 40 hours/week) at the controlled area, where persons can always enter and 1.3 μSv/3month (2.6 mSv/hour with 500 hours/3month) at the non-controlled area. The results confirmed that the dose rates measured at all evaluation points were below those allowed in the radiation license application.

Radiological license upgrade

The specified radiological license upgrades for the MLF in FY2019 were not done.

2. Chemical safety

As an annual task, the usual chemical safety checks of user-brought chemical materials, such as specimen and reagents, to evaluate their toxicity and the stability of their actual physical state – powder, solid, liquid or gas, were performed successfully by the chemical-safety team, along with the approval of the actual materials for use by individual beamline staffs. As a result, the experiments were conducted without serious chemical problems. Figure 1 shows a trend for the amount of chemical materials subjected to safety checks over the last 10 years. The saturation of amount of user-brought chemical materials for chemical safety is seen from Fig. 1 under the stable 500-kW class operation.

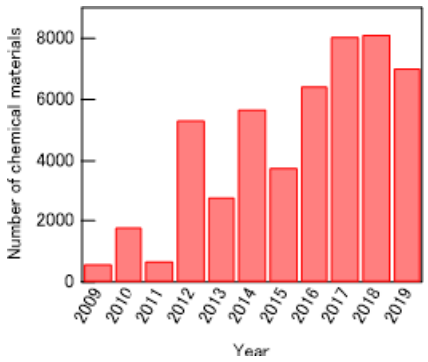

Figure 1. Trend of the amount of user-brought chemical materials for chemical safety check from the start of MLF operation to the last year.

Therefore, we can evaluate the amount of user-brought chemical materials at a 1-MW stable operation. It is expected to be around 15,000. Because of the enormously large number of chemical materials, we introduced online monitors for displaying a "sample risk assessment sheet" of chemical materials for individual proposals for that day in experimental halls to confirm them quickly and prepare them in advance.

Figure 2. Online monitor for displaying a "sample risk assessment sheet".

3. Sample environment safety

Table 1 shows the statistics of the common sample environment for experiments, such as a magnetic field apparatus and various kinds of cryostats and furnaces in the last year. The items with red letters are the new apparatus introduced in the MLF in the last year. They provide various kinds of external light field. The common sample environment equipment was used 50 times within 256 days in total. The common sample environment is maintained by a sample environment team, whose members include JAEA, KEK and CROSS staffs. The technology development section of the MLF must perform safety check of each common sample environment before it is approved for regular operation. For example, the maximum controllable value, the temperature of the equipment, the interlock system, and the electrical and structural integrity are examined in the safety check. If the specifications of each common sample environment have changed, it is necessary to do a new safety check. As a result, all common sample environment equipment operated well, and there were no safety problems, including with the newly introduced apparatus.

Table 1. Statistics of the common sample environment.

Equipment	Times	Total days
7T magnet	10	47
2K cryostat	9	29
3He cryostat	5	20
Dilution cryostat	9	48
Cryostat for residual stress measurement	4	9
GM cryo-furnace	1	2.5
Nb furnace	3	11.5
SANS furnace	1	4
Xenon lamp	1	4
Mercury lamp	3	6
LED light source	1	2.5
Total	47	183.5

4. Crane safety

Throughout the year, we use cranes to change sample environment equipment for experiments and to perform various kinds of maintenance of the neutron instruments. There are 50 t and 7.5 t cranes in experimental-hall No.1 and there are 50 t, 7.5 t and 15 t cranes in experimental-hall No.2 and its extension building. The operations of those cranes are limited to crane operators licensed by the government who were also trained by our crane safety staff and passed our skill check. In addition, before each individual crane operation, the crane working group must submit a dedicated usage sheet and its content, which includes information of suspended load, weight, total number and method of slinging by the crane staff, must be approved. As a result, last year, there were no problems with the crane operations. Figure 3 shows last year's statistics of crane use. All cranes in the experimental halls were used 244 times in total. The usage number increased by about 20% compared with the previous year. As usual, from June to October, which is the period of maintenance of the neutron instruments, the trend of crane usage was high. In addition, the highest crane usage number was recorded in March of this fiscal year. It was because the beam operation was performed in the end of March when the fabricated apparatus was delivered and tested in the experimental halls.

Figure 3. Trend of the total crane usage in one year.

M. Harada[1], M. Ooi[1], M. Sekijima[1], K. Kawakami[2], K. Aizawa[2], A. Hori[2], H. Tanaka[2], W. Kambara[2], M. Sawabe[2], K. Suzuya[3], N. Kawamura[4], Y. Sakaguchi[5], R. Takahashi[2], M. Ishikado[5], Y. Yamaguchi[5], and K. Soyama[6]

[1]Neutron Source Section, Materials and Life Science Division, J-PARC Center; [2]Technology Development Section, Materials and Life Science Division, J-PARC Center; [3]Neutron Science Section, Materials and Life Science Division, J-PARC Center; [4]Muon Science Section, Materials and Life Science Division, J-PARC Center; [5]Neutron Science and Technology Center, CROSS; [6]Materials and Life Science Division

MLF Operations in 2019

Beam Operation Status at the MLF

1. Overall

In Japanese Fiscal Year (JFY) 2019, the beam operation at the MLF started on April 2, 2019, with a beam power of 500 kW and ended on March 27, 2020. Table 1 shows the scheduled time and availability in JFY2019. In the schedule, the beam period of 2019A switched to 2019B on November 17. Since neutron Target #9, which was replaced in the summer of 2019 with Target #11, had the helium bubbler to mitigate cavitation erosion at the target vessel, the beam power was increased beyond 500 kW. The records of the beam power and the availability are shown in Fig. 1. In JFY2019, the beam operation started with a power of 500 kW with a double-bunch beam in the period from April 3 and to the end of March.

As shown in Table 1, a very stable beam operation with a 95.9% availability was maintained from April 3 to June 28, just before the summer outage period. R&D for a high-intensity beam operation were carried out. To minimize the negative influence on the users' work caused by potential target failure, we made a demonstration of the high-intensity beam operation after the user beam delivery. A successful beam operational demonstration with 1-MW power was carried out for 10.3 hours on July 3 with a remarkably high beam availability of 98.6%. For measurement for the emergency call in the case of failure, the demonstration had been limited by 10 PM, which was required by radiation safety group to achieve effeicency emergency call. Since the operation with 1 MW was proven to be safe, next year, the demonstration with the same power will not have a time limit.

Table 1. Run cycle, scheduled time, and availability.

Run	Duration	Scheduled time (h)	Beam time (h)	Availability (%)
82	Apr 2 – Jul 2	1840	1763.2	95.9
83	Nov 5– Dec 19	936	141.7	15.1
84	Jan 13 – Mar 31	1647	1522.5	94.3
2019A	Apr 2 – Nov 16	2071	1763.2	85.2
2019B	Nov 17 – Mar 31	2352	1694.2	72.0
Overall		4423	3457.4	78.2

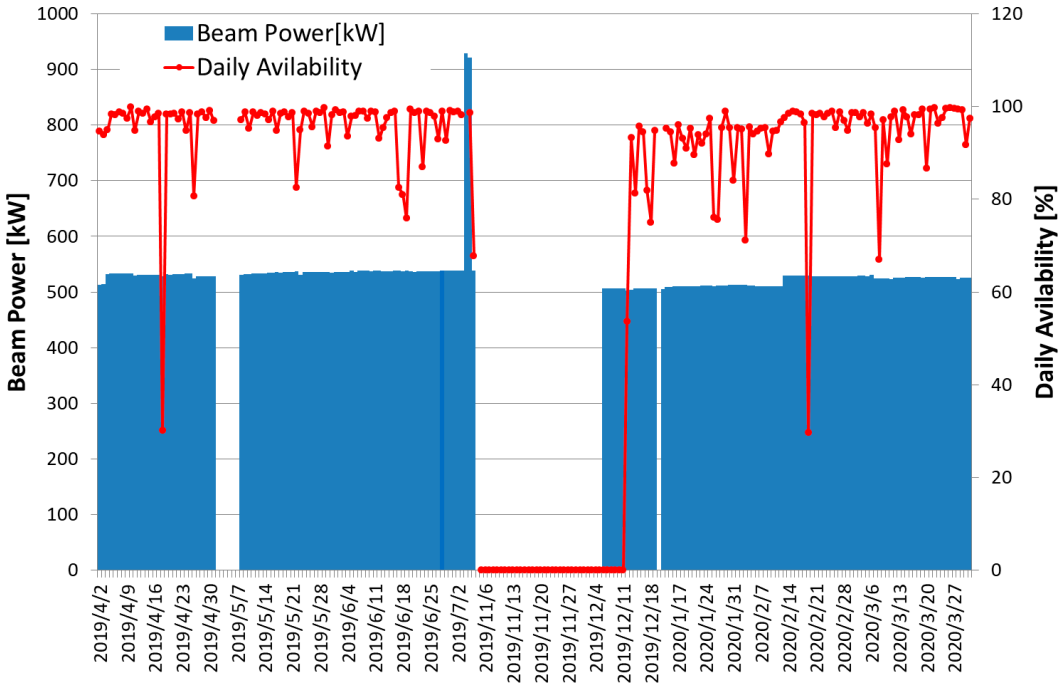

Figure 1. Beam power trend (blue line) at the MLF and availability per day (red line).

Table 2. Events that stopped the beam and reduced the daily availability to less than 80%.

Stop date	Cause of beam stop	Stop duration for each event [h]
4/18	LINAC ion source failure and replacement	16.8
6/18 and 6/19	RCS shift bump failure and MLF fire alarm malfunction	6.7
From 11/5 to 12/11	MLF gas handling system for target replacement	768
12/12	LINAC timing module failure	7.0
12/18	MR beam transport (3–50BT) water flow shortage	6.0
1/26 and 1/27	3NBT vacuum failure	11.6
2/3	MR beam transport (3–50BT) water flow shortage	7.0
3/8	LINAC klystron failure and recovery	8.0

After the summer outage period, the beam operation was planned to be resumed on November 5. Due to the failure of the gas handling system for the mercury target, the restart date was significantly postponed until the replacement of the mercury target was completed. The work to fix the system was the main reason for the beam stop. After the outage, the beam operation was resumed on December 6. Eventually, the overall availability in JFY2019 was 78.2%.

In the past, a relatively long beam shutdown period was required to complete the purification of the cryogenic system for the neutron moderator. In the summer of 2016, the impurities in the loop of the cryogenic system were removed completely; after that, the periodical purification was not required. Thus, a long uninterrupted work period of 3,459 h was attained in JFY2019.

The beam operation was stopped on several occasions due to minor failures. Typical causes of the beam stops with daily availability of less than 80% are summarized in Table 2 and described below.

2. Causes of the beam stop

LINAC:

During JFY2019, there were no shortages of water flow for the magnet at LINAC, which had been the main reason for beam stops in the last fiscal year. On April 18, the ion source stopped due to the failure of its RF antenna. It took 14 hours to replace it with a new ion source. After the replacement, the tuning of the accelerator tookr 4 hours.

3-GeV Rapid Cycling Synchrotron (RCS):

The power supply to the shift bump magnet at RCS failed in the early morning of June 18 due to the failure of the charger of the power supply. Following this event, a fire alarm malfunction happened at the MLF late at night.

Beam transport from RCS to the MLF (3NBT)

A malfunction of the vacuum system happened on January 16 at 3NBT due to the crack of a chain clamp used as a coupler at the vacuumed beam duct. With the help of the auxiliary vacuum pumps, the vacuum pressure recovered quickly. Due to the electrical noise of the auxiliary pump, malfunctions of the vacuum pressure gauge for fast closing value occurred several times while the cracked chain clamp was being changed. Next summer, all chain clamps vulnerable to cracking will be exchanged.

30-GeV Synchrotron (MR)

After fixing the failure of the beam-bending magnet at the 3–50 BT, which delivers the beam from the RCS to MR, the MR operation was resumed last summer. In JFY2019, the beam operation to MR started in beam sharing mode at RCS. Due to insufficient water flow to the magnet, the beam operation to the MLF was interrupted twice on December 18 and February 3.

S. Meigo
Neutron Source Section, Materials and Life Science Division, J-PARC Center

Users at the MLF

In fiscal year (FY) 2019, the MLF was running stably with a beam power of 500 kW throughout the year. Due to the delay caused by restoring of the gas handling system, the overall availability in JFY2019 was decreased to 78.2%. In addition, before the summer maintenance period, the 1-MW beam test was successfully operated on July 3, 2019, for 10.5 hours with a remarkably high beam delivery. The total number of users of the neutron and muon experimental facilities in FY2019 was 1,078, a slight decrease compared with FY2018, due to COVID-19.

The trend for the number of users at the MLF since the start of the operations in FY2008 is summarized in Table 1 and Fig. 1.

Table 1. The number of domestic and foreign users by fiscal year.

	FY2008		FY2009		FY2010		FY2011		FY2012		FY2013	
	Domestic Users	Foreign Users	Domestic Users	Foreign Users	Domestic Users	Foreign Users	Domestic Users	Foreign Users	Domestic Users	Foreign Users	Domestic Users	Foreign Users
Neutron	107		317		476		259		708		449	
	95	12	303	14	432	44	238	21	628	80	399	50
Muon	18		40		50		23		56		61	
	18	0	38	2	42	8	21	2	46	10	50	11

	FY2014		FY2015		FY2016		FY2017		FY2018		FY2019	
	Domestic Users	Foreign Users	Domestic Users	Foreign Users	Domestic Users	Foreign Users	Domestic Users	Foreign Users	Domestic Users	Foreign Users	Domestic Users	Foreign Users
Neutron	824		559		852		927		965		940	
	711	113	476	83	744	108	742	185	789	176	827	113
Muon	91		69		99		179		161		138	
	78	13	59	10	83	16	149	30	146	15	127	11

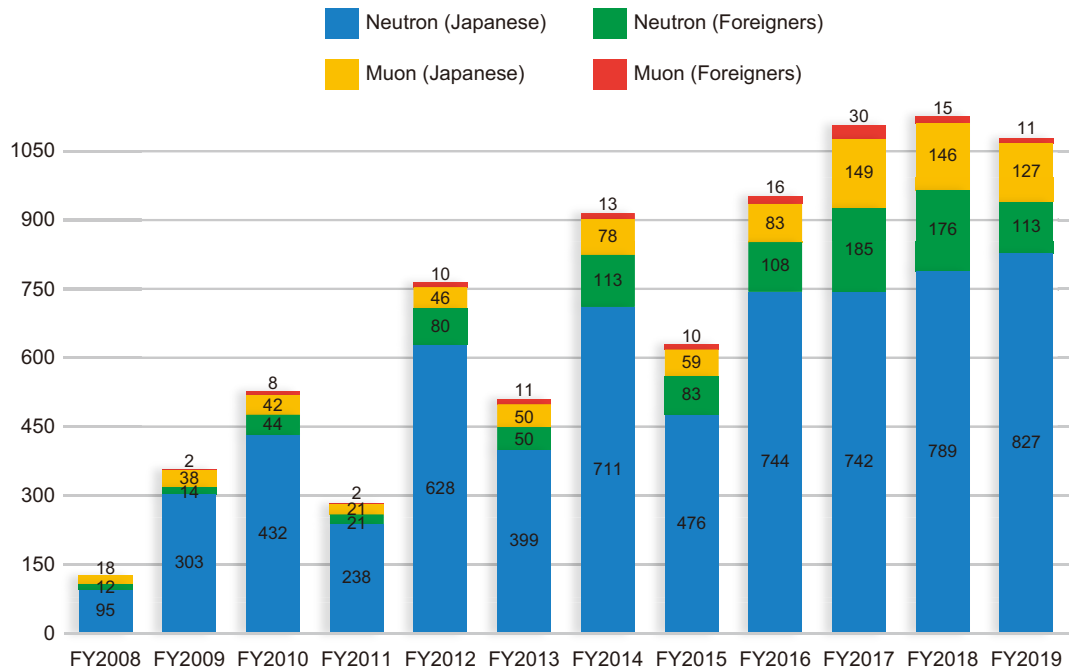

Figure 1. The number of domestic and foreign users by fiscal year.

MLF Proposals Summary – FY2019

Table 1. Breakdown of Proposals Numbers for the 2019 Rounds.

Beam-line	Instrument		2019A		2019B		Full Year			
			Submitted	Approved	Submitted	Approved	Submitted		Approved	
			GU	GU	GU	GU	PU/S	IU	PU/S	IU
BL01	4D-Space Access Neutron Spectrometer - ***4SEASONS***		16(0)	13(0)	26(1)	12(1)	1	1	1	1
BL02	Biomolecular Dynamics Spectrometer - ***DNA***		12(0)	8(0)	29(3)	10(3)	2	2	2	2
BL03	Ibaraki Biological Crystal Diffractometer - ***iBIX***	(100–β)‡	1	0	1	1	0	0	0	0
		(β)†	0	0	0	0	43※	0	43※	0
BL04	Accurate Neutron-Nucleus Reaction Measurement Instrument - ***ANNRI***		10	4	11	4	1	1	1	1
BL05	Neutron Optics and Physics - ***NOP***		5	5	5	5	1	0	1	0
BL06	Neutron Resonance Spin Echo Spectrometers - ***VIN ROSE***		4	3	4	2	1	0	1	0
BL08	Super High Resolution Powder Diffractometer - ***S-HRPD***		14	10	17	12	1	0	1	0
BL09	Special Environment Neutron Power Diffractometer - ***SPICA***		6	3	4	4	1	0	1	0
BL10	Neutron Beamline for Observation and Research Use - ***NOBORU***		8	8	13	7	3	1	3	1
BL11	High-Pressure Neutron Diffractometer - ***PLANET***		9(0)	9(0)	15(0)	10(0)	0	1	0	1
BL12	High Resolution Chopper Spectrometer - ***HRC***		5	5	10	5	1	0	1	0
BL14	Cold-neutron Disk-chopper Spectrometer - ***AMATERAS***		27	11	37	10	3	1	3	1
BL15	Small and Wide Angle Neutron Scattering Instrument - ***TAIKAN***		36(2)	14(2)	59(0)	13(0)	3	3	3	3
BL16	High-Performance Neutron Reflectometer with a horizontal Sample Geometry - ***SOFIA***		21	18	21	20	0	1	0	1
BL17	Polarized Neutron Reflectometer - ***SHARAKU***		19(2)	16(2)	27(2)	13(2)	1	3	1	3
BL18	Extreme Environment Single Crystal Neutron Diffractometer - ***SENJU***		13(0)	8(0)	25(1)	5(1)	1	1	1	1
BL19	Engineering Diffractometer - ***TAKUMI***		16	12	24	14	1	1	1	1
BL20	Ibaraki Materials Design Diffractometer - ***iMATERIA***	(100–β)‡	10	5	14	8	0	0	0	0
		(β)†	42	42	25	25	25	0	25	0
BL21	High Intensity Total Diffractometer - ***NOVA***		22	20	25	19	1	0	1	0
BL22	Energy Resolved Neutron Imaging System - ***RADEN***		17(0)	13(0)	21(0)	11(0)	1	2	1	2
BL23	Polarization Analysis Neutron Spectrometer - ***POLANO***		2	2	2	2	1	0	1	0
D1	Muon Spectrometer for Materials and Life Science Experiments - ***D1***		17(0)	8(0)	18(1)	8(1)	0	1	0	1
D2	Muon Spectrometer for Basic Science Experiments - ***D2***		8(1)	4(0)	12(4)	6(2)	0	1	0	1
S1	General purpose μSR spectrometer - ***ARTEMIS***		30(2)	25(1)	29(3)	23(3)	1	1	1	1
UA	Muon U		0	0	0	0	0	1	0	1
Total			**369**	**265**	**473**	**253**	**86**	**22**	**86**	**22**

GU : General Use **PU :** Project Use or Ibaraki Pref. Project Use **S :** S-type Proposals **IU :** Instrument Group Use
† : Ibaraki Pref. Exclusive Use Beamtime (β = 80% in FY2019) **‡ :** J-PARC Center General Use Beamtime (100–β = 20% in FY2019)
( ) : Proposal Numbers under the New User Promotion (BL01, BL02, BL11, BL15, BL17, BL18, BL22) or P-type proposals (D1,D2, S1) in GU
※ : Proposal rounds are held twice per year (for each of the A and B periods), with only the yearly total shown above.
The actual total number of proposals in each beamline named in the table does not match the number shown in the "Total" cell, because some proposals are submitted or approved across multiple beamlines.

Table 2. Proposals Numbers of Long Term Proposal for the 2019 Rounds.

Application FY	Submitted	Approved
2017	24	8
2018	9	5
2019	9	4

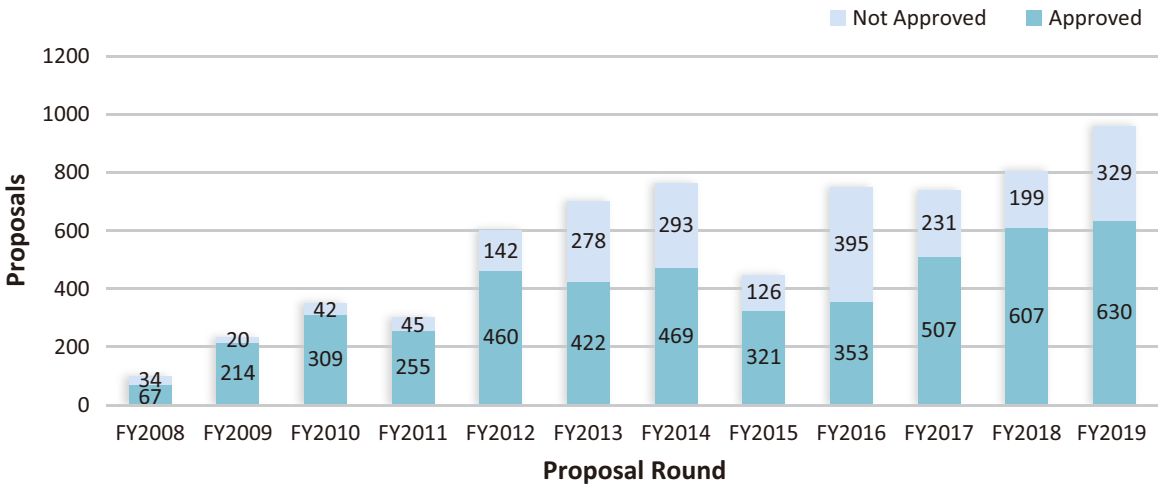

Figure 1. MLF Proposal Numbers over Time.

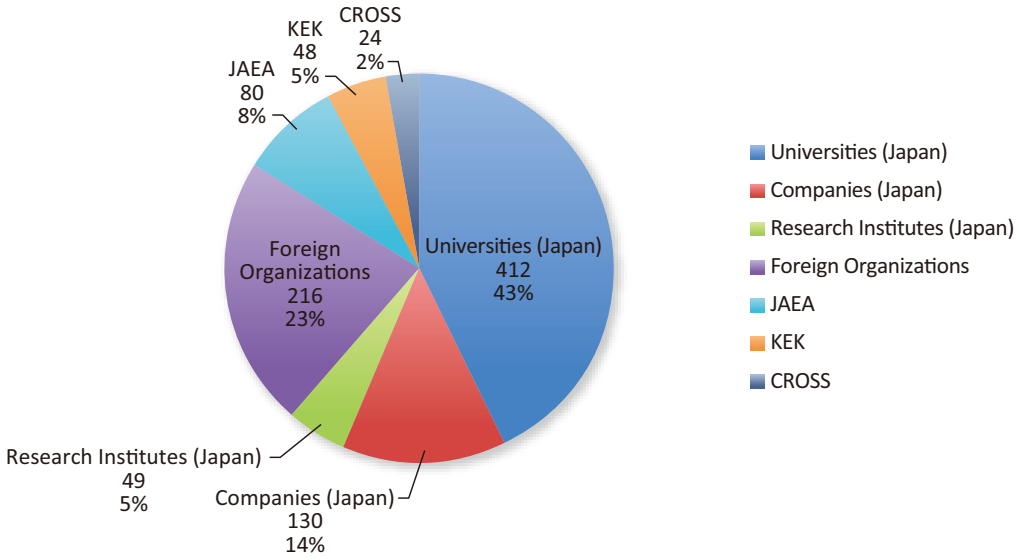

Figure 2. Origin of Submitted Proposals by affiliation - FY2019.

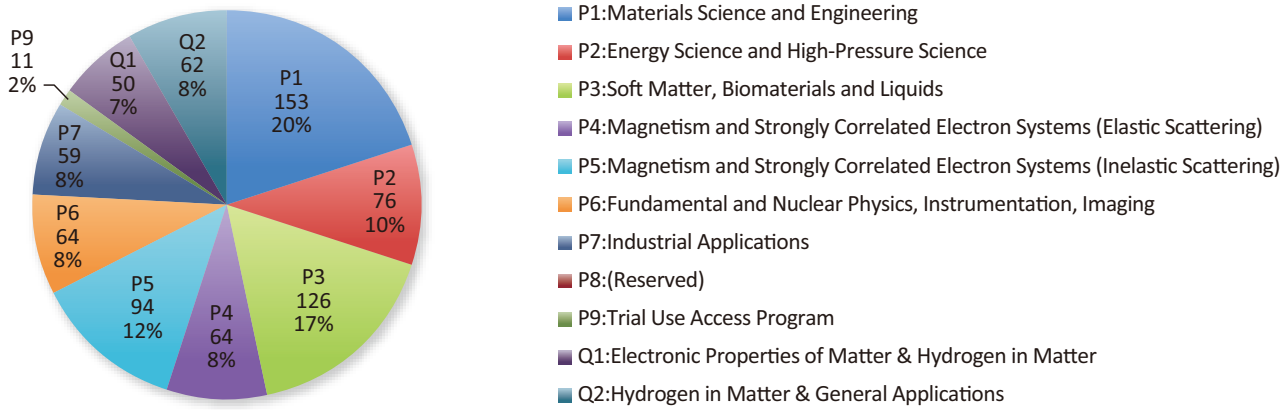

Figure 3. Submitted Proposals by Sub-committee/Expert Panel - FY2019.

MLF Division Staff 2019

Toshiji Kanaya (Head)
Kazuhiko Soyama (Deputy Head)
Toshiya Otomo (Deputy Head)
Yasuhiro Miyake (Deputy Head)
Kazuya Aizawa (Deputy Head)
Eiichi Wakai
Izumi Kuwahara

Neutron Source Section

*: additional duties

<JAEA>

Katsuhiro Haga (Leader)
Kenji Sakai (Sub-Leader)
Masahide Harada
Makoto Teshigawara
Hiroyuki Kogawa
Tomokazu Aso
Motoki Ooi
Takashi Naoe
Takashi Wakui
Masakazu Seki
Shiho Masuda
Akira Shibata
Hideyuki Nemoto
Akihiko Watanabe
Hideki Muto
Kouhei Hanano
Mitsuaki Sekijima
Yoshinori Kikuchi
Masakazu Nakamura
Hidemitsu Hosokawa
Atsushi Akutsu
Toshiyuki Yasuhara
Hiromi Inoue
Noriyuki Morikawa
Shigeto Tanaka
Shizuka Yoshinari
Kyoko Takahashi
Hiroshi Takada *
Shoichi Hasegawa *
Eiichi Wakai *
Shin-ichiro Meigo *
Hidetaka Kinoshita *
Kenichi Oikawa *
Tetsuya Kai *
Hiroyuki Uehara *

Neutron Science Section

*: additional duties

<JAEA>

Kenji Nakajima (Leader)
Yukinobu Kawakita (Sub-Leader)
Kentaro Suzuya
Ryoichi Kajimoto
Takanori Hattori
Mitsutaka Nakamura
Stefanus Harjo
Kenichi Oikawa
Takashi Ohhara
Takenao Shinohara
Tetsuya Kai
Seiko Kawamura
Shinichi Takata
Ryoji Kiyanagi
Kaoru Shibata
Asami Sano
Yasuhiro Inamura
Hiroyuki Aoki
Takuro Kawasaki
Kousuke Hiroi
Maiko Kofu
Naoki Murai
Yoshichika Seki
Takayuki Yamashita
Yusuke Tsuchikawa
Kanae Ito
Tatsuya Kikuchi
Masashi Harada
Daigo Setoyama
Takeshi Harada
Hideaki Isozaki
Keiichi Inoue
Misono Fujii
Naoko Shimizu
Toshiko Goto
Itaru Tamura *
Kouji Kaneko *
Hiroshi Nakagawa *
Hideo Harada *
Atsushi Kimura *
Shoji Nakamura *
Yosuke Toh *
Mariko Segawa *
Masahide Harada *
Kazuya Aizawa *
Masao Watanabe *
Dai Yamazaki *
Hiroshi Suzuki *

Satoshi Morooka *
Atsushi Moriai *
Shunsuke Endo *
Kazuo Kurihara *
Tarou Tamada *
Yuu Hirano *
Takeshi Hiromoto *

<KEK>

Shinichi Ito (Sub-Leader)
Hideki Seto
Toshiya Otomo *
Takashi Kamiyama
Hitoshi Endo
Testuya Yokoo
Takashi Ino
Norifumi Yamada
Takashi Honda
Naokatsu Kaneko
Shuki Torii
Hidetoshi Oshita
Kaoru Taketani
Kenji Mishima
Hiroyuki Aoki *
Asami Sano *
Kazutaka Ikeda
Masato Hagihala
Hiraku Saito
Takashi Saito
Cho Kwanghee

Technology Development Section

*: additional duties

<JAEA>

Kazuya Aizawa * (Leader)
Takayuki Oku (Sub-Leader)
Kazuyoshi Tatsumi
Takeshi Nakatani
Masao Watanabe
Yuhua Su
Ryota Komine
Takuya Okudaira
The Dang Vu
Wataru Kambara
Akihiro Hori
Hideaki Takahashi
Ryuta Takahashi
Wu Gong
Kazuhiro Kawakami
Hiromichi Tanaka
Hiroyuki Asai
Yukiko Nagai
Kenji Sakai *
Tetsuya Kai *
Hiroyuki Kogawa *
Motoki Ooi *
Kentaro Suzuya *
Mitsutaka Nakamura *
Shinichi Takata *
Kaoru Sakasai *
Tatsuya Nakamura *
Yasuhiro Inamura *
Masahide Harada *
Tomokazu Aso *
Seiko Kawamura *
Fumiaki Kono *
Rumi Shimizu *
Tatsuhito Matsuo *
Satoru Fujiwara *
Motoyasu Adachi *
Shigeki Arai *
Chie Shibazaki *

<KEK>

Tomohiro Seya
Setsuo Sato
Testuya Yokoo *
Shuki Torii *
Takashi Ino *
Naokatsu Kaneko *
Kaoru Taketani *
Naritoshi Kawamura *
Hiroshi Fujimori *
Shunsuke Makimura *

Neutron Instrumentation Section

*: additional duties

<JAEA>

Kaoru Sakasai (Leader)
Dai Yamazaki
Kentaro Toh
Tatsuya Nakamura
Ryuji Maruyama *
Tomokatsu Koizumi
Masashi Suzuki
Yukiko Uno
Masumi Ebine *

Muon Science Section

*: additional duties

<KEK>

Ryosuke Kadono (Leader)
Naritoshi Kawamura (Sub-Leader)
Yasuhiro Miyake *
Koichiro Shimomura
Akihiro Koda
Patrick Strasser
Takayuki Yamazaki
Hiroshi Fujimori
Yutaka Ikedo
Yasuo Kobayashi
Junpei Nakamura
Takashiro Yuasa
Yu Oishi
Yukinori Nagatani
Shiro Matoba
Soshi Takeshita
Hiroaki Natori
Dey Sourav Kumar
Shoichiro Nisimura
Masatoshi Hiraishi
Hirotaka Okabe
Motonobu Tanpo
Taihei Adachi
Tatsuhiko Tachibana
Hua Li
Shogo Doiuchi
Akiko Hashimoto
Yoshinori Ito
Izumi Umegaki

<JAEA>

Wataru Higemoto *
Takashi Ito *

CROSS Staff 2019

Director **Hideaki Yokomizo**

Science Coordinators

Kazuhisa Kakurai
Jun Sugiyama
Takashi Noma

Research & Development Division

*: additional duties

Jun-ichi Suzuki (Head)
Kenichi Funakoshi (Deputy Head)
Tsukasa Miyazaki * (Deputy Head)
Sayaka Suzuki *

<BL01 Group>
Kazuya Kamazawa (Leader)
Kazuhiko Ikeuchi
Kazuki Iida

<BL02 Group>
Masato Matsuura (Leader)
Takeshi Yamada
Taiki Tominaga

<BL11 Group>
Kenichi Funakoshi * (Leader)
Jun Abe
Shinichi Machida

<BL15 Group>
Kazuki Ohishi (Leader)
Jun-ichi Suzuki *
Hiroki Iwase
Yukihiko Kawamura

<BL17 Group>
Noboru Miyata (Leader)
Kazuhiro Akutsu
Takayasu Hanashima

<BL18 Group>
Akiko Nakao (Leader)
Koji Munakata
Yoshihisa Ishikawa

<BL22 Group>
Hirotoshi Hayashida (Leader)
Joseph Don Parker
Yoshihiro Matsumoto

<Technical Support Group>
Koji Kiriyama (Leader)
Takayoshi Ito (Sub-Leader)
Yoshifumi Sakaguchi
Hiroshi Kira
Motoyuki Ishikado
Nobuo Okazaki
Shuoyuan Zhang
Makoto Kobayashi
Satoshi Kasai
Toshiaki Morikawa
Hideyuki Hiramatsu
Kentaro Moriyama
Hiroshi Arima
Keiichi Ohuchi
Masae Sahara

Safety Division

*: additional duties

Yasuhiro Yamaguchi (Head)
Koji Kiriyama *
Tazuko Mizusawa *
Masae Sahara *

Utilization Promotion Division

*: additional duties

Junichi Sato (Head)
Tsukasa Miyazaki * (Deputy Head)
Atsuko Irie
Miho Igarashi
Seiya Konishi (Leader)
Tazuko Mizusawa
Taeko Ishikawa
Maya Endo
Toshiki Asai (Leader)
Emi Goto
Sayaka Suzuki
Yutaka Ebara
Takayoshi Ito *
Nobuo Okazaki *

Administration Division

Michihiko Murasawa (Head)
Takashi Hikita (Leader)
Rei Ohuchi
Tomoko Sakuma
Mutsumi Shiraishi
Shinobu Matsumoto

Industrial Collaboration Promotion Division

*: additional duties

Tsukasa Miyazaki (Head)
Takashi Noma *
Seiya Konishi *
Noboru Miyata *
Jun Abe *
Takeshi Yamada *

Ibaraki Neutron Beamline Staff in 2019

Ibaraki Prefectural Government

<Senior Director for Neutron Promotion>
Hironori Kodama

<Neutron Beamline Coordinator>
Michiko Konno
Tetsuroh Minemura

Ibaraki University *

* Trustee of the Beamline operations

<BL03 iBIX Group>
Katsuhiro Kusaka (Leader)
Taro Yamada
Naomine Yano
Ichiro Tanaka
Takaaki Hosoya

<BL20 iMATERIA Group>
Toru Ishigaki (Leader)
Akinori Hoshikawa
Takeshi Matsukawa
Yusuke Onuki
Satoshi Koizumi
Yohei Noda
Tomoki Maeda

<Technical Support Group>
Junichi Hiroki
Tomoyuki Nakazawa
Mitsuyuki Fujii
Shinju Shibata
Takumi Inada

Proposals Review System, Committees and Meetings

Proposal Review System

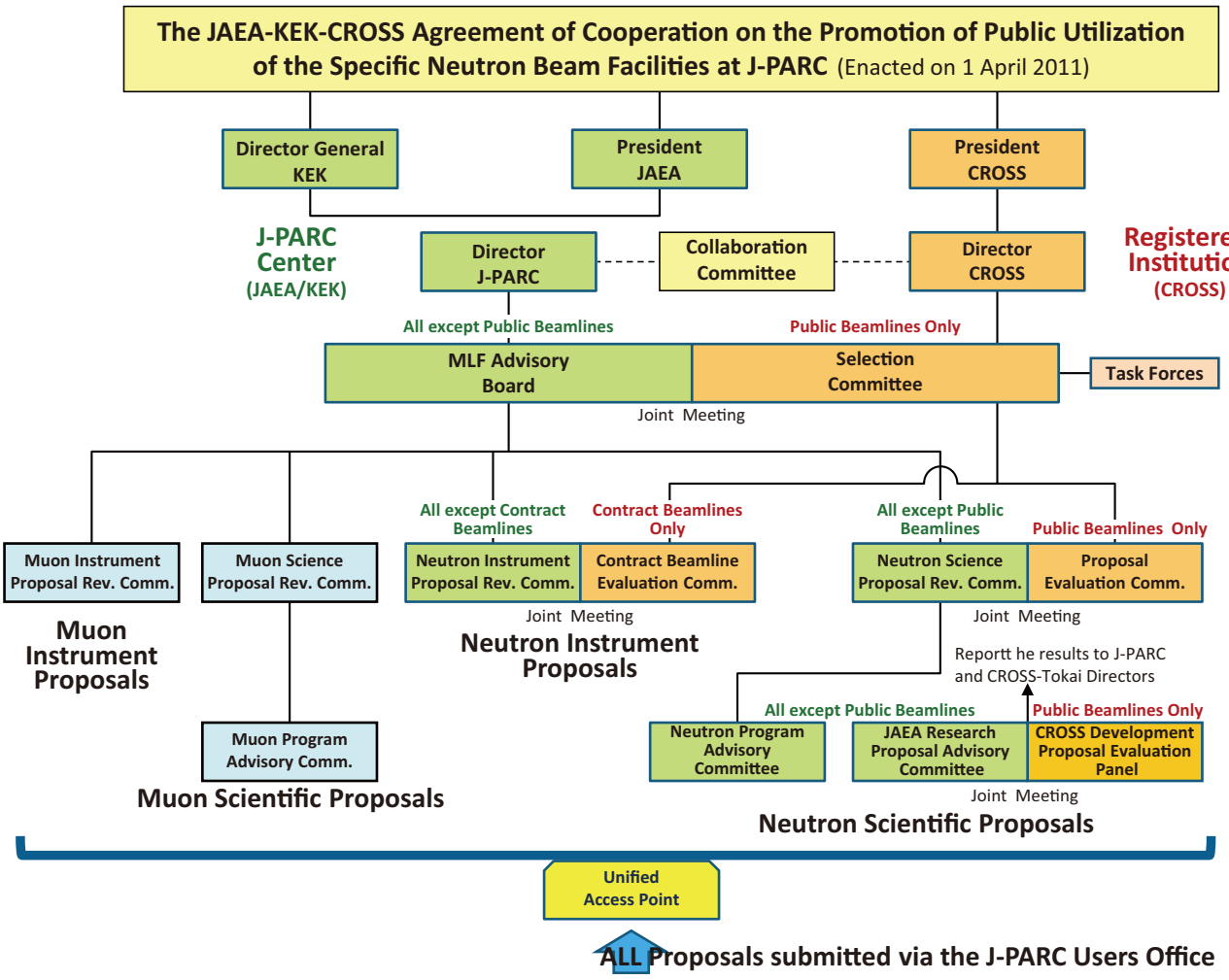

Figure 1. Proposals Review System Framework.

Materials and Life Science Facility Advisory Board

Kazuya Aizawa	Japan Atomic Energy Agency
Hiroshi Amitsuka	Hokkaido University
Taka-hisa Arima	The University of Tokyo
Ryosuke Kadono	High Energy Accelerator Research Organization
Kazuhisa Kakurai	Comprehensive Research Organization for Science and Society
Takashi Kamiyama	High Energy Accelerator Research Organization
Takashi Kamiyama	Hokkaido University
Toshiji Kanaya	High Energy Accelerator Research Organization
Yukinobu Kawakita	Japan Atomic Energy Agency
Takamitsu Kohzuma	Ibaraki University
Yoji Koike	Tohoku University
Kenya Kubo	International Christian University
Yasuhiro Miyake	High Energy Accelerator Research Organization
Kenji Nakajima	Japan Atomic Energy Agency
Toshiya Otomo	High Energy Accelerator Research Organization
Yoshiharu Sakurai	Japan Synchrotron Radiation Research Institute
Taku Sato	Tohoku University
Hideki Seto	High Energy Accelerator Research Organization
Mitsuhiro Shibayama	The University of Tokyo
Kazuhiko Soyama	Japan Atomic Energy Agency
Masaaki Sugiyama (chair)	Kyoto University
Jun-ichi Suzuki	Comprehensive Research Organization for Science and Society
Atsushi Takahara	Kyushu University
Masayasu Takeda	Japan Atomic Energy Agency
Toshio Yamaguchi	Fukuoka University

Term: through March 31, 2021

Neutron Science Proposal Review Committee

Hiroyuki Kagi	The University of Tokyo
Ryosuke Kadono	High Energy Accelerator Research Organization
Toshiji Kanaya	High Energy Accelerator Research Organization
Yoshiaki Kiyanagi	Nagoya University
Tsukasa Miyazaki	Comprehensive Research Organization for Science and Society
Kenji Nakajima	Japan Atomic Energy Agency
Kenji Ohoyama	Ibaraki University
Hideki Seto	High Energy Accelerator Research Organization
Shinichi Shamoto	Japan Atomic Energy Agency
Yuichi Shimakawa	Kyoto University
Hirohiko Shimizu	Nagoya University
Masaaki Sugiyama (chair)	Kyoto University
Masayasu Takeda	Japan Atomic Energy Agency
Ichiro Tanaka	Ibaraki University

Term: through September 30, 2019

Muon Science Proposal Review Committee

Tadashi Adachi	Sophia University
Kenta Amemiya	High Energy Accelerator Research Organization
Hiroshi Amitsuka	Hokkaido University
Hidehito Asaoka	Japan Atomic Energy Agency
Toshiyuki Azuma	Institute of Physical and Chemical Research
Katsuyuki Fukutani	The University of Tokyo
Wataru Higemoto	Japan Atomic Energy Agency
Adrian Hillier	Rutherford Appleton Laboratory
Ryosuke Kadono	High Energy Accelerator Research Organization
Toshiji Kanaya	High Energy Accelerator Research Organization
Naritoshi Kawamura	High Energy Accelerator Research Organization
Yasushi Kino	Tohoku University

Akihiro Koda	High Energy Accelerator Research Organization
Kenya Kubo (chair)	International Christian University
Roderick Macrae	Marian University
Yasuyuki Matsuda	The University of Tokyo
Tsutomu Mibe	High Energy Accelerator Research Organization
Yasuhiro Miyake	High Energy Accelerator Research Organization
Kenji Nakajima	Japan Atomic Energy Agency
Chihiro Ohmori	High Energy Accelerator Research Organization
Toshiya Otomo	High Energy Accelerator Research Organization
Hideki Seto	High Energy Accelerator Research Organization
Tatsushi Shima	Osaka University
Koichiro Shimomura	High Energy Accelerator Research Organization
Jun Sugiyama	Toyota Central R&D Labs.
Masaaki Sugiyama	Kyoto University
Toshiyuki Takayanagi	Saitama University
Hideki Tou	Kobe University

Term: through March 31, 2019

Proposal Evaluation Committee

Hiroyuki Kagi	The University of Tokyo
Toshiji Kanaya	High Energy Accelerator Research Organization
Yoshiaki Kiyanagi	Nagoya University
Tsukasa Miyazaki	Comprehensive Research Organization for Science and Society
Kenji Ohoyama	Ibaraki University
Shinichi Shamoto	Japan Atomic Energy Agency
Yuichi Shimakawa	Kyoto University
Hirohiko Shimizu	Nagoya University
Masaaki Sugiyama (chair)	Kyoto University
Ichiro Tanaka	Ibaraki University

Term: through September 30, 2019

Selection Committee

Taka-hisa Arima	The University of Tokyo
Yasuhiro Iye (chair)	Japan Society for Promotion of Science
Takashi Kamiyama	Hokkaido University
Hiroyuki Kishimoto	Sumitomo Rubber Industries, LTD.
Hideaki Kitazawa	Research Center for Strategic Materials
Yoji Koike	Tohoku University
Takamitsu Kohzuma	Ibaraki University
Yoshiharu Sakurai	Japan Synchrotron Radiation Research Institute
Taku Sato	Tohoku University
Mitsuhiro Shibayama	The University of Tokyo
Masaaki Sugiyama	Kyoto University
Atsushi Takahara	Kyushu University
Shinji Tsuneyuki	The University of Tokyo
Toshio Yamaguchi	Fukuoka University

Term: through March 31, 2021

Neutron Advisory Committee (NAC)

NAC convened on 17–18 February, 2020 at the J-PARC site, Tokai

Group photo of NAC

Neutron Advisory Committee (17–18 Feb. 2020)

Robert McGreevy (chair)	Rutherford Appleton Laboratory
Christiane Alba-Simionesco	Laboratoire Léon Brillouin
Bertrand Blau	Paul Scherrer Institut
Sung-Min Choi	Korea Advanced Institute of Science and Technology
Michael Dayton	Oak Ridge National Laboratory
Yoshiaki Kiyanagi	Nagoya University
Yoshie Ohtake	Institute of Physical and Chemical Research
Christian Rüegg	Paul Scherrer Institut
Andreas Schreyer	European Spallation Source
Jamie Schulz	Australian Nuclear Science and Technology Organization
Masaaki Sugiyama	Kyoto University

Muon Advisory Committee (MAC)

MAC convened on 25–26 February, 2020 at the KEK Tokai Campus, Tokai

Group photo of MAC

Muon Advisory Committee (25–26 Feb. 2020)

Thomas Prokscha (chair)	Paul Scherrer Institut
Hiroshi Amitsuka	Hokkaido University
Klaus Kirch	ETH Zurich and Paul Scherrer Institut
Kenya Kubo	International Christian University
Andrew Macfarlane	The University of British Columbia
Martin Månsson	KTH Royal Institute of Technology
Takashi Nakano	Osaka University
Tadayuki Takahashi	The University of Tokyo

Workshops, Conferences, Seminars and Schools in 2019

Conferences held jointly by J-PARC MLF and CROSS

2019 Meeting on J-PARC MLF Industrial Use
18–19 Jul. 2019, Akihabara Convention Hall, Tokyo


Photo of the 2019 Meeting on J-PARC MLF Industrial Use (photo courtesy of J-PARC Center)

The 3rd J-PARC Symposium (the 10th Anniversary)
23–26 Oct. 2019, Epochal Tsukuba, Ibaraki


Photo of The 3rd J-PARC Symposium (the 10th Anniversary) (photo courtesy of J-PARC Center)

AOCNS 2019 & 19th JSNS meeting
16–21 Nov. 2019, Kenting, Taiwan

MRM2019
10–14 Dec. 2019, Yokohama Symposia, Kanagawa

2019 Z-Code Beginner Level Training Course
7–8 Nov. 2019, Essam Kanda Hall, Tokyo

Workshops held by KEK

Fundamental Physics with Pulsed Cold Neutrons (BL05)
20–21 Dec. 2019, Nagoya Univ., Aichi

High-Resolution Neutron Powder Diffraction Method using SuperHRPD (BL08)
11 Dec. 2019, KEK Tokai Campus, Tokai

Dynamics using High Resolution Chopper Spectrometer (BL12)
16 Dec. 2019, KEK Tokai Campus, Tokai

Order-disorder structural analysis of functional materials using high-intensity neutron total scattering method (BL21)
29 Nov. 2019, KEK Tokai Campus, Tokai

Elucidation of cross-correlation physics using the Polarized Neutron Spectrometer, POLANO (BL23)
5 Dec. 2019, KEK Tokai Campus, Tokai

1st Symposium on Integration of Humanities and Science
27–28 Jul. 2019, National Museum of Nature and Science, Tokyo

2nd Symposium on Integration of Humanities and Science
25–26 Dec. 2019, Osaka University, Osaka

Workshops and Seminars held by CROSS and other organizations

1st Meeting on evaluation method of reinforced concrete using neutron
10 Apr. 2019, IBARAKI Quantum Beam Research Center, Tokai

Explanatory meeting on evaluation method of reinforced concrete using neutron
18 Apr. 2019, J-PARC Research Building, Tokai

1st Meeting on materials research using neutron under high pressure
15 Aug. 2019, TKP Tokyo

The 22nd CROSSroads Workshop
"Neutron Scattering for the Material Science of Water, Ice and Hydrides"
15 May 2019, IBARAKI Quantum Beam Research Center, Tokai

Group photo of the CROSSroads 22 (photo courtesy of CROSS)

2nd Meeting on evaluation method of reinforced concrete using neutron
20 Jun. 2019, Hazama Ando Corp., Tokyo

3rd Meeting on evaluation method of reinforced concrete using neutron
19 Aug. 2019, Tokyo University of Science, Noda campus, Chiba

2019 1st Workshop on Structural Biology
28 Nov. 2019, Essam Kanda Hall, Tokyo

2019 Workshop on Materials Science &
2019 2nd Workshop on iMATERIA
"Forefront of solar cell research"
20 Aug. 2019, Essam Kanda Hall, Tokyo

2019 Workshop on Soft Matter Neutron Scattering &
2019 2nd Workshop on iMATERIA
Current status and development of dynamic spin-polarized neutron small-angle scattering (DNP-SANS)
21 Aug. 2019, Essam Kanda Hall, Tokyo

Workshop of Tohoku Univ. & CROSS
"Development of new science by complemental use of polarized neutrons at J-PARC and JRR-3"
22–23 Aug. 2019, Tohoku Univ., Miyagi

6th Symposium on the Collaborative Use of Large Research Institutions and the KEI Super Computer 2019
17 Sep. 2019, Akihabara UDX, Tokyo

2nd Meeting on materials research using neutron under high pressure
28 Oct. 2019, TKP Tokyo station conference center, Tokyo

4th Meeting on evaluation method of reinforced concrete using neutron
31 Oct. 2019, Tokyo University of Science, Noda campus, Chiba

2019 Neutron experiment technique training course
29 Nov. 2019, Essam Kanda Hall, Tokyo

1st Joint Workshop for Complementary Use of Synchrotron Radiation and Neutrons
"Small-angle X-ray scattering measurement"
28 Nov. 2019, SPring-8, Hyogo

2nd Joint Workshop for Complementary Use of Synchrotron Radiation and Neutrons
"Toward mutual use of X-rays and neutron inelastic scattering"
9 Dec. 2019, SPring-8, Hyogo

2019 Workshop on Non-destructive Visualization and Analysis Methods
20 Dec. 2019, Essam Kanda Hall, Tokyo

23rd CROSSroads Workshop
"Sample Environment at Quantum Beam Experimental Facilities"
8 Jan. 2020, IBARAKI Quantum Beam Research Center, Tokai

2019 Workshop on Metallographic Structure
14 Jan. 2020, Essam Kanda Hall, Tokyo

2019 Workshop on Magnetic Materials
17 Jan. 2020, Essam Kanda Hall, Tokyo

2019 Workshop on Battery Materials &
2019 Workshop on Surfaces and Interfaces
29 Jan. 2020, Essam Kanda Hall, Tokyo

Schools in 2019

Hello Science from J-PARC: Exploring materials with muon
31 May 2019, iVil, Tokai

Hello Science from J-PARC: Identifying Energy Related Materials with Muon Particles
20 Sep. 2019, iVil, Tokai

Hello Science from J-PARC: Using Neutrons to Capture the Fleeting Moments of Bubbles
25 Oct. 2019, iVil, Tokai

The 4th Neutron and Muon School and MIRAI PhD School 2019
28 Oct. – 2 Nov. 2019, J-PARC Center and IBARAKI Quantum Beam Research Center, Tokai

Group photo of the 4th Neutron and Muon School (photo courtesy of J-PARC Center)

Award List

The Sawamura Award of the Iron and Steel Institute of Japan
In situ Neutron Diffraction Study on Ferrite and Pearlite Transformations for a 1.5Mn-1.5Si-0.2C Steel
Y. Tomota, Y. Wang, T. Ohmura, N. Sekido, S. Harjo, T. Kawasaki, W. Gong, A. Taniyama (2020-03-17)

Encouragement Award for Graduate Student, Department of Architecture Graduate School of Science, Tokyo University of Science
Research on deformation analysis of reinforced concrete using neutron imaging technology
K. Ueno (2020-03-17)

Japan Building Materials Association Outstanding Student Award
Research on deformation analysis of reinforced concrete using neutron imaging technology
K. Ueno (2020-03-05)

The Atomic Energy Society of Japan Kyushu Office Young Researcher Award
Measurement of SEU rates for SRAMs under Irradiation of Spallation Neutrons
J. Kuroda (2019-12-07)

3rd Asia-Oceanian Conference on Neutron Scattering Best Poster Award
Crystal structure of organic conductor I-(BETS)$_2$FeCl$_4$ studied by SENJU J-PARC
Y. Noda (2019-11-21)

3rd Asia-Oceanian Conference on Neutron Scattering Best Poster Award
Structures of mixed surfactants in solution for industrial application
M. Ohno (2019-11-20)

Best Poster Award (Second Place Award) -Session 1: Condensed Matter Physics- at the 3rd Asia-Oceanian Conference on Neutron Scattering
Localized magnetic excitations in the fully frustrated dimerized magnets
N. Kurita (2019)

The JSNS Achievement Prize
Pioneering research and leading role in the use of pulsed neutrons
M. Arai (2019-11-20)

The JSNS Technology Prize
Development of the neutron flatpanel detector
H. Takahashi, T. Fujiwara (2019-11-20)

The JSNS Young Researcher Prize
Investigations on low-dimensional and frustrated magnets
K. Nawa (2019-11-20)

The JSNS Young Researcher Prize
Microstructual characterizaton in steel using small-angle neutron scattering
Y. Oba (2019-11-20)

The Japan Society of Applied Physics Young Scientist Presentation Award
Synthesis and fast H- conduction of new lanthanum oxyhydride $LaH_{3-2x}O_x$
K. Fukui (2019-11-13)

Japan Association of Mineralogical Science Young Researcher Award
Elucidation of the behavior of carbon, hydrogen, and nitrogen-related substances in the interior of the Earth and icy celestial bodies.
A. Shinozaki (2019-09-22)

The 58th Annual Meeting of the Japan Oil Chemists' Society, Oral, Student Presentation Award
Rapid Control of Interfacial Property with Light Irradiation by Using Amphiphilic Lophine Dimers
K. Kobayashi (2019-09)

CerSJ Award for Advancements in Ceramic Science and Technology
Research of oxide type solid-state electrolytes and electrode activation materials
K. Kataoka (2019-06-07)

The Award from the Society of Rubber Science and Technology, Japan
Thermal property of bound rubber at interface with carbon
K. Hori (2019-05-23)

CerSJ Poster Award
Evaluation of magnetic anisotropy and magnetic structure of X-type hexaferrite crystal
M. Komabuchi (2019-05-15)

CerSJ Electronics Division Young Researchrs Award
Development of all-solid-state secondary lithium battery using garnett-type solid-state single-crystal electrolyte
K. Kataoka (2018-11-16)

JSNS: The Japanese Society for Neutron Science
CerSJ: The Ceramic Society of Japan

MLF Publication 2019

1 K. Mukai, M. Yashima, K. Hibino, and T. Terai,
Experimental Visualization of Interstitialcy Diffusion of Li Ion in β-Li_2TiO_3
ACS Appl. Energy Mater., **2** 5481–5489 (2019).

2 S. Goto, H. Kura, H. Yanagihara, E. Kita, M. Tsujikawa, R. Sasaki, M. Shirai, Y. Kobayashi, T. Honda, and K. Ono,
Positive Weiss Temperature in Layered Antiferromagnetic FeNiN for High-Performance Permanent Magnets
ACS Appl. Nano Mater., **2** 6909–6917 (2019).

3 M. Inutsuka, M. Haraguchi, M. Ozawa, N.L. Yamada, and K. Tanaka,
Adhesion Control of Elastomer Sheet on the Basis of Interfacial Segregation of Hyperbranched Polymer
ACS Macro Letters, **8** 267–271 (2019).

4 Y. Sawama, K. Ban, K. Akutsu-Suyama, H. Nakata, M. Mori, T. Yamada, T. Kawajiri, N. Yasukawa, K. Park, Y. Monguchi, Y. Takagi, M. Yoshimura, and H. Sajiki,
Birch-Type Reduction of Arenes in 2-Propanol Catalyzed by Zero-Valent Iron and Platinum on Carbon
ACS Omega, **4** 11522–11531 (2019).

5 Y. Shibuya, K. Katayama, K. Akutsu-Suyama, and A. Yamaguchi,
Continuous mesoporous aluminum oxide film with perpendicularly oriented mesopore channels
ACS Omega, **4** 17890–17893 (2019).

6 H. Fukui, M. Fujimoto, Y. Akahama, A. Sano-Furukawa, and T. Hattori,
Structure change of monoclinic ZrO_2 baddeleyite involving softenings of bulk modulus and atom vibrations
Acta Crystallogr. B, **75** 742–749 (2019).

7 K. Yamashita, K. Komatsu, T. Hattor, S. Machida, and H. Kagi,
Crystal structure of a high-pressure phase of magnesium chloride hexahydrate determined by in-situ X-ray and neutron diffraction methods
Acta Crystallogr. C Struct. Chem., **C75** 1605–1612 (2019).

8 A. Ahadi, T. Kawasaki, S. Harjo, W.-S. Ko, Q.P. Sun, and K. Tsuchiya,
Reversible elastocaloric effect at ultra-low temperatures in nanocrystalline shape memory alloys
Acta Mater., **165** 109–117 (2019).

9 A. Ahadi, R. Khaledialidusti, T. Kawasaki, S. Harjo, A. Barnoush, and K. Tsuchiya,
Neutron diffraction study of temperature-dependent elasticity of B19′ NiTi---Elinvar effect and elastic softening
Acta Mater., **173** 281–291 (2019).

10 K. Osamura, S. Machiya, K. Kajiwara, T. Kawasaki, S. Harjo, Y. Zhang, S. Fujita, Y. Iijima, and D.P. Hampshire,
Inverted-parabolic and weak strain dependencies on the critical current in practical<110> and<100> oriented REBCO tapes
AIP Adv., **9** 75216 (2019).

11 H. Kawasoko, K. Ohoyama, R. Sei, K. Matsumoto, D. Oka, A. Hoshikawa, T. Ishigaki, and T. Fukumura,
Investigation of magnetism and magnetic structure of anti-$ThCr_2Si_2$-type Tb_2O_2Bi by magnetization and neutron diffraction measurements
AIP Adv., **9** 115301 (2019).

12 Y. Zhong, Y. Kurokawa, G. Nagashima, S. Horiike, T. Hanashima, D. Schönke, P. Krautscheid, R.M. Reeve, M. Kläui, and H. Yuasa,
Determination of fine magnetic structure of magnetic multilayer with quasi antiferromagnetic layer by using polarized neutron reflectivity analysis
AIP Adv., **10** 015323 (2019).

13 Y. Wang, X. Dong, X. Tang, H. Zheng, K. Li, X. Lin, L. Fang, G. Sun, X. Chen, L. Xie, C.L. Bull, N.P. Funnell, T. Hattori, A. Sano-Furukawa, J. Chen, D.K. Hensley, G. Cody, Y. Ren, H.H. Lee, and H. Mao,
Pressure-Induced Diels-Alder Reactions in C_6H_6-C_6F_6 Cocrystal towards Graphane Structure
Angew. Chem. Int. Ed. Engl., **58** 1468–1473 (2019).

14 P. Miao, R. Wang, W. Zhu, J. Liu, T. Liu, J. Hu, S. Li, Z. Tan, A. Koda, F. Zhu, E. Feng, Y. Su, T. Kamiyama, Y. Xiao, and F. Pan,
Revealing magnetic ground state of a layered cathode material by muon spin relaxation and neutron scattering experiments
Appl. Phys. Lett., **114** 203901 (2019).

15 K.M. Kojima, M. Hiraishi, H. Okabe, A. Koda, R. Kadono, K. Ide, S. Matsuishi, H. Kumomi, T. Kamiya, and H. Hosono,
Electronic structure of interstitial hydrogen in In-Ga-Zn-O semiconductor simulated by muon
Appl. Phys. Lett., **115** 122104 (2019).

16 T. Sugiura, C. Takahashi, Y. Chuma, M. Fukuda, M. Yamada, U. Yoshida, H. Nakao, K. Ikeda, D. Khan, A.H. Nile, V.A. Bankaitis, and M. Nakano,
Biophysical parameters of the Sec14 phospholipid exchange cycle
Biophys. J., **116** 92–103 (2019).

17 Y. Kameda, Y. Amo, T. Usuki, Y. Umebayashi, K. Ikeda, and T. Otomo,
Origin of the Difference in Ion-Water Distances Determined by X-ray and Neutron Diffraction Measurements for Aqueous NaCl and KCl Solutions
Bull. Chem. Soc. Jpn., **92** 754–767 (2019).

18 M. Toshiyuki, S. Takagi, K. Shimoda, K. Okazaki, Y. Ishikawa, M. Yonemura, Y. Ukyo, T. Fukunaga, and E. Matsubara,
Comprehensive elucidation of crystal structures of lithium-intercalated graphite
Carbon, **142** 513–517 (2019).

19 N. Kitamura, Y. Tanabe, N. Ishida, and Y. Idemoto,
The atomic structure of a $MgCo_2O_4$ nanoparticle for a positive electrode of a Mg rechargeable battery
Chem. Commun., **55** 2517–2520 (2019).

20 M. Harada, K. Kudo, and N.L. Yamada,
Compositional Segregation in Cross Section of Wet Nafion Thin Film on Platinum Surface
Chem. Lett., **48** 51–54 (2019).

21 T. Sugahara, M. Akamatsu, H. Iwase, Y. Takamatsu, K. Sakai, and H. Sakai,
Small-angle neutron scattering study of micelle structure and hydration behavior of oleic acid-based gemini surfactant
Chem. Lett., **48** 1050–1053 (2019).

22 M. Nakano,
Evaluation of interbilayer and transbilayer transfer dynamics of phospholipids using time-resolved small-angle neutron scattering
Chem. Pharm. Bull., **67** 316–320 (2019).

23 S. Benz, R. Missong, G. Ogutu, R. Stoffel, U. Englert, S. Torii, P. Miao, T. Kamiyama, and R. Dronskowski,
Ammonothermal Synthesis, X-Ray and Time-of-Flight Neutron Crystal-Structure Determination, and Vibrational Properties of Barium Guanidinate, $Ba(CN_3H_4)_2$

ChemistryOpen, **8** 327–332 (2019).

24 T. Sato, L.L. Daemen, Y. Cheng, A.J. Ramirez-Cuesta, K. Ikeda, T. Aoki, T. Otomo, and S. Orimo,
Hydrogen-Release Reaction of a Complex Transition Metal Hydride with Covalently Bound Hydrogen and Hydride Ions
Chemphyschem, **20** 1392–1397 (2019).

25 N.V. Mdlovu, F.A. Mavuso, K.-S. Lin, T.-W. Chang, Y. Chen, Y.-H. Tsai, S.S.-S. Wang, C.-M. Wu, N.B. Mdlovu, and Y.-S. Lin,
Iron oxide-pluronic F127 polymer nanocomposites as carriers for doxorubicin drug delivery system
Colloids Surf. A Physicochem. Eng. Asp., **562** 361–369 (2019).

26 M. Ishikado, K. Kodama, R. Kajimoto, M. Nakamura, Y. Inamura, K. Ikeuchi, S. Ji, M. Arai, and S. Shamoto,
Q Dependence of Magnetic Resonance Mode on $FeTe_{0.5}Se_{0.5}$ Studied by Inelastic Neutron Scattering
Condens. Matter., **4** 69 (2019).

27 R. Maruyama, T. Bigault, T. Saerbeck, D. Honecker, K. Soyama, and P. Courtois,
Coherent magnetization rotation of a layered system observed by polarized neutron scattering under grazing incidence geometry
Crystals, **9** 383 (2019).

28 T.-N. Lam, Y.-S. Chou, Y.-J. Chang, T.-R. Sui, A.-F. Yeh, S. Harjo, S.Y. Lee, J. Jain, B.-H. Lai, and E.-W. Huang,
Comparing Cyclic Tension-Compression Effects on CoCrFeMnNi High-Entropy Alloy and Ni-Based Superalloy
Crystals, **9** 420 (2019).

29 T. Matsukawa, T. Honda, H. Ohshita, T. Otomo, and T. Ishigaki,
Average and local structures of κ-phase $CeZrO_4$ crystals by neutron powder diffraction
CrystEngComm, **21** 6335–6339 (2019).

30 M. Sugishima, K. Wada, M. Unno, and K. Fukuyama,
Bilin-metabolizing enzymes: site-specific reductions catalyzed by two different type of enzymes
Curr. Opin. Struct. Biol., **59** 73–80 (2019).

31 T. Nakane, S. Yoneyama, T. Kodama, K. Kikuchi, A. Nakao, T. Ohhara, R. Higashinaka, T.D. Matsuda, Y. Aoki, and W. Fujita,
Magnetic, thermal, and neutron diffraction studies of a coordination polymer: bis(glycolato)cobalt(II)
Dalton Trans., **48** 333 (2019).

32 Y. Idemoto, Y. Mizutani, C. Ishibashi, N. Ishida, and N. Kitamura,
Synthesis, crystal structure and electrode properties of spinel-type $MgCo_{2-x}Mn_xO_4$
Electrochemistry, **87** 220–228 (2019).

33 T. Kawamoto, M. Aoki, T. Kimura, P. Chinapang, T. Mizusawa, N.L. Yamada, F. Nemoto, T. Watanabe, H. Tanida, M. Matsumoto, H. Imai, J. Miyake, K. Miyatake, and J. Inukai,
Sublayered Structures of Hydrated Nafion® Thin Film Formed by Casting on Pt Substrate Analyzed by X-ray Absorption Spectroscopy under Ambient Conditions and Neutron Reflectometry at Temperature of 80°C and Relative Humidity of 30–80%
Electrochemistry, **87** 270–275 (2019).

34 P. Strasser, M. Abe, M. Aoki, S. Choi, Y. Fukao, Y. Higashi, T. Higuchi, H. Iinuma, Y. Ikedo, K. Ishida, T. Ito, T.U. Ito, M. Iwasaki, R. Kadono, O. Kamigaito, S. Kanda, K. Kawagoe, D. Kawall, N. Kawamura, M. Kitaguchi, A. Koda, K.M. Kojima, K. Kubo, M. Matama, Y. Matsuda, Y. Matsudate, T. Mibe, Y. Miyake, T. Mizutani, K. Nagamine, S. Nishimura, T. Ogitsu, N. Saito, K. Sasaki, S. Seo, H.M. Shimizu, K. Shimomura, T. Suehara, M. Tajima, K.S. Tanaka, T. Tanaka, J. Tojo, D. Tomono, H.A. Torii, E. Torikai, A. Toyoda, Y. Tsutsumi, K. Ueno, Y. Ueno, D. Yagi, A. Yamamoto, T. Yamanaka, T. Yamazaki, H. Yasuda, M. Yoshida, and T. Yoshioka,
New precise measurements of muonium hyperfine structure at J-PARC MUSE
EPJ Web Conf., **198** 3 (2019).

35 N. Nagakura, K. Hirota, S. Ieki, T. Ino, Y. Iwashita, M. Kitaguchi, R. Kitahara, J. Koga, K. Mishima, A. Morishita, Y. Nakano, H. Oide, H. Okabe, H. Otono, Y. Seki, D. Sekiba, T. Shima, H. Shimizu, N. Sumi, H. Sumino, K. Taketani, T. Tomita, H. Uehara, T. Yamada, S. Yamashita, M. Yokohashi, and T. Yoshioka,
New project for precise neutron lifetime measurement at J-PARC
EPJ Web Conf. (PPNS2018), **219** 03003 (2019).

36 C. Haddock, K. Hirota, T. Ino, M. Kitaguchi, K. Mishima, N. Oi, T. Shima, H. Shimizu, W.M. Snow, and T. Yoshioka,
A search for deviations from the inverse square law of gravity at nm range using a pulsed neutron beam
EPJ Web Conf. (PPNS2018), **219** 05002 (2019).

37 K. Mishima, T. Otomo, K. Ikeda, and H. Ohshita,
Neutron scattering cross section of diamond nanoparticle
EPJ Web Conf. (PPNS2018), **219** 10005 (2019).

38 T. Yamaguchi, M. Nishino, K. Yoshida, M. Takumi, K. Nagata, and T. Hattori,
Ion hydration and association in an aqueous calcium chloride solution in the GPa range
Eur. J. Inorg. Chem., **2019** 1170–1177 (2019).

39 K. Máthis, D. Drozdenko, G. Németh, S. Harjo, W. Gong, K. Aizawa, M. Yamasaki, and Y. Kawamura,
In-situ investigation of the microstructure evolution in long-period-stacking-ordered (LPSO) magnesium alloys as a function of the temperature
Front. Mater., **6** 270 (2019).

40 T. Hattori, A. Sano-Furukawa, S. Machida, J. Abe, K. Funakoshi, H. Arima, and N. Okazaki,
Development of a technique for high pressure neutron diffraction at 40 GPa with a Paris-Edinburgh press
High Press. Res., **39** 417–425 (2019).

41 J. Sugiyama,
Spin polarized beam for battery materials research: $\mu^{\pm}$SR and β-NMR
Hyperfine Interact., **240** 17 (2019).

42 W. Liao, M. Hashimoto1, S. Manabe, Y. Watanabe, S. Abe, K. Nakano, H. Takeshita, M. Tampo, S. Takeshita, and Y. Miyake,
Negative and Positive Muon-Induced SEU Cross Sections in 28-nm and 65-nm Planar Bulk CMOS SRAMs
IEEE International Reliability Physics Symposium Proceedings, **2019** 8720568 (2019).

43 H. Yamaguchi, K. Sasaki, T. Tanaka, M. Abe, D. Flay, D. Kawall, Tsutomu Mibe, S. Seo, K. Shimomura, Y. Ueno, and P. Winter,
Development of a CW-NMR Probe for Precise Measurement of Absolute Magnetic Field
IEEE Trans. Appl. Supercond., **29** 9000904 (2019).

44 S. Hashimoto, K. Kurozono, K. Yano, T. Yamauchi, K. Shibata, T. Yamada, K. Nakajima, T. Kikuchi, and K. Kamazawa,
Analysis on Enhancement of Thermal Conductivity in Nanofluids
Innovative Materials for Processes in Energy Systems (IMPRES 2019), D309 (2019).

45 Y. Yasui, E. Niwa, M. Matsui, K. Fujii, and M. Yashima,
Discovery of a Rare-Earth-Free Oxide-Ion Conductor $Ca_3Ga_4O_9$ by Screening through Bond Valence-Based Energy Calculations, Synthesis, and Characterization of Structural and Transport Properties
Inorg. Chem., **58** 9460–9468 (2019).

46 R. Kataoka, T. Kimura, K. Sakaki, M. Nozaki, T. Kojima, K. Ikeda, T. Otomo, N. Takeichi, and A. Kamegawa,

Facile Synthesis of LiH-Stabilized Face-Centered-Cubic YH_3 High-Pressure Phase by Ball Milling Process
Inorg. Chem., **58** 13102–13107 (2019).

47 J. Hu, K. Lin, Y. Cao, R. Huang, T. Matsukawa, T. Ishigaki, H. Fischer, K. Kato, T. Honda, K. Ikeda, T. Otomo, K. Ohoyama, J. Deng, J. Chen, and X. Xing,
A case of multifunctional intermetallic compounds: negative thermal expansion coupling with magnetocaloric effect in $(Gd,Ho)(Co,Fe)_2$
Inorg. Chem. Front., **6** 3146–3151 (2019).

48 A. Lavakumar, M.H. Park, S. Gao, A. Shibata, Y. Okitsu, W. Gong, S. Harjo, and N. Tsuji,
In-situ neutron diffraction study on the deformation of a TRIP-assisted multi-phase steel composed of ferrite, austenite and martensite
IOP Conf. Ser. Mater. Sci. Eng., **580** 012036 (2019).

49 H. Mizoguchi, S.-W. Park, K. Kishida, M. Kitano, J. Kim, M. Sasase, T. Honda, K. Ikeda, T. Otomo, and H. Hosono,
Zeolitic Intermetallics: LnNiSi (Ln = La–Nd)
J. Am. Chem. Soc., **141** 3376–3379 (2019).

50 Y. Yasuda, Y. Hidaka, K. Mayumi, T. Yamada, K. Fujimoto, S. Okazaki, H. Yokoyama, and K. Ito,
Molecular Dynamics of Polyrotaxane in Solution Investigated by Quasi-Elastic Neutron Scattering and Molecular Dynamics Simulation: Sliding Motion of Rings on Polymer
J. Am. Chem. Soc., **141** 9655–9663 (2019).

51 S. Koizumi, S. Ueda, T. Inada, Y. Noda, and R.A. Robinson,
Microstructure and water distribution in catalysts for polymer electrolyte fuel cells, elucidated by contrast variation small-angle neutron scattering
J. Appl. Crystallogr., **52** 791–799 (2019).

52 T. Yamada, N. Yano, T. Hosoya, and K. Kusaka,
Single-crystal time-of-flight neutron Laue methods: application to manganese catalase from Thermus thermophilus HB27
J. Appl. Crystallogr., **52** 972–983 (2019).

53 T. Kumada, K. Akutsu, K. Ohishi, T. Morikawa, Y. Kawamura, M. Sahara, J. Suzuki, and N. Torikai,
Development of spin-contrast-variation neutron reflectometry for the structural analysis of multilayer films
J. Appl. Crystallogr., **52** 1054–1060 (2019).

54 T. Fukuda, T. Yamaguchi, T. Kakeshita, S. Harjo, and T. Nakamoto,
Neutron diffraction study on martensitic transformation under compressive stress in an ordered Fe_3Pt
J. Appl. Phys., **126** 25107 (2019).

55 T. Komori, T. Hirose, T. Gushi, K. Toko, T. Hanashima, L. Vila, J.-P. Attanè, K. Amemiya, and T. Suemasu,
Magnetic reversal in rare-earth free $Mn_{4-x}Ni_xN$ epitaxial films below and above Ni composition needed for magnetic compensation around room temperature
J. Appl. Phys., **127** 043903 (2019).

56 M. Ooe, K. Miyata, J. Yoshioka, K. Fukao, F. Nemoto, and N.L. Yamada,
Direct observation of mobility of thin polymer layers via asymmetric interdiffusion using neutron reflectivity measurements
J. Chem. Phys., **151** 244905 (2019).

57 H. Iwase, R. Kawai, K. Morishima, S. Takata, T. Yoshimura, and M. Shibayama,
Rheo-SANS study on relationship between micellar structures and rheological behavior of cationic gemini surfactants in solution
J. Colloid Interface Sci., **538** 357–366 (2019).

58 H. Frielinghaus, K. Koch, V.P. Antonio, Y. Noda, and S. Koizumi,
The locally columnar model for clay/polymer systems: Connections to scattering experiments
J. Colloid Interface Sci., **544** 172–177 (2019).

59 K. Shimizu, H. Hayashida, H. Toda, T. Kai, Y. Matsumoto, and Y. Matsumoto,
Neutron Imaging Analysis of Hydrogen Content in Pure Palladium and Aluminum Alloys
J. Japan Inst. Met. Mater, **83** 434–440 (2019).

60 T. Matsushita, V. Sonnenschein, W. Guo, H. Hayashida, K. Hiroi, K. Hirota, T. Iguchi, D. Ito, M. Kitaguchi, Y. Kiyanagi, S. Kokuryu, W. Kubo, Y. Saito, H.M. Shimizu, T. Shinohara, S. Suzuki, H. Tomita, Y. Tsuji, and N. Wada,
Generation of $^4He_2^*$ Clusters via Neutron-^{3}He Absorption Reaction towards Visualization of Full Velocity Field in Quantum Turbulence
J. Low Temp. Phys., **196** 275–282 (2019).

61 K. Asami, M. Shiraiwa, J. Ueda, K. Fujii, K. Hongo, R. Maezono, M.G. Brik, M. Yashima, and S. Tanabe,
Crystal structure analysis and evidence of mixed anion coordination at the Ce^{3+} site in $Y_3Al_2(Al,Si)_3(O,N)_{12}$ oxynitride garnet phosphor
J. Mater. Chem. C Mater., **7** 1330–1336 (2019).

62 S. Fujiwara, F. Kono, T. Matsuo, Y. Sugimoto, T. Matsumoto, A. Narita, and K. Shibata,
Dynamic properties of human-synuclein related to propensity to amyloid fibril formation
J. Mol. Biol., **431** 3229–3245 (2019).

63 A. Hyde, M. Ohshio, C.V. Nguyen, S. Yusa, N.L. Yamada, and C.M. Phan,
Surface Properties of the Ethanol/Water Mixture: Thickness and Composition
J. Mol. Liq., **290** 111005 (2019).

64 H. Abe, T. Takekiyo, Y. Yoshimura, and A. Shimizu,
Static and dynamic properties of nano-confined water in room-temperature ionic liquids
J. Mol. Liq., **290** 111216 (2019).

65 K. Yoshida, T. Zenin, A. Fujiyoshi, Y. Sanada, T. Yamaguchi, K. Murata, S. Takata, K. Hiroi, T. Takekiyo, and Y. Yoshimura,
The effect of alkyl ammonium ionic liquids on thermal denaturation aggregation of β-lactoglobulin
J. Mol. Liq., **293** 111477 (2019).

66 S. Ohira-Kawamura, R. Takahashi, M. Ishikado, Y. Yamauchi, M. Nakamura, K. Ohuchi, H. Kira, W. Kambara, K. Aoyama, Y. Sakaguchi, M. Watanabe, and T. Oku,
Cryogenic sample environments shared at the MLF, J-PARC
J. Neutron Res., **21** 17–22 (2019).

67 Y. Sakaguchi, R. Takahashi, S. Kasai, K. Ohuchi, and T. Morikawa,
Sample environment equipment for light irradiation experiments at J-PARC
J. Neutron Res., **21** 23–28 (2019).

68 Y. Sakaguchi, S. Takata, H. Arima, and R. Takahashi,
High temperature furnace for small-angle neutron scattering instrument at J-PARC
J. Neutron Res., **21** 29–38 (2019).

69 M. Watanabea and H. Nojiri,
Pulsed magnet system at MLF in J-PARC
J. Neutron Res., **21** 39–45 (2019).

70 H. Ishikawa, T. Kai, H. Sato, and T. Kamiyama,
Neutron spectrum change with thermal moderator temperature in a compact electron accelerator-driven neutron source and its effects on spectroscopic neutron transmission imaging
J. Nucl. Sci. Technol., **56** 221 (2019).

71 A. Kimura, S. Nakamura, K. Terada, T. Nakao, K. Mizuyama, N.

Iwamoto, O. Iwamoto, H. Harada, T. Katabuchi, M. Igashira, T. Sano, Y. Takahashi, C.H. Pyeon, S. Fukutani, T. Fujii, T. Yagi, K. Takamiya, and J. Hori,
Measurements of the ^{243}Am neutron capture and total cross sections with ANNRI at J-PARC
J. Nucl. Sci. Technol., **56** 479–492 (2019).

72 M. Hirai, S. Ajito, S. Arai, M. Adachi, R. Shimizu, K. Wakamatsu, S. Takata, and H. Iwase,
Observation of protein and lipid membrane structures in a model mimicking the molecular-crowding environment of cells using neutron scattering and cell debris
J. Phys. Chem. B, **123** 3189–3198 (2019).

73 Y. Kameda, K. Sato, R. Hasebe, Y. Amo, T. Usuki, Y. Umebayashi, K. Ikeda, and T. Otomo,
Solvation Structure of Li+ in Methanol and 2-Propanol Solutions Studied by ATR-IR and Neutron Diffraction with ^{6}Li/^{7}Li Isotopic Substitution Methods
J. Phys. Chem. B, **123** 4967–4975 (2019).

74 N. Nishi, J. Uchiyashiki, Y. Ikeda, S. Katakura, T. Oda, M. Hino, and N.L. Yamada,
Potential-Dependent Structure of the Ionic Layer at the Electrode Interface of an Ionic Liquid Probed Using Neutron Reflectometry
J. Phys. Chem. C, **123** 9223–9230 (2019).

75 H. Akiba, H. Kobayashi, H. Kitagawa, K. Ikeda, T. Otomo, T. Yamamoto, S. Matsumura, and O. Yamamuro,
Structural and Thermodynamic Studies of Hydrogen Absorption/Desorption Processes on PdPt Nanoparticles
J. Phys. Chem. C, **123** 9471–9478 (2019).

76 M. Russina, G. Gunther, V. Grzimek, M.C. Schlegel, C.M. Veziri, G.N. Karanikolos, T. Yamada, and F. Mezei,
Nanoscale Dynamics and Transport in Highly Ordered Low-Dimensional Water
J. Phys. Chem. Lett., **10** 6339–6344 (2019).

77 S. Fujiwara, T. Matsuo, Y. Sugimoto, and K. Shibata,
Segment Motions of Proteins under Non-native States Evaluated Using Quasielastic Neutron Scatering
J. Phys. Chem. Lett., **10** 7505–7509 (2019).

78 R.Y. Umetsu, M. Tsujikawa, K. Saito, K. Ono, T. Ishigaki, R. Kainuma, and M. Shirai,
Atomic ordering, magnetic properties, and electronic structure of Mn_2CoGa Heusler alloy
J. Phys. Condens. Matter., **31** 65801 (2019).

79 Y. Nakazawa, H. Iinuma, Y. Iwata, Y. Iwashita, M. Otani, N. Kawamura, T. Mibe, T. Yamazaki, M. Yoshida, R. Kitamura, Y. Kondo, K. Hasegawa, T. Morishita, N. Saito, Y. Sue, N. Hayashizaki, and H. Yasuda,
Development of Inter-Digital H-Mode Drift-Tube Linac Prototype with Alternative Phase Focusing for a Muon Linac in the J-PARC Muon G-2/EDM Experiment
J. Phys. Conf. Ser., **1350** 012054 (2019).

80 M. Otani, Y. Fukao, K. Futatsukawa, N. Kawamura, S. Matoba, T. Mibe, Y. Miyake, K. Shimomura, T. Yamazaki, K. Hasegawa, R. Kitamura, Y. Kondo, T. Morishita, T. Iijima, K. Inami, Y. Sue, M. Yotsuzuka, H. Iinuma, Y. Nakazawa, K. Ishida, N. Saito, and H. Yasuda,
Negative Muonium Ion Production With a C12A7 Electride Film
J. Phys. Conf. Ser., **1350** 012067 (2019).

81 K. Kaneko, M.D. Frontzek, M. Matsuda, A. Nakao, K. Munakata, T. Ohhara, M. Kakihana, Y. Haga, M. Hedo, T. Nakama, and Y. Onuki,
Unique Helical Magnetic Order and Field-Induced Phase in Trillium Lattice Antiferromagnet EuPtSi
J. Physical Soc. Japan, **88** 013702 (2019).

82 T. Kim, K. Park, J.C. Leiner, and J.-G. Park,
Hybridization and Decay of Magnetic Excitations in Two-Dimensional Triangular Lattice Antiferromagnets
J. Physical Soc. Japan, **88** 081003 (2019).

83 S. Itoh and Y. Endoh,
Neutron Brillouin Scattering and Low-Q Dynamics in Condensed Matter
J. Physical Soc. Japan, **88** 081004 (2019).

84 K. Iwasa,
Neutron Scattering Studies on $4f^2$-Electron Multipoles in Pr-based Systems
J. Physical Soc. Japan, **88** 081005 (2019).

85 T. Nakajima and T. Arima,
Observation of magnetic skyrmions by neutron scattering
J. Physical Soc. Japan, **88** 081006 (2019).

86 S. Asano, K.M. Suzuki, K. Kudo, I. Watanabe, A. Koda, R. Kadono, T. Noji, Y. Koike, T. Taniguchi, S. Kitagawa, K. Ishida, and M. Fujita,
Oxidation Annealing Effects on the Spin-Glass-Like Magnetism and Appearance of Superconductivity in T-type $La_{1-x/2}Eu_{1-x/2}Sr_xCuO_4$ ($0.14 \leq x \leq 0.28$)*
J. Physical Soc. Japan, **88** 84709 (2019).

87 R. Kajimoto, K. Nakajima, M. Fujita, M. Ishikado, S. Torii, Y. Ishikawa, P. Miao, and T. Kamiyama,
Crystal Structures of Highly Hole-Doped Layered Perovskite Nickelate $Pr_{2-x}Sr_xNiO_4$ Studied by Neutron Diffraction
J. Physical Soc. Japan, **88** 114602 (2019).

88 Y. Idemoto, F. Tejima, N. Ishida, and N. Kitamura,
Average, electronic, and local structures of $LiMn_{2-x}Al_xO_4$ in charge-discharge process by neutron and synchrotron X-ray
J. Power Sources, **410-411** 38–44 (2019).

89 N. Kitamura, Y. Kubo, N. Ishida, and Y. Idemoto,
Study of atomic ordering across the layer in lithium-rich layered positive electrode material towards preparation process optimization
J. Power Sources, **437** 226905 (2019).

90 K. Ninomiya, T.U. Ito, W. Higemoto, N. Kawamura, P. Strasser, T. Nagatomo, K. Shimomura, Y. Miyake, M. Kita, A. Shinohara, K.M. Kubo, and T. Miura,
Negative muon capture ratios for nitrogen oxide molecules
J. Radioanal. Nucl. Chem., **319** 767 (2019).

91 G. Yoshida, K. Ninomiya, M. Inagaki, W. Higemoto, P. Strasser, N. Kawamura, K. Shimomura, Y. Miyake, T. Miura, K.M. Kubo, and A. Shinohara,
Initial quantum levels of captured muons in CO, CO_2, and COS
J. Radioanal. Nucl. Chem., **320** 283 (2019).

92 K. Ninomiya, T. Kudo, P. Strasser K. Terada, Y. Kawai, M. Tampo, Y. Miyake, A. Shinohara, and K.M. Kubo,
Development of non-destructive isotopic analysis methods using muon beams and their application to the analysis of lead
J. Radioanal. Nucl. Chem., **320** 801 (2019).

93 W. Huang, K. Yoshino, S. Hori, K. Suzukia, M. Yonemura, M. Hirayama, and R. Kanno,
Superionic lithium conductor with a cubic argyrodite-type structure in the Li–Al–Si–S system
J. Solid State Chem., **270** 487–492 (2019).

94 T. Kawamoto, M. Aoki, T. Kimura, T. Mizusawa, N.L. Yamada, J. Miyake, K. Miyatake, and J. Inukai,
In-Plane Distribution of Water inside Nafion Thin Film Analyzed by Neutron Reflectivity at Temperature of 80°C and Relative Humidity of 30-80% Based on 4-Layered Structural Model
Jpn. J. Appl. Phys., **58** SIID01 (2019).

95 Y. Kitanaka, K. Makisumi, Y. Noguchi, M. Miyayama, A. Hoshikawa, and T. Ishigaki,
Composition-driven structural variation in ferrielectric phase of $(Bi_{1/2}Na_{1/2})TiO_3$-$Ba(Mg_{1/3}Nb_{2/3})O_3$
Jpn. J. Appl. Phys., **58** SLLA04 (2019).

96 S. Koizumi and Y. Noda,
A Variety of Small-angle Neutron Scattering Instruments Available in Tokyo Area, Japan —Complimentary Use of Accelerator and Reactor—
JPS Conf. Proc., **25** 11004 (2019).

97 K. Kusaka, T. Yamada, N. Yano, T. Hosoya, T. Ohhara, and I. Tanaka,
Current Status and Future Prospects of Single Crystal Neutron Diffractometer iBIX
JPS Conf. Proc., **25** 11005 (2019).

98 I. Tanaka,
Necessity and Effectiveness of a Biological Diffractometer for Installation in Second Target Station as a New Neutron Pulsed Source in Japan
JPS Conf. Proc., **25** 11015 (2019).

99 K. Akutsu-Suyama, Y. Hasegawa, T. Niizeki, S. Suzuki, H. Aoki, and F. Nemoto,
Neutron Reflectometry Study of Penetration of Protective Coating Material by Deuterated Sodium Pyruvate
JPS Conf. Proc., **25** 11018 (2019).

100 T. Inada, S. Ueda, Y. Noda, T. Maeda, K. Kanie, and S. Koizumi,
Micellar Structure of Perfluorooctanesulfonic Acid in Water Investigated by Combination of SAXS and SANS
JPS Conf. Proc., **25** 11019 (2019).

101 M. Watanabe, H. Nojiri, S. Itoh, S. Ohira-Kawamura, T. Kihara, T. Masuda, T. Sahara, M. Soda, and R. Takahashi,
Development of Compact High Field Pulsed Magnet System for New Sample Environment Equipment at MLF in J-PARC
JPS Conf. Proc., **25** 11024 (2019).

102 Y. Onuki and S. Sato,
Anomalous Twinning as the Macroscopic Deformation Mechanism for AZ31 Magnesium Alloy
Key Eng. Mater., **810** 95–100 (2019).

103 T. Sakamaki, Y. Inutsuka, K. Igata, K. Higaki, N.L. Yamada, Y. Higaki, and A. Takahara,
Ion-Specific Hydration States of Zwitterionic Poly (sulfobetaine methacrylate) Brushes in Aqueous Solutions
Langmuir, **35** 1583–1589 (2019).

104 T. Miyazaki, N. Miyata, M. Asada, Y. Tsumura, N. Torikai, H. Aoki, K. Yamamoto, T. Kanaya, D. Kawaguchi, and K. Tanaka,
Elucidation of a Heterogeneous Layered Structure in the Thickness Direction of Poly(vinyl alcohol) Films with Solvent Vapor-Induced Swelling
Langmuir, **35** 11099–11107 (2019).

105 K. Imwiset, T. Hayakawa, Y. Fukushima, T. Yamada, and M. Ogawa,
Novel flexible supramolecular assembly of dioleyldimethylammonium ion in a two-dimensional nanospace studied by neutron scattering
Langmuir, **35** 13977–13982 (2019).

106 M. Shibayama, Y. Shudo, and A. Izumi,
Phenolic Resins - Recent Progress of Structure and Properties Investigations
Macromol. Symp., **385** 1800156 (2019).

107 K. Yamamoto, E. Ito, and Y. Mori,
SAXS and SANS studies on the phase-separated network structure of amphiphilic copolymer composed of poly(dimethyl siloxane) and poly(N,N-dimethyl acrylamide) gels swollen in water and a water/methanol mixture
Macromol. Symp., **385** 1800181 (2019).

108 F. Kaneko, A. Radulescu, H. Iwase, S. Takata, M. Nishiura, and Z. Hou,
Complexation of syndiotactic polystyrene with branched molecules
Macromol. Symp., **386** 1900008 (2019).

109 S. Lee, W. Lee, N.L. Yamada, K. Tanaka, J.H. Kim, H. Lee, and D.Y. Ryu,
Instability of Polystyrene Film and Thermal Behaviors Mediated by Unfavorable Silicon Oxide Inter-layer
Macromolecules, **52** 7524–7530 (2019).

110 N. Itagaki, D. Kawaguchi, Y. Oda, N.L. Yamada, T. Yamaguchi, and K. Tanaka,
A Surface Effect on Frictional Properties for Thin Hydrogel Films of Poly(vinyl ether)
Macromolecules, **52** 9632 (2019).

111 Y. Tomota, M. Ojima, S. Harjo, W. Gong, S. Sato, and T. Ungár,
Dislocation densities and intergranular stresses of plastically deformed austenitic steels
Mater. Sci. Eng. A Struct. Mater., **743** 32–39 (2019).

112 H. Chae, E.-W. Huang, J. Jain, H. Wang, W. Woo, S.-W. Chen, S. Harjo, T. Kawasaki, and S.Y. Lee,
Plastic anisotropy and deformation-induced phase transformation of additive manufactured stainless steel
Mater. Sci. Eng. A Struct. Mater., **762** 138065 (2019).

113 Y. Koyanagi, S. Ueta, T. Kawasaki, S. Harjo, K. Cho, and H.Y. Yasuda,
Investigation of strengthening mechanism in Ni–38Cr-3.8 Al alloy with fine lamellar structure by in situ neutron diffraction analysis
Mater. Sci. Eng. A Struct. Mater., **773** 138822 (2019).

114 M.-M. Schiavone, H. Iwase, S. Takata, and A. Radulescu,
The multilevel structure of sulfonated syndiotactic-polystyrene model polyelectrolyte membranes resolved by extended Q-range contrast variation SANS
Membranes, **9** 136 (2019).

115 Y. Onuki, T. Hirano, A. Hoshikawa, S. Sato, and T. Tomida,
In Situ Observation of Bainite Transformation and Simultaneous Carbon Enrichment in Austenite in Low-Alloyed TRIP Steel Using Time-of-Flight Neutron Diffraction Techniques
Metall. Mater. Trans. A Phys. Metall. Mater. Sci., **50** 4977–4986 (2019).

116 K. Kiriyama, S. Zhang, H. Hayashida, J. Suzuki, and T. Kuwabara,
Development of a biaxial tensile testing machine for pulsed neutron experiments
MethodsX, **6** 2166–2175 (2019).

117 K. Nagura, A. Bogdanov, N. Chumakova, A.K. Vorobiev, S. Moronaga, H. Imai, T. Matsuda, Y. Noda, T. Maeda, S. Koizumi, K. Sakamoto, T. Amano, F. Yoshino, T. Kato, N. Komatsu, and R. Tamura,
Size-tunable MRI-visible nitroxide-based magnetic mixed micelles: preparation, stability, and theranostic application
Nanotechnology, **30** 224002 (2019).

118 Y. Fujishiro, N. Kanazawa, T. Nakajima, X.Z. Yu, K. Ohishi, Y. Kawamura, K. Kakurai, T. Arima, H. Mitamura, A. Miyake, K. Akiba, M. Tokunaga, A. Matsuo, K. Kindo, T. Koretsune, R. Arita, and Y. Tokura,
Topological transitions among skyrmion- and hedgehog-lattice states in cubic chiral magnets
Nat. Commun., **10** 1059 (2019).

119 K. Nawa, K. Tanaka, N. Kurita, T.J. Sato, H. Sugiyama, H. Uekusa, S. Ohira-Kawamura, K. Nakajima, and H. Tanaka,
Triplon band splitting and topologically protected edge states in the dimerized antiferromagnet
Nat. Commun., **10** 2096 (2019).

120 K. Fukui, S. Iimura, T. Tada, S. Fujitsu, M. Sasase, H. Tamatsukuri, T. Honda, K. Ikeda, T. Otomo, and H. Hosono,
Characteristic fast H– ion conduction in oxygen-substituted lanthanum hydride
Nat. Commun., **10** 2578(1–7) (2019).

121 J. Wang, K. Ran, S. Li, Z. Ma, S. Bao, Z. Cai, Y. Zhang, K. Nakajima, S. Ohira-Kawamura, P. Cermak, A. Schneidewind, S. Savrasov, X. Wan, and J. Wen,
Evidence for singular-phonon-induced nematic superconductivity in a topological superconductor candidate Sr0.1Bi2Se3
Nat. Commun., **10** 2802 (2019).

122 M. Hirschberger, T. Nakajima, S. Gao, L. Peng, A. Kikkawa, T. Kurumaji, M. Kriener, Y. Yamasaki, H. Sagayama, H. Nakao, K. Ohishi, K. Kakurai, Y. Taguchi, X. Yu, T. Arima, and Y. Tokura,
Skyrmion phase and competing magnetic orders on a breathing Kagome lattice
Nat. Commun., **10** 5831 (2019).

123 B. Li, Y. Kawakita, S. Ohira-Kawamura, T. Sugahara, H. Wang, J. Wang, Y. Chen, S.I. Kawaguchi, K. Ohara, S. Kawaguchi, K. Li, D. Yu, R. Mole, T. Hattori, T. Kikuchi, S. Yano, Z. Zhang, Z. Zhang, W. Ren, S. Lin, O. Sakata, K. Nakajima, and Z. Zhang,
Colossal barocaloric effects in plastic crystals
Nature, **567** 506–510 (2019).

124 Y. Onodera, Y. Takimoto, H. Hijiya, T. Taniguchi, S. Urata, S. Inaba, S. Fujita, I. Obayashi, Y. Hiraoka, and S. Kohara,
Origin of the mixed alkali effect in silicate glass
NPG Asia Mater., **11** 75 (2019).

125 M. Hagihala, S. Hayashida, M. Avdeev, H. Manaka, H. Kikuchi, and T. Masuda,
Magnetic states of coupled spin tubes with frustrated geometry in $CsCrF_4$
NPJ Quantum Mater., **4** 14 (2019).

126 Y. Noda, and S. Koizumi,
Dynamic nuclear polarization apparatus for contrast variation neutron scattering experiments on iMATERIA spectrometer at J-PARC
Nucl. Instrum. Methods Phys. Res. A, **923** 127–133 (2019).

127 A.S. Tremsin, T. Shinohara, K. Oikawa, Jiaqi Li, and P.J.M. Monteiro,
Non-destructive mapping of water distribution through white-beam and energy-resolved neutron imaging
Nucl. Instrum. Methods Phys. Res. A, **927** 174–183 (2019).

128 M. Teshigawara, Y. Tsuchikawa, G. Ichikawa, S. Takata, K. Mishima, M. Harada, M. Ooi, Y. Kawamura, T. Kai, S. Ohira-Kawamura, K. Nakajima, Y. Ikeda, and Y. Kiyanagi,
Measurement of neutron scattering cross section of nano-diamond with particle diameter of approximately 5 nm in energy range of 0.2 meV to 100 meV
Nucl. Instrum. Methods Phys. Res. A, **929** 113–120 (2019).

129 A.D. Pant, T. Adachi, P. Strasser, Y. Ikedo, Y. Oishi, J. Nakamura, W. Higemoto, K. Shimomura, R. Kadono, Y. Miyake, and E. Torikai,
Characterization and optimization of ultra slow muon beam at J-PARC/MUSE: A simulation study
Nucl. Instrum. Methods Phys. Res. A, **929** 129–133 (2019).

130 Y. Nakazawa, S. Baeb, H. Choib, S. Choib, T. Iijimad, H. Iinuma, N. Kawamura, R. Kitamura, B. Kim, H.S. Ko, Y. Kondo, T. Mibe, M. Otani, G.P. Razuvaev, N. Saito, Y. Sue, E. Won, T. Yamazaki, and H. Yasuda,
Beam commissioning of muon beamline using negative hydrogen ions generated by ultraviolet light
Nucl. Instrum. Methods Phys. Res. A, **937** 164 (2019).

131 M. Otani, R. Kitamura, Y. Fukao, K. Hasegawa, K. Ishida, N. Kawamura, Y. Kondo, Y. Miyake, N. Saito, K. Shimomura, and P. Strasser,
Response of microchannel plates to positrons from muon-decays
Nucl. Instrum. Methods Phys. Res. A, **943** 162475 (2019).

132 S. Shimizu, K. Horie, Y. Igarashi, H. Ito, K. Kamada, S. Kimura, A. Kobayashi, M. Mihara, A. Yamaji, and A. Yoshikawa,
A new experimental method to search for T-violation using a sequential CeF_3 scintillating calorimeter
Nucl. Instrum. Methods Phys. Res. A, **945** 162587 (2019).

133 M. Otani, Y. Sue, K. Futatsukawa, T. Iijima, H. Iinuma, N. Kawamura, R. Kitamura, Y. Kondo, T. Morishita, Y. Nakazawa, H. Yasuda, M. Yotsuzuka, N. Saito, and T. Yamazaki,
Compact buncher cavity for muons accelerated by a radio-frequency quadrupole
Nucl. Instrum. Methods Phys. Res. A, **946** 162693 (2019).

134 T. Hosobata, N.L. Yamada, M. Hino, H. Yoshinaga, F. Nemoto, K. Hori, T. Kawai, Y. Yamagata, M. Takeda, and S. Takeda,
Elliptic neutron-focusing supermirror for illuminating small samples in neutron reflectometry
Opt. Express, **27** 26807 (2019).

135 S. Kobayashi, R. Kawagoe, H. Murakami, K. Ohishi, Y. Kawamura, and J. Suzuki,
Thermal aging effects on magnetisation reversals in a predeformed Fe-1wt%Cu alloy studied via first-order reversal curves
Philos. Mag. Lett., **99** 217–225 (2019).

136 K. Akutsu-Suyama, S. Mori, and T. Hanashima,
Design and Characterization of a 2-(2′-Hydroxyphenyl)benzimidazole-Based Sr^{2+}-Selective Fluorescent Probe in Organic and Micellar Solution Systems
Photochem. Photobiol. Sci., **18** 2531–2538 (2019).

137 K.L. Browning, J.F. Browning, M. Doucet, N.L. Yamada, G. Liu, and G.M. Veith,
Role of conductive binder to direct solid-electrolyte interphase formation over silicon anodes
Phys. Chem. Chem. Phys., **21** 17356 (2019).

138 K. Akutsu-Suyama, M. Cagnes, K. Tamura, T. Kanaya, and T.A. Darwish,
Controlled deuterium labelling of imidazolium ionic liquids to probe the fine structure of the electrical double layer using neutron reflectometry
Phys. Chem. Chem. Phys., **21** 17512–17516 (2019).

139 T. Takamuku, H. Sakurai, A. Ogawa, A. Tashiro, M. Kawano, Y. Kawazu, K. Sadakane, H. Iwase, and K. Ozutsumi,
Effects of the long octyl chain on complex formation of nickel(II) with dimethyl sulfoxide, methanol, and acetonitrile in Ionic liquid of $[C_8mim][TFSA]$
Phys. Chem. Chem. Phys., **21** 3154–3163 (2019).

140 A. Kyono, M. Kato, A. Sano-Furukawa, S. Machida, and T. Hattori,
Crystal structure change of katoite, $Ca_3Al_2(O_4D_4)_3$, with temperature at high pressure
Phys. Chem. Miner., **46** 459–469 (2019).

141 H. Kadowaki, M. Wakita, B. Fåk, J. Ollivier, S. Ohira-Kawamura, K. Nakajima, and J.W. Lynn,
Spin correlations of quantum-spin-liquid and quadrupole-ordered states of $Tb_{2+x}Ti_{2-x}O_{7+y}$
Phys. Rev. B, **99** 014406 (2019).

142 J. Yamaura, H. Hiraka, S. Iimura, Y. Muraba, J. Bang, K. Ikeuchi, M. Nakamura, Y. Inamura, T. Honda, M. Hiraishi, K.M. Kojima, R. Kadono, Y. Kuramoto, Y. Murakami, S. Matsuishi, and H. Hosono,
Quantum dynamics of hydrogen in the iron-based superconductor $LaFeAsO_{0.9}D_{0.1}$ measured with inelastic neutron spectroscopy
Phys. Rev. B, **99** 220505(R) (2019).

143 K. Matan, T. Ono, G. Gitgeatpong, K. de Roos, M. Ping, S. Torii, T.

Kamiyama, A. Miyata, A. Matsuo, K. Kindo, S. Takeyama, Y. Nambu, P. Piyawongwatthana, T.J. Sato, and H. Tanaka,
Magnetic structure and high-field magnetization of the distorted kagome lattice antiferromagnet $Cs_2Cu_3SnF_{12}$
Phys. Rev. B, **99** 224404 (2019).

144 K.P. Kramer, M. Horio, S.S. Tsirkin, Y. Sassa, K. Hauser, C.E. Matt, D. Sutter, A. Chikina, N.B.M. Schröter, J.A. Krieger, T. Schmitt, V.N. Strocov, N.C. Plumb, M. Shi, S. Pyon, T. Takayama, H. Takagi, T. Adachi, T. Ohgi, T. Kawamata, Y. Koike, and T. Kondo,
Band structure of overdoped cuprate superconductors: Density functional theory matching experiments
Phys. Rev. B, **99** 224509 (2019).

145 K. Iida, Y. Nagai, S. Ishida, M. Ishikado, N. Murai, A.D. Christianson, H. Yoshida, Y. Inamura, H. Nakamura, A. Nakao, K. Munakata, D. Kagerbauer, M. Eisterer, K. Kawashima, Y. Yoshida, H. Eisaki, and A. Iyo,
Coexisting spin resonance and long-range magnetic order of Eu in $EuRbFe_4As_4$
Phys. Rev. B, **100** 014506 (2019).

146 S. Klotz, M. Casula, K. Komatsu, S. Machida, and T. Hattori,
High-pressure structure and electronic properties of YbD_2 to 34 GPa
Phys. Rev. B, **100** 0210101(R) (2019).

147 H. Suzuki, A. Nambu, and M. Okamoto,
X-ray magnetic circular dichroism and neutron diffraction measurements of the magnetic moment of titanium in $Sm(Fe_{0.8}Co_{0.2})_{11}Ti$
Phys. Rev. B, **100** 144443 (2019).

148 H. Tamatsukuri, S. Mitsuda, T. Shimizu, M. Fujihala, H. Yokota, K. Takehana, Y. Imanaka, A. Nakao, and K. Munakata,
Nonlinear piezomagnetoelectric effect in $CuFeO_2$
Phys. Rev. B, **100** 201105 (2019).

149 S. Ideta, N. Murai, M. Nakajima, R. Kajimoto, and K. Tanaka,
Experimental investigation of the suppressed superconducting gap and double-resonance mode in $Ba_{1-x}K_xFe_2As_2$
Phys. Rev. B, **100** 235135 (2019).

150 A. Koda, H.T. Hirose, M. Miyazaki, H. Okabe, M. Hiraishi, I. Yamauchi, K.M. Kojima, I. Nagashima, J. Yamaura, Z. Hiroi, and R. Kadono,
Coupled spin-charge-phonon fluctuation in the all-in/all-out antiferromagnet $Cd_2Os_2O_7$
Phys. Rev. B, **100** 245113(1–6) (2019).

151 C.C. Haddock, M. Hiromoto, K. Hirota, T. Ino, M. Kitaguchi, K. Mishima, N. Oi, T. Shima, H.M. Shimizu, W.M. Snow, and T. Yoshioka,
Measurement of the total neutron-scattering cross-section ratios of noble gases of natural isotopic composition using a pulsed neutron beam
Phys. Rev. C, **100** 64002 (2019).

152 J. Guo, L. Yue, K. Iida, K. Kamazawa, L. Chen, T. Han, Y. Zhang, and Y. Li,
Preferred magnetic excitations in the iron-based $Sr_{1-x}Na_xFe_2As_2$ superconductor
Phys. Rev. Lett., **122** 017001 (2019).

153 H. Wo, Q. Wang, Y. Shen, X. Zhang, Y. Hao, Y. Feng, S. Shen, Z. He, B. Pan, W. Wang, K. Nakajima, S.O. -Kawamura, P. Steffens, M. Boehm, K. Schmalzl, J.T. Park, T.R. Forrest, M. Matsuda, Y. Zhao, J.W. Lynn, Z. Yin, and J. Zhao,
Coexistence of ferromagnetic and stripe-type antiferromagnetic spin fluctuations in YFe_2Ge_2
Phys. Rev. Lett., **122** 217003 (2019).

154 M. Mogi, T. Nakajima, V. Ukleev, A. Tsukazaki, R. Yoshimi, M. Kawamura, K.S. Takahashi, T. Hanashima, K. Kakurai, T. Arima, M. Kawasaki, and Y. Tokura,
Large Anomalous Hall Effect in Topological Insulators with Proximitized Ferromagnetic Insulators
Phys. Rev. Lett., **123** 016804 (2019).

155 N. Kurita, D. Yamamoto, T. Kanesaka, N. Furukawa, S. Ohira-Kawamura, K. Nakajima, and H. Tanaka,
Localized magnetic excitations in the fully frustrated dimerized magnet $Ba_2CoSi_2O_6Cl_2$
Phys. Rev. Lett., **123** 027206 (2019).

156 M. Matsuura, T. Sasaki, S. Iguchi, E. Gati, J. Müller, O. Stockert, A. Piovano, M. Böhm, J.T. Park, S. Biswas, S.M. Winter, R. Valentí, A. Nakao, and M. Lang,
Lattice Dynamics Coupled to Charge and Spin Degrees of Freedom in the Molecular Dimer-Mott Insulator κ–(BEDT–TTF)$_2$Cu[N(CN)$_2$]Cl
Phys. Rev. Lett., **123** 027601 (2019).

157 Y. Sakaguchi, T. Hanashima, A.-A.A. Simon, and M. Mitkova,
Structural transformation in Ge_xS_{100-x} ($10 \leq x \leq 40$) network glasses: Structural varieties in short-range, medium-range, and nanoscopic scale
Phys. Rev. Mater., **3** 35601 (2019).

158 J.N. Hendriks, A.W.T. Gregg, R.R. Jackson, C.M. Wensrich, A. Wills, A.S. Tremsin, T. Shinohara, V. Luzin, and O. Kirstein,
Tomographic reconstruction of triaxial strain fields from Bragg-edge neutron imaging
Phys. Rev. Mater., **3** 113803 (2019).

159 R. Kajimoto, M. Ishikado, H. Kira, K. Kaneko, M. Nakamura, K. Kamazawa, Y. Inamura, K. Ikeuchi, K. Iida, N. Murai, S. Ohira-Kawamura, R. Takahashi, K. Aoyama, and W. Kambara,
Study on use of superconducting magnet and first inelastic neutron scattering experiment under magnetic field at 4SEASONS spectrometer
Physica B Condens. Matter., **556** 26–30 (2019).

160 R. Kajimoto, T. Yokoo, M. Nakamura, Y. Kawakita, M. Matsuura, H. Endo, H. Seto, S. Itoh, K. Nakajima, and S. Ohira-Kawamura,
Status of neutron spectrometers at J-PARC
Physica B Condens. Matter., **562** 148–154 (2019).

161 T. Kikuchi, K. Nakajima, S. Ohira-Kawamura, Y. Inamura, M. Nakamura, D. Wakai, K. Aoyama, T. Iwahashi, and W. Kambara,
Background issues encountered by cold-neutron chopper spectrometer AMATERAS
Physica B Condens. Matter., **564** 45–53 (2019).

162 M. Nakamura, T. Kikuchi, and Y. Kawakita,
Applicability and limitations of G(r, E) analysis transformed from the inelastic neutron scattering data
Physica B Condens. Matter., **567** 61–64 (2019).

163 S. Itoh, T. Yokoo, T. Masuda, S. Asai, H. Saito, D. Kawana, R. Sugiura, T. Asami, and Y. Ihata,
Progress in High Resolution Chopper Spectrometer HRC by improving collimator and Fermi chopper
Physica B Condens. Matter., **568** 76–80 (2019).

164 M. Sakurai, G. Matsuba, K. Sotoyama, K. Nishida, T. Kanaya, and S. Takata,
Molecular weight component dependence of shish-kebab structure of polyethylene blends with X-ray and neutron scattering measurements covering a wide spatial scale
Polym. Cryst., **2** e10034 (2019).

165 H. Aoki,
Chain dynamics in spin-coated films of poly(methyl methacrylate) in a solvent annealing process
Polym. J., **51** 611–616 (2019).

166 T. Maeda, M. Kitagawa, A. Hotta, and S. Koizumi,

Thermo-Responsive Nanocomposite Hydrogels Based on PEG-b-PLGA Diblock Copolymer and Laponite
Polymers, **11** 250 (2019).

167 Y. Ueno, Y. Matsuda, S. Seo, T. Tanaka, H.A. Torii, D. Yagi, H. Yasuda, S. Nishimura, K.I. Sasaki, Y. Sato, K. Shimomura, P. Strasser, H. Yamaguchi, S. Kanda, K.S. Tanaka, T. Yamanaka on behalf of the MuSEUM collaboration,
New Precision Measurement of Muonium Hyperfine Structure
PoS (ICHEP2018), **340** 466 (2019).

168 S. Kanda, K. Ishida, and K. Shimomura,
Precision spectroscopy of exotic atoms involving muons
PoS (ICHEP2018), **341** 138 (2019).

169 M. Abe, S. Bae, G. Beer, G. Bunce, H. Choi, S. Choi, M. Chung, W. da Silva, S. Eidelman, M. Finger, Y. Fukao, T. Fukuyama, S. Haciomeroglu, K. Hasegawa, K. Hayasaka, N. Hayashizaki, H. Hisamatsu, T. Iijima, H. Iinuma, K. Inami, H. Ikeda, M. Ikeno, and K. Ishid,
A New Approach for Measuring the Muon Anomalous Magnetic Moment and Electric Dipole Moment
Prog. Theor. Exp. Phys., **2019** 053C02 (2019).

170 R. Kitahara, K. Hirota, S. Ieki, T. Ino, Y. Iwashita, M. Kitaguchi, J. Koga, K. Mishima, A. Morishita, N. Nagakura, H. Oide, H. Otono, Y. Seki, D. Sekiba, T. Shima, H.M. Shimizu, N. Sumi, H. Sumino, K. Taketani, T. Tomita, T. Yamada, S. Yamashita, and M. Yok,
Improved determination of thermal cross section of $^{14}N(n,p)^{14}C$ for the neutron lifetime measurement
Prog. Theor. Exp. Phys., **2019** 093C01 (2019).

171 Y. Sakaguchi, H. Asaoka, and M. Mitkova,
Kinetics of silver photodiffusion into amorphous S-rich germanium sulphide – neutron and optical reflectivity
Pure Appl. Chem., **91** 1821–1835 (2019).

172 F. Kaneko, T. Kawaguchi, A. Radulescu, H. Iwase, T. Morikawa, S. Takata, M. Nishiura, and Z. Hou,
A new simultaneous measurement system of wide Q-range small angle neutron scattering combined with polarized Fouier transform infrared spectroscopy
Rev. Sci. Instrum., **90** 093906 (2019).

173 T. Wu, A. Ishikawa, T. Honda, H. Tamatsukuri, K. Ikeda, T. Otomo, and S. Matsuishi,
Nephelauxetic effect of the hydride ligand in Sr_2LiSiO_4H as a host material for rare-earth-activated phosphors
RSC Adv., **9** 5282–5287 (2019).

174 S. Hayashida, M. Matsumoto, M. Hagihala, N. Kurita, H. Tanaka, S. Itoh, T. Hong, M. Soda, Y. Uwatoko, and T. Masuda,
Novel Excitations near Quantum Criticality in Geometrically Frustrated Antiferromagnet $CsFeCl_3$
Sci. Adv., **5** eaaw5639 (2019).

175 K. Sakurai, J. Jiang, M. Mizusawa, T. Ito, K. Akutsu, and N. Miyata,
Neutron visualization of inhomogeneous buried interfaces in thin films
Sci. Rep., **9** 571 (2019).

176 K. Iida, H. Yoshida, H. Okabe, N. Katayama, Y. Ishii, A. Koda, Y. Inamura, N. Murai, M. Ishikado, R. Kadono, and R. Kajimoto,
Quantum magnetisms in uniform triangular lattices $Li_2AMo_3O_8$ (A = In, Sc)
Sci. Rep., **9** 1826 (2019).

177 Y. Kitanaka, M. Miyayama, and Y. Noguchi,
Ferrielectric-mediated morphotropic phase boundaries in Bi-based polar perovskites
Sci. Rep., **9** 4087 (2019).

178 D. Ikuta, E. Ohtani, A. Sano-Furukawa, Y. Shibazaki, H. Terasaki, L. Yuan, and T. Hattori,
Interstitial hydrogen atoms in face-centered cubic iron in the Earth's core
Sci. Rep., **9** 7108 (2019).

179 A. Machida, H. Saitoh, T. Hattori, A. Sano-Furukawa, K. Funakoshi, T. Sato, S. Orimo, and K. Aoki,
Hexagonal closed packed iron hydride behind the conventional phase diagram
Sci. Rep., **9** 12290 (2019).

180 Y. Kitanaka, Y. Noguchi, and M. Miyayama,
Uncovering ferroelectric polarization in tetragonal $(Bi_{1/2}K_{1/2})TiO_3$–$(Bi_{1/2}Na_{1/2})TiO_3$ single crystals
Sci. Rep., **9** 19275 (2019).

181 J.G. Kim, J.W. Bae, J.M. Park, W. Woo, S. Harjo, K.-G. Chin, S. Lee, H.S. Kim Hyoung,
Synergetic strengthening of layered steel sheet investigated using an in situ neutron diffraction tensile test
Sci. Rep., **9** 43837 (2019).

182 A. Shibata, Y. Takeda, N. Park, L. Zhao, S. Harjo, T. Kawasaki, W. Gong, and N. Tsuji,
Nature of dynamic ferrite transformation revealed by in-situ neutron diffraction analysis during thermomechanical processing
Scr. Mater., **165** 44–49 (2019).

183 J.W. Bae, J.G. Kim, J.M. Park, W. Woo, S. Harjo, and H.S. Kim,
In situ neutron diffraction study of phase stress evolution in a ferrous medium-entropy alloy under low-temperature tensile loading
Scr. Mater., **165** 60–63 (2019).

184 F. Endo, N. Kurokawa, K. Tanimoto, H. Iwase, T. Maeda, and A. Hotta,
SANS study on the nano-crystalline network structure of quenched syndiotactic polypropylene gels
Soft Matter, **15** 5521–5528 (2019).

185 N. Ishida, S. Ando, N. Kitamura, and Y. Idemoto,
Crystal structure and cathode properties of delithiated $Li_{1-x}Mn_{1/3}Ni_{1/3}Co_{1/3}O_2$ for Mg rechargeable batteries
Solid State Ion., **343** 115080 (2019).

186 K. Mori, K. Iwase, Y. Oba, K. Ikeda, T. Otomo, and T. Fukunaga,
Structural and electrochemical features of $(Li_2S)_x(SiS_2)_{100-x}$ superionic glasses
Solid State Ion., **344** 115141 (2019).

187 Y. Iizawa, H. Shishido, K. Nishimura, T.D. Vu, K.M. Kojima, T. Koyama, K. Oikawa, M. Harada, S. Miyajima, M. Hidaka, T. Oku, K. Soyama, K. Aizawa, S.Y. Suzuki, and T. Ishida,
Energy-resolved neutron imaging with high spatial resolution using a superconducting delay-line kinetic inductance detector
Supercond. Sci. Technol., **32** 125009 (2019).

188 J. Sugiyama, I. Umegaki, M. Matsumoto, K. Miwa, H. Nozaki, Y. Higuchi, T. Noritake, O.K. Forslund, M. Månsson, S.P. Cottrell, A. Koda, E.J. Ansaldo, and J.H. Brewer,
Desorption reaction in MgH_2 studied with in situ μ^+SR
Sustain. Energy Fuels, **3** 956–964 (2019).

189 K. Hanawa, Y. Onuki, Y. Uemura, A. Hoshikawa, S. Suzuki, H. Otsuka, Y. Chiba, and S. Sato,
Analysis of Reverse Transformation Behavior in Iron-based Alloys Based on Quantitative Microstructure Information by Neutron Diffraction
Tetsu to Hagane, **105** 998–1007 (2019).

Editorial Board - MLF Annual Report 2019

Chief Editor
Kazuhiro Akutsu
CROSS

Takashi Naoe
Neutron Source Section

Miho Igarashi
CROSS

Yukinori Nagatani
Muon Science Section

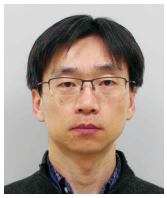

Kazutaka Ikeda
Neutron Science Section

Tazuko Mizusawa
CROSS

Yoshihisa Ishikawa
CROSS

Dai Yamazaki
Neutron Instrumentation Section

Kenichi Oikawa
Neutron Science Section

Taro Yamada
Ibaraki University

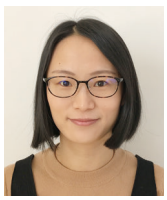

Yuhua Su
Technology Development Section

J-PARC

JAPAN PROTON ACCELERATOR RESEARCH COMPLEX

High Energy Accelerator Research Organization (KEK)
Japan Atomic Energy Agency (JAEA)

http://j-parc.jp/

Materials and Life Science Division
J-PARC Center

https://mlfinfo.jp/en

CROSS

Comprehensive Research Organization for Science and Society

https://neutron.cross.or.jp/en

J-PARC 20-02